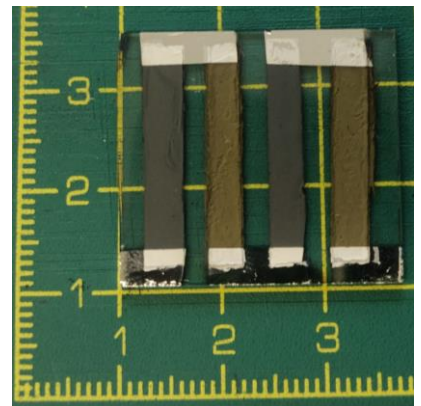
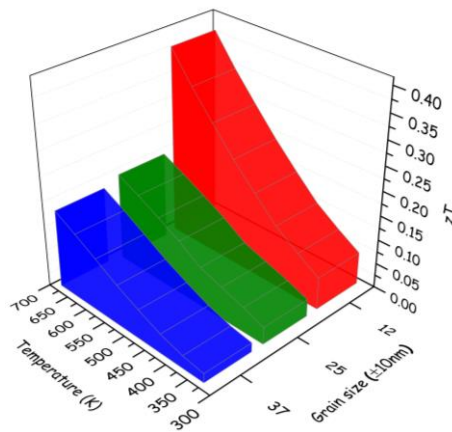
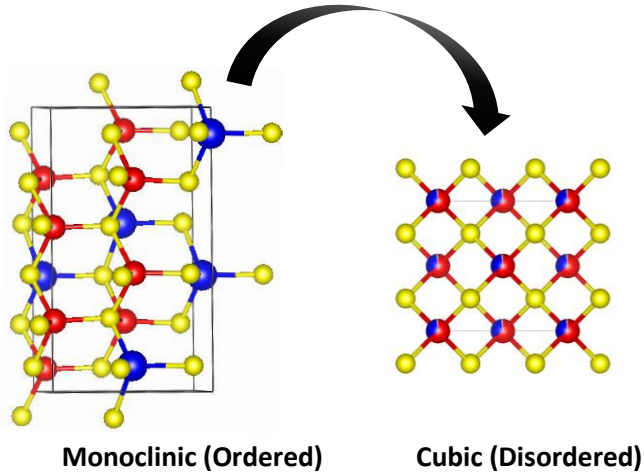


Ketan Lohani

## Development of $\text{Cu}_2\text{SnS}_3$ based thermoelectric materials and devices



UNIVERSITY OF TRENTO - Italy  
Department of Civil, Environmental  
and Mechanical Engineering



Doctoral School in Civil, Environmental and Mechanical Engineering  
Topic 2. Mechanics, Materials, Chemistry and Energy – 33° cycle 2018/2022

Doctoral Thesis – May 2022

Ketan Lohani

# **Development of $\text{Cu}_2\text{SnS}_3$ based thermoelectric materials and devices**

**Supervisors**

Prof. Paolo Scardi, University of Trento



Contents on this book are licensed under a Creative Common Attribution  
Non-Commercial - No Derivatives  
4.0 International License, except for the parts already published by other publishers.

University of Trento  
Doctoral School in Civil, Environmental and Mechanical Engineering  
<http://web.unitn.it/en/dricam>  
Via Mesiano 77, I-38123 Trento  
Tel. +39 0461 282670 / 2611 - [dicamphd@unitn.it](mailto:dicamphd@unitn.it)

तमसो मा ज्योतिर्गमय। (Tamaso m\u0101 jyotirgamaya.)  
From the darkness lead me to the light!

Brihadaranyaka Upanishad  
*9 – 6<sup>th</sup> century BCE*

## Acknowledgments

I received a great deal of support and assistance throughout this thesis work.

First and foremost, I would like to thank my supervisor Prof. Paolo Scardi, for guidance and encouragement through each stage of my doctoral research work.

I am grateful to my colleagues and members of the laboratory, Dr. Eleonora Isotta, Dr. Mirco D’Incau, Dr. Narges Ataollahi, Dr. Ubaidah Syafiq, Mr. Binayak Mukherjee, Mr. Himanshu Nautiyal, Mr. Sergio Setti, and Mrs. Wilma Vaona for their continuous professional and personal help and support. Additionally, a special thanks to Mr. Himanshu Nautiyal for helping with the computational method followed in this work.

I show my sincere gratitude to Dr. Carlo Fanciulli, Dr. Emmanuel Guilmeau, Mr. Alejandro Navarro Güell, Prof. Edgardo Saucedo, and Prof. Umberto Anselmi-Tamburini, for their treasured support, which was influential in shaping experiment methods and critiquing my results.

I am also thankful to Dr. Antonio Cervellino, Dr. Luca Rebuffi, Dr. Mahmoud Abdellatief, Dr. Nicola P. M. Casati, Dr. Pierric Lemoine, Dr. Sebastian Bette, Prof. Claudio Della Volpe, Prof. Dario Narducci, and Prof. Rosa Di Maggio for scientific support and discussions at various stages of this work.

I would like to acknowledge past and current members of our laboratory, Dr. Alberto Flor, Dr. Camilo Perez Demydenko, Ms. Eleonora Tomasino, Mr. Marcelo A. Malagutti, and Mr. Varun D N.

I am thankful to Dr. Anil Kumar Sinha for his teachings and supervision during my master’s thesis work. I also acknowledge all my mentors and teachers—especially Dr. Ajay Kumar, Dr. Archna Sagdeo, Dr. Awadhesh Kumar Dubey, and Dr. Jaswant Kumar.

I also express my gratitude to all the members of the G.S. Bolghera, Table tennis team of Trento. Last but not least, I am thankful to my family and friends.

## Abstract

Commercially available high-performance thermoelectric materials are often rare or toxic and therefore unsustainable. The present thesis work makes a case for eco-friendly, earth-abundant, and non-toxic *p*-type ceramic  $\text{Cu}_2\text{SnS}_3$  (CTS, hereafter) and, in general, the use of disordered materials for thermoelectric applications. The detailed study of polymorphism, synthesis conditions, porosity, grain size, and doping provides a systematic and in-depth experimental and computational analysis of thermoelectric properties and stability of CTS. These results can be generalized for numerous thermoelectric materials and other applications. Moreover, a case for functioning thermoelectric generators using non-toxic and cost-effective materials is also presented.

The thesis begins with a brief introduction to thermoelectricity, followed by a literature review and justification of the choice of the subject. The second chapter puts forward a novel approach to stabilize a disordered CTS polymorph without any chemical alteration through high-energy reactive ball milling. The third chapter deals with the stability of disordered samples under different synthesis and sintering conditions, highlighting the effect of synthesis environment, microstructure, and porosity. The fourth chapter employed a novel, facile, and cost-effective two-step synthesis method (high-energy ball milling combined with spark plasma sintering) to synthesize CTS bulk samples. The two-step synthesis method was able to constrain the CTS grain growth in the nanometric range, revealing the conductive nature of the CTS surfaces. The next chapter explores combining the two-step synthesis method with Ag substitution at the Sn lattice site to improve CTS's thermoelectric performance further. In the final stages of the thesis work, thin film thermoelectric generators were fabricated using CTS and similar chalcogenides, demonstrating power output comparable to existing thermoelectric materials used in the medium temperature range. The final chapter summarizes outlooks and future perspectives stemming from this research work.

---

# Contents

1. Introduction	1
1.1. A brief introduction to thermoelectricity	
1.2. A simple case	
1.3. Thermoelectric devices and materials	
1.3.1. Increased carrier concentration	
1.3.2. Increased mobility	
1.3.3. Increased effective mass of charge carriers:	
1.3.4. Use of small bandgap semiconductor or semimetal (Bipolar effect)	
1.3.5. Energy filtering	
1.3.6. Phonon-Glass-Electron-Crystal (PGEC) and Phonon- Liquid-Electron-Crystal (PLEC):	
1.3.7. Rattling cations:	
1.3.8. Band Engineering:	
1.3.9. Band degeneracy:	
1.3.10. Resonant states and Band convergence:	
1.4. State of the art	
1.5. Choice of the subject	
1.6. Literature review on $\text{Cu}_2\text{SnS}_3$	
1.7. Summary	
2. Disordered and Ordered $\text{Cu}_2\text{SnS}_3$ Polymorphs	14
2.1. Ultra-low thermal conductivity and improved thermoelectric performance in disordered nanostructured copper tin sulphide ( $\text{Cu}_2\text{SnS}_3$ , CTS)	
2.1.1. Abstract	
2.1.2. Introduction	
2.1.3. Experimental	
2.1.4. Results and Discussion	
2.1.5. Conclusions	
2.2. Experimental and <i>Ab Initio</i> Study of $\text{Cu}_2\text{SnS}_3$ (CTS) Polymorphs for Thermoelectric Applications	
2.2.1. Abstract	
2.2.2. Introduction	
2.2.3. Experimental Methods	
2.2.4. Computational Methods	
2.2.5. Results and Discussion	
2.2.6. Conclusions	

2.2.7. Appendix

3. Effects of Preparation Procedures and Porosity 60
- 3.1. Effects of Preparation Procedures and Porosity on Thermoelectric Bulk Samples of  $\text{Cu}_2\text{SnS}_3$  (CTS)
- 3.1.1. Abstract
- 3.1.2. Introduction
- 3.1.3. Materials and methods
- 3.1.4. Results and discussion
- 3.1.5. Conclusions
- 3.1.6. Appendix
4. Effects of Grain Size 87
- 4.1. Effects of Grain Size on the Thermoelectric Properties of  $\text{Cu}_2\text{SnS}_3$ : An Experimental and First-Principles Study
- 4.1.1. Abstract
- 4.1.2. Introduction
- 4.1.3. Experimental methods
- 4.1.4. Computational Methods
- 4.1.5. Results and Discussion
- 4.1.6. Conclusions
- 4.1.7. Appendix
5. Ag Substitution at the Sn Lattice Site 111
- 5.1. Synergistic optimization of thermoelectric properties of  $\text{Cu}_2\text{SnS}_3$  via Ag substitution at Sn site
- 5.1.1. Abstract
- 5.1.2. Introduction
- 5.1.3. Experimental methods
- 5.1.4. Computational Methods
- 5.1.5. Results
- 5.1.6. Discussion
- 5.1.7. Conclusions
- 5.1.8. Appendix
6. Chalcogenide Based Thermoelectric Generators 128
- 6.1. Facile and low-cost fabrication of Cu/Zn/Sn-based ternary and quaternary chalcogenides thermoelectric generators
- 6.1.1. Abstract

6.1.2. Introduction	
6.1.3. Synthesis of Cu/Zn/Sn-based chalcogenides inks	
6.1.4. Fabrication of chalcogenides/AZO thin film TEGs	
6.1.5. Chalcogenide/AZO thin film TEGs performance analysis	
6.1.6. Thin films characterization	
6.1.7. TE transport properties	
6.1.8. Chalcogenides/AZO TEGs performance analysis	
6.1.9. Effect of sulphurisation	
6.1.10. Conclusions	
6.1.11. Appendix	
7. Conclusions and Outlooks	158
8. Bibliography	164

## Introduction

From the controlled use of fire by early humans approximately 2 million years ago to today's fossil fuel-driven civilization, energy and its utilization are synonymous with human progress and development.

Non-renewable fossil fuels contribute to ~80% of the World's energy requirements.<sup>1</sup> However, the combustion of fossil fuel results in the by-products, such as carbon monoxide, carbon dioxide, sulfur dioxide, nitrogen dioxide, nitric oxide, volatile organic compounds, and hydrocarbons, which contributes to adverse environmental impacts, and global climate change. Thus, renewable and green energy sources are essential for sustainable energy solutions. One way to improve sustainability could be the recovery of waste heat.

Heat is a common by-product in almost all power generation and transmission processes. According to some studies,<sup>2,3</sup> ~ 67 % of energy produced remains unused in the form of waste heat.

Thermoelectric generators (TEGs) are solid-state devices that directly convert heat into electricity. TEGs are noise-free, reliable, scalable, and solid-state, making them ideal for waste heat recovery in many applications. In some cases, they can completely replace and, in others, reduce the dependence on conventional energy sources. Hence, a thorough understanding of the thermoelectric material properties is imperative to fulfilling the global energy demand.

### 1.1 A brief introduction to thermoelectricity

While performing the so-called “animal electricity” experiments in 1780 AD, Luigi Galvani (1737-98 AD) observed muscles contraction in dead frog samples. When the vital nerves of the sample were connected via a conductor, sparks were observed in a nearby electrical machine. Galvani concluded that muscles acted as a reservoir for electricity in living beings and were controlled by the brain.<sup>4</sup>

Triggered by Galvani's research, Alessandro Volta (1745-1827 AD) conducted similar experiments, considering the possibility that the muscles contraction observed by Galvani was due to some external

experimental effect. He connected the muscles of the dead frog sample through a dissimilar metal ark and noticed the muscle contraction, contradicting Galvani's animal electricity hypothesis. This experiment also led to the birth of electromagnetism and electrochemistry. However, when Volta conducted additional experiments, the dead frog sample was submerged in two glasses of water with different temperatures and connected by a bimetallic ark. He observed violent muscle contraction. Thus, concluding the electromotive force originates from the temperature difference between the junction of two dissimilar metals.<sup>5</sup>

Later, in 1821-23 AD, Thomas Johann Seebeck (1770-1831 AD) found that the circuit made from two dissimilar metals, with a junction at different temperatures would deflect a compass magnet, known as the "Seebeck effect."<sup>6</sup> Seebeck effect is historically extensively used in the thermocouples made of metals or metal alloys, e.g., chromel-alumel and copper–constantan thermocouples.<sup>7</sup>

A decade after the discovery of the Seebeck effect, Jean Peltier (1785-1845 AD) found that by passing an external current through a thermocouple, heating and cooling effects can be observed depending on the direction of the current flow. William Thomson (1824-1907 AD), also known as Lord Kelvin, established the interdependency between the Seebeck and Peltier effect in 1855 AD. His theory led to the discovery of the third thermoelectric effect, also known as the Thomson effect. His work showed that thermocouples could be used as a heat engine, generating electricity from a temperature gradient, or a refrigerator by applying external current.<sup>8</sup>

Nevertheless, it took more than a century (after the discovery of the Seebeck, Peltier, and Thomson effect) and the development of semiconductor physics to utilize the thermoelectric effects to produce functioning thermoelectric generators and coolers from 1950 onwards. In fact, in the beginning, the first thermoelectric generators were only used in niche and remote applications due to their low conversion efficiency. However, these generators attracted the space application community due to their long life span and solid-state nature.

## 1.2 A simple case

It is well known that metals are good conductors of heat and electricity due to the abundance of free electrons. Suppose a metal rod is heated to one end, electrons from that end start diffusing towards the cold side to reach equilibrium maximizing entropy. If we keep the hot side hot for some time, there will be a continuous flow of electrons from the hot end of the rod to the cold, generating a current (opposite to the direction of the flow of electrons) and a voltage difference. However, the flow of electrons will also carry heat toward the other end. Moreover, metals usually arrange their atoms in regular periodic arrangements (or crystals). So, a certain amount of heat will also be transferred by phonons. Consequently, the charge carriers will flow until the hot and cold sides reach thermal equilibrium.

Due to higher charge carrier density, metals can only produce a small voltage for a short time. Thus, a good thermoelectric material should present enough charge carriers to generate a voltage gradient. Simultaneously, it should effectively minimize the heat transfer so that the voltage difference can be maintained for a sufficiently long time. Extremely high ( $n > 10^{23}$ ) and low ( $n < 10^{16}$ ) carrier concentration of metals and insulators, respectively, makes them ill-suited for thermoelectric applications. Semiconductors and semimetals show the carrier concentration between these limits, making them suitable for thermoelectric applications.

## 1.3 Thermoelectric devices and materials:

TE devices consist of several pairs of  $p$  and  $n$ -type semiconducting legs connected electrically in series and thermally in parallel. Heat to electrical energy conversion of such a device is assessed by Carnot efficiency ( $\eta$ ).

$$\eta = \left( \frac{T_{hot} - T_{cold}}{T_{hot}} \right) \left[ \frac{\sqrt{(1 - zT_{avg})} - 1}{\sqrt{(1 + zT_{avg})} + \left( \frac{T_{cold}}{T_{hot}} \right)} \right] \quad 1.1$$

$$zT = \left( \frac{S^2}{\rho\kappa} \right) T \quad 1.2$$

Where  $T_{hot}$ ,  $T_{cold}$ , and  $zT_{avg}$  are hot-side temperature, cold-side temperature, and average TE figure of merit, respectively. TE figure of

merit of a material is defined in equation 1.2, where  $S$ ,  $\rho$ ,  $\kappa$ , and  $T$  are Seebeck coefficient or thermopower, electrical resistivity, thermal conductivity, and absolute temperature, respectively. Thus,  $p$  and  $n$ -type materials presenting a high figure of merit are essential to produce high-performing TE devices. In short, materials with a large Seebeck coefficient, high electrical conductivity, and low thermal conductivity consist of lattice ( $\kappa_l$ ) and electronic ( $\kappa_e$ ) contributions. However, the material parameters ( $S$ ,  $\rho$ , and  $\kappa_e = \kappa - \kappa_l$ ) determining the  $zT$  show strong interdependency, given by equation 1.3-1.5 discussed below.<sup>9</sup>

$$S = \frac{8\pi^2 k_B^2}{3eh^2} m^* T \left( \frac{\pi}{3n} \right)^{2/3} \quad 1.3$$

$$\rho = \frac{1}{ne\mu} \quad 1.4$$

$$\kappa_e = \frac{LT}{\rho} \quad 1.5$$

Where  $k_B$ ,  $m^*$ ,  $n$ ,  $e$ ,  $\mu$ ,  $L$  are Boltzmann constant, effective mass of charge carriers, carrier concentration, the charge of an electron, carrier mobility, and Lorenz number ( $2.4 \times 10^{-8} \text{ J}^2/\text{K}^2\text{C}^2$ ), respectively.

As evident from equations 1.3 and 1.4,  $S$  and  $\rho$  show a strong dependence on each-other through  $n$  and  $\mu$ . Other than these, the effective mass of charge carriers ( $m^*$ ) is another critical parameter, which is directly linked to the mobility of charge carriers. We have discussed the modification of various parameters and their interplay below.<sup>10</sup>

**1.3.1 Increased carrier concentration:** Enhancement of  $n$  is often done by doping or substitution, thus, decreasing the resistivity of a material. It has often been noticed that this approach can mildly increase the  $zT$  of materials. However, the higher carrier concentration adversely affects the thermopower and electronic contribution to thermal conductivity.

**1.3.2 Increased mobility:** Large and defect-free (near-perfect) crystals enable large mean-free paths to charge carriers, enhancing the carrier mobility and conductivity of a material. However, it has adverse effects on the Seebeck coefficient. Additionally, large wavelength

phonons dramatically increase the lattice thermal conductivity in the near-perfect crystals and limit  $zT$ .

**1.3.3 Increased effective mass of charge carriers:** Increasing  $m^*$  could boost the thermopower. Nevertheless, the heavy effective mass of the charge carrier also means that the material will have lower mobility, therefore, high resistivity.

Various methods to synergistically improve the TE properties are discussed below to overcome the above discussed strong interdependency.

**1.3.4. Use of small bandgap semiconductor or semimetal (Bipolar effect):** Performing TE materials are narrow-gap semiconductors or semimetals where both charge carriers (electrons and holes) are likely to affect the charge carrier transport. The thermopower in such cases is a weighted average of Seebeck coefficients associated with both types of carriers. Opposite signs of both charge carriers diminish the thermopower of the material. It is easy to imagine that this will also enhance resistivity. Furthermore, it introduces an additional bipolar term in the electronic contribution of thermal conductivity and dramatically enhances it. The presence of both types of charge carriers in the material has a detrimental effect on all parameters determining the TE figure of merit.

**1.3.5. Energy filtering:** In many recent works, this phenomenon has been exploited to boost the thermopower of a material. This phenomenon is associated with the effects of grain size on the TE properties, which is discussed in detail by Narducci et al.<sup>11</sup> In brief, the small grains can filter the low-energy charge carriers with short mean free paths resulting in a higher Seebeck coefficient. However, there is a trade-off between mobility and thermopower, as small grains also reduce the mobility of the carriers, resulting in higher resistivity.

**1.3.6 Phonon-Glass-Electron-Crystal (PGEC) and Phonon-Liquid-Electron-Crystal (PLEC):** These two models are associated with similar concepts, where the heat carriers (phonons) are penalized without significant effect on the electronic transport. In materials with

PGEC characteristics, phonons have very short mean free paths, like an amorphous solid, whereas electrons (charge carriers) have very long mean free paths, resulting in a thermal conductivity close to the theoretical minimum. PLEC could be an extension of PGEC; besides the very short mean path proposed for PGEC, PLEC behavior could reduce the thermal conductivity below that of glass by eliminating some vibrational modes.

**1.3.7 Rattling cations:** Materials with cage-like structures exhibit this unique phenomenon, such as skutterudite, where loosely bound ion in the middle of the cage disrupts the vibrational modes of the cage; consequently, the weak bonds results in higher anharmonicity. Low-frequency vibrational modes (acoustic modes) in such cases are asymmetric. This can be shown by the calculations of the Grüneisen parameter using computational means or by combining temperature-dependent Nuclear Inelastic Scattering (NIS) and X-ray Diffraction (XRD) data.

**1.3.8 Band Engineering:** Band engineering is typically used to overcome the strong interdependence between  $S$  and  $\mu$ . The large effective mass of the charge carriers boosts thermopower, but it simultaneously decreases mobility and increases  $\rho$ . This compromise between  $S$  and  $\rho$  impedes the enhancement of power factor ( $PF = S^2/\rho$ ), which can be overcome by increased band degeneracy or by the introduction of resonance states and, these two approaches are extensively used in thermoelectric materials for band engineering.

**1.3.9 Band degeneracy:** The effective mass of charge carriers and band effective mass ( $m_b^*$ ) are related by  $m^* = N_v^{2/3} m_b^*$ , where  $N_v$  is band degeneracy. Thus, high  $m^*$  is related to high  $m_b^*$  (heavy bands or flatter bands) or higher degeneracy, i.e., multiple band maxima overlap or are very close (bands with the energy within a few  $k_B T$ ). Band degeneracy can simultaneously boost the thermopower and electrical conductivity of materials.

**1.3.10 Resonant states and Band convergence:** These two phenomena are induced by different doping levels in the material. Band

convergence favours heavy doping, while resonant states favor light doping. In both band convergence and resonant states,  $S$  is increased without significantly penalizing electrical conductivity, resulting in higher  $PF$ . In resonant state engineering, the Density of States ( $DOS$ ) is distorted by creating a bump; differently, in-band convergence edges of valence and conduction bands are brought closer. Thus, the valley number is increased, boosting the material's performance.

Besides the above-discussed methods, researchers are also working on several modern material manipulation technologies, e.g., porous materials,<sup>12</sup> the introduction of magnetic impurities,<sup>13</sup> electron-phonon scattering, defect engineering,<sup>14</sup> strain-induced effects,<sup>15</sup> etc., to improve the TE performance of materials.

#### 1.4. State of the art

According to the optimal working temperature range, thermoelectric materials are characterized in four categories, i.e., low temperature ( $T < 300$  K), near room temperature (300 K – 500 K), medium temperature (500 K - 800 K), and high temperature ( $T > 900$  K) thermoelectric materials.

In the decade of 1950-60, alloys of Bismuth and Bismuth-Antimony were one of the first semiconducting materials studied for low-temperature applications. These alloys usually present a negative Seebeck coefficient or *n-type* semiconducting nature and a  $zT \sim 0.5$  around 120 K. The modern strategies of material manipulations can easily reach a  $zT \sim 1.5$  at the same temperature range. However, due to the very low operating temperature range, these alloys have a limited application perspective.<sup>16</sup>

Most commercially available thermoelectric materials work near the room temperature range, suitable for waste heat recovery applications in automobiles, air conditioners, households, commercial heaters, sensors, et cetera.  $\text{Bi}_2\text{Te}_3$ ,  $\text{Mg}_2\text{Sb}_2$ ,  $\text{Ag}_2\text{Se}$ ,  $\text{AgSbTe}_2$ ,  $\text{Sb}_2\text{Te}_3$ , et cetera. are well-known high-performing materials in this temperature range. Among all, *n-type*  $\text{Bi}_2\text{Te}_3$  and *p-type*  $\text{Sb}_2\text{Te}_3$  present maximum  $zT \sim 1.2$  and 1.5, respectively, around 400K.<sup>17</sup>

Medium temperature operational ranges offer various possibilities/applications and a wide temperature range for waste heat recovery and other applications. Therefore, the thermoelectric community is keen to investigate high-performing materials in the range. PbTe based materials, which can be used as *p* and *n*-type semiconductors, were considered the best performing materials. These alloys were used in various space missions by NASA. It is widely believed that the alloys used for space application in the 1960s showed  $zT \sim 0.8$ . At present, with suitable external doping, these alloys present approximately 2-fold higher  $zT \sim 1.5$ , in comparison with the alloys developed in 1960.<sup>18</sup>

In 2016, Duong et al.<sup>19</sup> reported Bi-doped SnSe single crystal achieving  $zT = 2.2$ . Recently, Zhou et al.<sup>20</sup> reported polycrystalline SnSe with record performance  $zT \sim 3.1$  at 783 K.

Since 1978, NASA has used Si-Ge alloys ( $zT \sim 1.0$  above 1000 K) to power various deep space missions, e.g., Voyager 1, Voyager 2, Galileo, Ulysses, Cassini, and New Horizons.<sup>21</sup> These devices used naturally decaying polonium oxide as the heat source. Nowadays, various metal oxides<sup>22</sup> and alloys of Pb-Te<sup>23</sup> are under investigation for high-temperature thermoelectric materials, as metal oxides are known to be thermally and chemically highly stable.

## 1.5. Choice of the subject

Most high-performing materials investigated for medium-temperature TE applications use either scarce or toxic elements, e.g., SnSe, PbTe. It is crucial to investigate cost-effective, non-toxic, and eco-friendly materials in this temperature range for low-cost, scalable, and widespread use in thermoelectric devices. Due to the aforementioned advantages, Cu-Sn-S-based systems have attracted the broad community of energy materials research, including photovoltaic, light-emitting-diode, sensors, batteries, supercapacitors, and thermoelectricity et cetera.<sup>24</sup> Cu-Sn-S-based systems have low formation energy; therefore, they are suitable for large-scale and low-

cost production. Moreover, these systems are safe to use in the medium temperature range due to the high melting temperature ( $\sim 1000$  K).

It is well-known that high-performing thermoelectric materials should have high electrical conductivity and lower thermal conductivity. Compared with metal-oxides, Cu-Sn-S-based systems show better electrical and thermal properties due to the so-called “Phonon-Glass-Electron-Crystal” (PGEC) characteristic. Moreover, these materials also arrange their atoms in various crystallographic structures, offering multiple possibilities of structural manipulation and band-engineering to boost their TE performance.

## 1.6. Literature review on $\text{Cu}_2\text{SnS}_3$

Copper tin sulfide,  $\text{Cu}_2\text{SnS}_3$  (CTS), is a *p*-type ceramic semiconductor. A tunable bandgap, earth-abundance, and non-toxic nature make it suitable for various applications, including photovoltaics, Light Emitting Diodes (LED), transistors, thermoelectric generators/cooler, optoelectronic devices, et cetera. Mao reported a novel synthesis of CTS in the laboratory in 1975. Subsequently, in 1984, Kovalenker extracted CTS from Kochbulak mine in Uzbekistan and named the mineral Mohit after Mao, and Wang (1974) proposed its triclinic structure (*PI*).<sup>25</sup> Stannite ( $\text{Cu}_2\text{FeSnS}_4$ ), Kuramite ( $\text{Cu}_3\text{SnS}_4$ ), and Mohit ( $\text{Cu}_2\text{SnS}_3$ ) are similar in chemistry and structure. In fact, their crystal structures are derived from the diamond-type sphalerite ( $\text{ZnS}$ ) structure, made of tetrahedral cages, where 1-cation (Zn, Cu, Sn, or Fe) is surrounded by 4-sulfur anions.<sup>25</sup> CTS thin films are widely studied for photovoltaic applications as absorber layers, as they exhibit a large optical absorption coefficient  $\sim 10^4 \text{ cm}^{-1}$  and a tunable band gap spanning 0.7-1.6 eV.

Crystalline materials arrange their atoms regularly and periodically in three dimensions or over a long-range. However, various crystalline materials present complex crystallographic structures, where long-range order is absent, also known as disordered materials. The disordered materials are mainly characterized by structural disorder induced by partial occupancy of cations in the unit cell and/or local deviation from the periodic arrangement. These materials can be

utilized to achieve Phonon-Glass-Electron-Crystal (PGEC) characteristics.<sup>10</sup>

One such example is cubic materials with Zincblende or Sphalerite-like ( $F-43m$ ) structures. Especially, polymorphs of  $\text{Cu}_2\text{SnS}_3$ <sup>26</sup>,  $\text{Cu}_2\text{SnSe}_3$ <sup>27</sup>,  $\text{CuFeS}_2$ <sup>28</sup>,  $\text{Cu}_5\text{Sn}_2\text{S}_7$ <sup>29</sup>,  $\text{Cu}_7\text{Sn}_3\text{S}_{10}$ <sup>30</sup>,  $\text{Cu}_2\text{ZnSnS}_4$ <sup>31</sup>, and numerous other materials show not only remarkably suppressed thermal conductivity; but also superior electrical properties than their ordered polymorphs. It has been verified by experimental and ab-initio methods that the above discussed cubic disordered materials also present higher Grüneisen parameters, which is a measure of anharmonicity, in comparison with their ordered polymorphs. Lattice distortions, irregular bond length, and soft bonds cause the higher anharmonicity, originating from structural disorder.

From a thermoelectric perspective, CTS has low electronegativity difference and high covalent character in the Cu/Sn-S bonds, thus possessing good electrical transport properties; meanwhile, these bonds are relatively soft, giving extremely lower thermal conductivity than oxides and silicides.<sup>32</sup> Although the first lab synthesized and naturally discovered CTS had a triclinic ( $PI$ ) structure, authors have diffusely reported monoclinic ( $Cc$ ) CTS synthesized by high temperature solid-state reactions from a thermoelectric perspective. Frequently, a blend of cubic ( $F-43m$ ) and tetragonal ( $I-42m$ ) CTS polymorphs can be observed with monoclinic CTS. The monoclinic CTS polymorph shows low  $zT \sim 0.05$  above 700 K due to its low carrier concentration and high thermal conductivity. However, external cation doping at the Sn site transforms the monoclinic polymorph into cubic ( $F-43m$ ). A  $zT \sim 0.4-0.8$  above 700 K is regularly reported for CTS by In<sup>33</sup>, Zn<sup>34</sup>, Mn<sup>35</sup>, Ni<sup>32</sup>, Fe<sup>13</sup>, Co<sup>36</sup>, and Cu<sup>37</sup> substitution at the Sn site, aiming to enhance the carrier concentration and reduce the thermal conductivity. Other similar systems, such as  $\text{Cu}_5\text{Sn}_2\text{S}_7$ <sup>38</sup>,  $\text{CuFeS}_2$ <sup>39</sup>,  $\text{Cu}_4\text{Sn}_7\text{S}_{16}$ <sup>40</sup>, and  $\text{Cu}_2\text{SnSe}_3$ <sup>41</sup>, also show a moderate  $zT$  ranging from 0.2–0.5, above 700 K.

## 1.7 Summary

The present thesis work studies  $\text{Cu}_2\text{SnS}_3$  based thermoelectric material and devices. The first chapter makes a case for eco-friendly, cost-effective, non-toxic thermoelectric materials for waste heat recovery and other applications. Moreover, we have briefly discussed the history of thermoelectricity, modern strategies to develop high-performing thermoelectric materials, Cu-Sn-S based thermoelectric materials, and finally, the summary of the thesis work.

In the second chapter, novel disordered CTS polymorph was synthesized using high-energy ball-milling from binary sulfides (CuS and SnS) and elemental powders (Cu, Sn, and S) in open and controlled environments, respectively. Disordered CTS polymorph shows a higher  $zT$  in comparison with its ordered phase. However, due to open environment synthesis, secondary phase oxides were present in these samples, which have an adverse effect on the thermoelectric properties.

The second part of this chapter produced ordered and disordered CTS polymorphs from elemental powders in a controlled atmosphere. However, total elimination of secondary phase oxides was not possible due to the low partial pressure of  $\text{SnO}/\text{O}_2$  formation. The experimental study shows that disordered CTS presents a higher power factor and an ultra-low thermal conductivity, resulting in a figure of merit markedly higher than in the stable ordered phase. This has been investigated in detail using several experimental methods supported by *ab initio* (DFT/DFPT) calculations to interpret the results. The *ab initio* study discloses unique vibrational properties and higher anharmonicity in the disordered phase, which was confirmed by Nuclear Inelastic Scattering (NIS) experiments combined with a high-resolution XRD study performed at various beamlines of PETRA III synchrotron source. The experimental work reveals a lower band gap and higher carrier concentration for the disordered CTS.

In the third chapter, the thermoelectric behavior and stability of various disorders CTS samples have been investigated in relation to different preparations and sintering conditions, leading to different microstructures and porosities. The as-milled powder was sintered in

two batches with different synthesis conditions to produce bulk CTS samples: manual cold pressing followed by traditional sintering (TS) or open die pressing (ODP). The low density or TS (traditionally) sintered samples showed 3-fold lower thermal conductivity than the high density or ODP (open die pressing) sintered samples. Despite the significant differences in densities, ~75% and ~90% of the theoretical density for TS and ODP, respectively. We do not observe any significant difference in electrical transport properties between TS and ODP samples. Moreover, the effects of porosity and various production and sintering conditions on transport properties and stability are highlighted. This study also shows that the CTS sample can be stabilized with different porosity fractions.

In the fourth chapter, we investigate a comparatively less-explored two-step synthesis method, where high-energy reactive ball-milling was combined with spark plasma sintering (SPS) to produce high-density nanostructured CTS samples, presenting average domain sizes below 50 nm. The experimental study shows a strong dependence of thermoelectric properties on the domain size of the grains. The samples with the smaller domain size showed a higher power factor and figure of merit due to their lower resistivity. This has been further investigated using Hall effect measurements and first principles DFT calculations. The Hall measurements showed a higher carrier concentration for the samples with smaller crystallite sizes. DFT calculations on CTS surfaces revealed the presence of localized states near the Fermi level due to the dangling bonds on the surface. These dangling bonds provide additional charge carriers (holes), which increase the carrier concentration leading to the degenerate semiconductor-like behavior, and higher  $zT$ .

To further improve the thermoelectric performance of CTS, the two-step synthesis method discussed in the third chapter was combined with Ag substitution at the Sn lattice Site.  $\text{Cu}_2\text{Ag}_{(x)}\text{Sn}_{(1-x)}\text{S}_3$  ( $x=0.05, 0.10, 0.125, 0.15, 0.20,$  and  $0.25$ ) samples were synthesized, and their thermoelectric properties were investigated using experimental and first principal methods. Interestingly  $x=0.125$  and  $x=0.15$ , Ag substituted samples showed a remarkable ~10 and ~2-fold improvement in the power factor compared to CTS samples produced in the first and third

chapter, respectively. First-principles calculation and experimental bandgap measurement revealed that bandgap suppression, leading to increased carrier concentration, was responsible for improving power factor. However, Ag substitution also had adverse effects on the thermal conductivity of the materials. Overall, we successfully reported Ag substitution in CTS using the two-step method and improved thermoelectric figure of merit.

In the last part of the thesis work, we have studied in-plane thermoelectric generators, consisting of chalcogenides and aluminum-doped zinc oxide (AZO) as *p*- and *n*-type legs, respectively. The maximum power output obtained for CTS TEGs was ~75 nW, at temperature difference ( $\Delta T$ ) 160 K. It is worth mentioning that sulfurization of *p*-type CTS leg significantly enhanced the device performance, achieving a maximum power output ~230 nW, which is a staggering 300% increase in performance. The per-unit planner area power output results are comparable to commercially available thermoelectric generators in this temperature range.

The final chapter summarizes outlooks and future perspectives stemming from this research work. New ideas to further improve the performance of CTS and other disordered materials are discussed. Currently, the efforts to replace AZO (*n*-type) with other Cu-Sn/Fe-S-based materials are in progress. Moreover, Ag substitution in bulk materials presented promising thermoelectric results, especially the high power factor. Therefore, fully optimized Ag-doped CTS thermoelectric generators would be a good starting point for future research, extending the reach of the present Thesis work.

## 2 Disordered and ordered $\text{Cu}_2\text{SnS}_3$ Polymorphs

### 2.1 Ultra-low thermal conductivity and improved thermoelectric performance in disordered nanostructured copper tin sulphide ( $\text{Cu}_2\text{SnS}_3$ , CTS)

Published under a © 2020 Elsevier B.V license.

This section is entirely taken from<sup>42</sup>: Lohani, K.; Isotta, E.; Ataollahi, N.; Fanciulli, C.; Chiappini, A.; Scardi, P. *Ultra-Low Thermal Conductivity and Improved Thermoelectric Performance in Disordered Nanostructured Copper Tin Sulphide ( $\text{Cu}_2\text{SnS}_3$ , CTS)*. *J. Alloys Compd.* 2020, 830, 154604.

<https://doi.org/10.1016/j.jallcom.2020.154604>

Please cite any part of this section as specified above.

K. Lohani<sup>a</sup>, E. Isotta<sup>a</sup>, N. Ataollahi<sup>a</sup>, C. Fanciulli<sup>b</sup>, A. Chiappini<sup>c</sup>, P. Scardi<sup>a\*</sup>

<sup>a\*</sup>Department of Civil, Environmental and Mechanical Engineering, University of Trento, Via Mesiano 77, 38123, Trento, Italy

<sup>b</sup>National Research Council of Italy-Institute of Condensed Matter Chemistry and Technologies for Energy (CNR-ICMATE), Lecco Unit, Via Previati 1/E, 23900, Lecco, Italy

<sup>c</sup>Institute of Photonics and Nanotechnologies IFN, National Research Council CNR CSMFO Lab. & Fondazione Bruno Kessler FBK, Centro Materiali e Microsistemi CMM, Via alla Cascata 56/C, 38123, Trento, Italy

\*Correspondence: [Paolo.Scardi@unitn.it](mailto:Paolo.Scardi@unitn.it)

Received: 30 October 2019; Revised: 28 January 2020; Accepted: 29 February 2020

### 2.1.1 Abstract

Copper tin sulphide (Cu<sub>2</sub>SnS<sub>3</sub>, CTS) is a promising *p*-type thermoelectric material. In the present work, we have investigated the cation disorder in CTS disks made by sintering powders produced via high-energy reactive ball-milling. The crystalline structures, electronic and thermal properties were systematically investigated. As-milled CTS shows a disordered cubic structure (c-CTS), preserved with thermal treatment up to 500 °C. By increasing the thermal treatment temperature, CTS gradually evolves towards the ordered monoclinic structure (m-CTS), reaching complete order at 650 °C. The disordered CTS has several times higher  $zT$  than the ordered CTS. In fact, ordered CTS has high thermopower, up to 700 μV/K, and high electrical resistivity leading to  $zT < 0.05$  above 700 K; whereas, disordered (c-CTS) has comparatively high  $zT \sim 0.30$  above 700 K. This has been related to the lower electrical resistivity, and the ultra-low thermal conductivity ( $k \sim 0.26$  W/m-K), resulting from the disordered structure, promoting Phonon-Glass-Electron-Crystal (PGEC) characteristics. To our best knowledge,  $zT \sim 0.30$  above 700 K is the highest in CTS samples without acting on the system's chemistry.

### 2.1.2 Introduction

Thermoelectric materials exploit temperature gradients, turning thermal energy into electrical energy based on the Seebeck effect.<sup>43</sup> Besides direct energy production in remote conditions, like deep space probes, they find increasingly more applications in devices for waste heat recovery.<sup>10</sup> The energy conversion efficiency of a thermoelectric material can be expressed by the dimensionless figure of merit,  $zT$ , defined as  $zT = S^2\sigma T/k$ ,<sup>44</sup> where  $S$  is the Seebeck coefficient,  $\sigma$  is the electrical conductivity,  $T$  is absolute temperature, and  $k$  is thermal conductivity, made of a phononic ( $k_{lat}$ ) and of an electronic ( $k_{ele}$ ) component.<sup>34,43,45</sup> Parameters  $S$ ,  $\sigma$ , and  $k$  in  $zT$  are interrelated through the carrier concentration ( $n$ ) so that it is difficult to optimize them independently.<sup>24</sup>

Copper tin sulphide (Cu<sub>2</sub>SnS<sub>3</sub>, CTS) is an earth-abundant, eco-friendly, non-toxic *p*-type ceramic material.<sup>34</sup> CTS has a 3-D conductive

network, showing Phonon-Glass-Electron-Crystal (PGEC) characteristic, with enhanced carrier transport and reduced thermal conductivity.<sup>13</sup> This makes CTS a promising thermoelectric material.<sup>46</sup> CTS is reported in polymorphic crystal structures, cubic (c-CTS; SG:  $F-43m$ ), monoclinic (m-CTS; SG:  $Cc$ ), and tetragonal (t-CTS; SG:  $I-42m$ ). These polymorphs are identified as disordered, ordered, and pseudo-ordered structures, respectively.<sup>35,47-49</sup> Different CTS polymorphs have different band gap energies.<sup>50</sup>

Recent work on similar CZTS ( $\text{Cu}_2\text{SnZnS}_4$ ) chalcogenides has put forward that cation disordered structures could improve thermoelectric properties of this class of semiconducting materials.<sup>51,52</sup> These results reveal that a disordered structure could enhance the density of state effective mass ( $m^*_{DOS}$ ) with an increase in  $n$ , while  $k_{lat}$  is largely suppressed.<sup>10,51</sup> Transitions to structurally disordered polymorphs, obtained via acceptor doping, have been studied in CTS systems by many researchers.<sup>13,35,36</sup> The ordered m-CTS has a low figure of merit,  $zT < 0.05$ , in the temperature range 50 °C–450 °C.<sup>13</sup> However, disordered c-CTS with acceptor dopants reaches much higher  $zT$  values. Shen et al. have reported a high  $zT \sim 0.58$  and low  $k = (0.9 \pm 0.4) \text{ Wm}^{-1}\text{K}^{-1}$  at 723K for disordered CTS with Zn doping<sup>34</sup>. Tan et al. via In doping observed high thermopower, up to 300  $\mu\text{V/K}$ , and low thermal conductivity, below  $1.0 \text{ Wm}^{-1}\text{K}^{-1}$ , leading to  $zT \sim 0.5$  above 700K.<sup>33</sup>

Zhang et al. have studied the effect of Mn doping on the transport properties of CTS. Via Mn doping, on the one hand,  $k_{lat}$  was suppressed because of phonon scattering enhancement due to order-disorder phenomena, while on the other hand,  $m^*_{DOS}$  and  $n$  were enhanced by increased symmetry, leading to  $zT \sim 0.68$  at 723K.<sup>35</sup> d-orbital-unfilled Co doping at Sn site was used by Zhao et al. to enhance the  $zT$  to  $\sim 0.84$ , with ultra-low lattice thermal conductivity  $0.3\text{--}0.4 \text{ Wm}^{-1}\text{K}^{-1}$  at 723K, which can be interpreted in terms of Umklapp type phonon-phonon interaction.<sup>36</sup> Zhao et al. have shown the effect of magnetic iron doping, leading to a large power factor,  $PF \sim 1.5 \text{ mWm}^{-1}\text{K}^{-2}$ , with low thermal conductivity due to phonon-glass feature in cubic CTS, leading to  $zT \sim 0.75$  at 723K.<sup>13</sup> All these works have focused on disordering the crystal structure via doping.

In this context, our work aims to bring some insights on the effect of structural disorder on the thermoelectric performance of nanostructured CTS. To our best knowledge, disordered-structure CTS has been reported only via acceptor doping, basing materials preparation on high-temperature Solid-State Reactions (SSR). Our approach, instead, relies on reactive ball milling, which is a bottom-up technique helpful to preserve the nanostructure, keeping a high density of crystalline defects with a non-homogeneous distribution of finely dispersed crystalline grains. These factors, involving a much-improved grain boundary scattering, can significantly suppress thermal conductivity. This work also throws light on the role of secondary phases, in particular on tin oxide development, which is widely reported in CTS and similar chalcogenides.

### 2.1.3 Experimental

CTS powder was produced via reactive ball milling (Fritsch P4 Pulverisette-4) from binary sulphides.  $\text{CuS}$  and  $\text{SnS}$  (both 99% pure powders from SigmaAldrich) were milled in 2:1 stoichiometric ratio using WC vial and balls with sample to ball weight ratio 1:100 and 150  $\mu\text{l}$   $\text{C}_2\text{H}_5\text{OH}$  as milling agent. Main disk and planetary speed were respectively 300 rpm and  $-540$  rpm. CTS powder with minimum WC contamination and minimum milling time was obtained with a 30 min operation. CTS disks, with diameter 16 mm and thickness  $\sim 1.5$  mm, were produced via cold pressing applying a load of 15 tons for 3 min. Disk samples were then treated at different temperatures (500  $^\circ\text{C}$ , 550  $^\circ\text{C}$ , 600  $^\circ\text{C}$  and 650  $^\circ\text{C}$ ) for 2 h in Ar flux with heating rate of 3  $^\circ\text{C}/\text{min}$ .

X-ray diffraction (XRD) was performed on as-milled powder and annealed disks in Bragg-Brentano geometry using a Rigaku PMG powder diffractometer, equipped with a graphite bent-crystal monochromator and using  $\text{Cu } K_\alpha$  radiation generated at 40 kV and 30 mA. Scan range was from 8 $^\circ$  to 82 $^\circ$  ( $2\theta$ ), with step size 0.05 $^\circ$  and counting time 40 s per step.

Raman spectra were collected using a LabRAM Aramis (Horiba Jobin-Yvon) equipped with an optical microscope and a 100 $\times$  objective. A

diode-pumped solid-state laser source of 532 nm was used for the excitation of the Raman signal that was detected with an air-cooled charge-coupled device. The slit width of the spectrometer was set at 100  $\mu\text{m}$ . A diffraction grating with 1800 lines  $\text{mm}^{-1}$  was used for the collection of all Raman spectra with an overall spectral resolution of  $\sim 1 \text{ cm}^{-1}$ . Raman spectra have been acquired with an overall acquisition time of 10 s by setting the laser power at 0.02 mW.

Selected Area Electron Diffraction (SAED) and morphological images were collected using Transmission Electron Microscopy (TEM), (HR-S/TEM ThermoFischer TALOS 200 s, Thermo Fischer Scientific, Waltham, MA, USA) in bright-field imaging mode operated at 200 kV. Thermoelectric properties were measured over the temperature range 323K–723K with and heating rate of 3 K/min. Absolute Seebeck coefficient ( $S$ , Pt standard) and resistivity ( $\rho$ ) were measured simultaneously on the disk samples in 4 contact configuration and He atmosphere, using a Linseis LZT-800 m instrument.

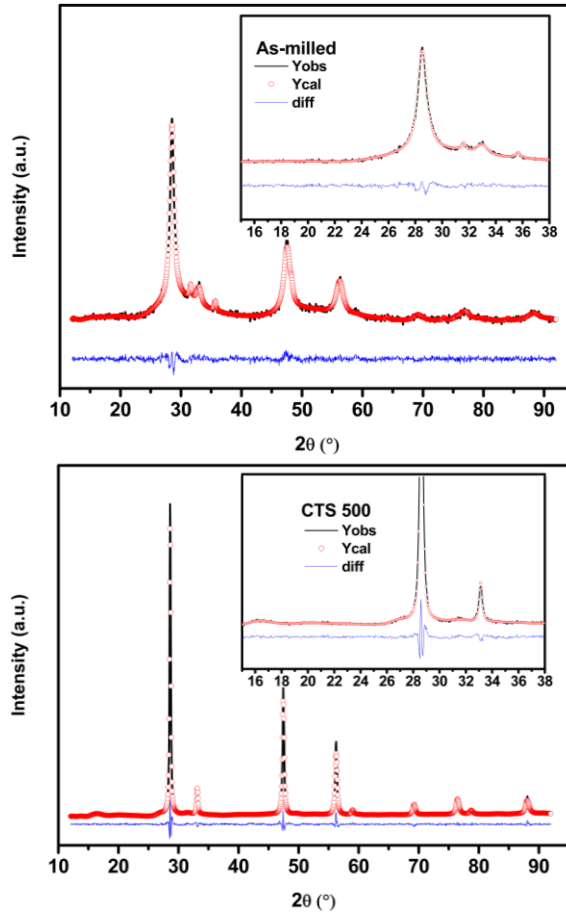
Thermal conductivity ( $k$ ) was calculated as  $k = DdC_p$ , where  $D$  is thermal diffusivity,  $d$  is density (measured with Archimedes' method) and  $C_p$  is specific heat. Thermal diffusivity was measured in the axial direction of the disks with a LaserFlash (Linseis LZT-800 m, He atmosphere).

$C_p$  was measured using a Thermal Analysis Q100 DSC instrument in modulated mode (MDSC), useful for studying materials with low thermal conductivity. A modulation with period 120 s and semi-amplitude 0.5 K was applied to isothermal measurements to determine the specific heat as a function of temperature, in the range 323–623 K. The measurements have been performed sealing samples in Ar atmosphere.

#### 2.1.4 Results and discussion

X-ray diffraction (XRD) patterns of different CTS samples are shown in Figure 2.1.1. The as-milled sample (as-milled) was identified as cubic CTS (SG:  $F-43 m$ ), which is characterized by a disordered cation structure. The diffuse background signal and Bragg-peak broadening indicate low crystallinity and small grain size. For the disk treated at

500 °C (CTS 500), no new peak evolution was observed other than background decrease and peak sharpening, suggesting an increase in crystallinity. This sample preserves the cubic structure. With a further increase in thermal treatment, CTS gradually evolves to the thermodynamically stable ordered monoclinic polymorph (SG:  $Cc$ ).<sup>53</sup> The c-CTS (disordered) and m-CTS (ordered) phases can be distinguished by Bragg-peak evolution below  $2\theta = 25^\circ$ , showing the peaks at  $2\theta=15.88^\circ$  (110),  $18.02^\circ$  (11-1) and  $20.88^\circ$  (021), distinctive of the monoclinic phase.



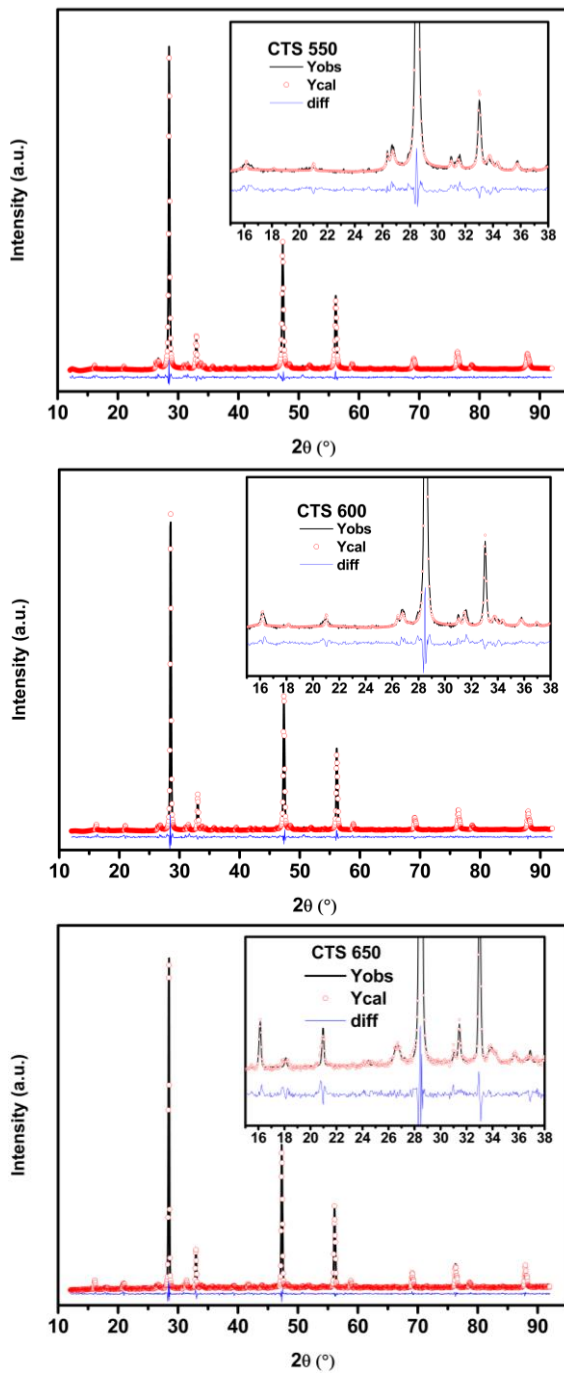


Figure 2.1.1. XRD pattern with Rietveld refinement for the as-milled (As-milled) and thermal treated samples, at 500 °C (CTS 500), 550 °C (CTS 550), 600 °C (CTS 600) and 650 °C (CTS 650) respectively. Observed pattern (solid black), calculated pattern

(dotted red), difference (solid blue). Insets show magnified XRD patterns from  $2\theta = 15^\circ$  to  $2\theta = 38^\circ$ .

Quantitative phase and structural analyses were performed on XRD data using Rietveld refinement<sup>54,55</sup> and Whole Powder Pattern Model (WPPM<sup>56</sup>) with the software TOPAS.<sup>57</sup> Results are shown in Table 2.

Table 2.1.1. Results of quantitative phase and structural analyses obtained with Rietveld refinement of XRD data performed with TOPAS for CTS samples treated at various temperatures.

Thermal treatment (°C)	Phase	S.G. and weight fraction (±1%)	Lattice parameter (±0.01 Å)			GoF	Average crystallite size (±10 nm)
			a	B	c		
500	CTS SnO <sub>2</sub>	<i>F-43m</i> 98% <i>P-63m</i> 2%	5.44	5.44	5.44	1.44	100
550	CTS SnO <sub>2</sub> SnO	<i>F-43m</i> 65% <i>Cc</i> 27% <i>P-63m</i> 6% <i>Pmn21</i> 2%	5.44 6.66	5.44 11.55	5.44 6.66	1.63	180 50
600	CTS SnO <sub>2</sub>	<i>F-43m</i> 35% <i>Cc</i> 60% <i>P-63m</i> 5%	5.44 6.66	5.44 11.55	5.44 6.66	1.76	320 80
650	CTS SnO <sub>2</sub>	<i>Cc</i> 96% <i>P-63m</i> 4%	6.66	11.55	6.66	1.55	140

From the data refinement, the crystal structure of CTS 500 is cubic, whereas for the samples treated at 550 °C (CTS 550) and 600 °C (CTS 600) a phase coexistence is present, respectively estimated as ~65% cubic and ~27% monoclinic, and ~35% cubic and ~60% monoclinic of the total CTS weight fraction. The sample annealed at 650 °C (CTS 650) displays a completely monoclinic structure. In this text, we refer to the completely cubic sample as disordered, to the ~27% and ~60% monoclinic samples as partially-disordered, and to the fully monoclinic as ordered CTS. A weak peak around  $2\theta = 36^\circ$  points out WC (SG: *P-6m2*) contamination from the vial. This peak is not observed in the pattern of disordered CTS (CTS 500), probably because absent from the superficial layer analysed by XRD. The small peaks around the most intense peak of CTS at  $2\theta = 28^\circ$  are identified as tin oxide,

$\text{SnO}_2$  (SG:  $Pbcn$ ) and  $\text{SnO}$  (SG:  $Pmn_21$ ). The presence of tin oxides as secondary is widely reported in the literature in CTS samples and similar chalcogenides,<sup>51,58,59</sup> and it is further discussed below. As-milled CTS has a mean crystallite size of  $20 \pm 10$  nm, increasing with the temperature of thermal treatment. Lattice parameters and average crystallite size for cubic and monoclinic fractions of all CTS samples are reported in Table 2.

Oxygen and an electrolyte (i.e. atmospheric moisture) are two major factors for corrosion and oxidation. Since all the samples were treated under a controlled Ar atmosphere, this adsorption might have come from the milling agent (ethanol) or post-synthesis exposure to air. Hence, for future samples, to avoid formation of  $\text{SnO}_2$  the preparation should be performed using a non-polar milling agent, like hexane, or in a controlled atmosphere. This involves modifications in the milling conditions and is the subject of current work.

A representation of the crystal structures of disordered c-CTS and ordered m-CTS is shown in Figure 2.1.2. CTS polymorphs derive from the Zinc Blende crystal structure, where Zn is stoichiometrically replaced by Cu and Sn.<sup>34,35</sup> In both disordered (c-CTS) and ordered (m-CTS) structures the central Cu/Sn atom is coordinated with four S atoms. In ordered CTS Cu and Sn atoms occupy separate  $4a$  tetrahedral Wyckoff sites orderly. In the disordered structure, Cu and Sn occupy  $4a$  sites with occupancy Cu 66.6% and Sn 33.3% and S occupies  $4c$  Wyckoff position.

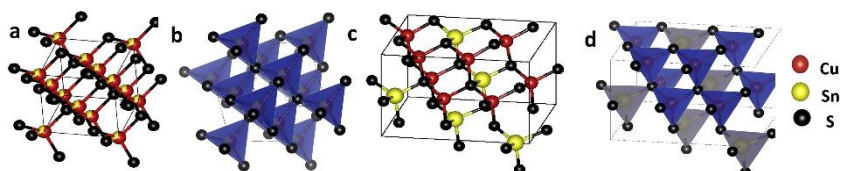


Figure 2.1.2. Cubic disordered CTS crystal structure (SG:  $F-43m$ ) (a), and with coordination tetrahedra (b); Monoclinic ordered CTS crystal structure (SG:  $Cc$ ) (c), and with coordination tetrahedra (d).

Figure 2.1.3 shows the Raman spectra of as-milled CTS and CTS samples after thermal treatment. The as-milled sample shows a weak signal, indicating low crystallinity, in agreement with the XRD patterns shown in Figure 2.1.1. The as-milled sample shows the presence of

$\text{Cu}_{2-x}\text{S}$  with the characteristic Raman peak at  $474\text{ cm}^{-1}$ ,<sup>60</sup> indicating the presence of unreacted binary sulphide. The presence of  $\text{Cu}_{2-x}\text{S}$  was not observed in the XRD pattern due to small volume fraction and same Bragg peak positions as CTS, which might be absorbed in diffused background signal and broad Bragg peaks.<sup>61</sup> The peak corresponding to  $\text{Cu}_{2-x}\text{S}$  at  $474\text{ cm}^{-1}$  is not observed after thermal treatment, indicating that pure CTS has been obtained. The two Raman modes around  $290\text{--}293\text{ cm}^{-1}$  and  $350\text{--}355\text{ cm}^{-1}$  are representative of monoclinic m-CTS.<sup>60,62</sup> For CTS 550, CTS 600 and CTS 650, Raman modes around  $290\text{ cm}^{-1}$  and  $350\text{ cm}^{-1}$  are visible. For cubic c-CTS, our results are consistent with the Raman modes reported by some authors as around  $287\text{ cm}^{-1}$  and  $345\text{ cm}^{-1}$ <sup>63,64</sup>. Other authors report instead Raman modes for cubic CTS as around  $300\text{ cm}^{-1}$  and  $350\text{ cm}^{-1}$ .<sup>48,65,66</sup>

At these locations we observe some shoulder peaks in our data for CTS 500. The discussion on XRD and the following discussion on TEM results makes it very clear that CTS 500 is cubic. Therefore, our results could be used to resolve the controversy in the literature on assigning the positions of the Raman peaks to the different phases. For what concerns the monoclinic phase, the peaks at  $223\text{ cm}^{-1}$ ,  $257\text{ cm}^{-1}$ ,  $316\text{ cm}^{-1}$ , and  $374\text{ cm}^{-1}$  have maintained similar positions in both CTS 600 and CTS 650. This finding is in agreement with the literature.<sup>67</sup>

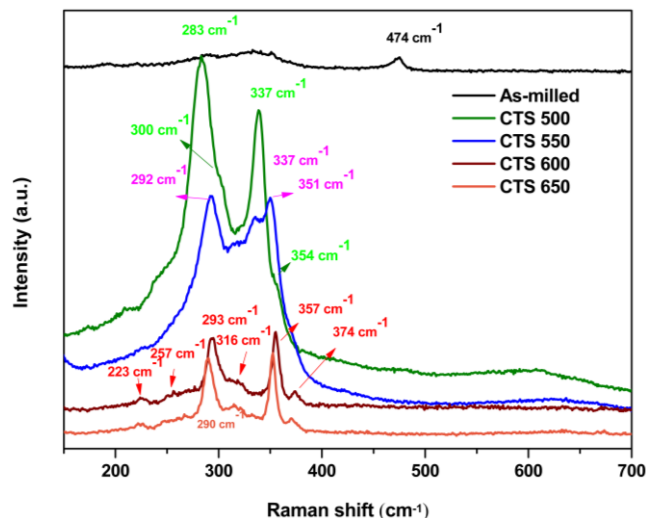


Figure 2.1.3. Raman spectra of as-milled CTS powder and samples after treatment at various temperatures.

TEM images and Selected Area Electron Diffraction (SAED) patterns for CTS 500 and CTS 650 are shown in Figure 2.1.4. For CTS 500, a dispersed distribution of grains is visible. The larger polycrystalline agglomerates are made of smaller grains with size ranging from few tens to 100 nm. In the case of CTS 650, the grain size is not as disperse as CTS 500 and the grains are comparatively larger, ranging from 300 nm to 500 nm. This is also evidenced by SAED rings, which are more dotted for CTS 650 indicating larger domains. SAED confirms the structural transformation from disorder c-CTS to ordered m-CTS occurred with the temperature. The Debye-Scherrer rings representing planes (11-1) and (021) are missing in the case of disordered c-CTS (Figure 2.1.4.), and Bragg-peaks corresponding to these planes are also not present in the XRD patterns (shown in the insets of Figure 2.1.1). These results are consistent with XRD and Raman spectroscopy. TEM images and SAED are providing clear evidence of the grain growth and phase transformation happening with the thermal treatment temperature increase, which we have also observed via Rietveld refinement of XRD data.

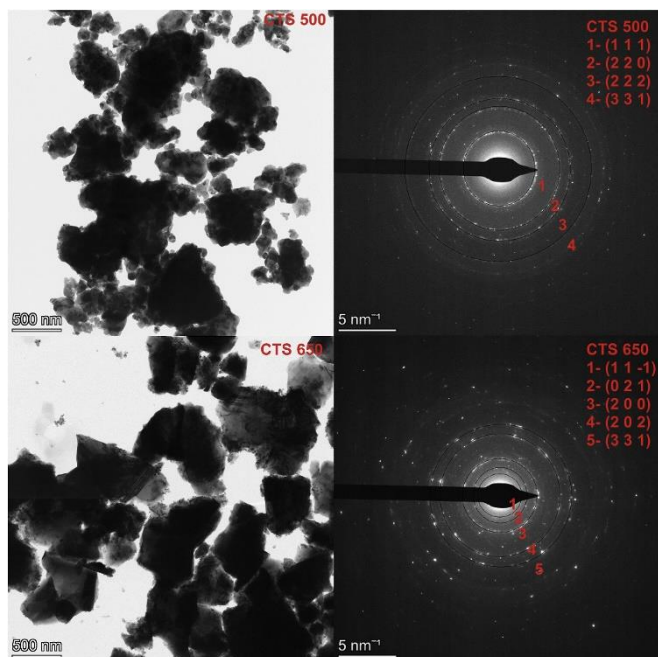
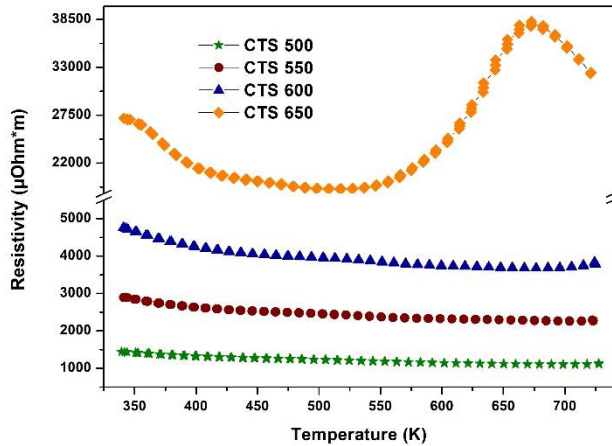


Figure 2.1.4. Transmission Electron Microscopy (TEM) and Selected Area Electron Diffraction (SAED) images for CTS 500 and CTS 650.

The temperature-dependent thermoelectric properties are shown in Figure 2.1.5, Figure 2.1.6, Figure 2.1.7. Electrical resistivity (Figure 2.1.5 (a)) displays a semiconductor-like nature (decreasing with the increase of temperature) for all the samples but the ordered monoclinic one. This can be justified by an increase of carriers (holes) with temperature. c-CTS (disordered sample, CTS 500) displays the lowest values of resistivity, which ranges from 1.4 mΩ\*m at 323K to 1 mΩ\*m at 773K. According to recent studies, structural disorder has a significant effect on electrical conductivity, due to lower band gap energy<sup>50,66</sup>. Furthermore, low-temperature annealing leads to smaller grain size and higher density of grain boundaries, both influencing the electrical conductivity. Partially-disordered samples, CTS 550 and CTS 600, are characterized by higher resistivity with respect to the disordered cubic, respectively in the range 3-2.2 mΩ\*m and 5-4 mΩ\*m.



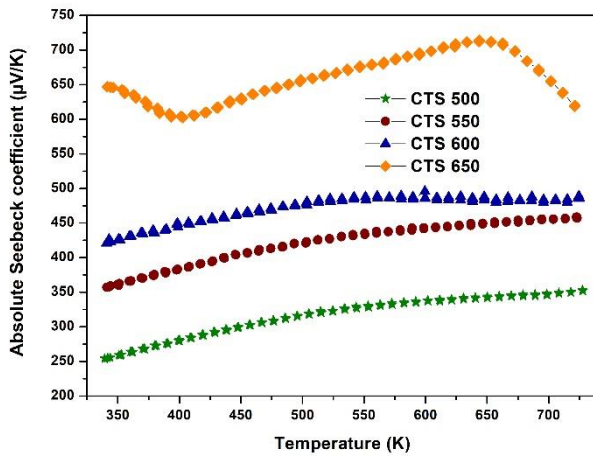
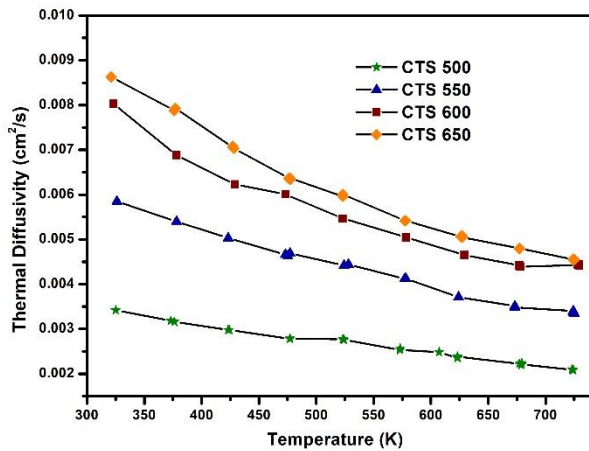


Figure 2.1.5. (a) Temperature-dependent electrical resistivity ( $\rho$ ) and (b) Seebeck coefficient ( $S$ ) for the different CTS samples.



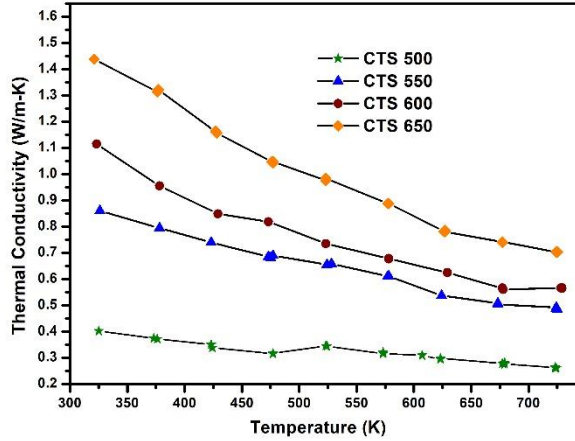


Figure 2.1.6. (a) Temperature-dependent thermal diffusivity ( $D$ ), and (b) thermal conductivity ( $k$ ) for the different CTS samples.

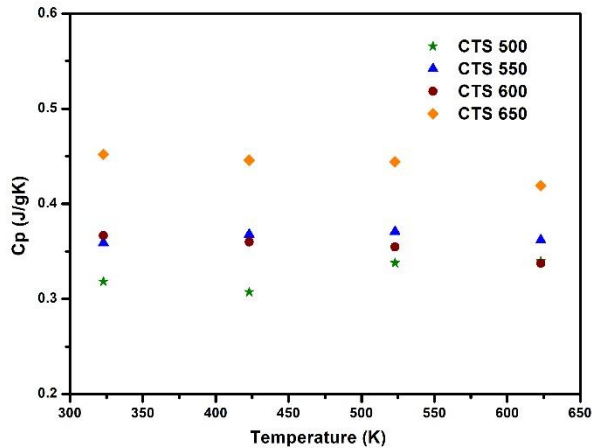


Figure 2.1.7. Temperature-dependent specific heat ( $C_p$ ) for the different CTS samples.

The ordered (CTS 650) sample shows a semiconductor-like nature up to 533K, followed by a metal-like behaviour in the range 533–673K. At higher temperatures the value of resistivity increases again, and this anomalous temperature dependence could be partially due to thermal excitation of bipolarons.<sup>24,36</sup> The higher values of  $\rho$  for this sample with respect to the others could be an indication of non-degenerate states

with lower carrier concentration.<sup>34</sup> The effect of increased grain size and crystallinity due to annealing cannot be ignored, as it leads to a reduction of grain boundary density. Nevertheless, accurate predictions based on the trends of resistivity cannot be made due to the low density of the samples, which is measured around 75% of the theoretical one and further commented below in the text.

To obtain large values of Seebeck coefficient, single type carriers are required.<sup>10</sup> CTS is a *p*-type semiconductor, since the Cu vacancies lead to holes as majority carriers.<sup>68</sup> This is confirmed by the positive values of Seebeck coefficient, which are increasing with temperature for the disordered and partially-disordered samples. However, in the case of ordered CTS 650, the thermopower presents a decrease at high temperature, in the range 650–723K. This could be due to the bipolaron excitation effect, in accordance also with resistivity data.<sup>34</sup> For the disordered CTS 500 sample Seebeck is in the range 255–350  $\mu\text{V/K}$ . Literature values of Seebeck coefficient for disordered c-CTS samples with various doping are reported being around five times lower (50–100  $\mu\text{V/K}$ ) in the same temperature range.<sup>13,34,35</sup> This might be due to a higher carrier concentration in the literature samples, which has an adverse effect on Seebeck coefficient. For the partially-disordered samples the thermopower is measured in the range 355–455  $\mu\text{V/K}$  and 425–485  $\mu\text{V/K}$ , for the CTS 550 and the CTS 600 sample respectively. It is worth noticing that reported values of Seebeck coefficient for ordered m-CTS samples are in the range 260–400  $\mu\text{V/K}$ <sup>35</sup>, 250–450  $\mu\text{V/K}$ <sup>36</sup>, 260–420  $\mu\text{V/K}$ <sup>34</sup>, and 300–420  $\mu\text{V/K}$ <sup>13</sup> all for the temperature range 323–723K. In the present work, Seebeck for the monoclinic sample is higher than in the literature, ranging from 600  $\mu\text{V/K}$  to 700  $\mu\text{V/K}$ . For all the samples, the value of Seebeck is correlated with that of resistivity, as specimens with higher thermopower present a higher resistivity as well.

The correlation between thermal treatment temperature, electrical resistivity and Seebeck coefficient is complex. The increase in the thermal treatment temperature is having two effects. First, the disordered (c-CTS) structure is gradually evolving to ordered (m-CTS). Second, crystalline defects and grain boundary density are decreasing. Both have an effect on the resistivity, and resistivity is connected to

Seebeck coefficient through carrier concentration. Here, cation disorder seems to be the prevailing and governing mechanism. Disordered (c-CTS), ordered (m-CTS) and pseudo-ordered (t-CTS) have been reported with various band gap ranging from 0.83 to 1.35 eV.<sup>66</sup> For disordered c-CTS, a bandgap in the range of 0.94–0.96 eV is reported by various researchers<sup>48,65–67</sup> while that of m-CTS is claimed displaying a band gap in the range 0.95–1.0 eV.<sup>48,69</sup> Given the thermoelectric results we obtain, we put forward that in the present case m-CTS has a higher band gap than c-CTS. This would lead to a lower carrier concentration with an increase in thermal treatment temperature, hence, higher Seebeck and resistivity.

Thermal diffusivity ( $D$ ) decreases with temperature for all the samples (Figure 2.1.6(a)). Density, measured with Archimedes' method is  $\sim 3.7$  g/cm<sup>3</sup> for all the samples, about 75% of the theoretical density of 4.855 g/cm<sup>3</sup>, estimated by XRD data refinement. This is expected for the production process based on cold pressing and relatively low sintering temperature, compared to the widely reported Spark Plasma Sintering.<sup>13,36</sup> Despite the low density, differences between ordered and disordered CTS samples are quite significant. The  $C_p$  was measured as 0.45 J/(g\*K) at room temperature for the monoclinic sample, in accordance with literature data.<sup>13</sup> For the disordered samples  $C_p$  is lower, possibly due to the simpler atomic bonds with less vibrational modes, being 0.318–0.340 J/(g\*K), 0.359–0.362 J/(g\*K), 0.367–0.337 J/(g\*K), and 0.452–0.419 J/(g\*K) for CTS 500, CTS 550, CTS 600 and CTS 650 respectively.

Thermal conductivity  $k$ , calculated as  $k = DC_p d$ , is shown in Figure 2.1.6 (b). The disordered CTS 500 sample exhibits an ultra-low thermal conductivity, spanning from 0.5 W/(m\*K) at 323K to 0.26 W/(m\*K) at 723K. These values are lower than all the literature reports on CTS, CTS produced via high temp SSR has  $k = 2.4$ – $0.9$  W/(m\*K) for ordered m-CTS, whereas disordered c-CTS produced via acceptor doping has  $k = 1.0$ – $0.5$  W/(m\*K) in temperature range 323–723K.<sup>13,34–36</sup> We put forward that a reason for ultra-low  $k$  for CTS 500 is disordered structure and soft-bonds.<sup>13,46</sup> In practice, phonons are more effectively scattered as the cation-cation neighbours are changing, randomly, Cu–Cu, Cu–Sn, Sn–Sn, and disorder extends also to second and higher neighbours.

Which enhances phonon scattering favouring low thermal conductivity. Moreover, cubic CTS benefits from low-temperature reactive ball-milling leading to the reduced grain size which increases interfaces and grain boundary density and further enhances phonon scattering. The ordered CTS 650 presents a thermal conductivity in the range 1.5–0.8  $\text{W}/(\text{m}\cdot\text{K})$ , which is a trend similar to the literature values reported for ordered m-CTS.<sup>33</sup> Partially disordered (CTS 550 and CTS 600) exhibit an intermediate thermal conductivity, as  $k$  ranges between 1.1 and 0.5  $\text{W}/(\text{m}\cdot\text{K})$  and 1.3–0.7  $\text{W}/(\text{m}\cdot\text{K})$ , for the ~27% and ~60% m-CTS samples respectively. Differences between thermal conductivity values for ordered and disordered CTS are quite evident. The decreasing trend of  $k$  is approximately proportional to  $T^{-1}$ , which gives a clue of phonon-phonon Umklapp processes.<sup>33,34</sup> Also, the presence of secondary phases such as WC  $2\theta \sim 36^\circ$  and SnO/SnO<sub>2</sub> around  $2\theta = 28^\circ$  (shown in the insets of Figure 2.1.1) that from the XRD-peak broadening appear in a nanostructured form, can give a contribution via the enhancement of phonon scattering.

The Power Factor ( $PF$ ), calculated as  $PF = S^2\sigma$ , is shown in Figure 2.1.8 (a). Disordered CTS 500 exhibits the highest  $PF$  in the range 0.45–1.1  $\mu\text{W}/\text{K}^2\text{cm}$ , to be attributed to the substantial decrease in resistivity, while partially disordered sample present comparatively lower values, respectively 0.45–0.90  $\mu\text{W}/\text{K}^2\text{cm}$  and 0.35–0.60  $\mu\text{W}/\text{K}^2\text{cm}$  for CTS 550 and CTS 600, respectively. The value for ordered CTS 650 is about 0.15  $\mu\text{W}/\text{K}^2\text{cm}$  in the entire temperature range. These results suggest that disorder structural plays a crucial role in the improvement of the  $PF$ .

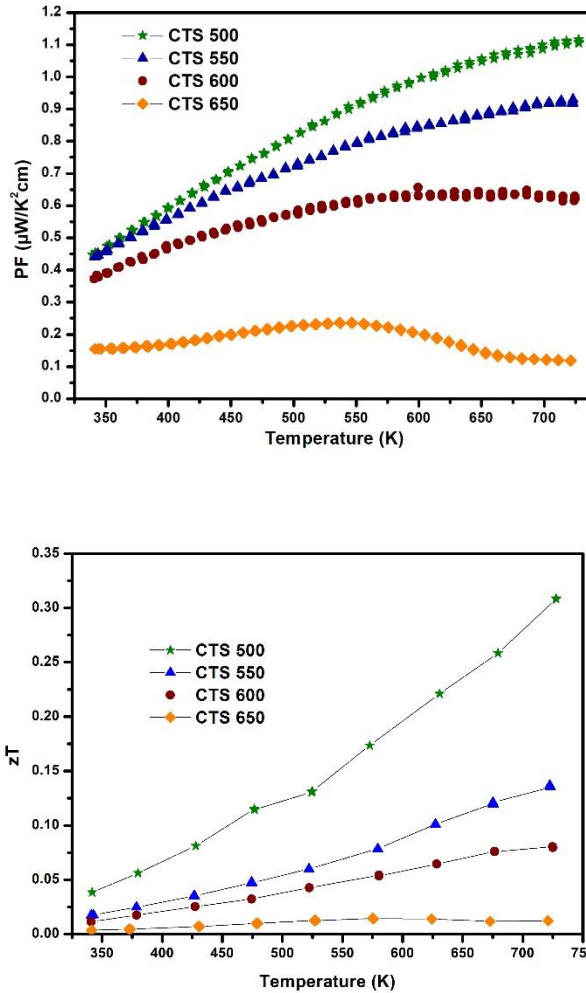


Figure 2.1.8. (a) Temperature-dependent Power Factor ( $PF$ ) and (b) figure of merit ( $zT$ ) for the different CTS samples.

The figure of merit  $zT$  is shown in Figure 2.1.8 (b). The highest  $zT$  belongs to the disordered (CTS 500), reaching a value of 0.30 at 723 K. Partially-disordered (CTS 550 and CTS 600) samples present a  $zT$  in the range 0.01–0.13 and 0.01–0.07 while the ordered (CTS 650) sample exhibits a figure of merit below 0.01 for the entire temperature range.  $zT$  values for ordered CTS are in agreement with the literature.<sup>13</sup> In literature, undoped ordered CTS has been reported with small  $zT \sim 0.1$ <sup>13,34–36</sup> and,  $zT \sim 0.2$ <sup>70</sup> above 700K whereas with Zn<sup>34</sup>,

$\text{Fe}^{13}$ ,  $\text{Mn}^{35}$ ,  $\text{Co}^{36}$  and,  $\text{In}^{70}$  doping  $zT > 0.5$  above 700K has been reported. In present work, disordered CTS presents an enhanced  $zT$  with respect to ordered CTS, which stand highest among CTS systems without doping. This is to be attributed primarily to the suppression of thermal transport leading to ultra-low thermal conductivity, as well as to the low electrical resistivity. In particular, thermal conductivity values for disordered CTS (CTS 500) are lower than all the reported results for CTS.

## 2.1.5 Conclusions

This work provides an alternative approach to produce disordered CTS via a synthesis method instead of acting on the chemistry by doping, a possibility, which is not investigated in the existing literature. The impact of cation disorder on the thermoelectric properties of CTS has then been investigated. The disordered structure indeed is playing a crucial role, providing ultra-low thermal conductivity 0.5 - 0.26 W/(m\*K) in the temperature range 323K–723K. At higher thermal treatment temperature, a partial transition to the ordered monoclinic phase happens as well as grain growth. This results in increased Seebeck and resistivity due to poor charge carrier concentration. Ordered CTS 650 has the highest Seebeck, resistivity and thermal conductivity, leading to small  $zT < 0.05$ , whereas the low Seebeck, low electrical resistivity and ultra-low thermal conductivity in disordered CTS 500 lead to the  $zT \sim 0.30$ . This is the highest in reported CTS systems without acting on the chemistry. The partially-disordered ( $\sim 27\%$  and  $\sim 60\%$  monoclinic) samples have intermediate  $zT$ , being  $zT \sim 0.13$  and  $zT \sim 0.07$  respectively, above 700K. The presence of tin oxide has been investigated, as it has a deteriorating effect on the resistivity of CTS: work is in progress to control and remove this problem. The present work affirms that a disordered cubic structure has better chances to stand as a high-performance thermoelectric material; and such a disordered structure can be produced without any doping. The present results also contribute to better understand the thermoelectric properties of CTS polymorphs.

## 2.2 Experimental and *Ab Initio* Study of Cu<sub>2</sub>SnS<sub>3</sub> (CTS) Polymorphs for Thermoelectric Applications

Published under a CC BY 4.0 license.

This section is entirely taken from<sup>71</sup>: Lohani, K.; Nautiyal, H.; Ataollahi, N.; Fanciulli, C.; Sergueev, I.; Etter, M.; Scardi, P. *Experimental and Ab Initio Study of Cu<sub>2</sub>SnS<sub>3</sub> (CTS) Polymorphs for Thermoelectric Applications. J. Phys. Chem. C* **2021**, *125*, 178–188.

<https://doi.org/10.1021/acs.jpcc.0c09139>

Please cite any part of this section as specified above.

Ketan Lohani<sup>a</sup>, Himanshu Nautiyal<sup>a</sup>, Narges Ataollahi<sup>a</sup>, Carlo Fanciulli<sup>b</sup>, Ilya Sergueev<sup>c</sup>, Martin Etter<sup>c</sup>, and Paolo Scardi<sup>a\*</sup>

<sup>a</sup>Department of Civil, Environmental and Mechanical Engineering, University of Trento, Via Mesiano 77, 38123, Trento, Italy

<sup>b</sup>National Research Council of Italy-Institute of Condensed Matter Chemistry and Technologies for Energy (CNR-ICMATE), Lecco Unit, Via Previati 1/E, 23900, Lecco, Italy

<sup>c</sup>Deutsches Elektronen-Synchrotron DESY, D22607 Hamburg, Germany

\*Correspondence: [Paolo.Scardi@unitn.it](mailto:Paolo.Scardi@unitn.it)

Received: 8 October 2020; Revised: 11 December 2020;  
Published: online 30 December 2020; Published: in issue 14 January 2021

## 2.2.1 Abstract

$\text{Cu}_2\text{SnS}_3$  (CTS) is a medium-temperature, ecofriendly, *p*-type thermoelectric material known for phonon-glass-electron-crystal characteristic. In the present work, ordered and disordered CTS samples were prepared from elemental powders, and their electronic and vibrational properties were systematically investigated by experimental methods and *ab initio* calculations. The disordered CTS polymorph presents a higher power factor,  $PF \sim 1.5 \mu\text{W}/\text{K}^2 \text{ cm}$ , than the ordered and stable phase,  $PF \sim 0.5 \mu\text{W}/\text{K}^2 \text{ cm}$ , above 700 K, as an effect of a smaller band gap and higher carrier concentration. It turns out that structural disorder contributes to the suppression of thermal conductivity. Most importantly, the disordered CTS shows an ultralow thermal conductivity,  $k \sim 0.4\text{--}0.2 \text{ W}/\text{m K}$ , as compared to ordered,  $k \sim 1.0\text{--}0.4 \text{ W}/\text{m K}$ , in the temperature range of 323 – 723 K. The combined effect of a higher PF and lower  $k$  results in a higher figure of merit,  $zT \sim 0.5$  at 723 K, obtained for disordered CTS without resorting to chemical alloying. While group velocity of acoustic phonons, as shown both by experiments and *ab initio* calculations, is similar in the two polymorphs, a strong anharmonicity characterizes the disordered CTS, resulting in the presence of low-lying optical modes acting as traps for heat transmission. Density functional theory/density functional perturbation theory simulations and nuclear inelastic scattering combined with high-resolution diffraction studies of the lattice parameters reveal details of phonon–phonon interactions in CTS with unprecedented effectiveness.

## 2.2.2 Introduction

Thermoelectric (TE) materials attract increasing interest in applications involving thermal gradients for durable, noise-free, and scalable solid-state power generators and coolers.<sup>9,10,24,72</sup> Performing TE devices require an optimal combination of properties—Seebeck coefficient ( $S$ ), electrical conductivity ( $\sigma$ ), and thermal conductivity ( $k$ )—to maximize the figure of merit,  $zT = TS^2\sigma/k$ . Therefore, an ideal TE material would require a high power factor ( $PF = S^2\sigma$ ) and a low  $k$  (involving an

electronic ( $k_e$ ) and a lattice ( $k_l$ ) component). In particular, obtaining an ultralow thermal conductivity is one of the main goals of the current research on TE materials.<sup>73–75</sup>

The  $\text{Cu}_2\text{SnS}_3$  mineral phase was first reported in 1983, as a new sulfide with a triclinic structure (SG:  $P1$ ).<sup>25</sup> It has been widely studied as an absorber material for photovoltaic devices owing to its high ( $\sim 10^4 \text{ cm}^{-1}$ ) optical absorption coefficient and tunable band gap spanning from 0.7 to 1.6 eV.<sup>65,76–79</sup> In recent years, CTS has attracted interest from the TE community for its 3D hole conductive network and ultralow thermal conductivity, a so-called “phonon-glass-electron-crystal” characteristic.<sup>80</sup> At first, in 2016, Tan et al.<sup>33</sup> and Shen et al.<sup>34</sup> reported CTS as a potential TE material, using In and Zn doping, respectively. Other researchers have reported Mn<sup>35</sup>, Ni<sup>32</sup>, Fe<sup>13</sup>, and Co<sup>36</sup> doping to enhance the TE performance of CTS.

The experimental literature suggests that undoped CTS forms an ordered monoclinic (SG:  $Cc$ ) phase.<sup>48</sup> However, this ordered CTS polymorph has high electrical resistivity ( $\rho$ ) and  $k$  values, resulting in a low  $zT$ .<sup>13</sup> One way to lower  $k$  is to hinder the propagation of phonon waves, and to do this, some researchers produced a disordered cubic (SG:  $F43m$ ) polymorph.<sup>36</sup> This, however, required acceptor cation doping, except in our recent work,<sup>26</sup> where we have shown how to stabilize the disordered CTS polymorph using a bottom-up (reactive milling) production technique that does not require any doping.

CTS polymorphs are a variant of the zinc blende ( $\text{ZnS}$ ) structure (Figure 2.2.1 (a)), made of tetrahedral cages (Figure 2.2.1 (b)) of S (Wyckoff position  $(4c)$ ) with a cation (Zn) positioned in the middle ( $4a$ ). For ordered (Figure 2.2.1(c)) and disordered (Figure 2.2.1d) CTS, the Zn cation is stoichiometrically replaced by Cu and Sn, respectively, in an ordered and in a random manner. This results in a partial cation occupancy of  $2/3$ , and  $1/3$ , for Cu and Sn, respectively.<sup>81</sup> These polymorphs can also be understood as an assembly of S coordination motifs, in which each S anion is connected to four (Cu/Sn) cations, making tetrahedral motifs. Zawadzki *et al.*<sup>82</sup> have put forward that cations in CTS structures contain five possible  $\text{S-Cu}_i\text{Sn}_{4-i}$  motifs, where  $i \in \{0, \dots, 4\}$ , but the  $\text{S-Cu}_4$ ,  $\text{S-CuSn}_3$ , and  $\text{S-Sn}_4$  motifs are energetically unlikely to form. The ordered CTS has a regular

distribution of  $\text{S-Cu}_2\text{Sn}_2$  and  $\text{S-Cu}_3\text{Sn}$  motifs, while in disorder CTS,  $\text{S-Cu}_2\text{Sn}_2$  motifs form nanometer-scale clusters. Additionally, because the octet rule is not locally respected in these structures, all of this brings the crystal structure, especially in the disordered phase, close to instability. In the present work, the abovementioned clustering effect was not considered for *ab initio* calculations because of the limitation of computational resources, rather two, Sn-rich and Sn-poor disordered cells. Zhai *et al.*<sup>68</sup> have discussed the difficulty in the *ab initio* simulation of similar  $\text{Cu}_2\text{SnX}_3$  ( $X=\text{S}/\text{Se}$ ) disordered structures, and how this limits the electronic information from band structures. However, the electronic bands for the ordered phase are diffusely discussed in the literature.<sup>68,83,84</sup>

In the similar CTSe system,<sup>41</sup> the disordered polymorph shows a lower band gap energy than the corresponding ordered phase, which promotes a higher carrier concentration ( $n$ ), resulting in a higher  $PF$ . Recently, we have shown that the disordered CTS polymorph without acceptor doping presents a higher  $PF \sim 1.1 \mu\text{W}/\text{K}^2 \text{ cm}$  than the ordered polymorph,  $PF \sim 0.1 \mu\text{W}/\text{K}^2 \text{ cm}$ , above 700 K. In fact, the disordered polymorph has a lower Seebeck ( $S \sim 250\text{--}325 \mu\text{V}/\text{K}$ ) and resistivity ( $\rho \sim 1.5\text{--}1.0 \Omega \text{ cm}$ ) than the ordered polymorph ( $S \sim 600\text{--}700 \mu\text{V}/\text{K}$ ,  $\rho \sim 27\text{--}30 \Omega \text{ cm}$ ), in the temperature range of 323–723 K.<sup>26</sup>

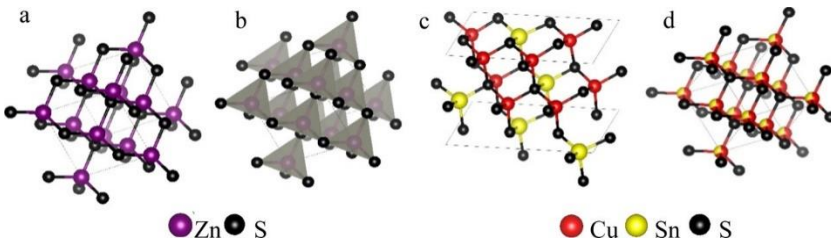


Figure 2.2.1. ZnS structure (a) with tetrahedral drawn (d) and monoclinic (SG:  $Cc$ ) ordered (a), cubic (SG:  $F43m$ ) disordered (b) CTS.

Both polymorphs show a decreasing  $k$  trend with increasing temperature, indicating the presence of a dominating phonon–phonon interaction.<sup>36</sup> However, it is the ultralow thermal conductivity ( $k < 0.5 \text{ W}/\text{K m}$ ) shown by the disordered polymorph which is particularly interesting<sup>35</sup> and still little studied. Several mechanisms could be at the origin of this much-desired behavior, such as an enhanced phonon

scattering because of the increase in crystal symmetry, cation disorder, soft bonds, alloy scattering, and possible suppression of normal phonon scattering process because of random cations and dopant distribution.<sup>13,34</sup>

In this work, ordered and disordered CTS polymorphs were produced in a highly controlled environment from elemental powders (Cu, Sn, and S) using a high-energy reactive ball-mill, followed by sintering at various temperatures. We started from the experimental results for PF and thermal conductivity for both the phases, stating the higher performance of the disordered form of CTS. Therefore, we have investigated the mechanisms leading to the improvements observed, looking for a full understanding of the CTS system. The work presents a unique mix of experimental analyses and theoretical calculations that are able to achieve a complete description of the CTS property dependence by the structural phase disorder. We have studied electronic and vibrational properties using density functional theory (DFT) and density functional perturbation theory (DFPT) simulations, respectively. The *ab initio* calculations provide insights on the possible origin of the ultralow  $k$ , which is identified as a distinct behavior of the cations in the disordered structure. By investigating the vibrational density of states (DOS) and phonon dispersion curves and correlating them with the mode Grüneisen parameters ( $\gamma_i$ ) and electron localization function (ELF) curves, we unveil the vibrational properties of CTS. Nuclear inelastic scattering (NIS) from Sn provides direct experimental evidence on the vibrational DOS, validating the DFPT results, and in particular, the mechanism underlying the ultralow thermal conductivity of the cubic disordered CTS phase. Moreover, by combining NIS and high-resolution X-ray diffraction (XRD) measurements, Grüneisen parameters were experimentally calculated for the disordered sample. The investigation proposed in this work, covering most of the material characteristics, can be the base for the design of novel solutions for the development of materials based on CTS with improved TE properties.

### 2.2.3 Experimental Methods

Elemental powders of Cu, Sn, and S, procured from Sigma-Aldrich (99% pure) were fed in ball-mill vials made of WC, and anhydrous

$\text{C}_2\text{H}_5\text{OH}$  (100  $\mu\text{l}$ .) was added to the mixture as a lubricant. High-energy ball-milling Fritsch P4 was used for the milling. The mill was operated for 30 and 60 min, with a fixed main disk and spinning speed of 300 rpm and  $-540$  rpm, respectively. Two circular pellets (thickness  $\sim 1.5$  mm, diameter  $\sim 16$  mm) were prepared using a manual cold press. One sample was sintered at  $500^\circ\text{C}$ , and the other was sintered at  $650^\circ\text{C}$ , for 2 h in Ar flux. The entire synthesis process was performed in a highly controlled environment ( $\text{O}_2$  and  $\text{H}_2\text{O} < 10$  ppm).

XRD was performed on as-milled powders and sintered disks, in Bragg–Brentano geometry using a Rigaku PMG powder diffractometer equipped with a graphite bent-crystal monochromator, and  $\text{Cu K}\alpha$  source operated at 40 kV and 30 mA. The optical properties of CTS polymorphs were investigated using a PerkinElmer spectrophotometer (PerkinElmer, Milan, Italy), model LAMBDA 750, equipped with a 150 mm integrating sphere.

The polycrystalline samples were dispersed in ethanol and sonicated for 1 h, and the optical absorption spectra were collected. Mobility ( $\mu$ ) and carrier concentration ( $n$ ) were measured with an MMR K-20 and an H-50 measurement system by applying a magnetic field of 6720 Gauss, in temperature range 300–450 K.

The absolute Seebeck coefficient ( $S$ ) was measured using a Pt Standard, while resistivity ( $\rho$ ) was measured by four-contact measurements using a Linseis LSR-3 instrument. Thermal diffusivity ( $D$ ) was measured using a Linseis LFA-500.  $S$ ,  $\rho$ , and  $D$  measurements were performed over the temperature range of 323–723 K.

To verify our theoretical findings, we have used NIS with  $^{119}\text{Sn}$  nuclear resonance. The method provides the partial phonon-DOS (pDOS) of Sn atoms. Experiments were carried out at the dynamics beamline P01 at PETRAIII (DESY, Hamburg) using a high-resolution monochromator with 1.4 meV energy resolution at 23.9 keV, the energy of the  $^{119}\text{Sn}$  nuclear transition. The measurements were performed on samples with natural enrichment by  $^{119}\text{Sn}$  (8.6%) inserted into the closed cycle He cryostat and kept at 43 and 295 K. The nuclear resonance signal was separated in time from electronic X-ray

fluorescence and measured using a Si avalanche photodiode detector. This measurement was combined with high-resolution XRD studies of the lattice parameters between 100 and 300 K at the beamline P02.1 at PETRAIII. The combination of the phonon and lattice parameter measurements provides the possibility to obtain the mode Grüneisen parameters.

## 2.2.4 Computational Methods

The electronic structures were studied using DFT as implemented in the Vienna ab initio simulation package.<sup>85,86</sup> The interaction between the electron ion was described using the projector augmented wave method. The generalized gradient approximation with Perdew–Burke–Ernzerhof (PBE)<sup>87</sup> electron exchange–correlation was employed for band structure and DOS calculations.

The ternary ordered and disordered CTS polymorphs present *Cc* and *F4̄3m* structural symmetry, respectively. As already pointed out, in the ordered CTS, each S anion is tetrahedrally bonded by four cations (Cu/Sn), forming S–Cu<sub>2</sub>Sn<sub>2</sub> and S–Cu<sub>3</sub>Sn motifs. The disordered CTS system is possible when the cations (Cu/Sn) randomly replace Zn with an occupancy of 66.66 and 33.33%, respectively, in a diamond-like ZnS structure. This partial occupancy leads to a primitive cell that cannot be simulated exactly.<sup>68</sup> To satisfy the partial occupancy and respect the stoichiometry, one needs to make large cells that are computationally nonviable to solve. To overcome this limitation, two disordered cells were modeled by a slight alteration of the partial occupancy of Cu and Sn, respectively. The first cell was modeled with Cu (65.625%) and Sn (34.375%), and the second cell was modeled with Cu (68.75%) and Sn (31.25%). Hereafter, the first and second disordered cells are referred to as disordered Sn-rich and disordered Sn-poor, respectively.

The plane wave cutoff and electronic convergence were set to 500 eV and 10<sup>-6</sup> eV, respectively. All the structures were relaxed until the force on each atom was <0.01 eV/Å, using a Gaussian smearing with  $\sigma = 0.05$ . Two k-point mesh of 4 × 3 × 4 and 4 × 4 × 4 were used for ordered and disordered systems, respectively, using the Monkhorst–Pack

technique centered at the  $\Gamma$ -point.<sup>88</sup> For single-point self-consistent field calculation, the tetrahedron method and Blöchl corrections were considered. The high symmetry path was provided by Seek-Path.<sup>89</sup> The DOS was calculated on a dense k-mesh of  $12 \times 12 \times 12$  and  $8 \times 8 \times 8$  grids.

The phonon dispersion curve and pDOS were calculated using the Phonopy code.<sup>90</sup> For DFPT calculations, local density approximation<sup>91</sup> was used with a  $10^{-8}$  eV convergence criteria. These calculations were performed on the ordered supercell ( $2 \times 2 \times 2$ ), whereas, for both the disordered cells, a much larger, 64-atom cell was used. The mode Grüneisen parameter ( $\gamma_i$ ) was calculated using a quasi-harmonic approximation, by expanding and contracting the relaxed cell volume by  $\pm 1\%$ .

## 2.2.5 Results and Discussion

Structural Analysis: XRD measurements were performed on elemental powder milled for 30 and 60 min, and samples were sintered at 500 and 650 °C (shown in Figure 2.2.2). The 30 min milled powder was observed as a blend of partially formed CTS, binary sulfides (SnS and CuS), and metallic elements (Cu and Sn). With a longer milling time of 60 min, the CTS (SG:  $F\bar{4}3m$ ) formation was complete, although one weak Sn peak ( $2\theta \sim 32^\circ$ ) could still be observed. Because of the use of WC vials for the milling, traces of WC (SG:  $P\bar{6}m2$ ) were present in the as-milled powder. Broad peaks with diffuse background for the as-milled powder suggests the presence of small crystalline domains and a possibly amorphous fraction. As expected, the sintering step increases both crystallinity and grain size. The CTS sample sintered at 500 °C shows a disordered cubic structure alike as-milled CTS, identified by three characteristic peaks at  $2\theta \sim 28.5, 47,$  and  $56^\circ$ , representing planes (111), (220), and (311), respectively. However, the sample sintered at 650 °C shows three additional peaks located at  $2\theta \sim 16, 18,$  and  $21^\circ$ , respectively, representing planes (110),  $(11\bar{1})$ , and (021), characteristic of the ordered monoclinic structure (SG:  $Cc$ ).

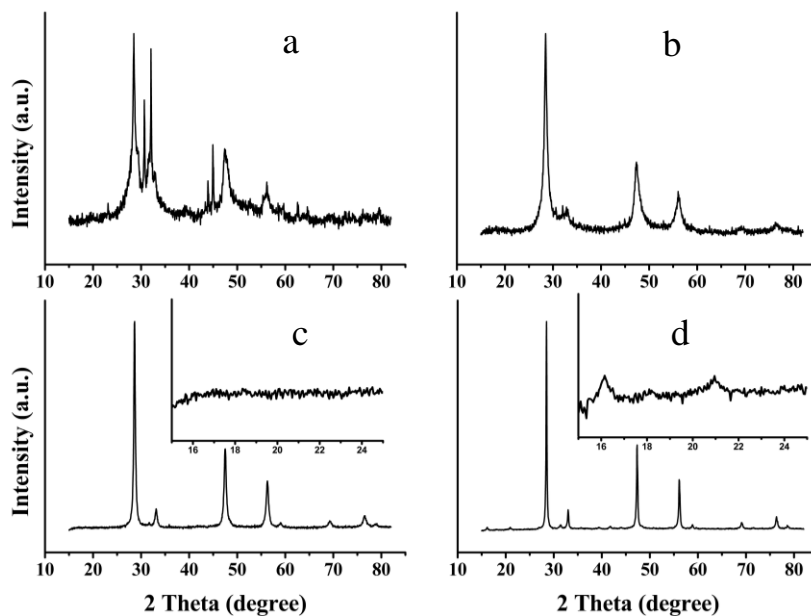


Figure 2.2.2. XRD pattern of CTS samples after 30 (a), and 60 min milling (b); then, in the sintered disordered (c) and ordered (d) forms. The insets show details of the distinctive peaks of the monoclinic phase.

To confirm the crystallographic structure and to get quantitative information on the crystallite size, the Rietveld refinement<sup>55</sup> was performed using the whole powder pattern modeling<sup>56</sup> approach, as implemented in the recent release of the software TOPAS 7.<sup>57</sup> The underlying assumption is that the crystalline domains are approximated by spheres with a lognormal distribution of diameters. Modeling results are shown in Figure 3 and Table 2.2.1.

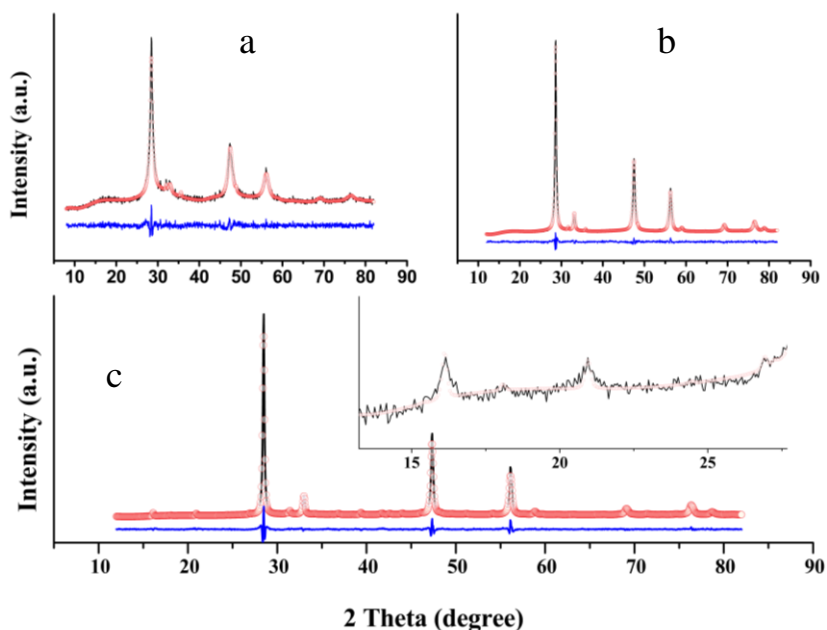


Figure 2.2.3. Rietveld refinement performed on 60 min milled powder (a), disordered (b), and ordered (c) sintered CTS samples. Experimental data (circle), model (line) and their difference, or residual (line below).

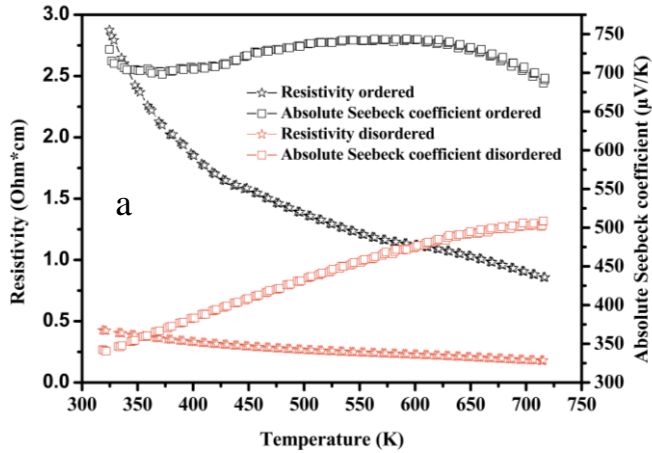
Table 2.2.1. Lattice Parameter and Average Crystallite Size for 60 min Milled Powder, Disordered, and Ordered Sintered CTS Samples (*cf.* Figure 2.2.3\_a,b,c, Respectively)

Sample	Lattice parameters ( $\pm 0.01 \text{ \AA}$ )	Angle ( $^\circ$ )	Average crystallite size ( $\pm 10 \text{ nm}$ )
60 min milled	$a = b = c = 5.44$	$\alpha = \beta = \gamma = 90$	20
disordered	$a = b = c = 5.44$	$\alpha = \beta = \gamma = 90$	50
ordered	$a = 6.66, b = 11.5,$ $c = 6.66$	$\alpha = \gamma = 90,$ $\beta = 109.39$	200

The formation of tin oxides is a known problem for this family of materials, which deteriorates the TE performance in temperature.<sup>51</sup> These oxide phases are hard to eliminate because of the low partial pressure for tin oxide formation.<sup>92</sup> Comparatively, a higher amount (2–5% weight fraction) of tin oxides was observed in CTS samples prepared using binary sulfides ( $\text{CuS}$  and  $\text{SnS}$ ). Rather, the present samples prepared from elemental powders ( $\text{Cu}$ ,  $\text{Sn}$ , and  $\text{S}$ ) processed in a strictly controlled environment do not show the formation of secondary phase oxides in the disordered CTS, which is a

substantial improvement from previous studies.<sup>26</sup> Nevertheless, a small amount of SnO<sub>2</sub> (<1% in weights) was observed in the ordered CTS.

Figure 2.2.4 (a) shows the electrical resistivity and Seebeck coefficient for the CTS polymorphs. Both phases show an overall decreasing trend of resistivity with the temperature, while  $S$  has positive values and an increasing trend, typical of nondegenerate  $p$ -type semiconductors. Nevertheless, the ordered sample shows a decrease in  $S$  above  $\sim 600$  K, likely caused by thermal excitation of bipolarons.<sup>36</sup> The disordered sample presents a lower resistivity ( $\rho \sim 0.5\text{--}0.2 \text{ } \Omega \text{ cm}$ ) than the ordered ( $\rho \sim 3.0\text{--}1.0 \text{ } \Omega \text{ cm}$ ). Optical measurements (Figure 2.2.5) show band gaps  $\sim 0.99$  and  $\sim 0.95$  eV for the ordered and disordered samples, respectively. A lower band gap promotes a higher carrier concentration, and indeed, the average value of carrier concentration for the disordered sample ( $n \sim 1.9 \times 10^{18} \text{ cm}^{-3}$ ) is 10-fold higher than the ordered ( $n \sim 2.7 \times 10^{17} \text{ cm}^{-3}$ ). The two polymorphs show similar mobility ( $\mu \sim 20 \text{ cm}^2/\text{Vs}$ ) and values compatible with those expected for the stable CTS phase (spanning from 1 to  $80 \text{ cm}^2/\text{Vs}$ <sup>93</sup>) (shown in Figure 2.2.S2, in appendix 2.2.7). According to the Mott equation,<sup>9</sup> both  $n$  and  $\mu$  have an inverse relation with the Seebeck coefficient, and this explains the lower  $S$  ( $\sim 320\text{--}500 \text{ } \mu\text{V}/\text{K}$ ) for the disordered sample. Overall, above 700 K, the disordered CTS presents a higher PF ( $\sim 1.5 \text{ } \mu\text{W}/\text{K}^2 \text{ cm}$ ) than the ordered polymorph ( $\sim 0.5 \text{ } \mu\text{W}/\text{K}^2 \text{ cm}$ ); see Figure 2.2.4 (b).



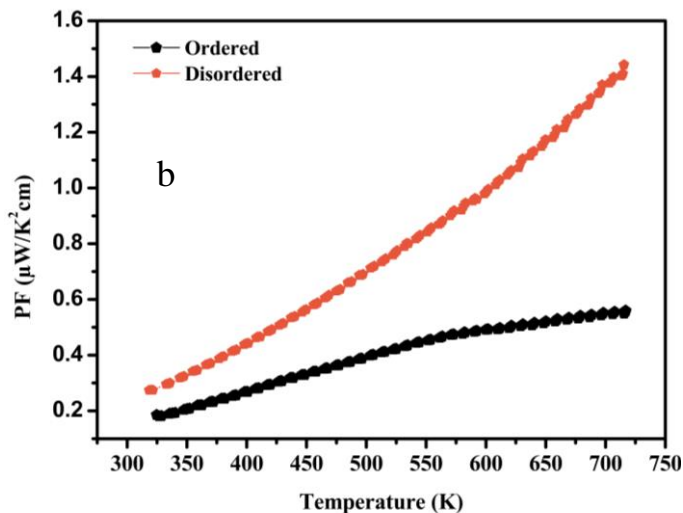


Figure 2.2.4. Resistivity (star) and absolute Seebeck coefficient (circle) for ordered (black) and disordered (orange) phases (a); corresponding power factor calculated as  $\text{PF} = S^2/\rho$  for ordered (black) and disordered (orange) CTS (b).

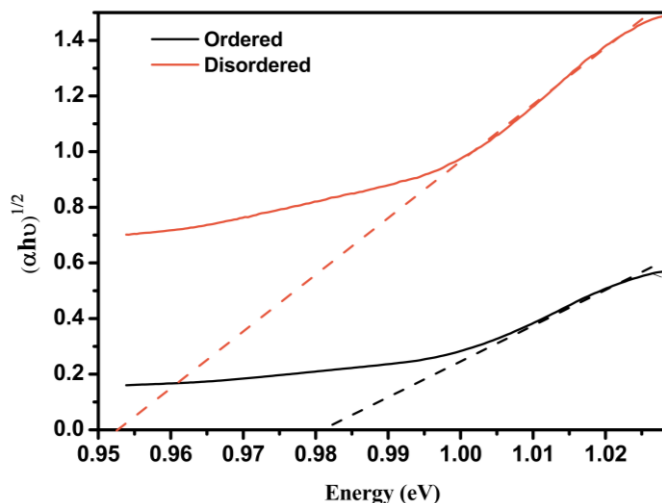


Figure 2.2.5. Band gap ( $E_g$ ) estimated by linear extrapolation in the Tauc plot, using the equation  $\alpha h\nu = A(h\nu - E_g)^{1/2}$ , where  $\alpha$ ,  $h$ ,  $\nu$ ,  $A$ , and  $E_g$  are absorption coefficient, Planck constant, frequency, transition constant, and band gap, respectively (optical absorption spectra is shown in the appendix 2.2.7 file, Figure S 2.2.1).

In order to further understand the differences between the results obtained for ordered and disordered samples, the electronic properties were investigated by DFT. As already pointed out, the ordered structure was simulated with its exact stoichiometry, using 24-atoms (8-Cu, 4-

Sn, and 12-S), whereas for the disordered phase, the constraint of occupancy and the structure<sup>68</sup> led us to simulate two slightly off-stoichiometric structures, Sn-rich (21-Cu, 11-Sn, and 32-S) and Sn-poor (22-Cu, 10-Sn, and 32-S), respectively. Total and atomic projected electronic DOS are shown in Figure 2.2.6 for both CTS structures. The total DOS is higher in the valence band (VB) side than in the conduction band (CB), for all the structures, confirming the p-type nature of CTS. In VB, the main contribution to the projected-atomic DOS is given by Cu 3d and S 3p orbitals, whereas the CB is composed of Sn 5s and S 3p orbitals.

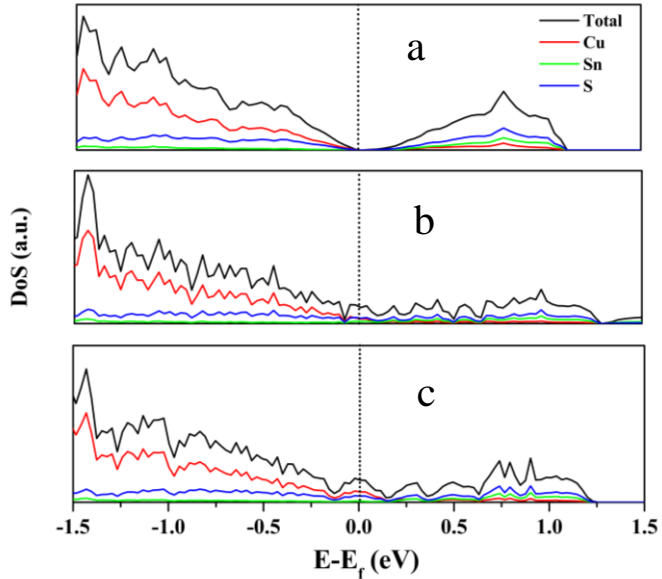


Figure 2.2.6. Total DOS and atomic projected DOS for ordered (a), Sn-rich disordered (b), and Sn-poor disordered (c) cells; the Fermi energy is shown by the dotted line.

Band structures are shown in Figure 2.2.S3 of the appendix 2.2.7 file. This for the ordered CTS is in agreement with the literature,<sup>68,94</sup> also showing a largely underestimated band gap value. This is even more relevant for the cubic phase, where no band gap is observed in the DFT results, as it has also been found for analogous simulations of the disordered copper–tin–selenide system.<sup>41</sup> The random distribution of Cu and Sn atoms in the disordered structures causes band tailing, which points out the presence of available states in the DOS curve near the Fermi energy.<sup>53</sup> It is likely that the structures in the gap region and the tailing of the DOS at the Fermi energy play a role in enhancing the

carrier concentration, as we observed experimentally. Even if the PBE exchange–correlation tends to underestimate the band gap,<sup>95</sup> the band tailing reduces the band gap, in agreement with the optical absorption results of Figure 2.2.5.

Thermal conductivity was calculated as  $k = DdC_p$ , where  $D$ ,  $d$ , and  $C_p$  are thermal diffusivity, density, and specific heat capacity, respectively. Thermal diffusivity and density were measured using a xenon flash instrument and Archimedes' method, respectively, while the value of  $C_p$  was taken from our previous work.<sup>26</sup>

As shown in Figure 2.2.7, the thermal conductivity of the ordered CTS ranges from 1.0 to 0.45 W/m K, whereas it is ultralow for the disordered CTS, with values 0.45–0.20 W/m K, in the temperature range 323–723 K. The trend of  $k$  decreases with temperature, indicative of increased phonon–phonon interactions. The present values of  $k$  are lower than in CTS prepared by high-temperature solid-state reactions.<sup>35</sup> Reasons are likely related to the bottom-up production method, which limits the grain growth, as well as to a lower density. However, the effect of the lower density on thermal conductivity can be ignored for the comparison between samples of the two polymorphs because they have similar densities ( $\sim 3.7 \text{ g/cm}^3$ ), lower than theoretical ( $\sim 4.85 \text{ g/cm}^3$ ). Furthermore, near room temperature ( $T = 323 \text{ K}$ ), the lattice component of thermal conductivity was estimated using the single parabolic band (SPB) approximation (calculations used are shown in the appendix 2.2.7). As it happens in highly resistive semiconductors, the thermal conductivity is dominated by the lattice part. For ordered and disordered samples, the  $k_l$  is  $\sim 0.44$  and  $\sim 0.99 \text{ W/m K}$ , respectively; such values are close to the experimentally measured values for total thermal conductivity, confirming the main role of phonon contribution to thermal transport. However, the difference between the values achieved by the two samples suggests a relevant discrepancy in the pDOS for the two structures.

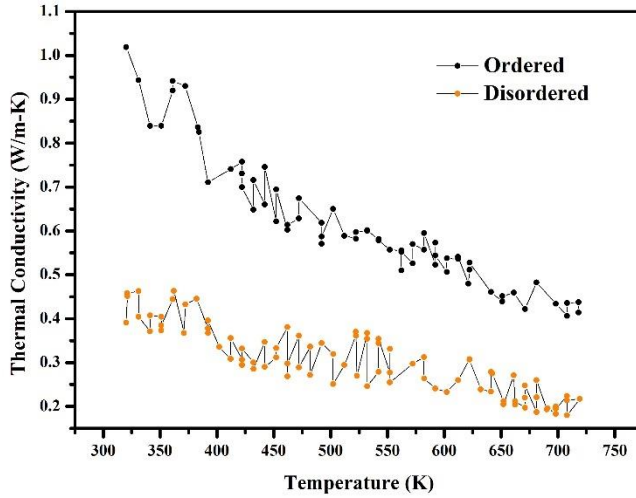


Figure 2.2.7. Thermal conductivity for CTS polymorphs in the temperature range of 323–723 K.

The phonon dispersion curves were investigated using first-principle calculations to shed light on the lower  $k_1$  of the disordered polymorph. The primitive cell of the ordered CTS has 12 atoms, whereas the disordered cells were simulated with 64 atoms. Therefore, the phonon dispersion curves show  $3N$  ( $N$  = number of atoms), 36 and 192, branches of vibrational modes, respectively (see Figure 2.2.8 (a–c)). Three low-frequency modes are acoustical, rest ( $3N-3$ ) of the branches correspond to the optical modes. The low-frequency modes in all three cells are dominated by heavy Cu and Sn, while S, a much lighter atom, dominates the high-frequency modes. The difference in atomic-projected pDOS can be observed in a frequency of  $<1$  THz, in ordered and Sn-poor cells; these modes are dominated by Cu vibrations, whereas Sn vibrations dominate in the Sn-rich cell<sup>96</sup> The acoustic modes in the disordered Sn-rich cell are softer as compared to the ordered. Additionally, simulations show a weak bonding and a strong anharmonicity along the  $\Gamma$ -X and  $\Gamma$ -Z directions,<sup>97</sup> whereas these effects are less evident for the Sn-poor cell. The vibrational modes for the disordered cells are shifted to lower frequencies (see Figure 2.2.8 (d)), and the gap between low- and high-lying optical modes is narrower with higher population of low-lying optical modes. Moreover, optical modes cut the acoustical modes at a lower ( $\sim 1.1$  THz) frequency in the

disordered cells than in the ordered ( $\sim 1.9$  THz), suppressing the lattice thermal conductivity by scattering the heat-carrying acoustic modes.<sup>96</sup>

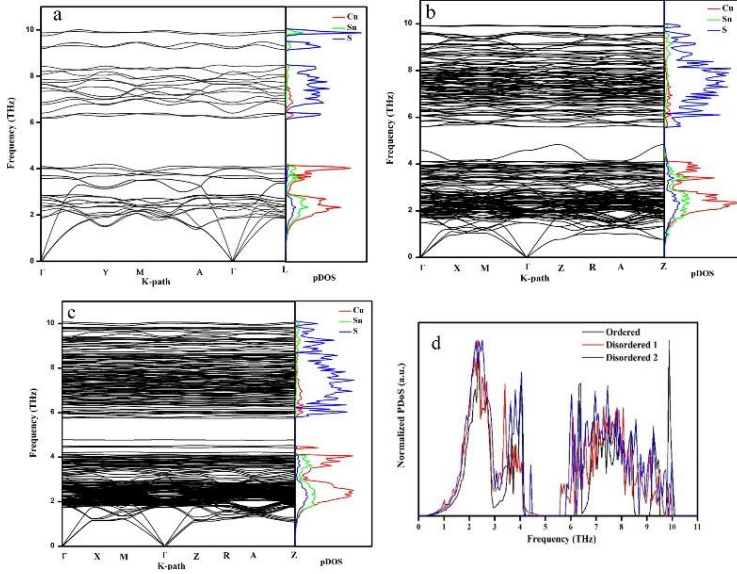


Figure 2.2.8. Phonon dispersion curves ( $\omega$  vs  $k$ ) and atomic-projected pDOS for ordered (a), disordered Sn-rich (b), disordered Sn-poor (c) cells, and a comparison among normalized total pDOS (d).

The optical phonon branches in the disordered cells are flatter than the ordered cell, suggesting a lower group velocity of optical phonons. The mode level phonon group velocity ( $V_g = d\omega/dk$ ) is shown in Figure 2.2.S4 of the appendix 2.2.7. The acoustic modes of all three cells show a similar  $V_g \sim 50$  THz Å. However, the experimentally obtained  $k$  for the disordered CTS has an approximately twofold lower value than that of the ordered, which cannot be explained in terms of a lower  $V_g$  only. This suggests the possibility of heat being trapped in low-velocity optical modes, as discussed with the phonon dispersion curves.<sup>98</sup>

Moreover, a strong anharmonic effect in bonding contributes to a low lattice thermal conductivity. The mode Grüneisen parameter ( $\gamma_i$ ), shown for all cells in Figure 2.2.9 is a measure of lattice anharmonicity, as it reflects the extent of deviations of phonon vibrations from the harmonic oscillations.

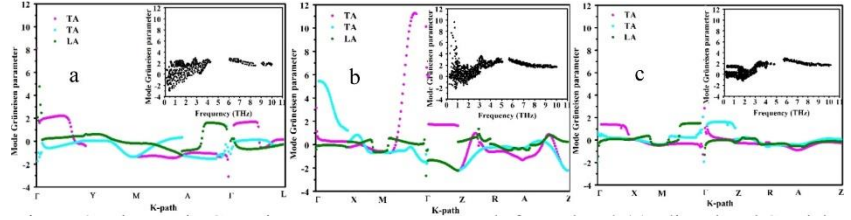


Figure 2.2.9. Mode Grüneisen parameter vs  $K$ -path for ordered (a), disordered Sn-rich, (b), and disordered Sn-poor (c) cells; the corresponding Grüneisen parameter vs frequency ( $\omega$ ) is shown in the insets.

For all cells, the fluctuation in the values of the mode Grüneisen parameter decreases for increasing frequency (shown in the insets of Figure 2.2.9), indicating a weak interaction between different vibrations at higher frequencies.<sup>99</sup> The Sn-rich cell shows a much higher mode Grüneisen parameter, whereas comparatively lower values were observed for the ordered and Sn-poor cells, suggesting the anharmonicity in the disordered structures is highly dependent on the concentration of Sn-atoms.

The atomic bonds were investigated by the ELF plots (Figure 2.2.10). Cu–S and Sn–S bonds show an ionic and covalent nature, respectively.<sup>100</sup> All Sn-atoms have similar electron localization (Figure 2.2.10 (a)) in the ordered cell because of the regular arrangement of S– $\text{Cu}_2\text{Sn}_2$  and S– $\text{CuSn}_3$  motifs. However, a variation in electron localization is observed in the disordered cells (Figure 2.2.10 (b,c)), indicating the inhomogeneous nature of Sn–S bonds<sup>101</sup> (see Figure 2.2.S5 of the appendix 2.2.7 for the contribution of every Cu and Sn atom to the atomic pDOS). In low frequencies (1–3 THz), an identical contribution of Sn can be observed for the ordered cell, whereas it is dispersed for disordered cells. These observations suggest a distinct nature of Sn atoms in the disordered cells, that might scatter phonons more efficiently than in the structure of the stable ordered CTS.

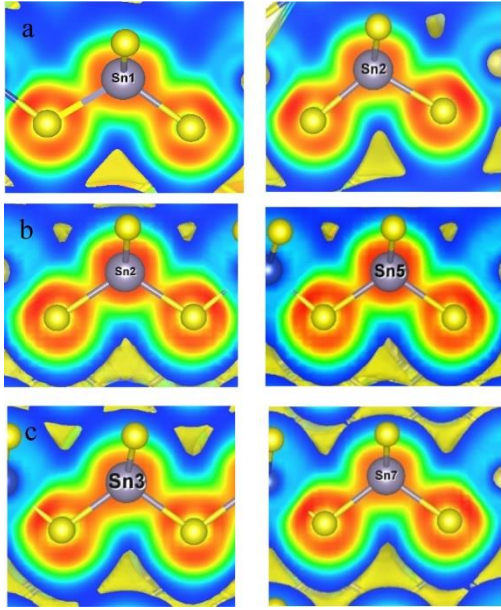


Figure 10. Magnified view of ELF plots for Sn atoms in ordered (a), disordered Sn-rich (b), and disordered Sn-poor (c) cells.

To validate the above conclusions on the Sn pDOS obtained by DFPT, NIS experiments (Figure 2.2.11) were performed at 43 K on both samples; an additional measurement was performed on the disordered sample at 295 K. The Debye energy was calculated by fitting the reduced pDOS ( $\text{pDOS}/E^2$ ) in the range 0.5–1.2 THz, using the parabolic function,  $\text{pDOS}(E)/E^2 = 3/E_D^3 + bE^2$ , where  $E$ ,  $E_D$ , and  $b$  are energy, Debye energy, and a fitting parameter, respectively<sup>102</sup>. The Debye energy together with other parameters obtained from Sn pDOS are presented in Table 2.2.2.

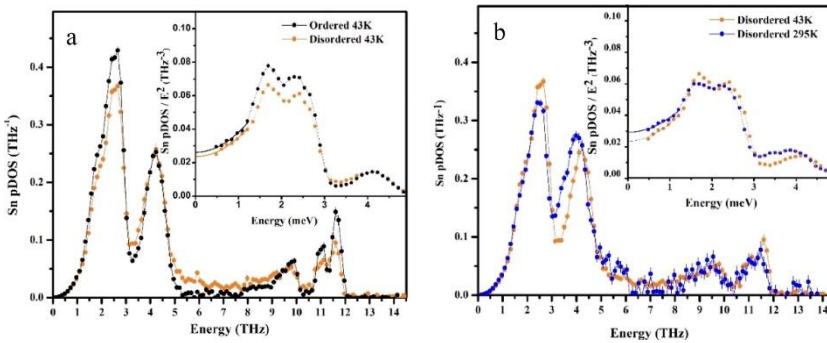


Figure 2.2.11. Sn pDOS-ordered and disordered CTS samples at 43 K (a) and disordered CTS samples at 43 and 295 K (b). Reduced Sn pDOS plots are shown in the inset for both figures.

Table 2.2.2. Parameters Obtained from the Sn VDOS of the Samples Measured at 43 and 295 K: The Lamb–Mössbauer Factor ( $f_{LM}$ ), the Sn Atomic Displacement Parameter ( $U_{eq}$ ), the Mean Force Constant ( $F$ ), the Debye Energy ( $E_D$ ), and the Mean Sound Velocity  $V$ .

	$f_{LM}$	$U_{eq}$ (Å <sup>2</sup> )	$F$ (N/m)	$E_D$ (THz)	$V$ (km/s)
ordered at 43 K	0.754 (1)	0.00180 (2)	224 (2)	5.13 (5)	2.69
disordered at 43 K	0.769 (1)	0.00193 (2)	221 (1)	5.02 (5)	2.81
disordered at 295 K	0.291 (4)	0.00844 (5)	196 (5)	4.67 (5)	2.62

The experimentally observed trend of Sn pDOS at 43 K agrees with the theoretical results for both samples. The disordered sample shows a broad phonon band (5–9 THz), consistently with the atomic-projected pDOS and individual atomic pDOS of Figure 2.2.8. The value of the Debye energies and mean sound velocities (see Table 2.2.2) are similar for both polymorphs, suggesting similar group velocities, as observed from mode level group velocity calculations.

The NIS measurement performed at 295 K on a disordered CTS sample reveals significant phonon mode softening for the acoustical part of the pDOS and a higher Debye level compared with the low T measurement. The relative energy shifts  $\Delta E/E$  of the specific peaks can be obtained from the pDOS measured at 43 and 295 K using the procedure described in refs <sup>103</sup> and <sup>104</sup>. XRD measurements were performed from 300 to 100 K with a step of 20 K (shown in the of the appendix 2.2.7), and the relative volume change  $\Delta V/V = 0.0065$  between 43 and 295 K was estimated by fitting a parabolic function (see Figure 2.2.12 (b)). Thus, using both relative volume and energy change Grüneisen parameters for specific phonon peaks were obtained and are shown in Figure 2.2.12 (a), which agrees with the results obtained via ab initio calculations presented in Figure 2.2.9. In particular, the high Grüneisen parameter was observed for the 0 energy and 4 THz peak.

The 0-energy value of the Grüneisen parameter was obtained by comparison of the Debye energy.

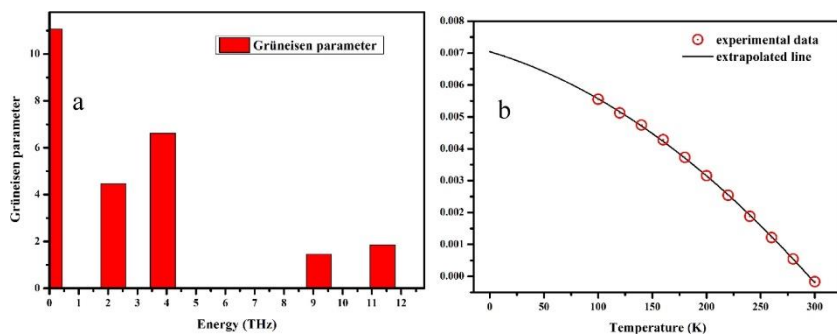


Figure 2.2.12. Grüneisen parameters of the specific phonon peaks of the disordered compound obtained from the NIS measurements at 43 and 295 K (a) and relative volume change  $\Delta V/V_{295\text{K}}$  from the XRD data collected in temperature range 300–100 K (b).

Hence, from the analyses performed on the samples and the good agreement achieved with the theoretical calculations, the ultralow thermal conductivity in the disordered sample is shown to be because of the random arrangement of Sn and Cu atoms, which not only blocks the normal phonon scattering but also shows strong anharmonicity for the inhomogeneous nature of the Sn–S bonds. The low-lying optical modes support acoustical-optical phonon scattering, and the higher value of the Grüneisen parameter obtained from DFPT and NIS results confirm the higher anharmonicity in the disordered structure. However, a lower mode Grüneisen parameter was observed in the Sn-poor cell, suggesting that anharmonicity in the disordered system is largely dependent on the Sn-atoms. Moreover, a small crystallite size (<100 nm) and the coexistence of secondary phases (WC, SnO, and  $\text{SnO}_2$ ) should also serve to additional phonon scattering.

The results achieved up to here are well summarized combining the electric and thermal transport properties in the dimensionless figure of merit,  $zT$  (Figure 2.2.13). For the ordered sample,  $zT \sim 0.05$  is in agreement with the values commonly reported in literature,<sup>13</sup> whereas  $zT \sim 0.5$  was observed for the disordered CTS polymorphs above 700 K, which is fairly high for an undoped material.<sup>24</sup> In particular, as demonstrated by our results, the

enhanced  $zT$  for the disordered CTS is an attribute of its high PF and ultralow thermal conductivity.

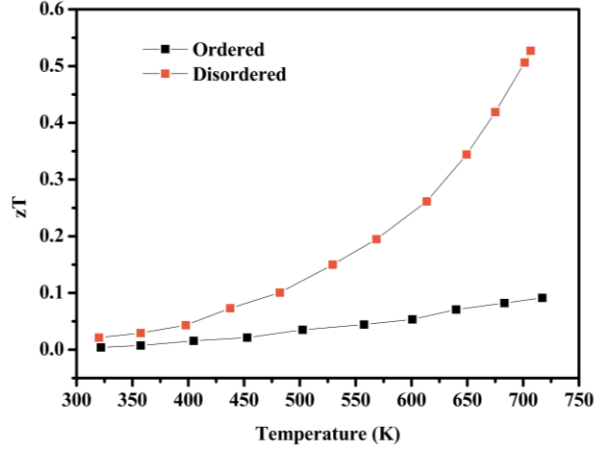


Figure 2.2.13. Calculated  $zT$  for ordered and disordered CTS samples.

## 2.2.6 Conclusions

In this work, a study of the dependence of TE properties of CTS by structural characteristics has been presented. In particular, the effect of structural disorder on electronic and thermal transport properties have been investigated, taking advantage of different experimental techniques. The disordered CTS polymorph shows a better TE performance than the ordered and stable CTS phase, mainly because of an enhanced carrier concentration and ultralow thermal conductivity observed in the former phase. In the present study, we have experimentally determined Seebeck coefficient, resistivity, and thermal conductivity and correlated them with the band gap, mobility, and carrier concentration obtained also from experimental measurements. First principles simulations disclose the presence of low-lying optical modes in the disordered cubic structure, with significant variation in the Sn bonding, leading to a strong anharmonicity. A variation in values of the mode Grüneisen parameter for Sn-rich and Sn-poor disordered cells confirms that the anharmonicity is dependent on the Sn-atoms. The overall picture emerging from DFT and DFPT simulations finds confirmation in NIS experiments, as the Sn-pDOS is in agreement with the *ab initio* results. NIS experiments performed at low (43 K) and near-

room temperature (295 K) show evidence of a strong anharmonicity, presence of softer modes, and a higher Debye level in the disordered polymorph. The results presented in this work cover most of the material characteristics providing a detailed understanding of the mechanisms promoting a relevant improvement in TE properties of CTS-based materials. In particular, the structural disorder results to have a major impact on the enhancement of material performance. Therefore, these results suggest the strategy for the design of novel solutions for the development of materials based on CTS with improved TE properties.

### 2.2.7 Appendix

The optical absorption spectra for the ordered and disordered CTS samples.

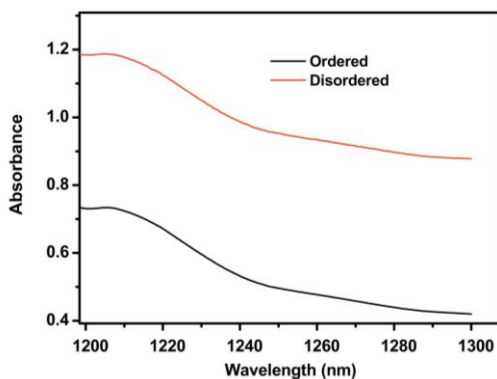


Figure 2.2.S1. optical absorption spectra for the ordered and disordered CTS samples.

Carrier concentration ( $n$ ) and mobility ( $\mu$ ) measured from in temperature range 300-450 K.

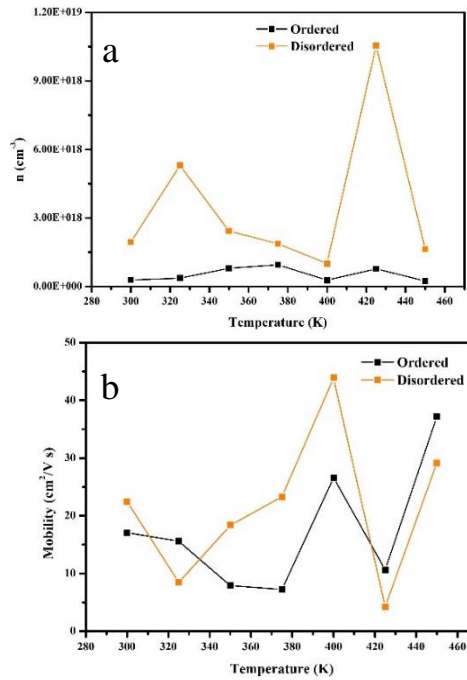


Figure 2.2.S2. Carrier concentration (a), and mobility (b) for ordered and disordered CTS samples.

Band structures: Band structures for the ordered, Sn-rich disordered, and Sn-poor disordered cells are shown in figure 2.2.S3, the band structures for the Ordered CTS are in agreement with the literature.<sup>68,84</sup>

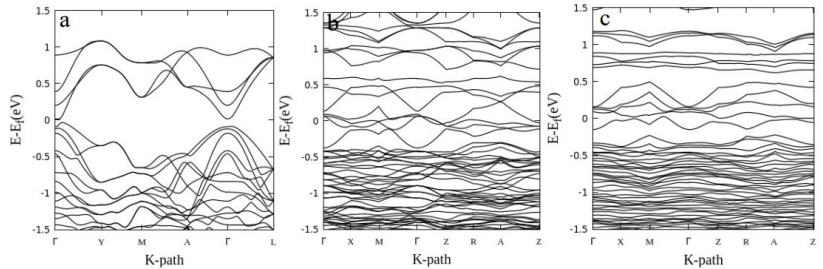


Figure 2.2.S3. Band structures for ordered (a), Sn-rich disordered (b), and Sn-poor disordered (c) cells.

Mode level phonon group velocity ( $V_g$ ): The mode level phonon group velocity ( $V_g = d\omega/dk$ ) curves are shown in figure 2.2.S4. Three low frequency ( $< 2$  THz) peaks green, orange, and blue are corresponding to the acoustical modes, showing a similar  $V_g$ , for all three cells.

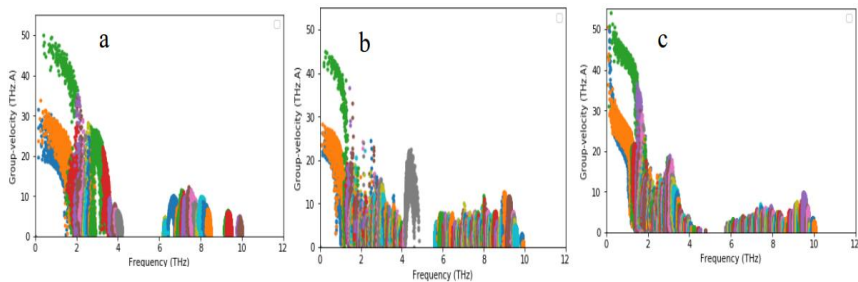
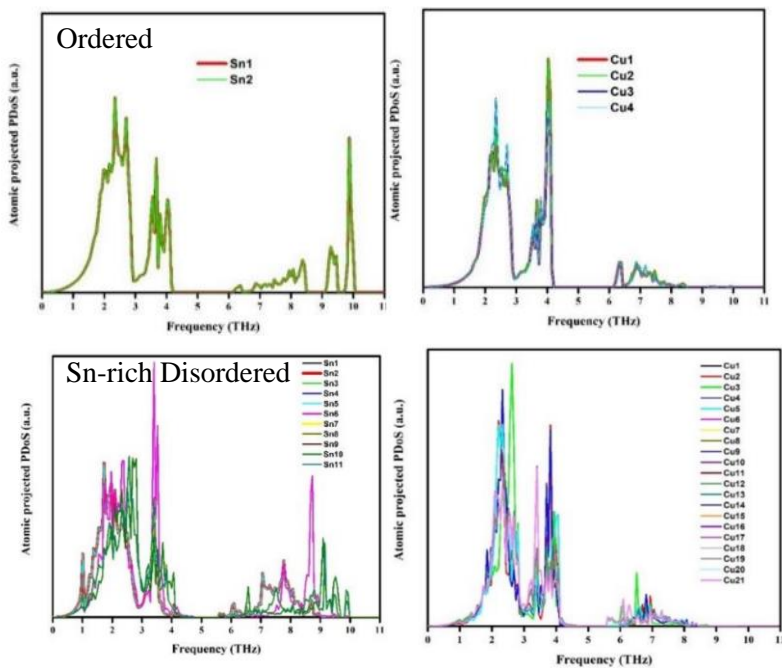


Figure 2.2.S4. Mode level phonon group velocity ( $V_g$ ) vs. frequency ( $\nu$ ) plots for ordered (a), Sn-rich disordered (b) and, Sn-poor disordered (c) CTS cell.

The contribution of every Cu and Sn atom on individual atomic pDOS is shown in figure 2.2.S5.



Sn-poor Disordered

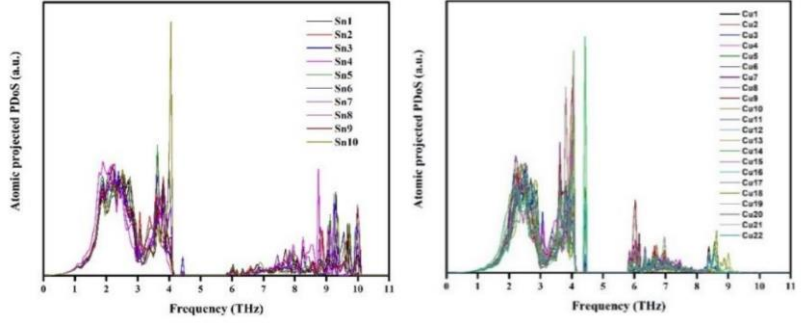


Figure 2.2.S5. Each Sn and Cu atom contribution in the individual pDOS for ordered, Sn-rich disordered, and Sn-poor disordered CTS cells.

Lattice thermal conductivity ( $k_l$ ) calculations using Single Parabolic Band (SPB) approximation:

Total thermal conductivity:  $k = k_e + k_l$

Electronic thermal conductivity:  $k_e = k - k_l$

Wiedemann-Franz law:  $k_e = LT\sigma$

We have estimated the Lorenz number, L, by fitting the Seebeck coefficient (S) to the reduced chemical potential.

$$L = \left(\frac{k_B}{e}\right)^2 \frac{3F_0(\eta)F_2(\eta) - 4F_1^2(\eta)}{F_0^2(\eta)}$$

$$S = \left(\frac{k_B}{e}\right) \left(\frac{2F_1(\eta)}{F_0(\eta)} - \eta\right)$$

$$F_n(\eta) = \int_0^\infty \frac{x^n}{1 + e^{x-\eta}} dx$$

Where  $k_B$ ,  $e$ ,  $\eta$ , and  $F_n(\eta)$  are Boltzmann constant, charge of electron, reduced Fermi energy, and Fermi integral of order n, respectively<sup>34</sup>.

High-resolution X-ray diffraction studies of the lattice parameters in the temperature range 295 K to 100 K at the beamline P02.1 at PETRAIII synchrotron source: High-resolution X-ray powder diffraction data were collected at a wavelength of 0.20761 Å on a disordered CTS sample in a glass capillary with 0.8 mm diameter (manufacturer WJM, Berlin). The sample was spun during the measurement and cooled with an Oxford Cryostreamer. The beam size was 1x1 mm<sup>2</sup>. Data was

collected on PerkinElmer XRD1621 area detector ( $200 \times 200 \mu\text{m}^2$  pixel size,  $2048 \times 2048$  pixel area). The 2D data sets were azimuthally integrated to 1D data using the DAWN Science package<sup>105</sup>. The lattice parameters of the disordered CTS sample were then determined by Rietveld refinements using the TOPAS software.

Table 2.2.S1. Lattice parameter (a) and cell volume (V) for the disordered (cubic) CTS in temperature range 300 K to 100 K.

Temperature	Lattice Parameter		Cell Volume	
	a (Å)	e.s.d.	V (Å <sup>3</sup> )	e.s.d.
300	5.43614	2.80E-04	160.64699	0.02444
280	5.43485	2.70E-04	160.53262	0.02408
260	5.43364	2.70E-04	160.42521	0.02374
240	5.43243	2.60E-04	160.31784	0.02332
220	5.43123	2.60E-04	160.212	0.02292
200	5.43012	2.60E-04	160.11347	0.02256
180	5.42907	2.50E-04	160.02093	0.02225
160	5.42806	2.50E-04	159.93181	0.02196
140	5.42722	2.40E-04	159.85763	0.02156
120	5.42654	2.40E-04	159.79713	0.02133
100	5.42576	2.40E-04	159.72824	0.02095

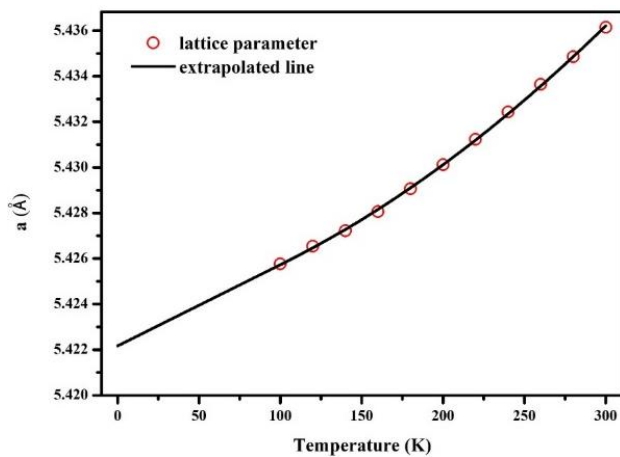


Figure 2.2.S6. The lattice parameter of disordered (cubic) CTS in temperature range 300K to 100 K shown in table 2.2.S1 with a parabolic function.

## 3 Effects of Preparation Procedures and Porosity

### 3.1 Effects of Preparation Procedures and Porosity on Thermoelectric Bulk Samples of Cu<sub>2</sub>SnS<sub>3</sub> (CTS)

Published under a CC BY 4.0 license.

This section is entirely taken from<sup>106</sup>: Lohani, K.; Fanciulli, C.; Scardi, P. *Effects of Preparation Procedures and Porosity on Thermoelectric Bulk Samples of Cu<sub>2</sub>SnS<sub>3</sub> (CTS)*. *Materials* 2022, 15, 712. <https://doi.org/10.3390/ma15030712>

Please cite any part of this section as specified above.

K. Lohani<sup>a</sup>, C.Fanciulli<sup>b</sup>, P. Scardi<sup>a\*</sup>

<sup>a</sup>Department of Civil, Environmental and Mechanical Engineering, University of Trento, Via Mesiano 77, 38123, Trento, Italy

<sup>b</sup>National Research Council of Italy-Institute of Condensed Matter Chemistry and Technologies for Energy (CNR-ICMATE), Lecco Unit, Via Previati 1/E, 23900, Lecco, Italy

\*Correspondence: [Paolo.Scardi@unitn.it](mailto:Paolo.Scardi@unitn.it)

Received: 13 December 2021; Revised: 4 January 2022; Accepted: 10 January 2022; Published: 18 January 2022

### 3.1.1 Abstract

The thermoelectric behavior and stability of  $\text{Cu}_2\text{SnS}_3$  (CTS) has been investigated in relation to different preparations and sintering conditions, leading to different microstructures and porosities. The studied system is CTS in its cubic polymorph, produced in powder form via a bottom-up approach based on high-energy reactive milling. The as-milled powder was sintered in two batches with different synthesis conditions to produce bulk CTS samples: manual cold pressing followed by traditional sintering (TS), or open die pressing (ODP). Despite the significant differences in densities,  $\sim 75\%$  and  $\sim 90\%$  of the theoretical density for TS and ODP, respectively, we observed no significant difference in electrical transport. The stable, best performing TS samples reached  $zT \sim 0.45$ , above 700 K, whereas  $zT$  reached  $\sim 0.34$  for the best performing ODP in the same conditions. The higher  $zT$  of the TS sintered sample is due to the ultra-low thermal conductivity ( $\kappa \sim 0.3\text{--}0.2$  W/mK), three-fold lower than ODP in the entire measured temperature range. The effect of porosity and production conditions on the transport properties is highlighted, which could pave the way to produce high-performing TE materials.

### 3.1.2 Introduction

Thermoelectric (TE) materials are a class of functional materials employed in solid-state energy generators and coolers, without the use of fossil fuels and combustion processes, and with no moving parts, exploiting only the temperature gradients. For this reason, TE materials were first successfully utilized in deep-space probes in the second half of the last century.<sup>10</sup> In recent years, TE materials have drawn attention as efficient, eco-friendly, durable, noise-free, and scalable solutions for the recovery of waste heat, like in exhaust systems (automotive TE generators).<sup>107</sup> Current research on TE materials seeks greater efficiency, as well as non-toxic and cost-effective solutions<sup>9</sup>. The performance of a TE material can be assessed by means of the figure of merit,  $zT = (S^2/\rho\kappa)T$ , where  $S$ ,  $\rho$ ,  $\kappa$ , and  $T$  are the Seebeck coefficient, electrical resistivity, thermal conductivity, and absolute temperature, respectively. Thus, a high  $zT$  TE material requires a high power factor ( $S^2/\rho$ ) and low  $\kappa$ , which consists of lattice ( $\kappa_l$ ) and electronic ( $\kappa_e$ )

contributions. That being said, it is not the only important parameter as the stability and durability of TE materials are also vital for producing reliable TE devices.

Cu-Sn-S-based systems are studied as both *p*-type and *n*-type semiconductors.<sup>26,108</sup> CTS is a tetrahedrally bonded direct bandgap semiconductor, showing a bandgap  $\sim 1.0$  eV, which is higher or lower depending on whether the CTS polymorph is ordered or disordered<sup>71</sup>. The unfilled Cu-3*d* orbitals introduce holes in the CTS system, making it a *p*-type semiconductor. CTS components are earth-abundant, eco-friendly, non-toxic, non-hazardous, and have low formation energies; therefore, they are explored for various applications, such as TE,<sup>34</sup> photovoltaic,<sup>109</sup> optoelectronics,<sup>48</sup> photoelectrochemical,<sup>110</sup> and supercapacitors,<sup>111</sup> just to name a few. CTS has attracted the TE community for its remarkable crystallographic structures with different degrees of cation-disorder, which helps in the suppression of thermal conductivity to an ultra-low level, without much hindrance to the electronic transport, also known as the so-called “phonon-glass-electron-crystal (PGEC)” behavior. The well-known ordered or monoclinic CTS polymorph arranges its atoms in the *Cc* space group (SG). In the past, we reported the production of a pure disordered or cubic CTS polymorph (SG: F-43m) via high-energy reactive ball-milling.<sup>26</sup> Recently, Wei et al.<sup>112</sup> reported the production of another disordered CTS polymorph, i.e., pure tetragonal (SG: *I*-42*m*) CTS by the colloidal method.

Interestingly, both the disordered CTS polymorphs (cubic and tetragonal) present  $\kappa_l < 0.5$  W/m-K, above 700 K, approaching its theoretical minimum ( $\kappa_l \sim 0.3$  W/m-K). In a recent report, Li et al.<sup>113</sup> showed the introduction of dislocations as an effective way to suppress the lattice thermal conductivity in Ni-doped CTS (Cu<sub>2</sub>Ni<sub>0.1</sub>Sn<sub>0.9</sub>S<sub>3</sub>), reporting  $\kappa_l = 0.41$  W/m-K at 723 K. Wei et al.<sup>112</sup> demonstrated that the abundance of twin-boundaries in pristine and In-doped CTS (Cu<sub>2</sub>Sn<sub>0.95</sub>In<sub>0.05</sub>S<sub>3</sub>) contributes to a low  $\kappa_l = 1.02$  W/m-K at room temperature (RT), which further reduces to  $\kappa_l < 0.50$  W/m-K around 700 K. It is important to notice that most materials presenting a high  $zT$  in the medium temperature range (500 K  $< T <$  800 K) are either scarce or toxic, e.g., PbTe and SnSe. In this temperature range,

sulphides of copper and tin or copper and iron can be viable alternatives. Gu et al.<sup>114</sup> discussed 3D modulation doping of  $\text{CuCo}_2\text{S}_4$  in CTS and reported a  $zT \sim 0.82$  at 773 K. Zhao et al.<sup>115</sup> reported simultaneous Co and Sb substitution in the CTS system resulting in a  $zT$  of  $\sim 0.88$  at 773 K. Furthermore, Deng et al.<sup>30</sup> reported a  $zT$  of  $\sim 1$  in a similar  $\text{Cu}_7\text{Sn}_3\text{S}_{10}$  system through Br-doping. A  $zT$  of  $\sim 0.4\text{--}0.8$  above 700 K is regularly reported for CTS by In,<sup>33</sup> Zn,<sup>34</sup> Mn,<sup>35</sup> Ni,<sup>32</sup> Fe,<sup>13</sup> Co,<sup>36</sup>s and  $\text{Cu}^{37}$  substitution at the Sn site, aiming to enhance the carrier concentration and reduce the thermal conductivity. Other similar systems, such as  $\text{Cu}_5\text{Sn}_2\text{S}_7$ ,<sup>38</sup>  $\text{CuFeS}_2$ ,<sup>39</sup>  $\text{Cu}_4\text{Sn}_7\text{S}_{16}$ ,<sup>40</sup> and  $\text{Cu}_2\text{SnSe}_3$ <sup>41</sup> also show a moderate  $zT$  ranging from 0.2–0.5, above 700 K.

Manipulation of porosity in materials is a less-explored subject for TE applications. Many articles have put forward a crucial need to investigate porous TE materials.<sup>9,12,116,117</sup> Porous materials are lightweight and require lower quantities of materials, therefore, they are suitable for portable and wearable TE devices.<sup>116</sup> Xu et al.<sup>118</sup> showed  $zT > 1$ , and 2–4 fold lower  $\kappa_l$  in hollow nanostructured  $\text{Be}_2\text{Te}_{2.5}\text{Se}_{0.5}$  than in the existing literature. Hong et al.<sup>119</sup> showed improved PF in mesoporous ZnO thin films. Tiwari et al.<sup>120</sup> investigated porous CTS for photovoltaics using a solid-state reaction at 200 °C, but they only reported the Seebeck coefficient near RT and temperature-dependent conductivity measurement. Thermal cycling during the TE power generation process could promote the annealing of defects, reduction of grain boundaries, increased density, and transformation of crystal structures, driving these materials towards instability. The authors discussed surface oxidation, the role of secondary phases, and the loss of a nano and microstructure after thermal cycling above a certain temperature, which alters the TE properties of a material.<sup>121</sup> This makes the technological advancement and scientific understanding of these materials challenging.<sup>122</sup> In particular for large-scale production and durable use, a mechanically and thermodynamically stable material is required.

Herein, we stabilized the disordered CTS polymorph using different production conditions and sintering techniques. CTS samples from two batches (three samples each) were produced, and their TE properties and thermal stability were systematically investigated by repeated

Seebeck and resistivity measurements (heating and cooling) in the temperature range of 323–723 K. Pellets of samples were produced using manual cold pressing followed by sintering in a traditional tubular furnace (TS batch), or via open die pressing (ODP batch)<sup>123</sup>. Information on the crystallographic structures and phase purity was obtained by Rietveld refinement of X-ray diffraction (XRD) patterns, before and after the repeated TE measurements. Surface topology, porosity, and chemical variations were investigated by morphological images and energy dispersive X-ray (EDX) spectroscopy, using both scanning electron microscopy (SEM) and transmission electron microscopy (TEM). This work provides a general overview and highlights the cautions to produce stable CTS and similar chalcogenides. The effect of porosity on TE properties is highlighted.

### 3.1.3 Materials and Methods

CTS samples were produced from the elemental powders using a high-energy reactive ball-mill (Fritsch, Idar-Oberstein, Germany), according to a well-assessed procedure with details discussed elsewhere<sup>9</sup>. Three different samples were prepared using the manual cold press (load 15 tons for 3 min) and sintered at 500 °C for 2 h with a heating rate of 3 °C/min. Sample TS1 was processed in an open environment, whereas samples TS2 and TS3 were produced in a highly controlled environment ( $\text{O}_2$  and  $\text{H}_2\text{O}$  < 10 ppm). All the samples were sintered in Ar flux. Additionally, sample TS3 was sintered in the presence of sulfur powder (1 g).

The other three samples (ODP1, ODP2, and ODP3) were produced in a controlled environment with the above-mentioned preconditions. Differently, the sintering was performed via ODP using an iron die. To prevent possible reactions between the die and the powders, a boron nitride layer was used to cover the internal surface of the die. Such a layer also prevents sticking phenomena, allowing for an easier extraction of the sintered bulk. Sample ODP1 was sintered at 400 °C for 30 min, whereas samples ODP2 and ODP3 were sintered at 500 °C for 10 and 30 min, respectively. During all the sintering processes, a ~100 MPa axial pressure was applied.

Table 3.1. Quantitative phase and average crystallite size before and after TE measurements, measured densities, and relative densities.

Sample	Weight ( $\pm 1\%$ )					Average domain size ( $\pm 10$ nm)	Measured density ( $\pm 0.1$ g/cm <sup>3</sup> )	Relative density (%)
	CTS	WC	SnO <sub>2</sub>	SnO	SnS			
TS1 before TE measurements	96	2	2	-	-	40	3.52	74.7
TS1 after TE measurements	88	2	8	-	2	75		
TS2 before TE measurements	98	2	-	-	-	75	3.48	73.8
TS2 after TE measurements	89	2	8	1	-	75		
TS3 before TE measurements	98	2	-	-	-	70	3.68	78.1
TS3 after TE measurements	87	2	10	1	-	70		
ODP1 before TE measurements	100	-	-	-	-	42	4.26	90.4
ODP1 after TE measurements	100	-	-	-	-	42		
ODP2 before TE measurements	100	-	-	-	-	54	4.36	92.5
ODP2 after TE measurements	99	1	-	-	-	54		
ODP3 before TE measurements	98	1	1	-	-	68	4.43	94.0
ODP3 after TE measurements	91	1	8	-	-	68		

It should be emphasized that ODP was performed on a large quantity of the as-milled powder, namely ~30–40 g. The as-sintered samples from

ODP are usually large bulk samples, which are cut into the required sample sizes for various measurements (large as-sintered ODP samples are shown in Figure 3.S1). The densities of the TS (TS1, TS2, and TS3) and ODP (ODP1, ODP2, and ODP3) sintered samples were  $\sim 75\%$  and  $\sim 90\%$  of the theoretical density (see Table 3.1), respectively.

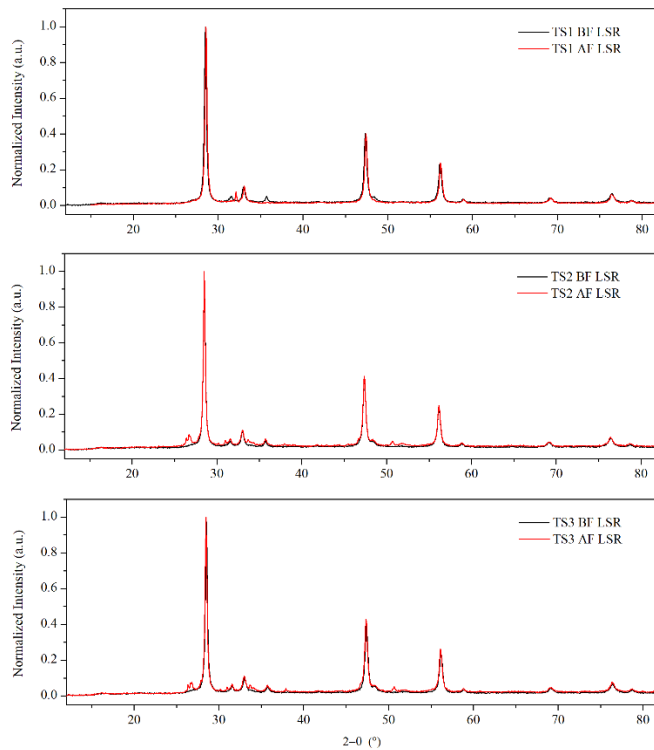
The structural characterization of TS samples was performed in Bragg–Brentano geometry using a Rigaku PMG (Rigaku PMG, Tokyo, Japan) powder diffractometer, equipped with a  $\text{Cu } K\alpha$  ( $\lambda = 1.5406 \text{ \AA}$ ) source and a scintillation counter detector. XRD data on the ODP samples were collected in Bragg–Brentano geometry using a Bruker D8 (Bruker, Billerica, MA, USA) diffractometer equipped with a  $\text{Co } K\alpha$  ( $\lambda = 1.7889 \text{ \AA}$ ) source and area linear (1D) detector. After the phase identification, Rietveld refinement<sup>55</sup> was performed using Whole Powder Pattern Modelling (WPPM) macros<sup>56</sup> as implemented in Topas 7<sup>57</sup> software (Coelho Software, Brisbane, Australia).

Simultaneous Seebeck coefficient and resistivity measurements were performed in four contact set-up using LSR-3 (Linseis Messgeraete GmbH, Selb, Germany), at a temperature ranging from 323–723 K. Thermal diffusivity ( $D$ ) was measured using a LFA-500 (Linseis Messgeraete GmbH, Selb, Germany), equipped with a xenon-flash lamp over a temperature range of 323–723 K. Seebeck and resistivity measurements were performed under an He atmosphere (0.1 bar). However, the diffusivity was measured under a vacuum ( $\sim 10^{-3}$  bar).

After the TE measurements, morphological images of the selected area electron diffraction (SAED) were collected on powder produced by crushing the sample pellets, and EDX spectroscopy was performed using transmission electron microscopy (TEM; HR-S/TEM ThermoFischer TALOS 200 s, Thermo Fischer Scientific, Waltham, MA, USA). Moreover, morphological images and EDX data were collected on pellet samples to investigate the microstructure and bulk chemistry using a Jeol IT300 scanning electron microscope (SEM) equipped with a tungsten source (Jeol, Ltd., Tokyo, Japan).

### 3.1.3. Results and Discussions

XRD measurements were performed on all of the polycrystalline samples (Figure 3.1). The diffraction patterns showed fingerprint peaks at  $2\theta \sim 28.5^\circ$ ,  $47.3^\circ$ , and  $56.0^\circ$ , and  $2\theta \sim 33.2^\circ$ ,  $55.5^\circ$ , and  $66.3^\circ$  using *Cu K $\alpha$*  and *Co K $\alpha$*  X-ray sources, respectively. These Bragg peaks represent planes (1 1 1), (2 2 0), and (3 1 1), respectively, confirming the disordered cubic CTS structure, which is derived from the zinc-blende structure (SG: *F-43m*). A small amount of WC (SG: *P-6m2*) is present in all of the samples due to the use of WC vials for milling. Additionally, a weak peak ( $2\theta \sim 27^\circ$ ) of SnO<sub>2</sub> (SG: *P-42mnm*) was observed in the pattern of sample TS1 (see Figure 3.S2). XRD patterns of all the ODP sintered samples also showed Bragg peaks representing the disordered cubic CTS phase. Nevertheless, small amounts of WC and SnO/SnO<sub>2</sub> phases were also observed in some ODP sintered samples.



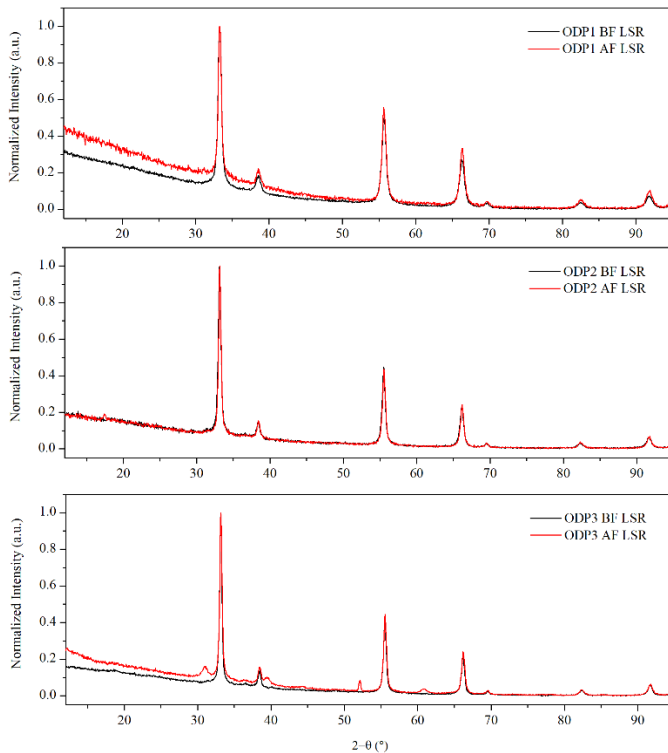


Figure 1. XRD data before and after repeated TE measurements on TS and ODP sintered samples. The difference in diffuse background and shifts in Bragg peaks between TS and ODP samples is due to the use of different diffractometers equipped with  $\text{Cu K}\alpha$  ( $\lambda = 1.5406 \text{ \AA}$ ) and  $\text{Co K}\alpha$  ( $\lambda = 1.7889 \text{ \AA}$ ) sources, respectively. Rietveld refinement on the XRD data with marked phases is shown in Figure 3.S2.

Different crystallographic phases were identified, and their respective weight fractions were obtained by the Rietveld method<sup>55,124</sup>. Information provided by powder pattern refinements, including the average crystallite size, is reported in Table 3.1. The lattice parameters for all the samples are  $a = 5.43 \pm 0.01 \text{ \AA}$  and  $\alpha = \beta = \gamma = 90^\circ$ . The average crystallite size for samples TS1, TS2, and TS3 is  $40 \pm 10$ ,  $75 \pm 10$ , and  $70 \pm 10$  nm, respectively. All the samples have a  $\sim 1\text{--}2\%$  weight of WC. Additionally, sample TS1 has a small quantity ( $\sim 2\%$  weight) of  $\text{SnO}_2$ , which is possibly formed due to open environment processing. We did not observe the formation of secondary phase oxides in samples TS2 and TS3, produced in a strictly controlled environment. ODP, like spark plasma sintering (SPS), is a fast-sintering technique needing a short sintering time and applying external pressure. The applied pressure during ODP decreases the sintering temperature and time,

simultaneously improving the densification kinetics. Thus, the crystalline domains show limited growth, while reaching full densification. The average domain sizes for the ODP1, ODP2, and ODP3 samples are  $42\pm 10$ ,  $54\pm 10$ , and  $64\pm 10$  nm, respectively. In our recent work, we showed that SPS on as-milled CTS powder can constrain the grain growth below 50 nm<sup>125</sup>.

After the repeated TE measurements (discussed in the next section), the XRD data were collected for the second time. All TS samples showed an increase in the weight fraction of SnO<sub>2</sub>. Samples TS2 and TS3 showed the formation of a new secondary phase, SnO (SG: *Pnm*<sub>21</sub>), possibly due to an oxygen-deficient production environment. We also observed the presence of SnS (SG: *Pbmn*) in sample TS1, confirming the chemical instability of the sample prepared in an open environment. Samples sintered using ODP were less prone to growth in the secondary phases. We did not observe any grain growth or increase in the weight fraction of secondary phases for ODP1 and ODP2. The applied pressure during sintering seems to better stabilize the samples than traditional sintering. Nevertheless, an increased amount of SnO<sub>2</sub> was observed for ODP3, due to its extended sintering time in comparison to ODP2. The densities of ODP3 and ODP2 samples are similar, in spite of the different sintering times of 30 and 10 min, respectively. Therefore, the densification was complete within ~10 min of sintering. Furthermore, extended sintering mainly promotes phase degradation, leading to the formation of SnO<sub>2</sub>.

As discussed in the Introduction, the loss of nanostructure has adverse effects on the TE properties of the material, which could drive it towards instability. The average crystalline size for the TS1 sample increased from  $40\pm 10$  to  $75\pm 10$  nm after repeated TE measurements, whereas samples TS2 and TS3 did not lose their nanostructure, maintaining their average crystallite size of  $75\pm 10$  and  $70\pm 10$  nm, respectively. Similarly, the ODP sintered samples maintained their average domain size of  $42\pm 10$ ,  $54\pm 10$ , and  $68\pm 10$  nm for ODP1, ODP2, and ODP3 samples, respectively, after repeated TE measurements.

SEM micrographs at different magnifications collected on TS and ODP sintered sample surfaces are shown in Figure 3.2. The difference

between the two samples is noticeable. Morphological images of the bulk TS samples (Figure 3.2 (a,b)) reveal an uneven topology and the presence of microscopic pores. As expected, the ODP sintered samples (Figure 3.2 (c,d)) had a lower porosity compared to TS, with intact grains. It is also evident through the density measurements that the ODP sintered samples were  $\sim 20\%$  denser than TS. Here, it is worth mentioning that similar samples sintered via SPS showed almost no porosity and the density was slightly ( $\sim 2\text{--}4\%$ ) higher than the ODP sintered samples (morphological images of SPS sintered samples are shown in Figure 3.S3).<sup>125</sup>

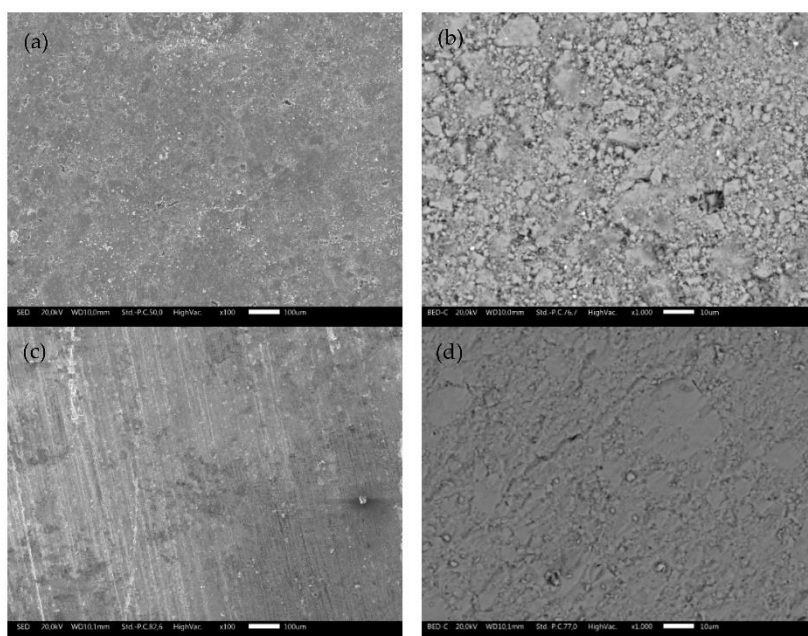


Figure 3.2. SEM micrographs collected on the surfaces of bulk TS (a,b) and ODP (c,d) sintered samples showing highly intact grains with a lower porosity in comparison with the TS sintered samples at different magnifications.

The morphological image and SAED using TEM on TS1, shown in Figure 3.S4 (right bottom inset), reveals many small ( $d \sim 10$  nm) grains surrounding the bigger (CTS) grains. EDX was performed, focusing on the surrounding small dark grains. Strong peaks of oxygen and tin can be observed in the EDX spectra of TS1, and the atomic fraction was found to be oxygen and tin-rich (see Table 3.2), suggesting that these are  $\text{SnO}_2$  grains, as we observed from the XRD. The evolution

of SnO<sub>2</sub> grains makes the sample unstable during TE measurements by unbalancing the stoichiometry. For samples TS2 and TS3, no SnO<sub>2</sub>/SnO grains appeared in the micrographs, although a weak peak for oxygen could be observed by EDX. The chemical composition for the TS2 sample was copper-rich, whereas, for the sulfurized sample (TS3), the stoichiometry was close to the theoretical (see Table 3.2).

Table 3.2. Atomic fraction for samples TS1, TS2, and TS3 estimated from the TEM-EDX analysis (corresponding EDX spectra are shown in Figure 3.S4).

Sample Name	Atomic Fraction ( $\pm 1\%$ )			
	Cu	Sn	Cu	O
TS1	15.11	TS1	15.11	TS1
TS2	40.09	TS2	40.09	TS2
TS3	30.31	TS3	30.31	TS3

SEM-EDX analysis was performed on the ODP sintered samples, including chemical maps on large ODP samples to investigate the overall chemical homogeneity. As discussed in the Experimental Methods, ODP was performed on a large quantity (30–40 g) of ball-milled powder, producing large samples (see Figure 3.S1). The SEM chemical maps (shown in Figure 3.3) revealed non-homogeneous chemistry on the surfaces of the ODP sintered samples. As ODP is a fast-sintering technique and was performed on a large quantity of materials, variations in chemical composition are likely. However, the overall chemistry of the samples was close to theoretical (shown in Table 3.3). On the contrary, the SPS sintered samples produced in our past work showed a homogeneous chemical distribution and comparatively lower crystalline domain size.<sup>125</sup>

Table 3.3. Atomic fraction of samples ODP1, ODP2, and ODP3 samples, estimated using SEM-EDX analysis (corresponding EDX spectra are shown in Figure 3.S6).

Sample Name	Atomic Fraction ( $\pm 1\%$ )			
	Cu	Sn	S	O
ODP1	16.90	32.03	46.92	4.05
ODP2	15.46	30.13	45.11	9.27
ODP3	16.82	31.68	49.21	2.29

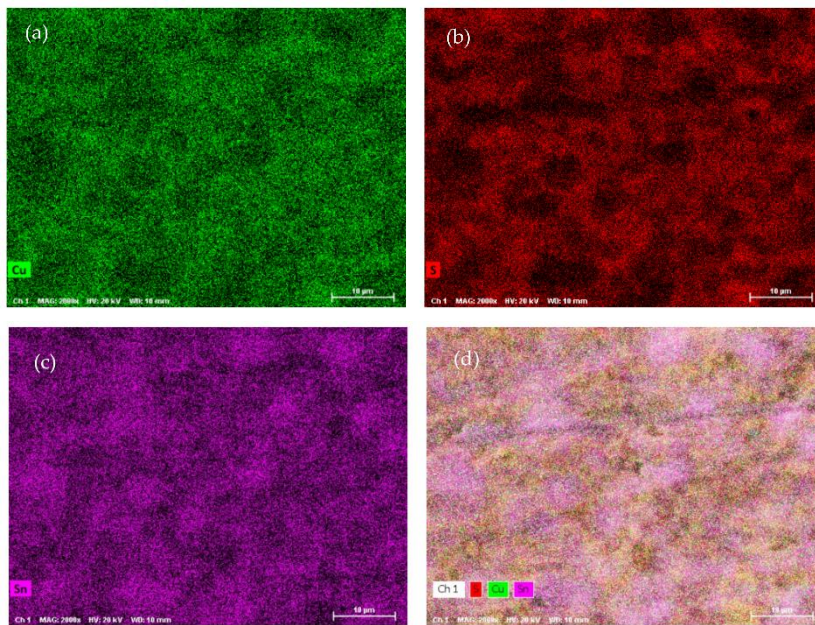


Figure 3.3. SEM micrographs collected on ODP samples and chemical maps for individual elements Cu (a), S (b), and Sn (c), and simultaneously for all elements (d) (corresponding EDX spectra are shown in Figure 3.S5).

Repeated Seebeck and resistivity measurements are shown in Figure 3.4. All the samples, and TS and ODP batches, showed positive values for the absolute Seebeck coefficient, indicating holes as majority charge carriers, thus confirming a *p*-type semiconducting nature. The trend of resistivity for sample TS1 is increasing with the temperature, whereas it is decreasing for all other samples, typical of degenerate and non-degenerate semiconductors, respectively.

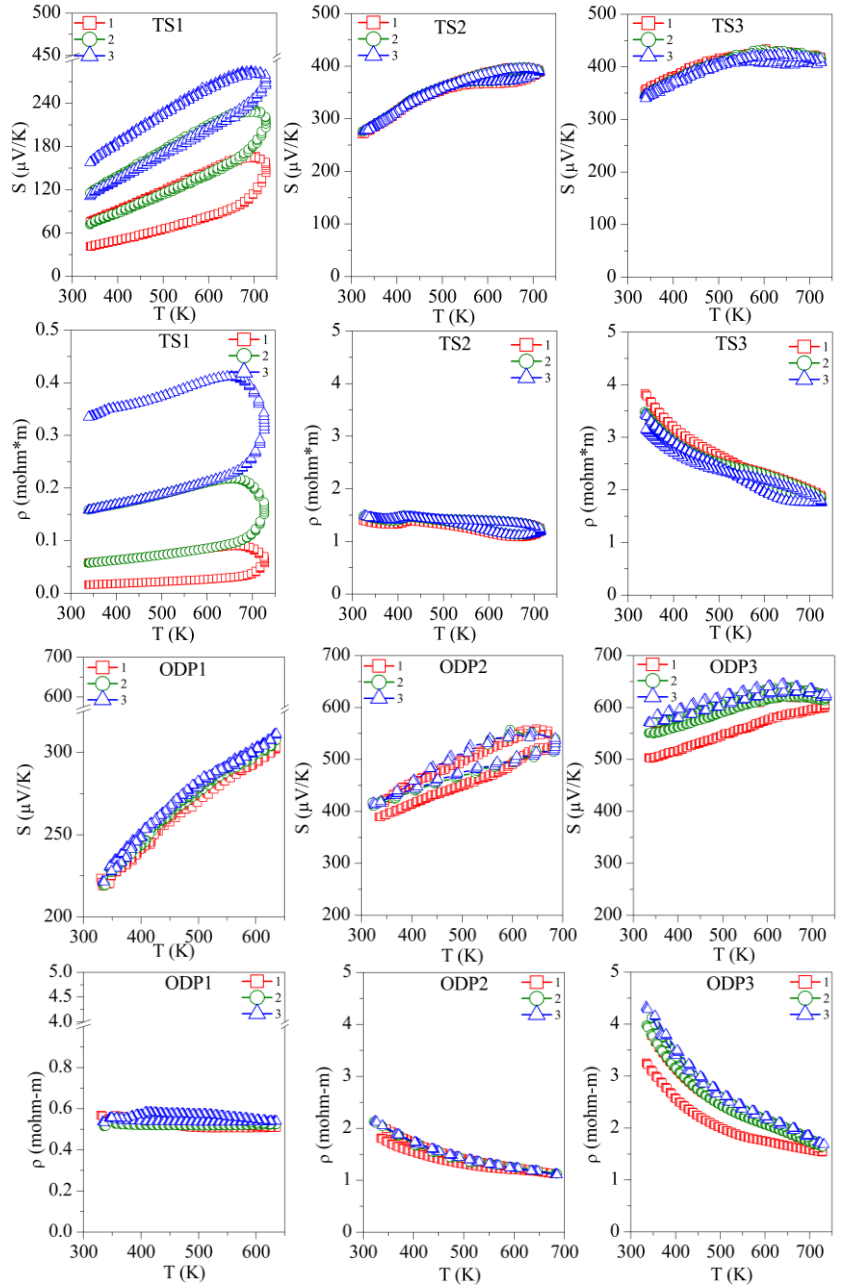


Figure 4. Repeated absolute Seebeck coefficient ( $S$ ) and resistivity ( $\rho$ ) measurements in temperature for the TS and ODP sintered samples. In the figure, markers 1 (red squares), 2 (green circles), and 3 (blue triangles) represent first, second, and third measurements cycles, respectively.

The first measurement on the TS1 sample shows the lowest values of  $S$  (40–100  $\mu\text{V/K}$ ) and  $\rho$  (0.01–0.03  $\text{m}\Omega\text{-m}$ ). However, these measurements are not reproducible during the second and third measurement cycles. The low Seebeck and resistivity with a non-degenerate semiconducting trend suggest the presence of a higher carrier concentration in sample TS1. This could be due to the alteration in chemical composition, as we observed a large amount of  $\text{SnO}_2$  using TEM-EDX and XRD. The XRD on the same sample after repeated TE measurement cycles revealed the segregation of SnS (see Table 3.1), making the sample copper-rich or possibly leading to the formation of CuS. In a recent work on non-stoichiometric (copper-rich) CTS<sup>35</sup>, lower Seebeck ( $\sim 50 \mu\text{V/K}$  at 300 K) and high electrical conductivity were reported. Other than the formation of SnS and  $\text{SnO}_2$ , the non-repeatability of  $S$  and  $\rho$  during the thermal cycles also confirms the instability of sample TS1. Noticeably, after the three measurements cycles, significant grain growth was observed for TS1, with the average domain size increasing from  $40\pm 10$  to  $75\pm 10$  nm.

For samples TS2 ( $S \sim 250\text{--}400 \mu\text{V/K}$ ,  $\rho \sim 1.5\text{--}1.1 \text{m}\Omega\text{-m}$ ) and TS3 ( $S \sim 325\text{--}425 \mu\text{V/K}$ ,  $\rho \sim 3.5\text{--}1.5 \text{m}\Omega\text{-m}$ ), the TE measurements were repeatable during the measurement cycles, and the values of  $S$  and  $\rho$  were in agreement with the literature.<sup>34,115</sup> Although we observed an increased amount of  $\text{SnO}_2$  and the formation of a new SnO phase, segregation of SnS was not observed. Similar values of  $S$  and  $\rho$  during several measurement cycles confirmed that the CTS samples prepared in a strictly controlled environment were stable. It is known that sulfurization leads to the formation of stoichiometric CTS,<sup>63</sup> which could be the case for sample TS3, leading to a higher Seebeck and resistivity.

The repeated TE measurements on ODP sintered samples were reproducible, especially after the first measurement cycle, and for the second and third measurements cycles, the  $S$  and  $\rho$  measurements were coherent. The ODP1 sample sintered at 400 °C for 30 min showed the lowest values of  $S$  (180–310  $\mu\text{V/K}$ ) and  $\rho$  (0.55–0.50  $\text{m}\Omega\text{-m}$ ). ODP2 and ODP3 samples sintered at 500 °C for 10 min and 30 min showed increasing values of  $S$  and  $\rho$ . The Seebeck coefficients and resistivities for the ODP2 and ODP3 samples were  $S \sim 400\text{--}550 \mu\text{V/K}$  and  $\rho \sim 2.2\text{--}$

1.0 m $\Omega$ -mm, and  $S \sim 550\text{--}650$   $\mu\text{V/K}$  and  $\rho \sim 4.0\text{--}1.7$  m $\Omega$ -m, respectively. The increase in  $S$  and  $\rho$  have a clear relation with the increased average domain size of the samples. These results are in agreement with our recent work showing the effects of grain growth on SPS sintered CTS samples, owing to the conduction based on the metallic nature of surfaces due to dangling bonds.<sup>125</sup> Moreover, Ming et al.<sup>126</sup> showed a similar effect in Cu<sub>2</sub>SnSe<sub>3</sub>.

However, it is important to notice here that two different sintering were used for the sample preparation, resulting in significantly different densities, even if we did not observe a significant difference in the resistivity of the same samples. Thus, we put forward that electrical transport is less likely affected by porosity in these systems. However, we noticed that the TS sintered samples had a lower  $S$  in comparison with the ODP samples. This could be related to the overall chemical composition of the TS samples, where we noticed a large chemical fluctuation in TEM-EDX. Some chemical fluctuations were also present in the ODP samples, but the overall chemistry of ODP samples was close to the theoretical, as observed by means of the chemical maps.

Thermal diffusivity ( $D$ ) was measured using a xenon flash instrument, and the thermal conductivity ( $\kappa$ ) was calculated as,  $\kappa = D \times d \times C_p$ , where,  $d$  and  $C_p$  are the density of the sample and specific heat capacity, respectively. The density was measured using the Archimedes method (see Table 3.1), and  $C_p$  obtained on TS samples is discussed elsewhere, whereas  $C_p$  measurements on ODP sintered samples are shown in Figure 3.S7.

All the samples showed a decreasing trend of thermal conductivity with temperature, implying that the phonon–phonon (Umklapp process) is dominating the phonon transport (see Figure 3.5). Here, it is worth mentioning that all the samples of this work have a disordered cubic structure with partial occupancies of cations (Cu and Sn), which results in a comparatively lower thermal conductivity than the ordered or monoclinic CTS polymorph.<sup>71</sup> The thermal conductivity of sample TS1 ranges from 0.70 W/mK to 0.45 W/mK, whereas it is ultra-low for samples TS2 and TS3, with values of 0.40–0.30 W/mK and 0.30–0.20 W/mK, respectively, in the entire measured temperature range of 323–

723 K. Samples TS2 and TS3 have a similar  $\kappa$  as we recently reported for CTS.<sup>9</sup> However, the unstable sample TS1 has the highest  $\kappa$  in the TS batch. The higher thermal conductivity of sample TS1 is due to its higher electrical conductivity, as observed by the degenerate semiconductor trend of resistivity, probably resulting from the formation of Cu-rich CTS or CuS. The thermal conductivity of ODP sintered samples is in the range of other CTS and Cu-Sn-S-based systems.<sup>34,35</sup> A clear correlation between densities and  $\kappa$  can be noticed in the ODP samples as well. The densities of ODP samples are similar to the literature for CTS polymorphs.<sup>34,35,112</sup> The difference in  $\kappa$  between TS2 and TS3 is also likely to be due to their lower and higher densities, respectively. It is noteworthy that the  $\kappa$  of TS samples is  $\sim 3$ -fold lower in the entire temperature range than for the ODP sintered samples. However, we observed a more or less same behavior for the electrical transport, e.g., samples TS2 and ODP2 have  $\rho \sim 1.5$ – $1.0 \text{ m}\Omega\text{-m}$  and  $\sim 2.0$ – $1.2 \text{ m}\Omega\text{-m}$ , respectively, but TS2 has a  $\sim 3$ -fold lower  $\kappa$  ( $0.3$ – $0.2 \text{ W/mK}$ ) than ODP2 ( $0.8$ – $0.6 \text{ W/mK}$ ).

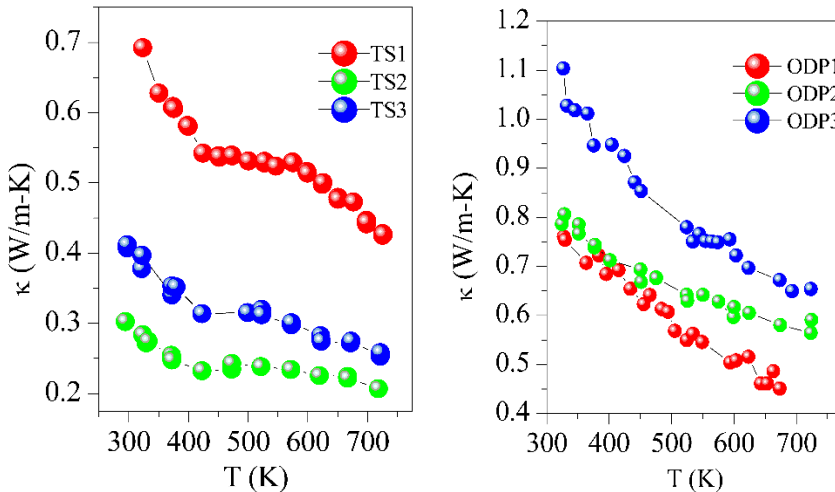


Figure 3.5. Thermal conductivity ( $\kappa$ ) for TS and ODP sintered samples.

The power factor was calculated as  $PF = S^2/\rho$ , and is shown in Figure 3.6. The first measurement on Sample TS1 has the highest  $PF \sim 3.5 \mu\text{W}/\text{K}^2 \text{ cm}$ , above 700 K, which is continuously decreasing with successive measurements. Samples TS2 and TS3 showed  $PF \sim 1.25 \mu\text{W}/\text{K}^2 \text{ cm}$  and  $\sim 1 \mu\text{W}/\text{K}^2 \text{ cm}$ , respectively, above 700 K, but they are stable over repeated measurements. Due to the reproducibility of  $S$  and  $\rho$ , ODP sintered samples showed reproducible PF. Among all the ODP sintered samples, ODP2 has the highest  $PF \sim 2.75 \mu\text{W}/\text{K}^2 \text{ cm}$ , above 700 K, because of moderate  $S$  and  $\rho$ . However, lower  $S$  and very high  $\rho$  for samples ODP1 and ODP3, respectively, have an adverse effect on each other, resulting in a comparatively lower  $PF \sim 1.75 \mu\text{W}/\text{K}^2 \text{ cm}$  and  $\sim 2.25 \mu\text{W}/\text{K}^2 \text{ cm}$ , respectively.

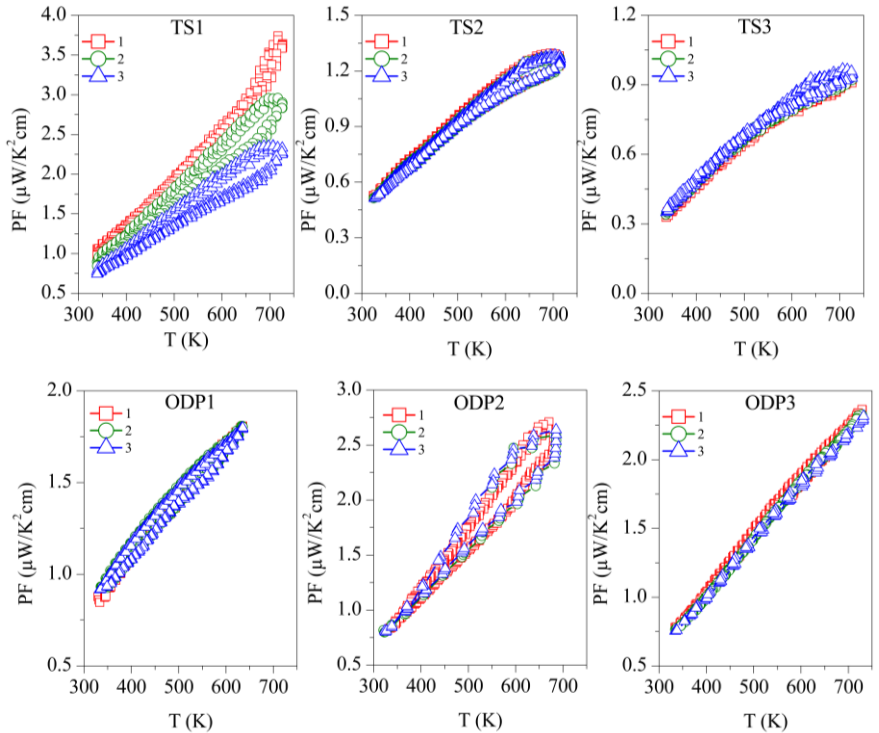
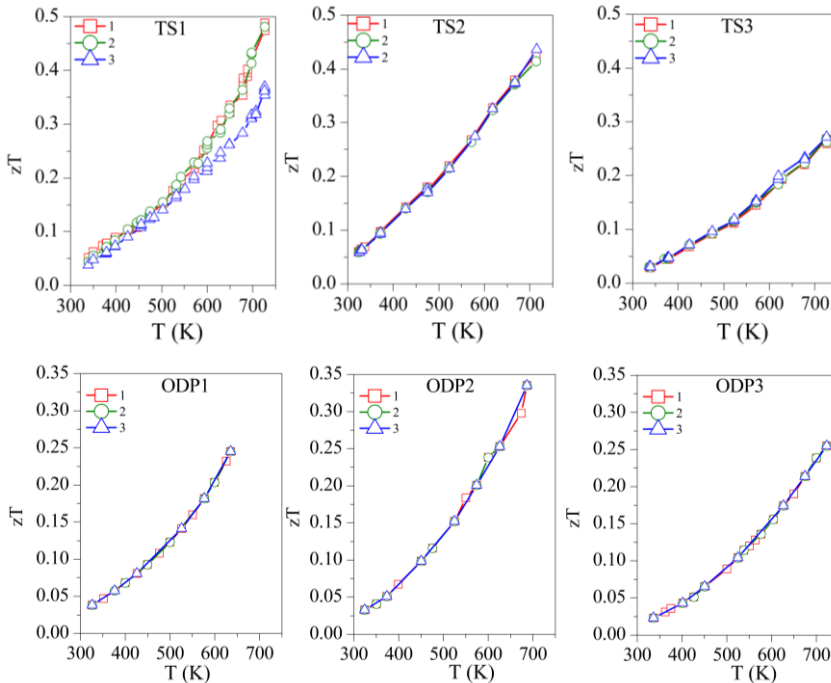


Figure 3.6. Repeated power factor (PF) for TS and ODP sintered samples. In the figure, markers 1 (red squares), 2 (green circles), and 3 (blue triangles) represent the power factors during the first, second, and third measurements cycles, respectively.

Concerning the figure of merit, samples TS1, TS2, and TS3 show  $zT \sim 0.50, 0.45,$  and  $0.27,$  respectively, above 700 K (Figure 3.7). Although TS1 has the highest  $zT$ , it is not stable and  $zT$  decreases with subsequent measurements. Among the stable TS samples, TS2 has the highest  $zT$  of  $\sim 0.45$ . The competitively high  $zT$  of TS2 is supported by its lower  $\kappa$  and  $\rho$ . ODP sintered samples present  $zT$  ranging from 0.25–0.34, around 700 K. The ODP2 sample has the highest  $zT$  of  $\sim 0.34$ , around 700 K, thanks to the low thermal conductivity throughout the measured temperature span. It is evident from the discussions above that the comparatively higher  $zT$  of the TS samples is supported by their lower density (high porosity), which blocked the thermal transport effectively. Importantly, the many folds reduction of  $\kappa$  due to the pores does not show a significant increase in the resistivity of the TS samples. Furthermore, the porous CTS samples also showed reproducible results during many measurements cycles. Total elimination of secondary phase oxides is not easy due to the low partial pressure of their formations, but a small amount of tin oxides does not seem to affect the TE properties during repeated TE measurements.



**Figure 7.** The repeated figure of merit ( $zT$ ) for TS and ODP samples. In the figure, markers 1 (red star), 2 (green circles), and 3 (blue triangles) represent the first, second, and third measurement cycles, respectively.

### 3.1.5 Conclusions

The present work shows that porosity leads to a significant suppression of thermal conductivity, and CTS pellets can be stabilized with different fractions of porosity. The low density or TS samples ( $\kappa \sim 0.3\text{--}0.2$  W/mK) showed  $\sim 3$  times lower thermal conductivity than the high density or ODP sintered samples ( $\kappa \sim 0.8\text{--}0.6$  W/mK). However, we did not observe any significant difference in electrical transport properties between the TS and ODP samples. The best performing stable TS samples present  $zT \sim 0.45$ , whereas the best performing ODP sample showed  $zT$  of  $\sim 0.34$ , around 700 K, a result clearly due to the ultra-low thermal conductivity of the traditionally sintered, porous samples.

Due to the low partial pressure of tin oxides formation, it is difficult to produce pure CTS and similar chalcogenides. However, the continuous evolution of secondary phase oxides can be eliminated by using a highly controlled environment, and a small fraction of secondary phase oxides seem to have little effect on the TE properties and stability of the samples. The results presented in this work give a general overview of the effects of different experimental conditions and porosity on the stability and TE performance of CTS samples. Similar considerations should hold for other Cu-Sn/Fe-S/Se-based systems, chalcogenides, colusites, and chalcopyrite, etc., used for various applications, ranging from photovoltaics to thermoelectricity and LED production.

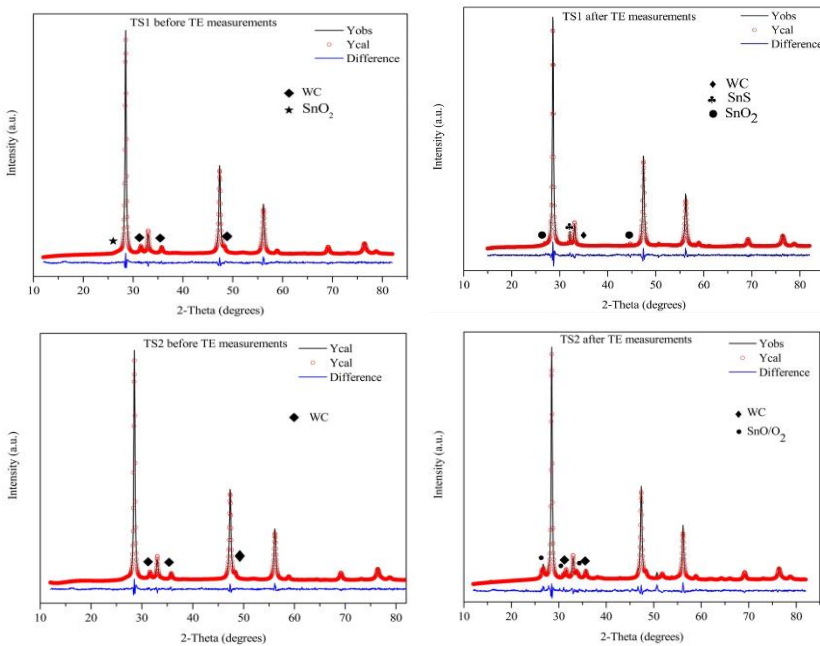
### 3.1.6 Appendix

Images of as-sintered ODP samples.



Figure 3.S1. Open die pressed (ODP) sintered CTS samples.

Rietveld refinement was performed on XRD patterns before and after repeated Seebeck and resistivity measurement cycles. The Whole Powder Pattern Modelling (WPPM) method as implemented in Topas 7 software was used for the Rietveld refinement, which considers a log-normal distribution of grains.



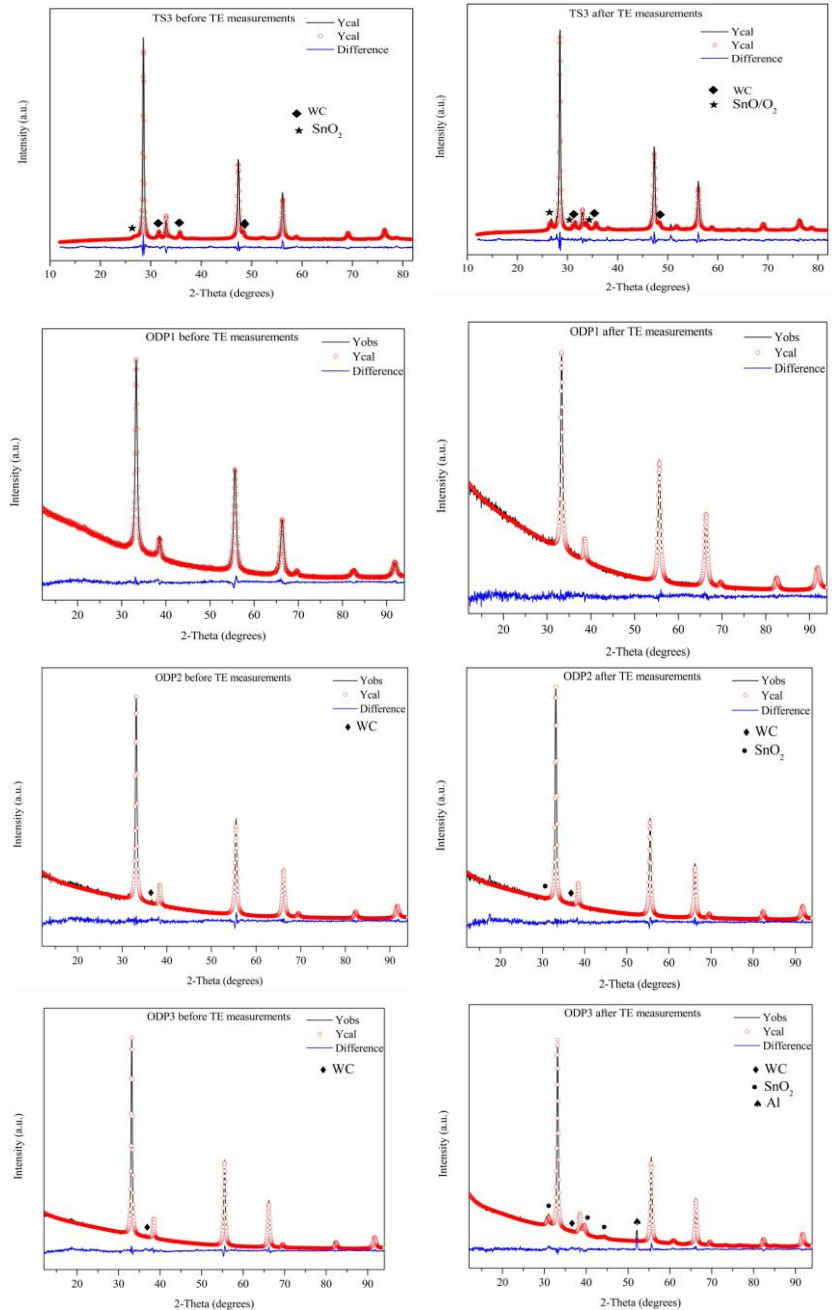


Figure 3.S2. The SAED for all samples shows similar 3 high-intensity Debye-Scherrer rings, representing the fingerprint planes for cubic CTS, (1 1 1), (2 2 0), and (3 1 1), respectively, as observed in the XRD patterns.

Morphological image of SPS Sintered CTS Sample at different magnifications.s

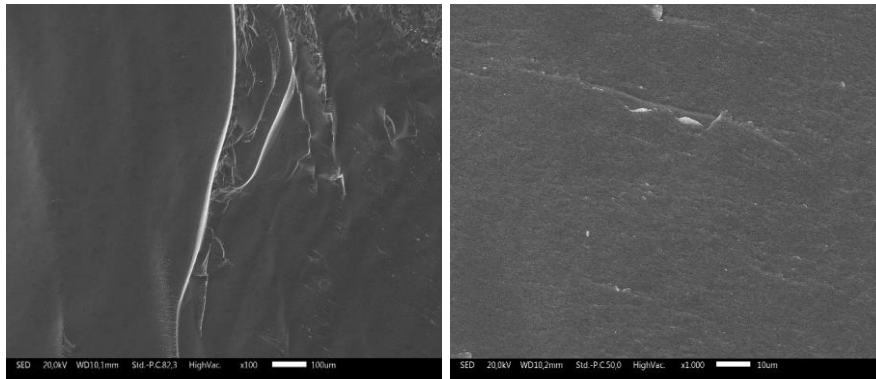


Figure 3.S3. Morphological image of SPS Sintered CTS Sample at different magnifications.

The SAED for all the samples shows similar 3 high-intensity Debye-Scherrer rings, representing the fingerprint planes for cubic CTS, (1 1 1), (2 2 0), and (3 1 1), respectively, as observed in the XRD patterns. The micrographs collected on sample TS1 is shown in Figure S4 (right bottom inset) revealed numerous small  $\text{SnO}_2$  grains surrounding the bigger (CTS) grains. In the cases of samples TS2 and TS3, these grains were not observed. However, we observed some variations in the chemistry.

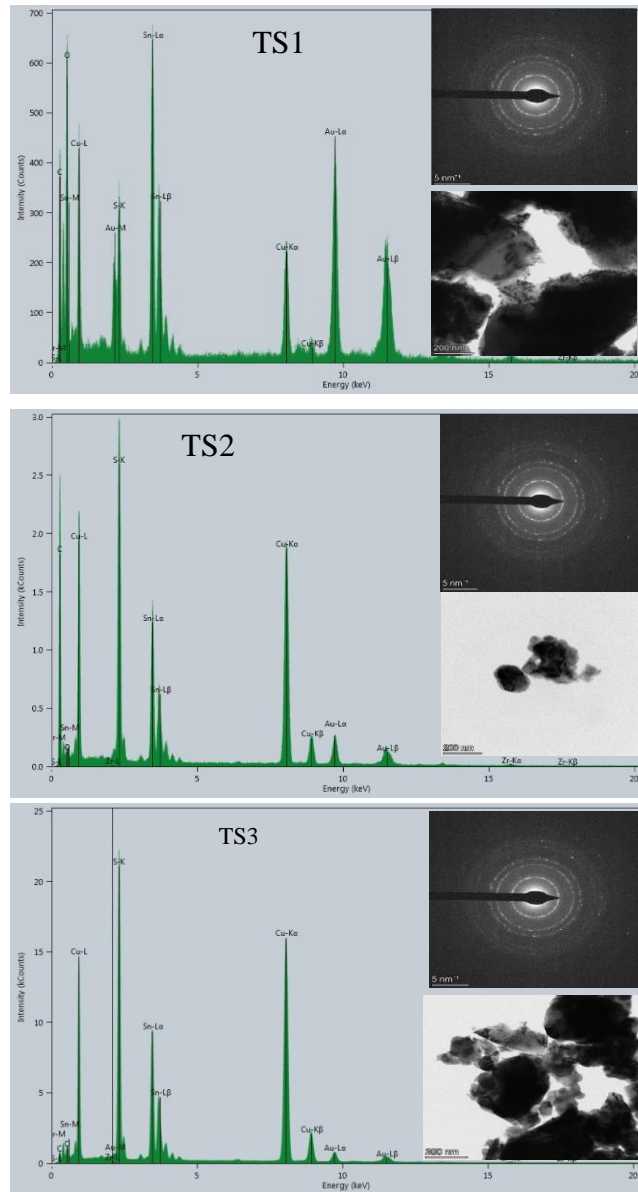
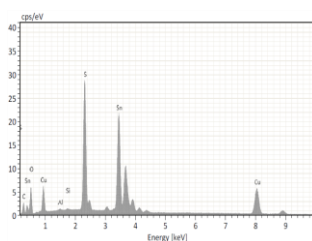
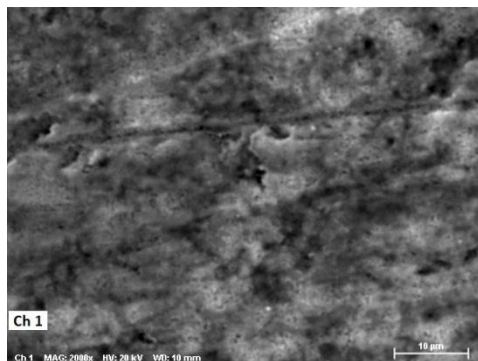
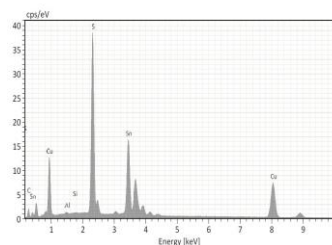


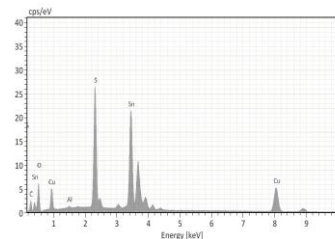
Figure 3.S4. EDX-spectra, SAED, and TEM micrographs for samples TS1, TS2, and TS3, respectively.



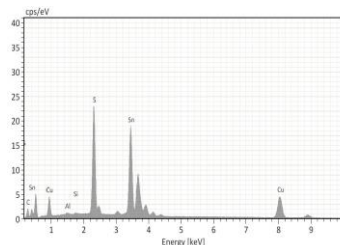
Element	At. No.	Netto	Mass [%]	Mass Norm. [%]	Atom [%]	abs. error [% (1 sigma)]	rel. error [% (1 sigma)]
Sulfur	16	135624	18.02	19.83	41.49	0.67	3.73
Copper	29	46729	24.44	26.89	28.39	0.69	2.82
Tin	50	200451	48.42	53.28	30.12	1.45	3.00
Sum		90.87	100.00	100.00			



Element	At. No.	Netto	Mass [%]	Mass Norm. [%]	Atom [%]	abs. error [% (1 sigma)]	rel. error [% (1 sigma)]
Sulfur	16	182434	23.74	25.69	47.75	0.88	3.69
Copper	29	61688	31.70	34.31	32.17	0.88	2.79
Tin	50	151456	36.96	40.00	20.08	1.12	3.02
Sum		92.41	100.00	100.00			

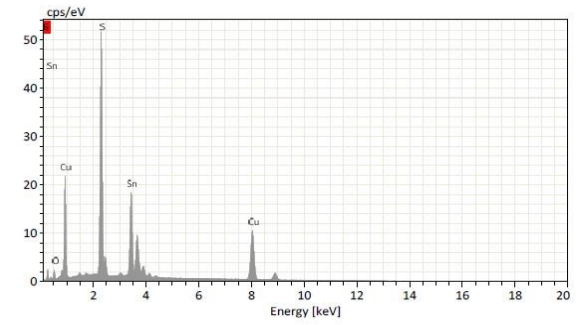


Element	At. No.	Netto	Mass [%]	Mass Norm. [%]	Atom [%]	abs. error [% (1 sigma)]	rel. error [% (1 sigma)]
Sulfur	16	124245	17.13	18.66	39.99	0.64	3.74
Copper	29	43491	23.62	25.73	27.82	0.67	2.83
Tin	50	200480	51.07	55.62	32.19	1.53	3.00
Sum		91.83	100.00	100.00			

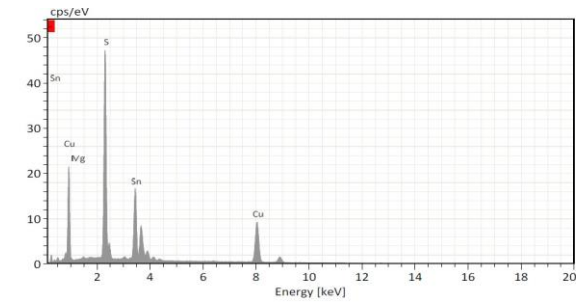


Element	At. No.	Netto	Mass [%]	Mass Norm. [%]	Atom [%]	abs. error [% (1 sigma)]	rel. error [% (1 sigma)]
Sulfur	16	107760	16.92	18.77	40.08	0.63	3.74
Copper	29	37322	23.49	26.06	28.08	0.67	2.84
Tin	50	171768	49.74	55.18	31.83	1.49	3.00
Sum		90.14	100.00	100.00			

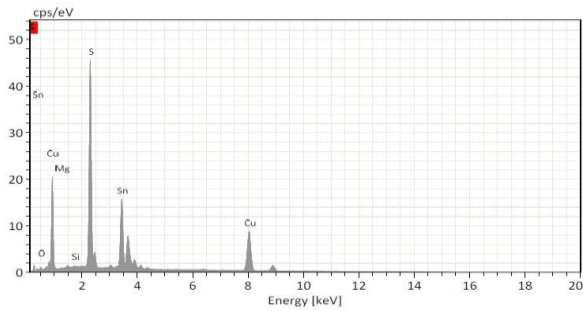
Figure 3. S5. Corresponding SEM-EDX data on chemical maps shown in Figure 3 for individual elements (Cu, Sn, and S) and simultaneously for all elements.



Element	At. No.	Netto	Mass [%]	Mass Norm. [%]	Atom [%]	abs. error [% (1 sigma)]	rel. error [% (1 sigma)]
Oxygen	8	3852	2.64	2.77	9.27	0.46	17.39
Sulfur	16	242471	25.72	27.05	45.11	0.95	3.68
Copper	29	87490	34.04	35.80	30.13	0.94	2.77
Tin	50	168949	32.69	34.38	15.49	0.99	3.03
Sum		95.08		100.00	100.00		



Element	At. No.	Netto	Mass [%]	Mass Norm. [%]	Atom [%]	abs. error [% (1 sigma)]	rel. error [% (1 sigma)]
Oxygen	8	1403	1.11	1.19	4.16	0.25	22.94
Sulfur	16	220367	25.02	26.81	46.92	0.92	3.68
Copper	29	76078	33.84	36.26	32.03	0.94	2.77
Tin	50	148533	33.35	35.74	16.90	1.01	3.03
Sum		93.32		100.00	100.00		



Element	At. No.	Netto	Mass [%]	Mass Norm. [%]	Atom [%]	abs. error [% (1 sigma)]	rel. error [% (1 sigma)]
Oxygen	8	730	0.62	0.65	2.29	0.18	28.84
Sulfur	16	212711	26.74	28.06	49.21	0.98	3.68
Copper	29	72644	34.11	35.79	31.68	0.95	2.77
Tin	50	142692	33.84	35.51	16.82	1.02	3.03
Sum		95.32		100.00	100.00		

Figure 3. S6. SEM-EDX on ODP1, ODP2, and ODP3 samples.

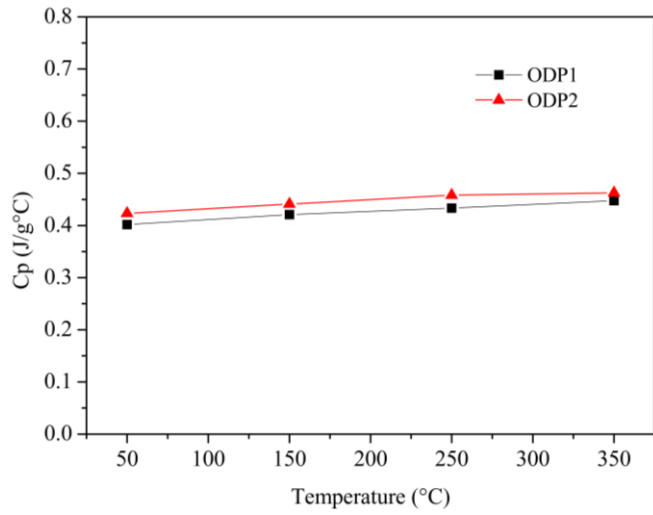


Figure 3.S7. Specific heat capacity ( $C_p$ ) measurements on ODP sintered samples

## 4 Effects of Grain Size

### 4.1 Effects of Grain Size on the Thermoelectric Properties of $\text{Cu}_2\text{SnS}_3$ : An Experimental and First-Principles Study

Published under a CC BY 4.0 license.

This section is entirely taken from<sup>125</sup>: Lohani, K.; Nautiyal, H.; Ataollahi, N.; Maji, K.; Guilmeau, E.; Scardi P. *Effects of Grain Size on the Thermoelectric Properties of  $\text{Cu}_2\text{SnS}_3$ : An Experimental and First-Principles Study*. *ACS Applied Energy Materials* 2021, 4 (11), 12604-12612.

<https://doi.org/10.1021/acsaem.1c02377>

Please cite any part of this section as specified above.

K. Lohani<sup>a</sup>, H. Nautiyal, N. Ataollahi<sup>a</sup>, K. Maji<sup>b</sup>, E. Guilmeau<sup>b\*</sup>, P. Scardi<sup>a\*</sup>

<sup>a</sup>Department of Civil, Environmental and Mechanical Engineering, University of Trento, Via Mesiano 77, 38123, Trento, Italy

<sup>b</sup>CRISMAT, CNRS, Normandie Univ, ENSICAEN, UNICAEN, 14000 Caen, France

\*Correspondence: [Paolo.Scardi@unitn.it](mailto:Paolo.Scardi@unitn.it) & [emmanuel.guilmeau@ensicaen.fr](mailto:emmanuel.guilmeau@ensicaen.fr)

Received: 6 August 2021; Accepted: 21 September 2021; Published online: 19 October 2021; Published in issue 22 November 2022

### 4.1.1 Abstract

Cu–Sn-based sulfides are earth-abundant and nontoxic compounds of special interest for low-cost energy harvesting applications. In the present work, we have investigated the effect of grain size on the thermoelectric properties of  $\text{Cu}_2\text{SnS}_3$  (CTS). Three dense CTS samples with nanometric grains were produced by mechanical alloying combined with spark plasma sintering, preserving the small size of crystalline domains to 12, 25, and 37 nm, respectively. The experimental results show that the Seebeck coefficient ( $S$ ) and electrical resistivity ( $\rho$ ) decrease with decreasing domain sizes, while the thermal conductivity ( $\kappa$ ) increases. A smaller domain size correlates with a lower resistivity and a degenerate semiconductor-like behavior due to higher carrier concentration. At the same time, our synthesis method leads to materials with very low lattice thermal conductivity, thanks to the nanometric size of grains and structural disorder. As a result, the sample with the smallest grain size exhibits the highest  $zT$  of  $\sim 0.4$  at 650 K. First-principles density functional theory (DFT) simulations on various CTS crystallite surfaces revealed localized states near the Fermi level and the absence of band gap, indicating the metallic nature of the surfaces. Various CTS systems were tested by DFT, showing the following order of increasing formation energy: stoichiometric CTS, Cu vacancy, Cu-rich, Sn vacancy, and Sn-rich.

### 4.1.2 Introduction

Most commercially available thermoelectric (TE) devices use toxic and scarce materials, making them expensive and potentially hazardous, for example,  $\text{Sb}_2\text{Te}_3$ ,  $\text{Bi}_2\text{Te}_3$ , and so forth. In recent years, the search for high-performance, nontoxic, ecofriendly, and earth-abundant TE materials has led to the exploration of multinary sulfides,<sup>9,127</sup> Chalcogenides,<sup>46</sup> colusites,<sup>128,129</sup> and other metal-based sulfides<sup>130,131</sup> could be viable alternatives to existing materials<sup>132</sup>. Cu-based sulfides have low formation energy so that it is possible to produce them by short-period reactive milling using a planetary or vibrating mill. As also shown in the present work, high-energy reactive ball milling, also called mechanical alloying, can be employed with success to synthesize new and disordered phases. In addition, milling

offers the advantage of facile and scalable production for industrial use.<sup>133</sup>

The energy conversion efficiency of a TE material is determined by a dimensionless figure of merit ( $zT$ ) expressed as  $zT = S^2/\rho\kappa^*T$ , where  $S$ ,  $\rho$ ,  $\kappa$ , and  $T$  are the Seebeck coefficient, electrical resistivity, thermal conductivity, and absolute temperature, respectively.  $S^2/\rho$  is referred to as the power factor ( $PF$ ). The Seebeck coefficient and electrical resistivity are strongly dependent on the carrier concentration ( $n$ ), mobility ( $\mu$ ), and effective mass of the charge carriers ( $m^*$ ) (see eqs 4.1 and 4.2 below). A low carrier concentration and high effective mass of charge carriers can increase the Seebeck coefficient, but it also penalizes the electrical conductivity ( $\sigma$ ) and vice versa<sup>9,10</sup>.

$$S = Am^* \left( \frac{\pi}{3n} \right)^{\frac{2}{3}} T \quad 4.1$$

$$\sigma = ne\mu \quad 4.2$$

$$\kappa_e = \frac{LT}{\rho} \quad 4.3$$

where  $A$ ,  $e$ , and  $L$  represent a constant, charge of an electron, and the Lorenz number, respectively.

Besides high PF, TE materials also require low thermal conductivity ( $\kappa$ ), composed of a lattice ( $\kappa_l$ ) and an electronic contribution ( $\kappa_e$ ), combined as  $\kappa = \kappa_l + \kappa_e$ . The lattice contribution can be decreased by increasing the grain boundary density, vacancies, defects, impurities, strain, and so forth. Differently,  $\kappa_e$  shows a strong dependence on the electrical resistivity, as in the Wiedemann–Franz law (see eq 3).<sup>129</sup> More recently, the determination of the TE quality factor ( $\beta$ ) given by  $\beta \propto \mu_0 m_{dos}^{*3/2} / \kappa_l$  (where  $\mu_0$  and  $m_{dos}^*$  are the nondegenerate mobility and density of state effective mass, respectively) is in practice for the simultaneous optimization of all TE parameters.<sup>8,134</sup>

$\text{Cu}_{2+x}\text{Sn}_{1-x}\text{S}_3$  (CTS) polymorphs are studied for many applications such as photovoltaics, transistors, LEDs, and TE materials. A recent study has also suggested a potential use of CTS quantum dots for photodetector applications.<sup>135</sup> CTS polymorphs have been extensively studied as  $p$ -type TE materials showing moderately high PF with high or low thermal conductivity, depending on whether the crystal structure

is ordered or disordered.<sup>26,34,38</sup> To increase the TE performance, different cationic substitutions have been investigated with the aim to tune the carrier concentration and to introduce structural disorder. Among the various studies, Zhao et al. have reported the highest  $zT \sim 0.9$  (at  $T > 700$  K) so far by simultaneous cobalt and antimony doping.<sup>32</sup>

Zhai et al.<sup>68</sup> and Shigemi et al.<sup>94</sup> have shown that the hybridization of Cu  $3d$  and S  $3p$  orbitals in the valence band (VB) is responsible for the  $p$ -type nature of CTS. Heavy acceptor doping due to unfilled  $d$ -orbitals of Co,<sup>36</sup> Cu,<sup>37</sup> Ni,<sup>32</sup> Fe,<sup>13</sup> and Mn<sup>35</sup> enhances the density-of-state (DOS) effective mass of carriers (holes) and electrical conductivity, resulting in a high  $PF \sim 10 \mu\text{W}/\text{cmK}^2$  around 700 K. Cationic substitution also transforms the CTS crystal structure from ordered (monoclinic  $Cc$ ),<sup>136</sup> to tetragonal  $I4\bar{2}m$  and disordered (cubic:  $F\bar{4}3m$ ).<sup>34</sup> In most of the cases, a mixture of different phases is obtained. Deng et al.<sup>37</sup> have shown the influence of the Cu/Sn ratio in  $\text{Cu}_{2+x}\text{Sn}_{1-x}\text{S}_3$  on the electrical and thermal properties. More recently, Pavan Kumar et al.<sup>38</sup> have discovered a new ordered monoclinic structure  $\text{Cu}_5\text{Sn}_2\text{S}_7$  by increasing the Cu/Sn ratio up to  $x = 0.15$ , leading to a specific ordering of Cu and Sn in the structure. In summary, the hole doping in CTS compounds, induced by the substitution of Cu, Sn, or S by aliovalent cations, or by Cu for Sn substitution, increases the carrier concentration. Disorder phenomena, usually induced by the cationic/anionic substitution, scatter the phonon waves more effectively, resulting in a higher TE figure of merit.

The disordered cubic CTS and  $\text{Cu}_2\text{SnSe}_3$  (CTSe) phases can also be produced and stabilized without chemical alteration.<sup>26,41,71</sup> The optical absorption measurements revealed a lower band gap for the disordered CTS/Se polymorphs. The lower band gap enhances the carrier concentration, resulting in a higher PF compared to its ordered polymorph. Furthermore, in a theoretical study, Baranowski et al.<sup>81</sup> have also reported band tailing and midgap states for the disordered CTS phase.<sup>71,81</sup> The structural disorder introduces potential energy fluctuations in the lattice that allow energy levels within the forbidden gap, responsible for the band tailing and reduced band gap. Moreover, Dahule et al.<sup>137</sup> have studied the electronic structure properties of (200) and (-131) surfaces of monoclinic CTS and have shown their metallic

character. It is worth mentioning that the metallic character was confirmed using different potentials, including the Heyd–Scuseria–Ernzerhof potential, which results in a better estimation of the band gap. In terms of synthesis, the literature suggests a three-step top-down approach to produce CTS samples for TE applications. First, CTS is produced from the elemental powders (Cu, Sn, S, and dopant elements) using an extended high-temperature solid-state reaction<sup>34</sup>. In the second step, the grain size is sometimes reduced by ball milling. Finally, high-density pellets are produced using spark-plasma sintering (SPS) or hot pressing. This approach results in highly crystalline materials with average domain sizes ranging from half to several microns. This synthesis method requires a long annealing time at high temperatures, which is time- and resource-consuming.

Alternatively, CTS compounds, as many other Cu-based sulfides, can be produced by combined high-energy reactive ball milling (mechanical alloying) and SPS or hot pressing.<sup>39,138</sup> Mechanical alloying allows us to produce fine, homogeneous, precrystallized, and highly reactive powders, which usually lead to high-purity, crystalline, and dense samples after sintering with small grain and crystallite sizes. Furthermore, a highly dense disordered CTS polymorph can be stabilized without any chemical substitution.<sup>133</sup>

The present work aims to shed light on the degenerate semiconductor-like behavior of nanocrystalline CTS samples. Three dense CTS samples were produced using powder synthesized by high-energy reactive ball milling and SPS. We have investigated the effects of grain size on the TE properties. Structural and microstructural analyses suggested a stoichiometry deviation in CTS phases sintered at low temperature, together with a very small crystallite and grain size. *Ab initio* calculations using density functional theory (DFT) indicated the metallic nature of CTS surfaces, leading to a degenerate semiconductor-like trend with temperature. Further evidence is presented on the formation energies for various CTS systems with vacancies and chemical deviations.

#### 4.1.4 Experimental methods

Elemental powders (Cu, Sn, and S) were weighted in a stoichiometric ratio and fed in WC vials with WC balls. A Fritsch PULVERISETTE-4 mill was operated for 1 h, producing ~6 g of the as-milled CTS powder. The entire production process was performed in a glovebox with an argon-filled environment. During the milling, no lubricant was introduced to avoid any contamination. The production of CTS powder by high-energy ball milling of elemental powders and binary sulfides is discussed in detail elsewhere.<sup>42,71</sup>

The as-milled powder was sintered using a SPS machine (FCT HPD 25) at various temperatures and pressures to optimize the sintering conditions (Table 4.1). The relative densities of the samples are 86, 96, and 94% for sample A, B, and C, respectively.

Table 4.1. Sample Names, sintering conditions, densities, phase purity, and average grain size for various CTS samples.

Sample name	Sintering die	Sintering pressure (MPa)	Sintering temp. (°C)	Dwell time (min)	Density (g/cm <sup>3</sup> )	Weight fraction (±1%)		Average domain size (±10 nm)
						CTS	SnO <sub>2</sub>	
A	WC	500	400	60	4.06	99	1	12
B	graphite	64	512	30	4.52	100		25
C	graphite	64	500	30	4.45	99	1	37

Structural analysis was performed using X-ray diffraction (XRD). XRD data were collected in  $\theta/2\theta$  Bragg–Brentano geometry using a PANalytical X'Pert Pro diffractometer equipped with a  $\text{Cu } K\alpha$  ( $\lambda = 1.5406 \text{ \AA}$ ) source. Micrographs and energy-dispersive X-ray (EDX) spectroscopy analyses were collected using a JEOL JSM 7200F scanning electron microscope equipped with an EDX X-Flash Bruker detector.

The electrical resistivity ( $\rho$ ) and Seebeck coefficient ( $S$ ) were measured simultaneously from 300 up to 700 K on bar-shaped samples of typical

dimensions  $2 \times 3 \times 10 \text{ mm}^3$  using an ULVAC-ZEM3 instrument under partial helium pressure.

A NETZSCH LFA-457 apparatus was used for measuring the thermal diffusivity under argon flow. The thermal conductivity ( $\kappa$ ) was determined as the product of the geometrical density, the thermal diffusivity, and the theoretical heat capacity using the Dulong–Petit approximation. The lattice contribution to the thermal conductivity ( $\kappa_l$ ) was determined by subtracting the estimated electronic component ( $\kappa_e$ ) from the measured total thermal conductivity,  $\kappa$ . The measurement uncertainties are estimated to be 6% for the Seebeck coefficient, 8% for the electrical resistivity, 11% for the thermal conductivity, and 16% for the final dimensionless figure of merit.

Hall effect measurements at RT were carried out using a physical property measurement system (Quantum Design) under an applied magnetic field of 9 T.

### 4.1.5 Computational Methods

The electronic structure calculations were performed using DFT as implemented in the Vienna ab initio simulation package<sup>85,86</sup>. The interaction between electrons and ions was described using the projector-augmented-wave (PAW) method. The generalized gradient approximation with Perdew–Burke–Ernzerhof<sup>87</sup> electron exchange–correlation was used for the calculations.

We have performed the calculations for (001), (010), and (100) slabs of monoclinic CTS and two disordered CTS cells with sulfur termination. We considered two cases for the disordered cell, one with the Cu-rich and the other with Sn-rich atomic layer below the terminating sulfur layer. For all the calculations, CTS stoichiometry was preserved. A vacuum of 15 Å was created to minimize the interaction between the periodic copies. In the disordered cells, the atoms of the lower four layers were fixed in a position, whereas the atoms of the upper four layers were free to move. Relaxation was performed with a plane-wave kinetic energy cutoff and an electronic convergence of 350 and 10–5 eV, respectively. The involvement of core electrons was seized by

freezing. Only  $3d^{10}4s^1$ ,  $4d^{10}5s^25p^2$ , and  $3s^23p^4$  electrons were treated as valence electrons for Cu, Sn, and S, respectively. The cell parameters were fixed, whereas the atomic position was allowed to change for relaxation. The electronic convergence was set to  $10^{-6}$  eV for DOS calculations. Brillion zone sampling was performed on a k-point grid of  $9\times9\times1$  and  $5\times5\times1$  for monoclinic slabs and disordered cells, respectively. The k-mesh was reduced for the disordered cell due to its larger size.

The formation energy calculations were performed on Cu-rich, Cu-vacant, Sn-rich, and Sn-vacant cells. For these calculations, the plane wave kinetic energy cutoff and electronic convergence were changed to 400 and  $10^{-6}$  eV, respectively. A Monkhorst–Pack<sup>88</sup> k-point mesh of  $7\times7\times7$  (centered at the gamma point) was used to integrate the Brillion zone. One atom was removed from the supercell, and the remaining atoms were allowed to relax for the vacancy calculations. The off-stoichiometry calculations were performed on a supercell of 72 atoms with a stable monoclinic phase, where one Cu atom was replaced by one Sn atom and vice versa, respectively, for the Sn-rich and Cu-rich simulations.

#### 4.1.4 Results and Discussion

XRD patterns collected on the as-milled powder with increasing milling times are shown in Figure 4.1. Due to its low formation energy, short milling of 15 min led to the formation of binary sulfides, especially CuS. As the milling time was increased to 30 min, the appearance of diffraction peaks of sphalerite-type structures can be noticed. However, unreacted SnS and Sn powder were still present in the sample. With the further increase of the milling time to 1 h, the as-milled powder showed four broad diffraction peaks, implying the formation of a sphalerite-type crystal structure. It is worth mentioning here that, among all the elements, Sn incorporated last in the CTS system. Broad Bragg-peaks with diffuse backgrounds imply that the one-hour milled powder consists of less crystalline CTS grains with a small domain size.

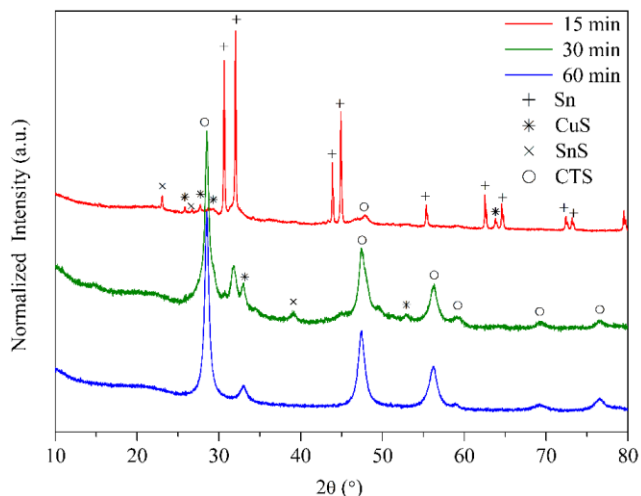


Figure 4.1. XRD patterns for the powder milled for 15, 30, and 60 min.

SEM–EDX data collected on 60 min milled powder at full-frame image showed the presence of stoichiometric CTS. On the same sample, various micrographs and EDX data were collected at different magnifications from different parts of the SEM grid. It indicated that the as-milled powder has a nonhomogeneous chemical distribution with a small domain size, which tends to agglomerate in larger particles (Figure 4.S1).

High-density bulk CTS samples were produced by SPS under different sintering conditions (listed in Table 4.1). Sintered samples maintained the same Bragg-peak positions as the as-milled powder. However, sharper Bragg peaks for sintered samples indicate an increased crystallinity and crystallite size. XRD line profile analysis was performed by the Rietveld method<sup>124</sup> using Topas 7 software<sup>57</sup>. We employed the whole powder pattern modeling macro<sup>56</sup> to simulate the peak profile. The instrumental profile was obtained from a LaB<sub>6</sub> standard sample.<sup>139</sup> A nine-point Chebyshev polynomial and a  $1/x$ -function were used to simulate the background and low-angle intensity, respectively. Subsequently, zero shift and other parameters were systematically refined<sup>55</sup>. During the refinement, the variation of the Debye–Waller coefficients (thermal factors) was restricted between 0 and 2 for all atoms. For all the samples discussed below, the goodness of fit was  $\sim 1.1$ – $1.3$ .

Disordered CTS has a zinc-blende (ZnS)-like (cubic) close-packed face-centered structure, which arranges its atoms in the (216) space group. The  $4a$  Wyckoff position is occupied by Cu and Sn atoms with occupancy  $2/3$  and  $1/3$ , respectively, while the  $4c$  site is occupied by S atoms with occupancy 1. The lattice parameter, phase density, and cell volume determined from Rietveld refinement were  $5.43 \text{ \AA}$ ,  $4.71 \text{ g/cm}^3$ , and  $160.50 \text{ \AA}^3$ , respectively. No microstrain was observed for any sample. The average domain size and the weight fraction of CTS and secondary phases are listed in Table 4.1 for different sintering conditions. All the samples showed disordered cubic CTS structures. However, a small amount (weight fraction  $<0.5\%$ ) of  $\text{SnO}_2$  was observed for samples A and C. For sample B (see Figure 4.2 (a)), two Bragg peaks around  $2\theta \sim 16$  and  $\sim 31^\circ$  were observed. Sample B may have a small amount of the monoclinic phase. However, the two peaks are quite broad which makes it hard to quantify the monoclinic phase reliably, and it is certainly below 1% in weight.

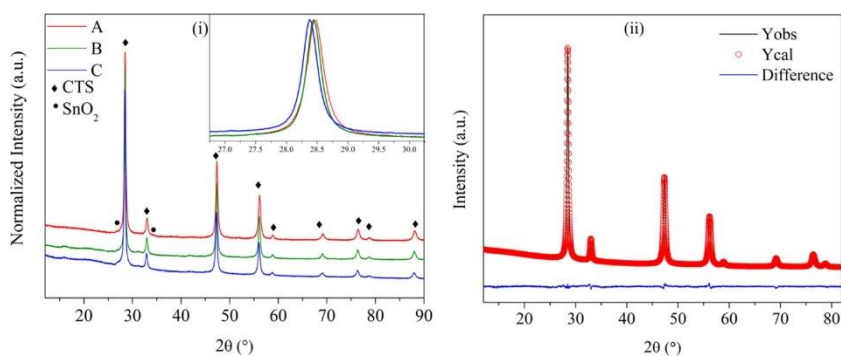


Figure 4.2. (i) XRD patterns of samples sintered under various conditions.; (ii) Rietveld refinement data for sample A collected (Yobs), calculated (Ycal), difference (difference) pattern. See Figure 3.S2 for the Rietveld refinement data for samples B and C.

The sizes of crystalline domains were estimated as  $12 \pm 10$ ,  $25 \pm 10$ , and  $37 \pm 10$  nm for samples A, B, and C, respectively. The reported average grain size for high-density CTS samples prepared by the three-step method (discussed in the Introduction) is in the range of 500–600 nm,<sup>33</sup> and in some cases, micron-size grains are also reported<sup>36</sup>. In contrast, traditionally sintered samples (without applying pressure) showed smaller grains, domain size ranging from  $\sim 50$  nm to a few 100 nm, and low density<sup>42</sup>. The mechanical alloying combined with the

SPS method proposed here constrained the grain size below 50 nm<sup>39</sup> while promoting densification at a relatively low sintering temperature.

SEM micrographs on bulk samples reveal a dense microstructure, that is, highly intact grains with almost no porosity (shown in Figure 4.3, 4.S3 and 4.S4). Unlike the as-milled powder, EDX analysis on the sintered samples revealed a homogeneous chemical distribution, with the exception of sample A, in which a small amount of SnS was found, likely due to an incomplete reaction at 400 °C (Figures 4.3i, 4.S3, and 4.S5). Some bright spots in the micrographs revealed traces of WC particles. However, WC and SnS signals were not observed in the XRD patterns because of their small weight fraction, which was below the detection limit ( $\ll 1\%$ ). Comparative SEM–EDX analysis was performed on samples A and B (before and after polishing), and SEM–EDX data are shown in the Appendix (Figures 4.S3–S6). Sample A has a higher amount of the SnS phase compared to sample B, probably due to a lower sintering temperature. However, the matrix composition for both samples is similar, suggesting that stoichiometric deviation in CTS grains is quite small. These micrographs also confirm that the average grain size is much smaller than the magnification of the microscope allows to see.

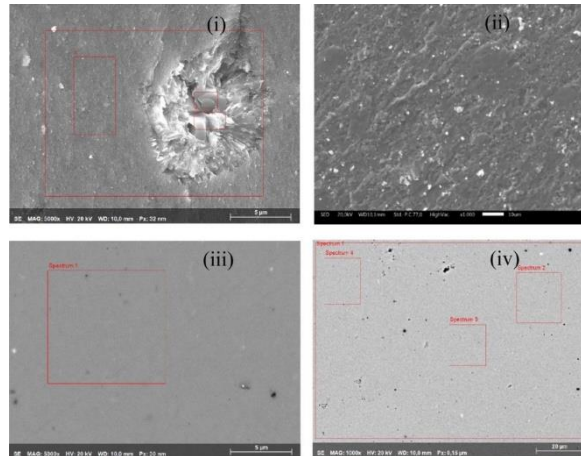


Figure 4.3. (i) SEM micrograph of the surface of SPS sintered sample A showing a compact sample with almost no pores and the presence of SnS; (ii) WC particles on one of the samples (bright spots in the micrograph, identified by EDX); (iii) micrographs of polished samples A and (iv) B. EDX data are provided in Table 4.S1.

Figures 4.4 (i,ii) shows the absolute Seebeck coefficient ( $S$ ) and resistivity ( $\rho$ ), respectively, for the CTS samples in Table 4.1. Although there is a variation in the values of  $S$ , all the samples show a positive Seebeck coefficient increasing with temperature. Samples A, B, and C present  $S \sim 100$ , 180, and 160  $\mu\text{V}/\text{K}$ , respectively, at room-temperature (RT), which are lower than the reported RT values for the CTS compound ( $S \sim 500\text{--}700 \mu\text{V}/\text{K}$ ).<sup>26,37,71</sup> A general trend of increasing values of the Seebeck coefficient with increasing sintering temperature and grain size can be observed. The Cu–Sn–S-based systems exist in numerous phases, such as  $\text{Cu}_2\text{SnS}_3$ ,<sup>26</sup>  $\text{Cu}_3\text{SnS}_4$ ,<sup>140</sup>  $\text{Cu}_5\text{Sn}_2\text{S}_7$ ,<sup>38</sup>  $\text{Cu}_7\text{Sn}_3\text{S}_{10}$ ,<sup>30</sup> and so forth.<sup>127</sup> Mostly, these systems show a  $p$ -type semiconducting nature due to the unfilled Cu 3d-orbitals. Additionally, Cu–S bonds in Cu–Sn–S-based systems form a three-dimensional conduction network which enhances their electrical conductivity.<sup>34</sup>

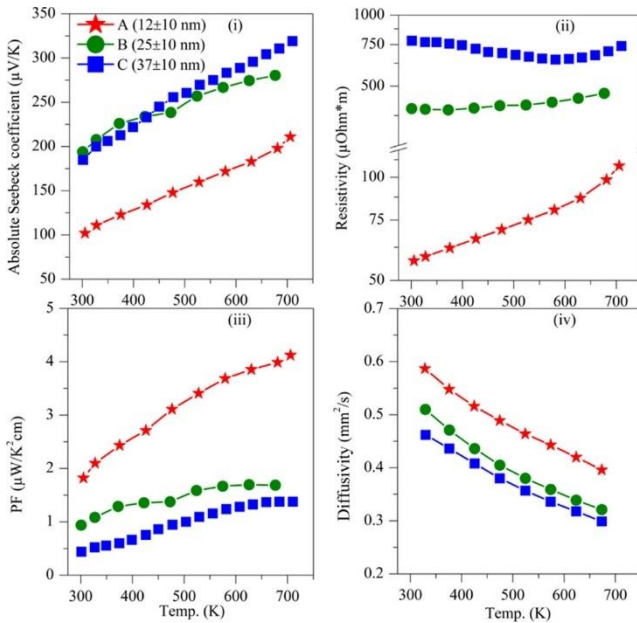


Figure 4.4. Temperature-dependent (i) absolute Seebeck coefficient, (ii) resistivity, (iii)  $PF$ , and (iv) diffusivity for sintered samples A, B, and C.

It is well known that undoped CTS is highly resistive with a nondegenerate semiconductor-like trend in temperature owing to its low carrier concentration.<sup>42</sup> However, samples A and B show a degenerate semiconductor-like nature, whereas sample C, with the

largest  $S$  ( $\sim 320 \mu\text{V/K}$ , above 650 K), shows a nondegenerate trend up to  $\sim 650$  K. As expected, samples with a higher Seebeck coefficient have higher electrical resistivity and vice versa, but a trend of decreasing electrical resistivity can also be observed with the decrease in the crystalline domain size. It is worth mentioning here that off-stoichiometry in CTS compounds can lead to similar results, although such deviations should have a Cu/Sn ratio  $>2$ . In fact, Deng et al.<sup>37</sup> show that an excess of Cu in  $\text{Cu}_{2+x}\text{Sn}_{1-x}\text{S}_3$  ( $x \geq 0.016$ ) changes the electrical resistivity from a nondegenerate to degenerate behavior. This suggests that the CTS phase, especially when sintered at low  $T$  (400 °C, sample A), is nonstoichiometric.

In general, a small grain size leads to a higher Seebeck coefficient due to the scattering of charge carriers by the grain boundary, otherwise known as energy filtering.<sup>11</sup> This, however, decreases the mobility and, in turn, increases the electrical resistivity. The lower grain size is also crucial in the suppression of thermal conductivity by scattering phonon waves effectively. The results shown here contrast with the energy filtering mechanism. The samples with smaller domains are more conductive, and we observe a trend of increasing resistivity with an increase in grain size. Carrier concentration measurements on these samples revealed that the higher conductivity of samples with small domains correlates with a higher carrier concentration,  $8.6 \times 10^{20}$  and  $7.4 \times 10^{19} \text{ cm}^{-3}$  for samples A and B, respectively. These values are 1–2 orders of magnitude higher than the reported values for the CTS.<sup>71</sup> However, other Cu–Sn–S-based compounds with higher Cu/Sn ratios presented increasing carrier concentration with increasing Cu/Sn ratio, that is,  $2.6 \times 10^{21}$  and  $5.6 \times 10^{21} \text{ cm}^{-3}$  for  $\text{Cu}_7\text{Sn}_3\text{S}_{10}$ <sup>30</sup> and  $\text{Cu}_5\text{Sn}_2\text{S}_7$ ,<sup>38</sup> respectively. Sample A sintered at a low sintering temperature has a lower carrier mobility ( $1.2 \text{ cm}^2/\text{V s}$ ) than sample B ( $2.1 \text{ cm}^2/\text{V s}$ ), which is explained by the larger carrier concentration (increased probability of charge carrier collision) and lower grain size in sample A.

Due to the decreased electrical resistivity, sample A shows the highest  $PF$  value of  $\sim 4.5 \mu\text{W/K}^2 \text{ cm}$ , above 650 K, which is 3-fold and 9-fold higher than cubic (disordered) CTS ( $PF \sim 1.5 \mu\text{W/K}^2 \text{ cm}$ )<sup>71</sup> and monoclinic (ordered) CTS ( $PF \sim 0.47 \mu\text{W/K}^2 \text{ cm}$ ),<sup>34</sup> respectively.

Samples B and C have comparatively lower  $PF$  values of  $\sim 1.5$  and  $\sim 1.2 \mu\text{W}/\text{K}^2 \text{ cm}$ , respectively. The thermal diffusivity measurements are shown in Figure 4.4(iv). It is evident from the data that samples with smaller domains (more conductive) have a higher diffusivity. From the above considerations, it appears that the electrical properties are strongly dependent on the sintering temperature and grain size. Additional results following the same trend of the Seebeck coefficient and electrical resistivity with grain size support this statement (Figure 4.S7). As mentioned above, a slight stoichiometric deviation can occur in the small grains due to the incomplete reaction and crystallization at low temperature, leading to high carrier concentration and electrical conductivity. The fast kinetics of the reaction and crystallization during SPS may also lead to variation of compositions at the grain surfaces and boundaries, which could be highly conductive and possibly injecting additional charge carriers in the system.

To investigate this further, three ordered and two disordered CTS surfaces (shown in Figures 4.5 and 4.6, respectively) were studied. The first three images in Figure 4.5 show ordered CTS slabs with (001), (010), and (100) planes. The other two images show disordered structures consisting of a Cu-rich layer and a Sn-rich layer, just below the terminating sulfur layer. Please note that the overall chemistry of the CTS system was respected while making all the structures shown in Figures 4.5 and 4.6. For each structure in Figures 5 and 6, the corresponding DOS are shown with the structures. After minimization, large distortions were observed for the surface atoms of all the structures. The reason is that surface atoms form incomplete bonds due to the change in the coordination number caused by the surface termination. The DOS on the VB side is higher than that on the CB side, showing p-type nature. However, no band gap was observed, suggesting a metallic character of all the studied structures. The localized states are visible near the Fermi level due to the dangling bonds on the surface. These dangling bonds provide additional charge carriers (holes), which increase the carrier concentration, leading to the degenerate semiconductor-like behavior observed in Figure 4.4. We are aware that the calculated structures are not an exact model of the grain boundary effects. Since the grains could terminate with any plane or orientation (favored by the local environment), these calculations only

make the hypothesis plausible that CTS grains should have dangling bonds, which would lead to localized states at the Fermi level and increased electrical conductivity. These results are in agreement with a recent report by Dahule et al.,<sup>137</sup> although limited to the monoclinic phase.

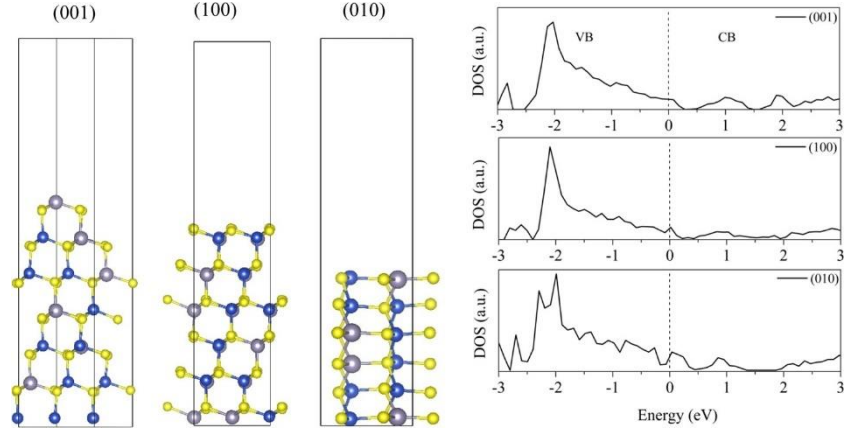


Figure 4.5. Monoclinic (ordered) CTS slabs with orientations (001), (100), and (010) and corresponding DOS plots. Here, the Fermi level is set to zero. Cu, Sn, and S atoms are represented by blue, gray, yellow colors, respectively.

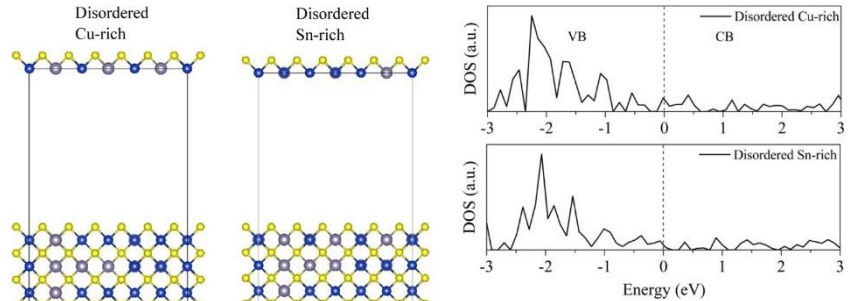


Figure 4.6. Structures and corresponding DOS for two disordered structures, where one has a Cu-rich and the other has a Sn-rich layer, just below the terminating sulfur layer. Here, the Fermi level is set to zero.

Table 4.2 reports the formation energy per unit atom for vacancy and off-stoichiometry in CTS, as obtained from DFT simulations. It is evident from the reported values that after the stoichiometric CTS, Cu-vacant and Cu-rich systems are energetically more viable, whereas Sn-vacant and Sn-rich systems seem less likely to form. The corresponding DOS plots are shown in Figure 4.S6. Thermodynamically, these conclusions could be generalized to the whole family of Cu–Sn–S systems. In other Cu–Sn–S systems, Cu-vacant and Cu-rich systems

would be more likely to form than Sn-rich and Sn-poor phases. Moreover, in this family of materials, Cu vacancy, Cu excess, and Sn vacancy would enable *p*-type doping-like effects, whereas Sn excess showed *n*-type behavior.

Table 4.2. Energy of the System, Formation Energy, and Formation Energy per Unit Atom for Various CTS Systems

System	Configuration	Energy of the system (eV)	Formation energy (eV)	Formation energy per unit atom (eV/atom)
CTS	24-Cu, 12-Sn, and 36-S	-308.0450	-23.8016	-0.3306
Cu-vacant	23-Cu, 12-Sn, and 36-S	-303.7652	-23.2520	-0.3275
Cu-rich	25-Cu, 11-Sn, and 36-S	-307.5523	-23.4263	-0.3254
Sn-rich	23-Cu, 13-Sn, and 36-S	-306.7s465	-22.3857	-0.3109
Sn-vacant	24-Cu, 11-Sn, and 36-S	-302.2878	-21.8920	-0.3083

The thermal conductivity and figure of merit are shown in Figure 4.7 (i,ii), respectively. Since we are considering the heat capacity well above the Debye temperature ( $\theta_D \sim 213$  K), the total thermal conductivity was calculated considering a constant value of  $C_p \sim 0.44$  J/g K for all samples. The total thermal conductivity for all samples decreases with temperature due to an increased phonon–phonon interaction (Umklapp process or U-process). The electronic part of thermal conductivity ( $\kappa_e$ ) was estimated according to the Wiedemann–Franz law (see equation 4.3), where the Lorenz number ( $L$ ) was calculated using eq 4.<sup>141</sup>

$$L = 1.5 + e^{-\left(\frac{|S|}{116}\right)} \quad 4.4$$

where  $L$  is in  $10^{-8}$  W $\Omega$ /K<sup>2</sup> and  $S$  in  $\mu$ V/K.

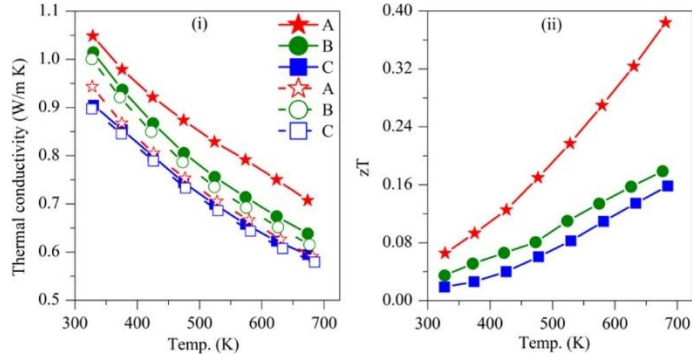


Figure 4.7. Temperature-dependent (i) total thermal conductivity (filled markers connected with the solid line) and lattice component of thermal conductivity (empty markers connected with the dashed line) and (ii) figure of merit.

It is evident from Figure 4.7 (i) that at higher temperatures, the lattice part of thermal conductivity is similar for all the samples,  $\kappa_l \sim 0.6$  W/m K, above 673 K. This value is comparatively lower than the diamond-like  $\text{CuFeS}_{2+x}$  system, where  $\kappa_l \sim 1.0$  W/m K is reported at 650 K.<sup>142</sup> However, other Cu–Sn–S-based compounds such as  $\text{Cu}_3\text{SnS}_4$  and  $\text{Cu}_7\text{SnS}_{10}$  show a similar  $\kappa_l$  around 650 K, which further decreases to  $\kappa_l \sim 0.4$  W/m K at 750 K.<sup>140,143</sup> The electronic contribution of thermal conductivity is the highest for sample A, and it decreases for samples B and C. This agrees with the corresponding resistivity and carrier concentration measurements as samples A, B, and C have increasing resistivity (decreasing carrier concentration) in the same order. The figures of merit of samples A, B, and C are equal to 0.40, 0.17, and 0.14 at 673 K, respectively. Overall, the two-step production method can be used to produce high-density nanostructured pellets. The experimental results indicate that a similar  $zT$  is reported for  $\text{Cu}_{2+x}\text{Sn}_{1-x}\text{S}_3$  systems with Sn substitution ( $x = 0.2$ ) by Zn,<sup>34</sup> Ni,<sup>32</sup> In,<sup>33</sup> etc.

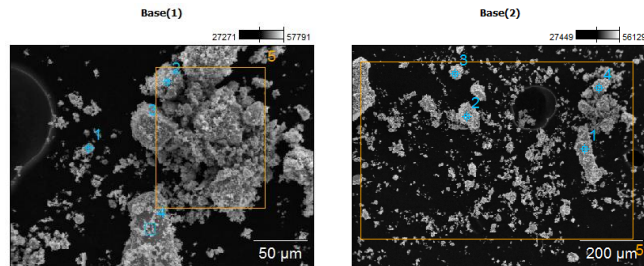
#### 4.1.4 Conclusions

We have studied the effects of crystalline domain size on the TE properties using experimental analyses and first-principles simulations. A CTS powder was produced from elemental powders (Cu, Sn, and S) by high-energy reactive ball milling, and subsequently, high-density pellets were produced using SPS. This method adds a distinct advantage

by maintaining the nanostructure while reaching the required high density. Rietveld refinement of the XRD patterns revealed average domain sizes below 50 nm for samples sintered under different conditions. Low-temperature SPS sintering of mechanically alloyed powders allows to maintain structural disorder of the CTS phase while resulting in nanostructured ceramics. This leads to extremely low lattice thermal conductivity. On the other hand, the sample with the smallest average domain size also presents the lowest resistivity and Seebeck coefficient, resulting in the highest  $PF$ . Experimental evidence suggests that  $S$  and  $\rho$  correlate with the sintering temperature, which induces stoichiometric deviations and different grain sizes. First-principles (DFT) simulations of three ordered and two disordered surfaces revealed the presence of dangling bonds and localized states near the Fermi level. DOS at the Fermi level was continuous, that is, band gap was absent, suggesting that CTS grain boundary is conductive. Formation energies for stoichiometric CTS, Cu-vacant, Cu-rich, Sn-vacant, and Sn-rich CTS are in the increasing order, implying that stoichiometric CTS is energetically the most favorable, followed by Cu-vacant and Cu-rich systems. The Cu-vacant, Cu-rich, and Sn-vacant systems increase the p-type behavior and carrier concentration, thus explaining the observed low resistivity of the sintered components. The samples with average domain sizes of  $12 \pm 10$ ,  $25 \pm 10$ , and  $37 \pm 10$  nm displayed figures of merit  $zT$  of 0.40, 0.17, and 0.14, respectively, around 673 K. The results presented here for various CTS surfaces, formation energies, and doping effects can be generalized to a broad family of Cu–Sn–S-based systems. Our synthesis method also provides an interesting route for many materials to synergistically tune their electrical and thermal properties.

### 4.1.5 Appendix

SEM-EDX data on 60-min milled CTS powder. Data collected on different parts of SEM grid.



Atomic %	C (±1%)	O (±1%)	S (±1%)	Cu (±1%)	Sn (±1%)
pt1	36.6	11.1	22.9	21.9	7.5
pt2	8.1	8.9	24.7	45.6	12.8
pt3	6.1	8.4	39.6	30.6	15.3
pt4	10.1	19.1	35	2.5	33.3
pt5	14.8	12.3	30.1	30.9	11.9
Atomic %	C (±1%)	O (±1%)	S (±1%)	Cu (±1%)	Sn (±1%)
pt1	No Data collected				
pt2	9.6	07.7	26.5	41.7	14.5
pt3	17.4	09.4	09.8	57.2	06.2
pt4	28.0	13.8	13.2	37.9	07.1
pt5	58.7	26.3	06.6	05.6	02.8

Figure 4.S1. SEM Micrographs and corresponding EDX data collected on 60-min milled powder from the different parts of SEM grid. Corresponding atomic % and errors are listed in table below.

Rietveld refinement was performed on XRD data collected on samples B and C.

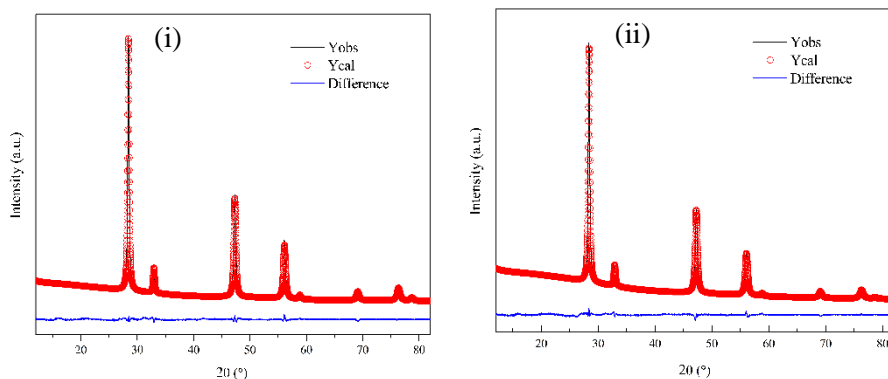


Figure 4.S2. Rietveld refinement data for samples (i) B and (ii) C, respectively.

EDX data for Figure 3 (i), 3(iii), and 3(iv), respectively.

Atomic %	Map	Spectrum 1	Spectrum 2	Spectrum 3
S	50,25	44,59	51,09	48,02
Cu	22,72	1,69	31,99	1,62
Sn	27,03	53,72	16,92	50,36
Total	100	100	100	100,01
	CTS	SnS	CTS	SnS
Ratio	Map	Spectrum 1	Spectrum 2	Spectrum 3
S/Sn	1,86	0,83	3,02	0,953
Cu/Sn	0,84		1,89	
Sn/Sn	1	1	1	1
	Sn-rich	SnS	CTS	SnS

Atomic %	Spetrum 1	Ratio	Spetrum 1
S	48,67	S/Sn	2,82
Cu	34,05	Cu/Sn	1,97
Sn	17,28	Sn/Sn	1
Total	100		
	CTS		CTS

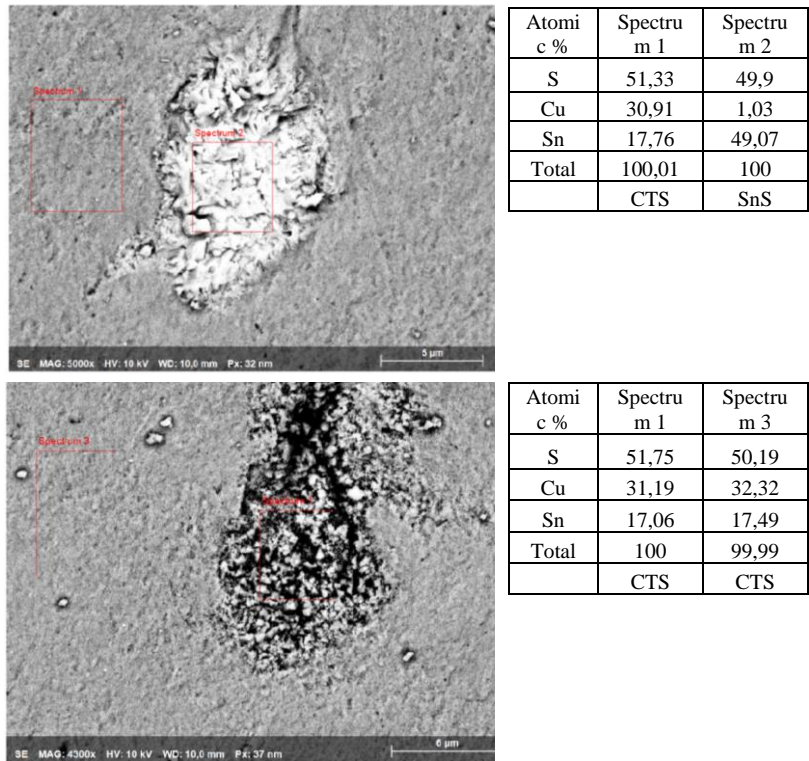
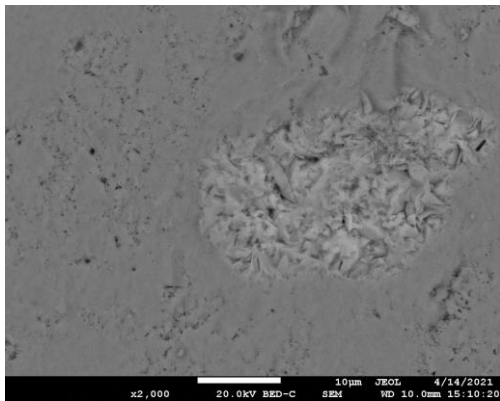


Figure S3. Morphological images and corresponding EDX data on unpolished Sample A.

Atomic %	Spetrum 1	Spetrum 2	Spetrum 3	Spetrum 4
	49,14	49,14	49,19	49,13
Cu	33,71	33,71	33,68	33,6
Sn	17,15	17,15	17,13	17,27
Total	100	100	100	100
	CTS	CTS	CTS	CTS
Ratio	Spetrum 1	Spetrum 2	Spetrum 3	Spetrum 4
S/Sn	2,86	2,87	2,84	2,84
Cu/Sn	1,96	1,96	1,94	1,94
Sn/Sn	1	1	1	1
	CTS	CTS	CTS	CTS

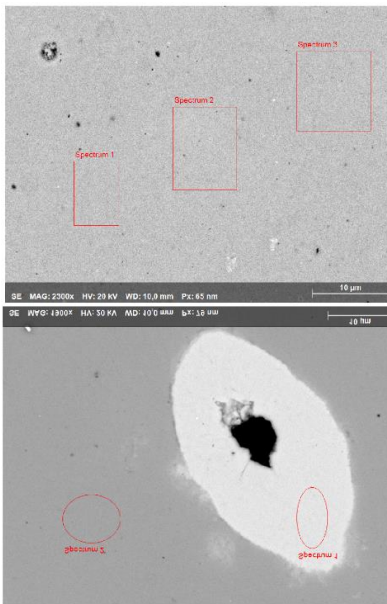
Table 4.S1. SEM-EDX data for Figure 4.3.

Comparative SEM-EDX data on unpolished and polished Sample A and B.



Atomic %	Spectrum 1	Spectrum 2
S	47,77	48,32
Cu	35,03	34,13
Sn	17,20	17,54
Total	100	99,99
	CTS	CTS

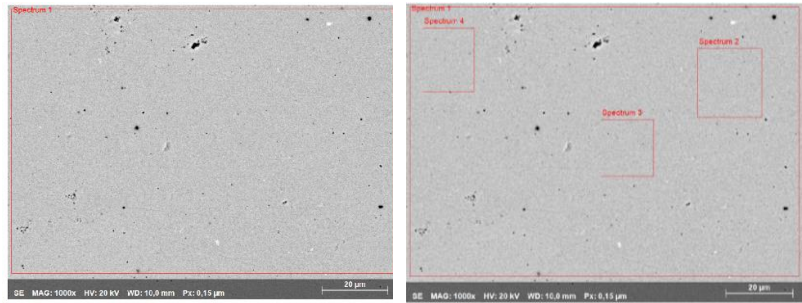
Figure S4. Morphological images and corresponding EDX data on unpolished Sample B.



Atomic %	Spectrum 1	Spectrum 2	Spectrum 3
S	48,61	48,75	48,67
Cu	34,26	33,89	34,03
Sn	17,13	17,37	17,3
Total	100	100,01	100
	CTS	CTS	CTS

	Spectrum 1	Spectrum 2
S	47,39	48,97
Cu	0	33,6
Sn	52,61	17,43
Total	100	100
	SnS	CTS

Figure 4.S5. Morphological images and corresponding EDX data on polished Sample A..



Atomic %	Spectrum 1	Ratio	Spectrum 1	Atomic %	Spectrum 1	Spectrum 2	Spectrum 3
S	49,15	S /Sn	2,85	S	49,14	49,14	49,19
Cu	33,61	Cu /Sn	1,95	Cu	33,71	33,71	33,68
Sn	17,24	Sn /Sn	1	Sn	17,15	17,15	17,13
Total	100			Total	100	100	100
	CTS		CTS		CTS	CTS	CTS

Figure 4.S6. Morphological images and corresponding EDX data on polished Sample B.

Temperature-dependent absolute Seebeck coefficient and resistivity for various CTS samples with increasing average domain size.

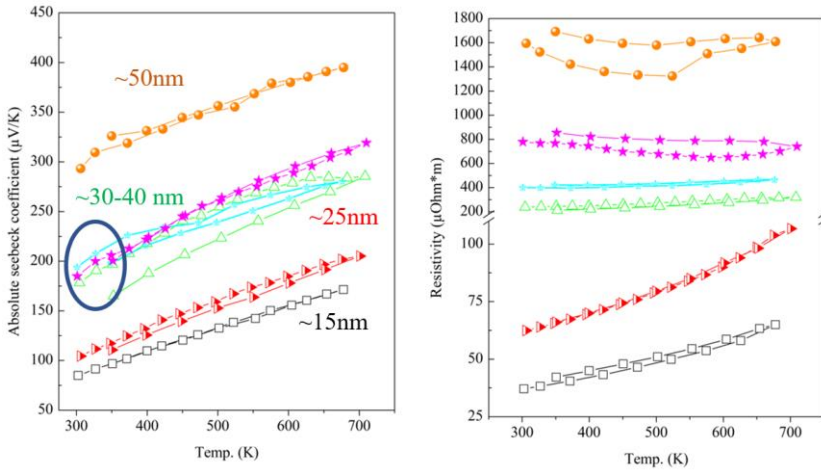


Figure 4.S7. Temperature dependent absolute Seebeck coefficient and resistivity data on many CTS samples with different average domain sizes.

The Density of States (DOS) for Stoichiometric, Cu-vacant, Cu-rich, Sn-vacant, and Sn-rich CTS systems.

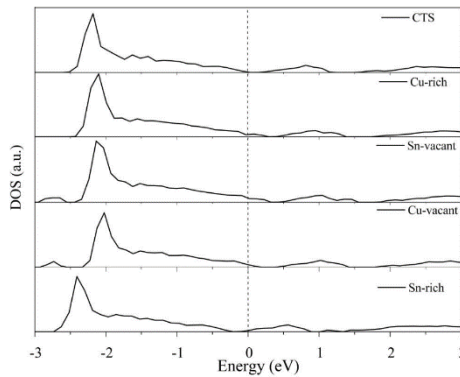


Figure 4.S8. DOS for Stoichiometric, Cu-vacant, Cu-rich, Sn-vacant, and Sn-rich CTS systems. Here the Fermi energy is set to zero. In the Cu-vacant and Sn-vacant systems, the vacancy is acting as acceptor states, it shifts the Fermi level inside the valence band. Alike, the Cu-vacant and Sn-vacant systems in the Cu-rich system, the Fermi energy shifts in the VB, reason being introduction of unfilled d-orbitals of Cu atom, in the place of Sn. However, in the case of the Sn-rich cell, the Fermi energy shifts towards the conduction band.

## 5 Ag substitution at the Sn Lattice Site

### 5.1 Synergistic optimization of thermoelectric properties of $\text{Cu}_2\text{SnS}_3$ via Ag substitution at Sn site

#### 5.1.1 Abstract

In the present work, a two-step synthesis method (mechanical alloying + spark plasma sintering, discussed in detail in Chapters 3 and 4) was combined with Ag substitution at Sn Site to improve the thermoelectric performance of CTS. Various  $\text{Cu}_2\text{Ag}_x\text{Sn}_{(1-x)}\text{S}_3$  ( $0.05 \leq x \leq 0.25$ ) samples were synthesized, and their thermoelectric properties were systematically investigated using experimental and first principles methods. Rietveld refinement of XRD data and SEM-EDX chemical maps confirmed successful Ag substitution in the Sn lattice site for  $x \leq 0.15$  samples. The  $x = 0.15$  sample presented  $\sim 10$  and  $\sim 3$  fold higher power factor than undoped CTS (Disordered CTS sample discussed in Chapter 2) and the smallest domain size CTS sample (Sample A discussed in Chapter 4), respectively. Although the  $x=0.125$  sample presented a lower power factor than the  $x = 0.15$ , due to its lower thermal conductivity, both  $x = 0.125$  and  $0.15$ , samples showed the highest  $zT \sim 0.5$  at 723 K, which is comparable to the results present in the literature for earth-abundant and eco-friendly thermoelectric materials.

The enhancement in  $zT$  is directly linked to the bandgap reduction, which was investigated by experimental and *ab-initio* methods. Moreover, the formation energy calculations showed the reason behind the structural transformation in CTS and similar diamond-like structures towards high symmetry polymorphs via external doping.

#### 5.1.2 Introduction

Heat is a low-grade energy source and a common by-product in almost all power generation and transmission processes. Thermoelectric (TE) devices are solid-state, scalable, and noise-free, and they can convert waste heat into electrical energy. TE devices consist of several pairs of

*p*- and *n*-type semiconducting legs connected electrically in series and thermally in parallel. Heat to electrical energy conversion of such a device is assessed by Carnot efficiency ( $\eta$ ).<sup>7</sup> (Equations taken from Chapter 1.)

$$\eta = \left( \frac{T_{hot} - T_{cold}}{T_{hot}} \right) \left[ \frac{\sqrt{(1 - zT_{avg})} - 1}{\sqrt{(1 + zT_{avg})} + \left( \frac{T_{cold}}{T_{hot}} \right)} \right] \quad 1.1$$

$$zT = \left( \frac{S^2}{\rho\kappa} \right) T \quad 1.2$$

Where  $T_{hot}$ ,  $T_{cold}$ , and  $zT_{avg}$  are hot-side temperature, cold-side temperature, and average TE figure of merit, respectively. TE figure of merit of a material is defined in equation 1.2, where  $S$ ,  $\rho$ ,  $\kappa$ , and  $T$  are Seebeck coefficient, electrical resistivity, thermal conductivity, and absolute temperature, respectively. Thus, *p*- and *n*-type materials presenting a high figure of merit are essential to produce high-performing TE devices. However, various physical properties determining  $zT$  of materials show strong interdependency, limiting its enhancement. Many strategies to enhance the  $zT$  of material are discussed in the literature, such as nanostructuring<sup>39</sup>, alloying<sup>42</sup>, band engineering,<sup>46</sup> energy-filtering<sup>11</sup>, etc.

Cu<sub>2</sub>SnS<sub>3</sub> is a non-toxic, eco-friendly, and low-cost thermoelectric material. Although the first lab synthesized and naturally discovered CTS had a triclinic (*P1*) structure,<sup>25</sup> authors have diffusely reported monoclinic (*Cc*) CTS synthesized by high temperate solid-state reactions from a thermoelectric perspective. Frequently, a blend of cubic (*F-43m*) and tetragonal (*I-42m*) CTS polymorphs can be observed with monoclinic CTS. The monoclinic CTS polymorph shows low  $zT \sim 0.05$  above 700 K due to its low carrier concentration and high thermal conductivity. However, external cation doping at the Sn site transforms the monoclinic polymorph into cubic (*F-43m*). It is worth mentioning that partially (SG: *I4̄2m*) or fully (SG: *F-43m*) disordered CTS polymorphs can also be obtained by synthesis methods, e.g. colloidal method<sup>112</sup> and high-energy reactive ball milling<sup>42</sup>. Polymorphism in these materials offers multiple possibilities of structural manipulation and band engineering to boost the TE performance. Moreover, Cu-Sn-S-based systems have low formation energy; therefore, they are suitable

for large-scale and low-cost production. These systems are safe to use in the medium temperature range due to the high melting temperature (~1000 K).

Generally, crystalline materials arrange their atoms regularly and periodically in three dimensions or over a long range. However, various crystalline materials present complex crystallographic structures, where long-range order is absent, also known as disordered materials. The disordered materials are mainly characterized by structural disorder induced by partial occupancy of cations in the unit cell and/or local deviation from the periodic arrangement. These materials can be utilized to achieve so-called Phonon-Glass-Electron-Crystal (PGEC) characteristics. Disordered polymorphs of  $\text{Cu}_2\text{SnS}_3$ <sup>71</sup>,  $\text{Cu}_2\text{SnSe}_3$ <sup>27</sup>,  $\text{CuFeS}_2$ <sup>28</sup>,  $\text{Cu}_5\text{Sn}_2\text{S}_7$ <sup>29</sup>,  $\text{Cu}_7\text{Sn}_3\text{S}_{10}$ <sup>30</sup>,  $\text{Cu}_2\text{ZnSnS}_4$ <sup>144</sup>, and numerous other materials show remarkably suppressed thermal conductivity than their ordered polymorphs. It has been verified by experimental and ab-initio methods that the above discussed cubic materials also present higher Grüneisen parameters, which is a measure of anharmonicity, in comparison with their ordered polymorphs. Lattice distortions, irregular bond length, and soft bonds cause higher anharmonicity, originating from structural disorder. Moreover, the low electronegativity difference and high covalent character of its bonds and band tailing<sup>32</sup> enhance the electronic transport properties.

Ag is the most conductive metal. However, in a thermoelectric perspective, Ag-doping has been used to enhance ( $\text{SnSe}$ <sup>145</sup>,  $\text{Cu}_2\text{SnZnS}_4$ <sup>146</sup>,  $\text{Cu}_2\text{SnSe}_3$ <sup>27</sup>, etc.) and reduce ( $\text{Cu}_2\text{Se}$ <sup>147</sup>,  $\text{Cu}_2\text{Te}$ <sup>147</sup>,  $\text{SnTe}$ <sup>148</sup>, etc.) the carrier concentration, depending on whether the materials have high or low carrier density. In 1970, Ag-containing  $\text{Cu}_2\text{Se}$  based materials were considered a potential candidate for radioisotope TEG.<sup>149</sup> At RT, Ag-doped  $\text{Cu}_2\text{Se}$  shows multiple phases. However, it transforms its crystallographic structure into the cubic phase when sintered above 410 K.<sup>149</sup>

Sharma et al.<sup>146</sup> have studied TE properties of Ag nanoparticles blended in  $\text{Cu}_2\text{ZnSnS}_4$  (CZTS) microsphere via microwave method followed by hot pressing. They observed that Ag nanoparticles were mainly a secondary phase in the materials, acting as a bridge between CZTS grain for electrical transport and scattering center for phonons. Overall,

Ag mixed CZTS present a maximum  $zT = 0.14$  at 623 K. Cheng et al.<sup>150</sup> investigated Ag substitution at Cu site in a similar  $\text{Cu}_2\text{SnSe}_3$  system, which resulted in a  $zT \sim 1$  at 800 K. They extended the study by simultaneous In-doping at Sn site and introduction of  $\text{Ag}_2\text{S}$ , forming a  $\text{Cu}_{1.85}\text{Ag}_{0.15}\text{Sn}_{0.91}\text{In}_{0.09}\text{Se}_3 / 4\% \text{Ag}_2\text{S}$  composite. The combined effect of band structure engineering (via doping) and microstructural engineering (via  $\text{Ag}_2\text{S}$ ) enhanced its  $zT$  to 1.58 at 800K, which is two-fold higher than  $\text{Cu}_2\text{SnSe}_3$ . Moreover, Mehmood et al.<sup>151</sup> reported a 2.5 times increase in the  $zT$  of  $\text{Cu}_2\text{ZnSnSe}_4$  by Ag alloying.

The present work combines a two-step high-density thermoelectric sample preparation method (high-energy reactive ball-milling followed by Spark Plasma Sintering (SPS))<sup>152</sup> with Ag substitution at Sn site in CTS. Various  $\text{Cu}_2\text{Ag}_{(x)}\text{Sn}_{(1-x)}\text{S}_3$  ( $0.05 \leq x \leq 0.25$ ) samples were prepared, and their thermoelectric properties were systematically investigated. It is well known that the holes in CTS and similar systems ( $\text{Cu}_2\text{SnZnS}_4$ ,  $\text{Cu}_2\text{SnZnSe}_4$ ,  $\text{Cu}_2\text{SnSe}_3$ , etc.) are generated by unfilled Cu  $3d$  orbital. The maximum contribution to the DOS comes from Cu  $3d$  orbital, followed by S  $3p$  orbital, and the contribution of Sn  $5s$  orbital is minimal. The Sn atoms contribute minimally to electronic transport. Thus, an effort has been presented to improve the thermoelectric properties of CTS using Ag substitution at the Sn site.

### 5.1.3 Experimental methods

$\text{Cu}_2\text{Ag}_{(x)}\text{Sn}_{(1-x)}\text{S}_3$  ( $x=0.05, 0.10, 0.15, 0.20,$  and  $0.25$ ), powder samples were synthesized from elemental powders using high energy ball milling (Fritsch P4). Elemental powder of Cu, Ag, Sn, and S were fed in WC vials in stoichiometric ratio and milled for three hours, producing ~6 g powder sample (Rotation and spinning speed of 1080 rpm and 300 rpm, respectively).

The as-milled powder was sintered at 400°C for 10-15 min under 50 MPa pressure using SPS equipped with WC die. A boron nitrate layer was applied to the as-milled power to avoid current passing through the sample and contamination from the die.

Structural, microstructural, and chemical information on the samples were collected by combining results from X-ray Diffraction (XRD), Scanning Electron Microscopy (SEM), and Energy-Dispersive X-ray spectroscopy (SEM-EDX) analysis. The XRD patterns were collected in Bragg–Brentano geometry using a Bruker D8 (Bruker, Billerica, MA, USA) diffractometer equipped with a Co K $\alpha$  ( $\lambda = 1.7889 \text{ \AA}$ ) source. SEM-EDX measurements were performed using a Jeol IT300 (Jeol, Ltd., Japan) scanning electron microscope. Rietveld refinement<sup>55,153</sup> was performed on XRD data using WPPM modeling<sup>56</sup> as implemented in TOPAS 6<sup>57</sup> software.

Thermoelectric properties were investigated by temperature-dependent (323–723 K) resistivity, Seebeck coefficient, and thermal diffusivity measurements. Linseis Messgeraete GmbH's LSR-3 was used for Seebeck coefficient and resistivity measurements, whereas LFA-500 was used to measure the thermal diffusivity.

The optical absorption spectra on various CTS samples were collected using a UV-VIS-NIR spectrophotometer equipped with a 150 mm integrating sphere (PerkinElmer spectrophotometer, LAMBDA 750). The measurement was performed on a  $\sim 0.10$  g ground sample dispersed in  $\sim 40$  ml ethanol and sonicated for four hours.

### 5.1.4 Computational methods

The first principles calculations were performed using DFT code Vienna ab initio simulation package.<sup>85</sup> The generalized gradient approximation with Perdew–Burke–Ernzerhof<sup>87</sup> electron exchange–correlation was used for the Self-Consistent Field (SCF) calculations. The interaction between electrons–ions was described using the Projector-Augmented-Wave (PAW) method.

The calculations were performed on a 72-atom (24-Cu, 12-Sn, and 36-S) CTS supercell. Additionally, two more supercells were modeled. At first, a single Sn atom was replaced by Ag; in second, Ag atoms replaced 2 Sn atoms. These supercells are represented as CTS, CTS1, and CTS2, respectively.

The charge density and wavefunction obtained with the SCF calculations were then used to perform the Density of States (DOS) calculations with Heyd-Scuseria-Ernzerhof (HSE06)<sup>154</sup> potential. The cut-off energy for the plane-wave-basis set to 400 eV. The electronic convergence was set to  $10^{-6}$  eV for DOS calculations. Brillion zone sampling was performed on a  $k$ -mesh grid of  $4 \times 4 \times 4$  centered at the gamma point. Furthermore, the formation energy calculations were performed on the above-discussed supercells.

### 5.1.5 Results and discussions

XRD data was collected in Bragg-Brentano ( $\theta/2\theta$ ) geometry on all the  $\text{Cu}_2\text{Ag}_{(x)}\text{Sn}_{(1-x)}\text{S}_3$  ( $x=0.05, 0.10, 0.15, 0.20,$  and  $0.25$ ) samples (Shown in Figure 5.1). Samples with different weight percentages of Ag showed cubic Sphalerite-like phase, characterized by (111), (200), (220), and (311) Bragg peaks at  $2\theta \sim 33.5^\circ, 38.7^\circ, 55.8^\circ,$  and  $66.9^\circ$ , respectively. We do not observe additional Bragg peaks for Ag in XRD patterns, implying Ag substitution with different weight fractions was successful, and  $\text{Cu}_2\text{Ag}_{(x)}\text{Sn}_{(1-x)}\text{S}_3$  samples belong to the disordered cubic phase (lattice parameter shown Figure 5.2 (b)). Moreover, with the increased amount of Ag substitution, Bragg peaks show a shift towards higher  $2\theta$  or decreased interplanar spacing (See insert Figure 5.1).

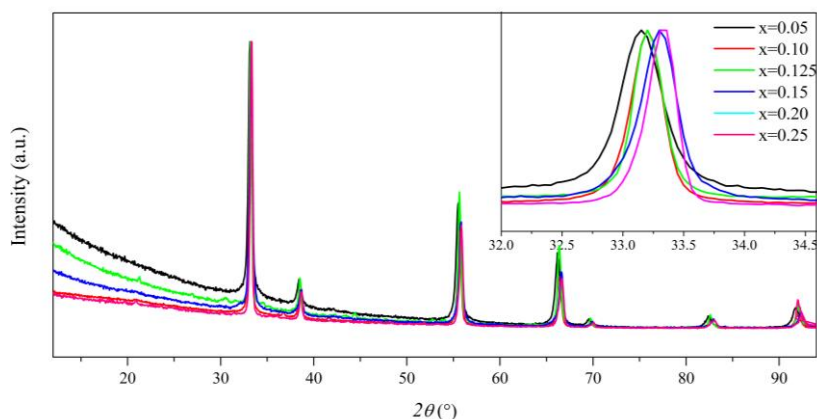


Figure 5.1. XRD data on  $\text{Cu}_2\text{Ag}_{(x)}\text{Sn}_{(1-x)}\text{S}_3$  samples insets show the highest intensity Bragg peak shift with increased Ag substitution.

The information on structure, lattice parameters, strain, and domain size were extracted using Rietveld refinement (shown in figure 5.2 (a)). The lattice parameters have shown a decrease up to  $\text{Cu}_2\text{Ag}_{(x)}\text{Sn}_{(1-x)}\text{S}_3$  ( $x=0.20$ ), and then saturation, possibly reaching the solubility limit of Ag substitution in the CTS system. Due to the smaller atomic radii of Ag as compared to Sn, the shrinking of lattice parameters with increased Ag substituted can be observed (shown in Figure 5.2 (b)). The average domain size of the samples is  $\sim 50$  nm. And no significant microstrain was observed for the samples.

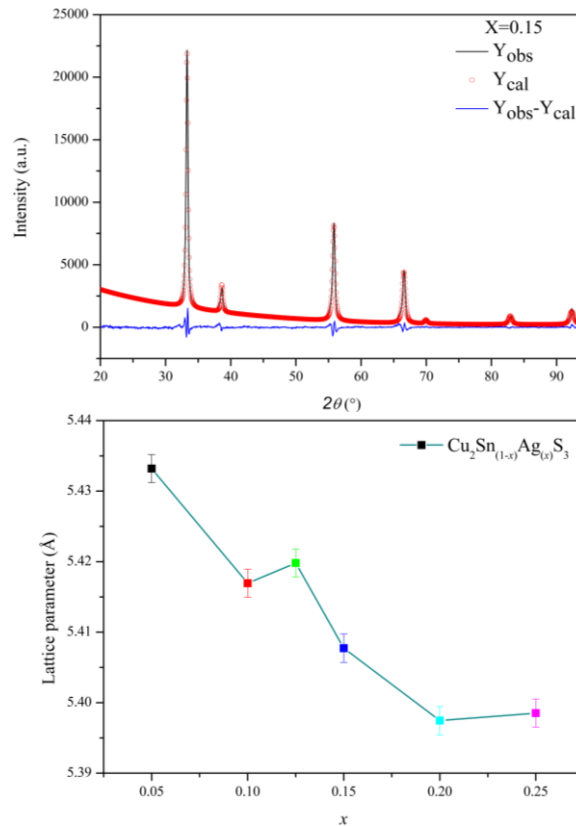


Figure 5.2 (a). Rietveld refinement performed on  $x=0.15$  sample, (b) change in lattice parameters with increased Ag substitution. (Rietveld refinement data on all CATS samples are shown in Figure S2).

SEM Micrographs and SEM-EDX analysis on samples surfaces showed dense microstructure with almost no porosity. The grains of the samples are much smaller than the magnification of the microscope (shown in Figure 5.S1). Chemical maps were collected, Cu, Sn, and S showed a homogeneous chemical distribution for all the samples. However,

samples with  $x \geq 0.20$  showed a non-homogeneous chemical distribution of Ag (Shown in Figure 5.3.). The chemical maps on various CTS samples also confirm the Rietveld refinement results,  $x < 0.20$ , Ag substitution was successful in the lattice. However, for  $x = 0.20$  and  $0.25$ , lattice parameters do not decrease. Chemical maps also show the non-homogeneous distribution of Ag is in the materials, implying some Ag has substituted Sn in lattice and rest in the bulk material. A similar observation was made by Sharma et al.,<sup>146</sup> for  $\text{Cu}_2\text{SnZnS}_4$  on adding Ag nanoparticles.

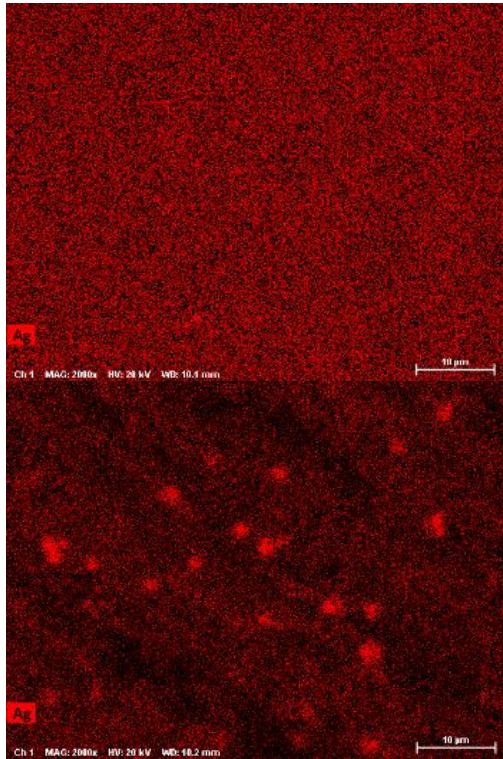


Figure 5. 3. Chemical maps collected using SEM-EDX on  $\text{Cu}_2\text{Ag}_{(x)}\text{Sn}_{(1-x)}\text{S}_3$  samples. Showing a homogeneous and non-homogeneous Ag substitution on (a)  $x \leq 0.15$  and (b)  $x \geq 0.20$  sample, respectively. (Elemental maps on all elements are shown in Figure 5.S3.)

Temperature-dependent thermoelectric measurement of  $\text{Cu}_2\text{Ag}_{(x)}\text{Sn}_{(1-x)}\text{S}_3$  ( $0.05 \leq x \leq 0.25$ ) samples are shown in Figure 5.4. All the CTS samples show *p*-type, degenerate semiconductor-like behavior, confirmed by the positive value of the Seebeck coefficient and increasing resistivity in temperature. With the increased Ag substitution, CTS has shown decreasing absolute Seebeck coefficient due to increased carrier concentration. For  $x = 0.05 - 0.15$ , samples

resistivity has also decreased with increasing Ag substitutions. However,  $x = 0.20$  and  $0.25$  samples show anomalous values, likely caused by the interplay between carrier concentration and mobility, as these samples have some Ag present in the lattice and rest in bulk.

The unreacted Ag grains in bulk would introduce free electrons in the system. However, we do not observe any sharp decrease in  $S$  and simultaneous increase in  $\rho$  at elevated temperatures, an effect of bipolar conduction. In such cases, the thermopower ( $S$ ) is a weighted average of Seebeck coefficients associated with both types of carriers. Opposite signs of both charge carriers diminish the thermopower of the material. However, the  $x = 0.25$  and  $0.20$  samples show  $S \sim 20 - 40 \mu\text{V/K}$  and  $S \sim 30 - 60 \mu\text{V/K}$  in the temperature range 300-723 K, which is one order of magnitude lower than undoped CTS<sup>155</sup> prepared using various synthesis and sintering techniques. It is worth mentioning here that with a small amount of external doping,  $x = 0.05$ , the  $S$  was 100-200  $\mu\text{V/K}$  in the same temperature span, which is comparable to the literature.<sup>37</sup>

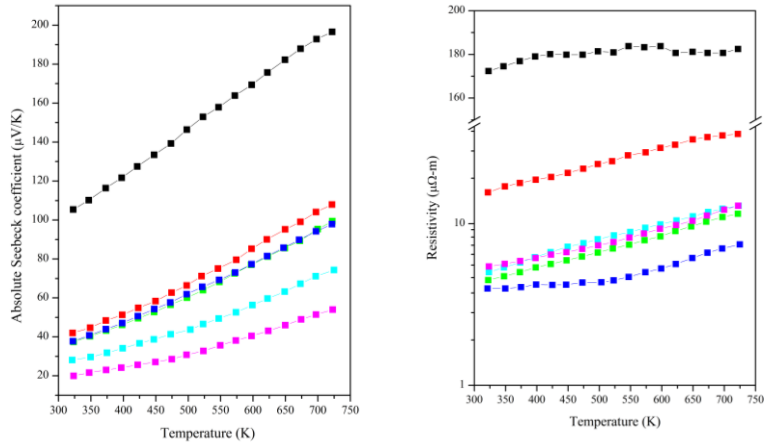


Figure 5.4. Temperature-dependent Absolute Seebeck Coefficient ( $S$ ), resistivity ( $\rho$ ) measurements on  $\text{Cu}_2\text{Ag}_x\text{Sn}_{(1-x)}\text{S}_3$  ( $0.05 \leq x \leq 0.25$ ) samples.

The temperature dependence of electrical resistivity of  $\text{Cu}_2\text{Ag}_x\text{Sn}_{(1-x)}\text{S}_3$  ( $0.05 \leq x \leq 0.25$ ) samples is shown in Figure 5.3 (b). Even with the lowest Ag ( $x=0.05$ ) substitution, CTS samples showed a non-degenerate or metal-like nature of resistivity.

The electronic DOS was calculated to validate the experimentally observed results, see Figure 5.5. The experimental results showed that the increased Ag content in the prepared samples leads to a decrease in

the  $S$  value, and  $\rho$ . This can be explained by considering that Cu, Sn, and S's oxidation state in CTS is +1, +4, and -2, respectively. Therefore, the non-isoelectronic replacement of Sn by Ag atom would give rise to additional holes in the system, enhancing the valence band edge.

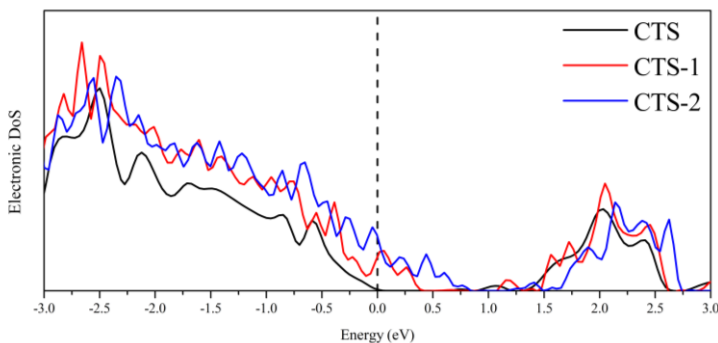


Figure 5.5. Calculated DOS on monoclinic CTS, and 1 Ag atom and 2 Ag atom substituted CTS systems, shown as CTS, CTS-1, and CTS-2, respectively. Here, the dotted line represents the Fermi level, set at zero. The Atomic projected DOS for all calculated structures are shown in Appendix Figure 5.S5.

The DOS of CTS and Ag substituted CTS systems is higher at the valence side than the conduction, confirming the  $p$ -type nature of all calculated supercells. The Valence Band (VB) edge shifted toward higher energy with the increased Ag-content. The Fermi level lies deep inside the VB for Ag substituted systems, with a shift of the Fermi level inside the valence band increasing with the substitution. Thus, the increased substitution of Ag in the lattice would enable a more degenerate semiconductor-like nature in CTS and other similar systems, such as  $\text{Cu}_2\text{SnZnS}_4$ <sup>146</sup>,  $\text{CuFeS}_2$ <sup>156</sup>,  $\text{Cu}_2\text{SnSe}_3$ <sup>157</sup>, etc.

The optical absorption spectrums were collected on  $\text{Cu}_2\text{Ag}_{(x)}\text{Sn}_{(1-x)}\text{S}_3$  ( $x=0.05, 0.10, 0.15, 0.20,$  and  $0.25$ ) samples. These measurements were performed on a  $\sim 0.10$  g ground sample, dispersed in  $\sim 40$  ml ethanol (Shown in Appendix 5.S4). Figure 5.6 shows the estimated bandgap ( $E_g$ ) by linear extrapolation in the Tauc plot, using the equation  $ah\nu = A(h\nu - E_g)^{1/2}$ , where  $\alpha$ ,  $h$ ,  $\nu$ ,  $A$ , and  $E_g$  are absorption coefficient, Planck constant, frequency, transmission constant, and bandgap, respectively. These measurements are qualitatively in agreement with the calculated DOS, and increased Ag substitutions have reduced the bandgap.

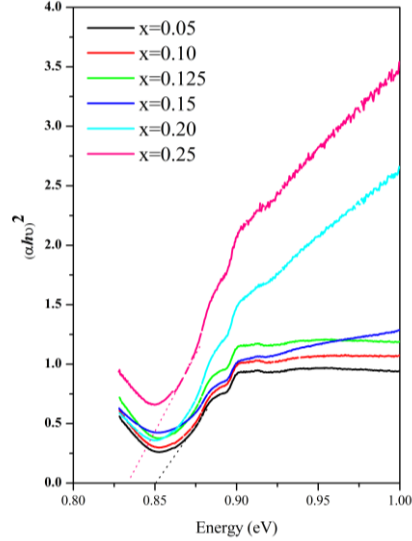


Figure 5.6. Bandgap measurements performed on various  $\text{Cu}_2\text{Ag}_x\text{Sn}_{(1-x)}\text{S}_3$  ( $0.05 \leq x \leq 0.25$ ) samples.

Undoped ordered and disordered CTS band gap values from the literature are  $\sim 0.99$  and  $\sim 0.95$  eV, respectively.<sup>71</sup> However, the  $x = 0.05$  sample showed a lower bandgap of  $\sim 0.85$  eV, which further decreased with increased Ag substitution (shown in Figure 5.6).

An essential aspect of external doping in the CTS system is the structural transformation from a monoclinic to a disordered cubic phase, which means a tendency toward higher symmetry. To understand this, additional DFT calculations were performed to calculate the formation energy of the 2 doped systems with respect to the monoclinic system. Table 5.1 reports the formation energy calculated for the three systems.

Table 5.1. The formation energy of CTS and AG-doped CTS systems.

System	Configuration	The energy of the system (eV)	Formation energy (eV)
CTS	Cu-24, Sn 12, S-36	-308.037	-24.117
CTS 1	Cu-24, Ag-1, Sn, 11, S-36	-305.925	-23.135
CTS 2	Cu-24, Ag-2, Sn, 10, S-36	-303.680	-22.020

Formation energy calculations confirm that the monoclinic CTS structure is the most stable, with the lowest formation energy. The

introduction of Ag at the Sn site increases the formation energy, making the Ag-doped systems less stable in monoclinic form. Therefore, external doping drives the system toward higher symmetry structures, or in some cases, disordered polymorphs in CTS and various similar diamond-like materials.<sup>13,34,36,41,71,158</sup>

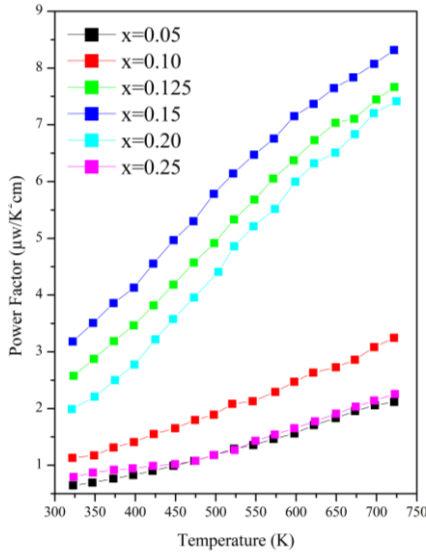


Figure 5.7. Temperature-dependent power factor ( $PF$ ) calculated as  $PF=S^2/\rho$  for  $\text{Cu}_2\text{Ag}_{(x)}\text{Sn}_{(1-x)}\text{S}_3$  ( $0.05 \leq x \leq 0.25$ ) samples.

The power factor ( $PF \sim 8.5 \mu\text{w}/\text{K}^2\text{cm}$ ) for the  $x = 0.15$  sample is highest, comparable to the literature for a similar system. It is worth mentioning that the  $PF$  for the  $x = 0.15$  sample is  $\sim 10$  and  $\sim 3$  fold higher than, respectively, undoped monoclinic CTS and disordered CTS with the smallest domain size, i.e., 12nm, discussed in Chapter 4. Similar  $\text{Cu}_3\text{SnS}_4$ ,<sup>140</sup>  $\text{Cu}_5\text{Sn}_2\text{S}_7$ , and  $\text{Cu}_7\text{Sn}_3\text{S}_{10}$ <sup>30</sup> systems also show similar  $PF$ . The highest  $PF$  of  $x = 0.15$  sample is followed by  $x = 0.125$  and  $x = 0.20$ , with  $PF$  values  $\sim 7.5$  and  $7.3 \mu\text{w}/\text{K}^2\text{cm}$ , respectively. The  $x = 0.10$  sample showed intermediate  $PF \sim 3.0$  at 723K. However,  $x = 0.25$ , and  $0.05$  samples presented the lowest  $PF \sim 1.75 \mu\text{w}/\text{K}^2\text{cm}$  at the same temperature.

The highest  $PF$  of  $x = 0.15$  sample is supported by its moderate Seebeck coefficient and extremely low electrical resistivity, which is highest among all  $\text{Cu}_2\text{Ag}_{(x)}\text{Sn}_{(1-x)}\text{S}_3$  ( $x = 0.05, 0.10, 0.15, 0.20,$  and  $0.25$ ) samples. Although the  $x = 0.25$  sample also has lower electrical

resistivity, the extremely suppressed Seebeck coefficient diminishes the power factor, making it the same as the lowest doped  $x = 0.05$  sample.

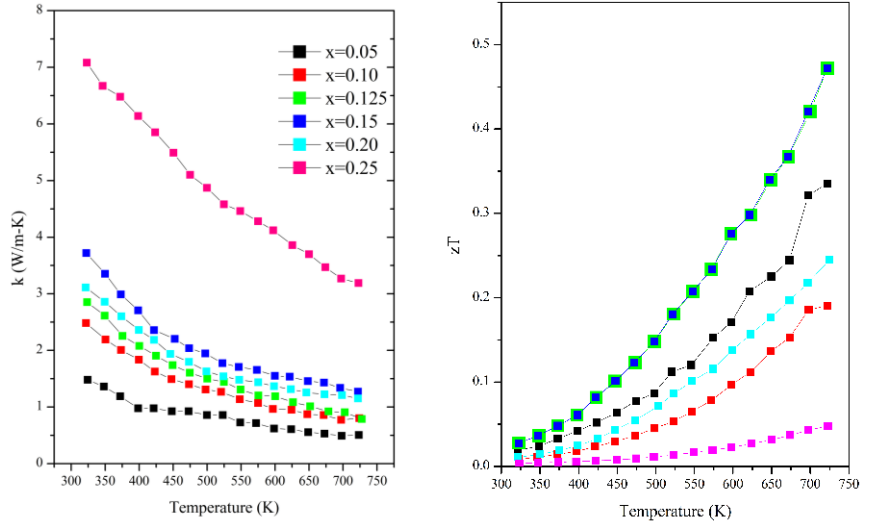


Figure 5.8. Thermal conductivity and figure of merit for  $\text{Cu}_2\text{Ag}_{(x)}\text{Sn}_{(1-x)}\text{S}_3$  ( $0.05 \leq x \leq 0.25$ ).

Ag substitution has significantly reduced the electrical resistivity of CTS, resulting in a higher  $PF$ . However, increased charge carrier density also increases the thermal conductivity of the samples. The thermal conductivity of  $\text{Cu}_2\text{Ag}_{(x)}\text{Sn}_{(1-x)}\text{S}_3$  ( $x = 0.05, 0.10, 0.15, 0.20,$  and  $0.25$ ) samples grows with increasing Ag substitution (Figure 5.8). The decreasing trend of  $\kappa$  with temperature shows increased phonon-phonon or Umklapp scattering.

The  $x = 0.05$  sample showed the lowest  $\kappa \sim 0.6$  W/m-K and the  $x = 0.10$  and  $0.125$  samples showed a similar  $\kappa \sim 1.0$  at 723K. The sample with the highest  $PF$  ( $x = 0.15$ ) showed a further increase in  $\kappa \sim 1.3$  W/m-K at the same temperature. However, the  $x = 0.25$  sample showed the highest  $\kappa \sim 7-4$  W/m-K in temperature span 300-723 K, which is  $\sim 10$  fold higher than the  $x = 0.05$  sample. As observed from SEM-EDX and chemical maps,  $x = 0.25$  samples showed the presence of Ag grains in bulk, which introduces free electrons in the system. In such a case, where both types of charge carriers are present in the materials, additional bipolar terms significantly increase the material's thermal conductivity.

Overall,  $x = 0.15$  and  $0.125$  samples show the highest  $zT \sim 0.5$  at 723 K. Although,  $x = 0.125$  has a slightly lower  $PF \sim 7.5$   $\mu\text{w}/\text{K}^2\text{cm}$  than  $x = 0.15$  ( $PF \sim 8.5$   $\mu\text{w}/\text{K}^2\text{cm}$ ) sample, the lower thermal conductivity of  $x = 0.125$  samples increases its  $zT$ . The highest  $zT$ , of  $x = 0.15$  and  $x =$

0.125 samples was followed by second highest  $zT \sim 0.3$  for the  $x = 0.05$  sample. Other samples,  $x = 0.20$  and  $x = 0.10$  showed  $zT \sim 0.25$  and  $zT \sim 0.10$ . However, sample containing highest amount of Ag ( $x = 0.25$ ) present lowest  $zT \sim 0.05$ , due to its extremely high thermal conductivity and low Seebeck Coefficient.

### 5.1.7 Conclusions

Herein, various Ag substituted disordered  $\text{Cu}_2\text{Ag}_{(x)}\text{Sn}_{(1-x)}\text{S}_3$  ( $0.05 \leq x \leq 0.25$ ) polymorph samples were stabilized by a two-step synthesis method, and experimental and computational methods were employed to study their thermoelectric properties. Rietveld refinement of XRD patterns and SEM-EDX chemical maps confirmed successful Ag substitution at Sn site up to  $x \leq 0.15$ . For samples  $x \geq 0.20$ , some Ag substituted Sn in the lattice; the rest was diffusely distributed in bulk. The  $\text{Cu}_2\text{Ag}_{(x)}\text{Sn}_{(1-x)}\text{S}_3$ ,  $x = 0.15$  sample presented  $\sim 10$ -fold higher  $PF$  ( $\sim 8.5 \mu\text{w}/\text{K}^2\text{cm}$ ) than that reported for monoclinic CTS. However, due to the interplay between  $\kappa$  and  $PF$ ,  $x = 0.125$  and  $x = 0.15$  showed the highest  $zT \sim 0.5$ , at 723 K. First principle DFT simulations revealed suppression of bandgap with increased Ag substitution at Sn site. The optical absorption spectra measurements on various  $\text{Cu}_2\text{Ag}_{(x)}\text{Sn}_{(1-x)}\text{S}_3$  confirm the DFT results. The formation energy of CTS increased with Ag substitution, making it less stable in monoclinic form than the undoped system, leading to the structural transformation toward high symmetry cubic and disordered polymorph. The two-step sample preparation method combined with doping is relatively cheap, as it does not require thermal treatment at very high temperatures. The results present in this work should also hold for other diamond-like materials, such as  $\text{Cu}_3\text{SnS}_4$ ,  $\text{Cu}_2\text{SnSe}_3$ ,  $\text{Cu}_2\text{SnZnS}_4$ ,  $\text{Cu}_2\text{SnZnSe}_4$ ,  $\text{Cu}_5\text{Sn}_2\text{S}_7$ ,  $\text{CuFeS}_2$ , etc.

## 5.1.8 Appendix

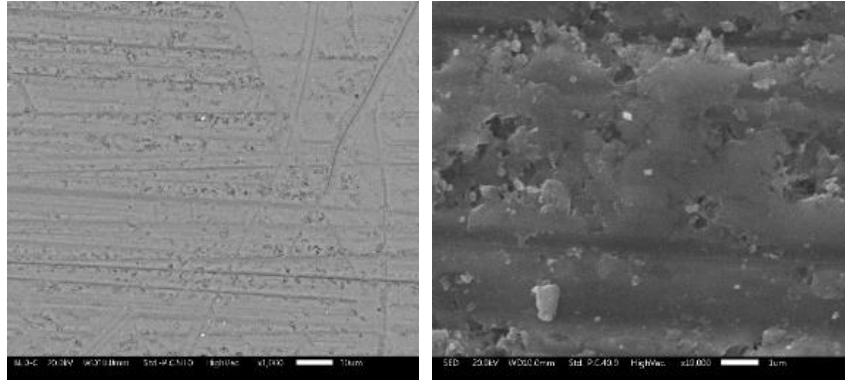
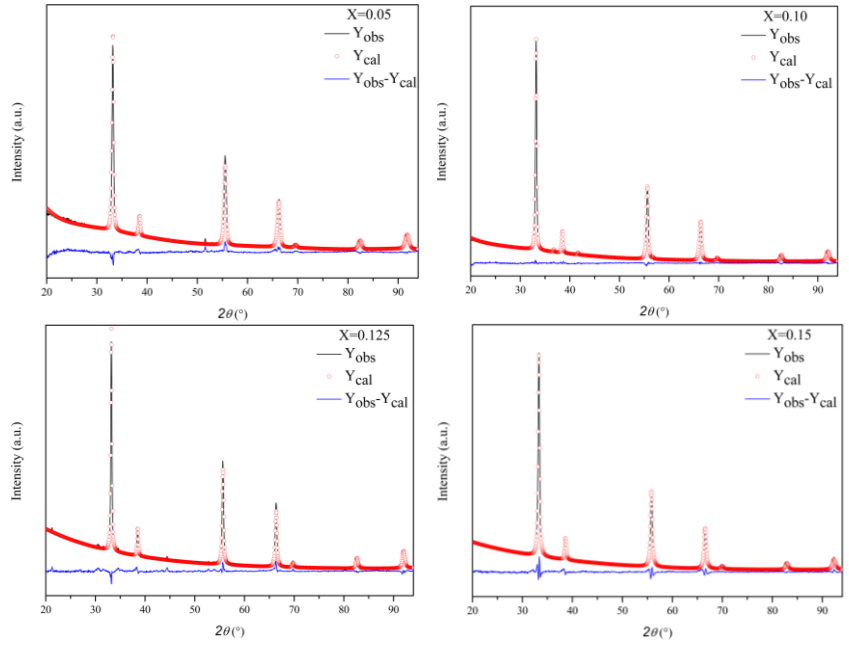


Figure 5.S1. Morphological image on  $\text{Cu}_2\text{Ag}_{(x)}\text{Sn}_{(1-x)}\text{S}_3$  samples in different magnification, showing dense microstructure with almost no porosity. Moreover, the grains of the samples are much smaller than the microscope's magnification.



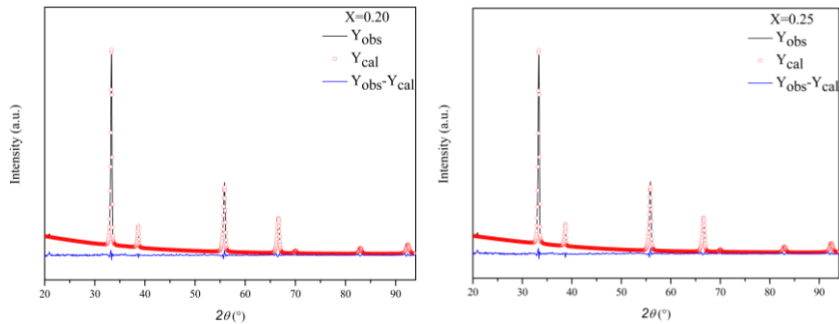


Figure 5.S2. Rietveld refinement data on  $\text{Cu}_2\text{Ag}_x\text{Sn}_{(1-x)}\text{S}_3$  ( $x = 0.05, 0.10, 0.15, 0.20,$  and  $0.25$ ) samples.

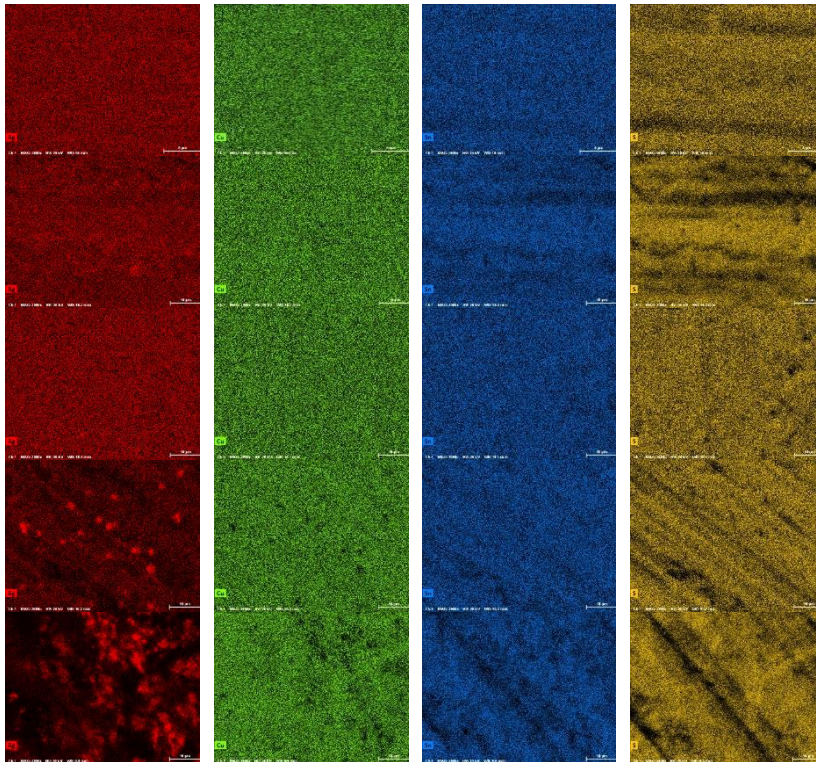


Figure 5.S3. Chemical maps collected on  $\text{Cu}_2\text{Ag}_x\text{Sn}_{(1-x)}\text{S}_3$  samples ( $x = 0.05, 0.10, 0.15, 0.20,$  and  $0.25$ ), respectively. Chemical maps for Cu (Green), Sn (Blue), and S (Yellow) are homogeneous for all the samples. However,  $x \leq 0.20$  samples show a non-homogeneous Ag (Red) distribution.

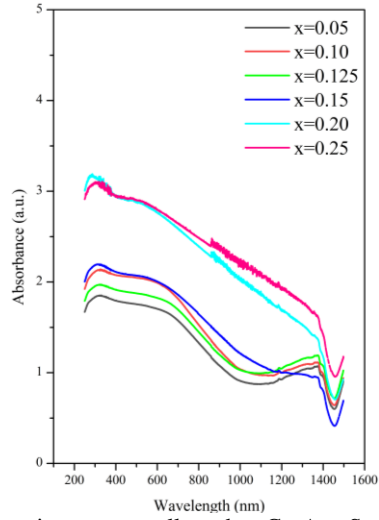


Figure 5.S4. optical absorption spectra collected on  $\text{Cu}_2\text{Ag}_x\text{Sn}_{(1-x)}\text{S}_3$  ( $x = 0.05, 0.10, 0.15, 0.20,$  and  $0.25$ ) samples.

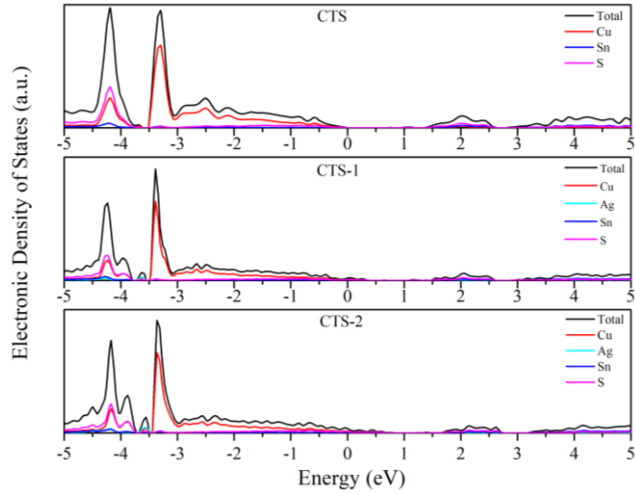


Figure 5.S5. Atomic projected Density of States (DOS) plot for monoclinic CTS, and 1 Ag atom and 2 Ag atom substituted CTS systems, shown as CTS, CTS-1, and CTS-2, respectively. Here, the Fermi level is set at zero.

## 6 Chalcogenide Based Thermoelectric Generators

### 6.1 Facile and low-cost fabrication of Cu/Zn/Sn-based ternary and quaternary chalcogenides thermoelectric generators

Published under a CC BY 4.0 license.

This section is entirely taken from <sup>159</sup>: Syafiq, U.; Isotta, E.; Ataollahi, N.; Lohani, K.; Luong, S.; Trifiletti, V.; Fenwick, O.; Scardi, P. Facile and low-cost fabrication of Cu/Zn/Sn-based ternary and quaternary chalcogenides thermoelectric generators, ACS Appl. Energy Mater. 2022, XXXX, XXX, XXX-XXX  
<https://doi.org/10.1021/acsaem.2c00268>

Please cite any part of this section as specified above.

U. Syafiq<sup>a,b,\*</sup>, E. Isotta<sup>a</sup>, N. Ataollahi<sup>a</sup>, K. Lohani<sup>a</sup>, S. Luong<sup>c</sup>, V. Trifiletti<sup>c</sup>, O. Fenwick<sup>c</sup>, and Paolo Scardi<sup>c,\*</sup>

<sup>a</sup>Department of Civil, Environmental and Mechanical Engineering, University of Trento, Trento, 38123 (TN), Italy

<sup>b</sup>Solar Energy Research Institute, National University of Malaysia (SERI-UKM), 43600 Bangi, Selangor, Malaysia

<sup>c</sup>School of Engineering and Materials Science, Queen Mary University of London, Mile End Road, London E1 4NS, UK

\*Correspondence: [Paolo.Scardi@unitn.it](mailto:Paolo.Scardi@unitn.it) & [muhammad.mustaffa@unitn.it](mailto:muhammad.mustaffa@unitn.it)

Received: 24 January 2022; Accepted: 10 March 2021; Published online: 19 April 2022

### 6.1.1 Abstract

In this work, Cu/Zn/Sn-based ternary and quaternary chalcogenides inks were synthesized via hot-injection and/or from ball-milled powders. The synthesized inks were used to fabricate thermoelectric generators (TEGs) based on *p*-type chalcogenide and *n*-type aluminium-doped zinc oxide (AZO) thin films via spin-coating and magnetron sputtering, respectively. This work highlights the first ever attempt in a facile and scalable method to fabricate thin film TEGs using safe, low-cost, and abundant materials. Four different TEGs were fabricated using  $\text{Cu}_2\text{ZnSnS}_4$  (CZTS),  $\text{Cu}_2\text{ZnSnSe}_4$  (CZTSe),  $\text{Cu}_{2.125}\text{Zn}_{0.875}\text{SnS}_3\text{Se}$  (CZTSSe), and  $\text{Cu}_2\text{SnS}_3$  (CTS) chalcogenides. Thermoelectric transport analysis confirmed the respective *p*- and *n*-type natures of the chalcogenides and AZO, with their Seebeck coefficients compatible to be coupled in a *p-n* device. Besides that, a full-device analysis has been carried out, and several factors affecting the performance of TEGs were investigated, including the composition, density, and presence of secondary phases in chalcogenide thin films. The maximum power per unit active planar area obtained for CZTS, CZTSe, CZTSSe, and CTS TEGs at temperature difference ( $\Delta T$ ) 160 K were  $\sim 188$  nW/cm<sup>2</sup>,  $\sim 59$  nW/cm<sup>2</sup>,  $\sim 43$  nW/cm<sup>2</sup>, and  $\sim 23$  nW/cm<sup>2</sup>, respectively, making CZTSe/AZO TEG the champion device.

### 6.1.2 Introduction

A thermoelectric generator (TEG) is a solid-state device that converts thermal energy into electrical energy, and vice versa, through the Seebeck effect.<sup>160</sup> TEGs possess attractive features for renewable energy applications, as they are characterized by no moving parts, no emissions of toxic gases, a long life span, low maintenance needs, and high reliability.<sup>161</sup> A TEG basic unit consists of a pair of thermoelements (*p*- and *n*-type semiconducting materials) connected electrically in series by a conducting strip and thermally in parallel. These units are used as building blocks for the construction of a TEG module.

Thermoelectricity nowadays has been studied and applied in a wider range of applications including medical applications,<sup>162</sup> coolers,<sup>163</sup> and temperature sensors.<sup>9</sup> Even though the development of TEG technologies has vastly improved in recent decades, a wide commercialization is still limited, mainly due to the complexity of integration, low efficiencies, and high cost of fabricating high-performance TEGs, which are usually made of alloys of expensive and rare-earth materials such as tellurium (Te) and bismuth (Bi).<sup>8</sup> Thus, any efforts in fabricating a low-cost TEGs with decent performance may push the development of this technology towards commercialization. Thickness reduction is an option to fabricate low-cost TEGs with improved performance. Indeed, a thin film configuration favours a number of mechanisms that can enhance thermoelectric transport properties such as low-dimensional quantum confinement and reduction of lattice thermal conductivity through the well-known effect of interface scattering between the thin film and substrate or between multilayers.<sup>164,165</sup> This approach gave a new paradigm for TE materials to untangle the interrelated electrical and thermal properties.<sup>166–168</sup> Due to the reduction in thickness, TE materials offer additional opportunities in micro-devices such as micro-TEGs, microcoolers,<sup>169,170</sup> and micro-sensors<sup>17</sup>.

Materials for TEG application can be divided into three classes based on their optimum working temperature ranges; low temperature (up to 450 K), middle temperature (up to 850 K) and high temperature (>850 K)<sup>18</sup>. Several materials have been explored to fabricate these devices, including semiconductors,<sup>164,171</sup> fibres,<sup>172</sup> and conducting polymers.<sup>173</sup> In recent years, chalcogenide semiconductors such as lead telluride (PbTe)<sup>22</sup> and bismuth telluride ( $\text{Bi}_2\text{Te}_3$ )<sup>174</sup> have been investigated for TE applications, owing to their high-power factors (PFs) due to the weaker covalent bonds on account of low electronegativity, along with the heavy atomic weights, which are beneficial in reducing thermal conductivity<sup>24</sup>. Unfortunately, due to their composition of mostly toxic and scarce elements, the attention diverted towards more sustainable and abundant chalcogenides, such as tin selenide ( $\text{SnSe}$ ),<sup>97</sup> copper zinc tin sulphide ( $\text{Cu}_2\text{ZnSnS}_4$ , CZTS),<sup>59,92,175</sup> and copper tin sulphide ( $\text{Cu}_2\text{SnS}_3$ , CTS)<sup>106</sup>.

Among the aforementioned chalcogenides, bulk  $\text{Cu}_2\text{ZnSnS}_4$  (CZTS) is considered as a good candidate for sustainable and “green” medium to high temperature TE material owing to its abundance and non-toxicity of the constituent elements,<sup>58</sup> along with good physical, thermal, and chemical properties.<sup>42</sup> In general, quaternary chalcogenides like CZTS possess chemical and structural degrees of freedom which offer flexibility in their physical properties.<sup>176</sup> In addition, by fully or partly replacing sulphur (S) with selenium (Se), CZTSe or CZTSSe can be produced. This replacement enables bandgap tuning,<sup>177</sup> which makes it a versatile semiconducting material to be used in various applications. Despite the vast knowledge acquired in the past two decades on CZTS fabrication and properties,<sup>178</sup> little has been explored regarding thermoelectricity in CZTS thin films. Several studies have been done in improving the thermoelectric properties of CZTS. Cation doping such as copper (Cu) doping<sup>179</sup> is proven as one of the efficacious strategies to enhance electrical and reduce thermal conductivities, which could be of benefit in improving the thermoelectric properties of CZTS.

CTS is another well-known, eco-friendly, non-toxic, and cost-effective *p*-type semiconducting material. CTS polymorphs are a variant of the zinc blende (ZnS) structure, made of tetrahedral cages of S-atoms with a Zn-atom positioned in the middle of the cage. In the ordered polymorph of CTS (Space Group: *Cc*), Zn is stoichiometrically replaced by Cu and Sn, in an ordered manner. Whereas in the disordered polymorph of CTS (Space Group: *F-43m*), the disorder takes the form of compositional inhomogeneities caused by entropy-driven clustering.<sup>81</sup> Disordered CTS shows a higher electrical conductivity, thanks to its lower bandgap. More importantly, the disorder induced by the partial occupancy of cations helps in the suppression of the thermal conductivity to an ultra-low level, presenting a ~10-fold higher  $zT$ , than its ordered counterpart.<sup>71</sup>

This study reports the synthesis of Cu/Zn/Sn-based ternary and quaternary chalcogenide inks including  $\text{Cu}_2\text{ZnSnS}_4$  (CZTS),  $\text{Cu}_2\text{ZnSnSe}_4$  (CZTSe),  $\text{Cu}_{2.125}\text{Zn}_{0.875}\text{SnS}_3\text{Se}$  (CZTSSe), and  $\text{Cu}_2\text{SnS}_3$  (CTS), using hot-injection synthesis or from ball-milled powders. The synthesised inks were then used to fabricate thin films which were then coupled with aluminium-doped zinc oxide (AZO) thin films for the fabrication of TEGs. Currently available methods for the fabrication of

thin film TEGs such as pulsed laser deposition,<sup>180</sup> molecular beam epitaxy<sup>43</sup>, and magnetron sputtering<sup>181</sup> involve the use of specialised equipment or time-consuming processes.<sup>182</sup> This study demonstrates the potential of using a facile, low-cost, and scalable method to fabricate thin film TEGs that are suitable for various applications.

Attempts of thin film TEGs have mainly involved conventional thermoelectric materials such as PbTe<sup>183</sup> and Bi<sub>2</sub>Te<sub>3</sub><sup>184</sup> in the past years. Besides that, several attempts using a more sustainable materials have also been reported for oxides and binary chalcogenides, such as SnSe<sup>47</sup> and aluminium oxide (Al<sub>2</sub>O<sub>3</sub>).<sup>185</sup> However, the class for ternary and quaternary Cu chalcogenides remains unexplored. To our best knowledge, this is a novel attempt at fabricating thin film TEGs using *p*-type Cu/Zn/Sn-based chalcogenides. In addition, performance analyses of the fabricated TEGs were discussed, along with suggestions for further improvement and optimization.

### 6.1.3 Synthesis of Cu/Zn/Sn-based chalcogenides inks

Synthesis of CZTS nanoparticles via hot-injection synthesis was performed according to the method from some of the authors' previous work<sup>49</sup>. Meanwhile, CZTSe and CZTSSe ball-milled powders were synthesised via reactive mechanical alloying with a procedure similar to previous reports,<sup>106</sup> with the addition or substitution of Se using Se powder (Se, 99%, Alfa Aesar). CTS ball-milled powders were synthesised via reactive mechanical alloying of binary sulphides as previously reported.<sup>155</sup> The synthesised ball-milled powders were then used to obtain the respective chalcogenide inks. Details of the synthesis are provided in Appendix 6.1.11.

A particle analyser (Delsa<sup>TM</sup>Nano C, Beckman Coulter, Indianapolis, USA) was used to measure the hydrodynamic size of ink particles. Details for DLS measurement is provided in the Appendix. DLS analysis in Table 6.1 revealed that the synthesised ink particles had average diameters of ~0.02 μm, ~0.37 μm, ~1.51 μm, and ~3.67 μm for CZTS, CZTSe, CZTSSe, and CTS, respectively. Ideally, an ink should have nanometric size particles for a stable dispersion. Unlike the hot-injection CZTS, OLA encapsulated the agglomerated nano-domains of

the ball-milled chalcogenides,<sup>125</sup> making the ink dispersions consist of polycrystalline agglomerates that are micrometric in size.

Table 6.1: DLS analysis of synthesized chalcogenides inks

Inks	Particle preparation	Average particle diameter ( $\mu\text{m}$ )
CZTS	Hot injection (HI)	0.020 $\pm$ 0.003
CZTSe	Ball-milling (BM)	0.37 $\pm$ 0.01
CZTSSe	Ball-milling (BM)	1.5 $\pm$ 0.4
CTS	Ball-milling (BM)	3.7 $\pm$ 0.4

Due to the micrometric size of particles in ball-milled (BM) chalcogenides inks, several challenges were posed during thin film fabrication. Bigger size translates to heavier mass, which consequently increases the sedimentation rate of the agglomerates to the bottom of the ink, reducing the ink's stability. As a workaround, the inks were sonicated for several minutes right before deposition. Besides that, the control of a film's thickness theoretically depends on the size of the polycrystalline agglomerates. Nevertheless, the synthesis of a more stable ink with smaller polycrystalline agglomerates is subject of ongoing work.

#### 6.1.4 Fabrication of chalcogenides/AZO thin film TEGs

Thin film chalcogenides were deposited on soda-lime glass (SLG) substrates using a vacuum spin-coater (Laurell WS 650), followed by thermal treatment in a tube furnace (Carbolite™ CTF wire-wound) with a continuous flow of N<sub>2</sub>.<sup>61</sup> Details of the fabrication is provided in the Appendix 6.. For the fabrication of chalcogenide/AZO thin film TEG (schematic shown in Figure 6.1 (a), the device was designed to consist of two *p*-type chalcogenide legs (*p*-legs) and two *n*-type AZO legs (*n*-legs) arranged in alternate, connected using silver (Ag) metal contact in a zig-zag pattern. Basically, the thermoelectric components are connected electrically in series and thermally in parallel. Kapton®-tape was used as the deposition mask on the SLG glass substrate and the *p*-legs were deposited by spin-coating, as previously mentioned, while the *n*-legs (*n*-legs) were deposited using magnetron sputtering. Finally, Ag metal contacts were deposited via thermal evaporation. Figure 6.1 (b) shows a fully fabricated thin film chalcogenide/AZO thin film TEG.

Additional details regarding AZO and Ag deposition are provided in the Appendix 6.1.11.

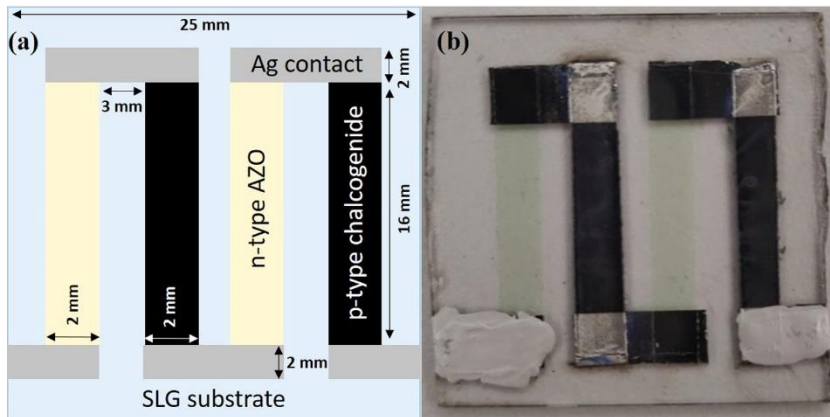


Figure 6. 1. (a) Schematic design of a chalcogenide/AZO thin film TEG (not drawn to scale), (b) Fabricated thin film chalcogenide/AZO thin film TEG.

### 6.1.5 Chalcogenide/AZO thin film TEGs performance analysis

The TEGs' internal resistances including each leg's resistance were measured using a handheld digital multimeter with a 200 mA/250 V fuse rating. Open-circuit voltage ( $V_{OC}$ ) vs  $\Delta T$  measurements were performed to evaluate the highest voltage that can be generated at varied temperature differences between the hot side ( $T_h$ ) and the cold side ( $T_c$ ) of the TEG. Figure 6.2 (a) shows the setup used to conduct the  $V_{OC}$  vs  $\Delta T$  measurements, where voltage measurements were taken from Keithley 2601A multimeter while  $T_h$  and  $T_c$  were captured by Fluke Ti25 Thermal Imager (Fluke Italia S.r.l., Brugherio, Italy) thermal camera. To avoid errors due to the differences in the emissivity of the materials,  $T_h$  and  $T_c$  values were taken on the glass substrate near the TEG legs as shown in Figure 6.2 (b). Validation for this assumption is discussed in Appendix 6.1.11.

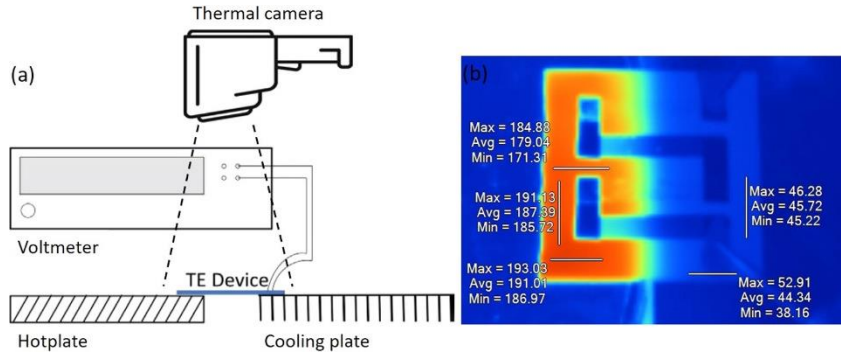


Figure 6.2.(a) Setup for  $V_{OC}$  vs  $\Delta T$  measurement, (b) Thermal image of a chalcogenide/AZO thin film TEG.

$I$ - $V$ - $P$  measurements were done to evaluate the performance of a TEG at specific temperature conditions (surrounding temperature,  $T_h$ , and  $T_c$ ). The schematic of the  $I$ - $V$ - $P$  setup is presented in Figure 6.3 (a), while Figure 6.3 (b) shows the homemade setup used. An ammeter (Hewlett-Packard 34401A multimeter) and a variable resistor were connected in series, while a voltmeter (Keithley 2601A multimeter) was connected in parallel, with respect to the TEG. This measurement can be explained by a reduction in voltage when a current ( $I_2$ ) is allowed by controlling  $R_C$  using the variable resistor. In open circuit,  $R_C$  is at infinity, only  $I_1$  current will flow, and the TEG will generate its highest voltage. However, there will be no power output due to the zero current. By reducing  $R_C$ , the voltage will decrease while  $I_2$  increases. Upon reaching short circuit condition (zero  $R_C$ ),  $I_2$  will achieve the maximum value while voltage will drop to zero. From the  $I$ - $V$  readings taken at varied  $R_C$ , the TEG's power curve can be calculated and plotted using  $P=VI$ .

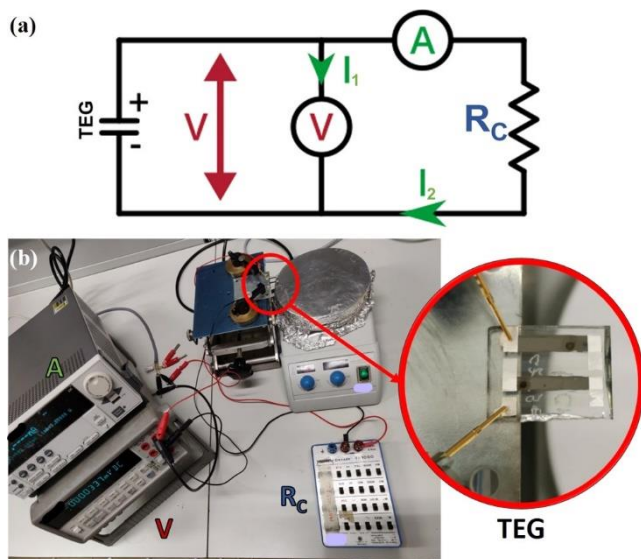


Figure 6.3.(a) Schematic setup for  $I$ - $V$ - $P$  measurement, (b) Picture of the in-house  $I$ - $V$ - $P$  measurement setup.

### 6.1.6 Thin films characterization

The structural and compositional characterization of HI CZTS thin films including SEM, EDXS, and XRD were investigated and reported in our previous paper.<sup>171</sup> Details for this discussion are provided in Appendix 6.1.11. As previously mentioned, the film thickness of fabricated Cu/Zn/Sn-based chalcogenides are varied, mainly due to the size of the encapsulated particles in their inks. On average, HI CZTS possesses a thickness of  $\sim 2.0 \mu\text{m}$ , thanks to the nanometric size of particles in its ink. However, BM chalcogenide thin films suffer from poor thickness control due to the micrometric size of particles in their inks. The average thicknesses for BM CZTSe, BM CZTSSe, and BM CTS thin films were  $\sim 4.8 \mu\text{m}$ ,  $\sim 4.1 \mu\text{m}$ , and  $\sim 5.1 \mu\text{m}$ , respectively (Figure 6.S5, Appendix 6.1.11).

In addition, 4-point probe resistance measurements on the films showed that BM CTS possesses the lowest sheet resistance ( $0.87 \pm 0.03 \text{ k}\Omega/\square$ ), followed by HI CZTS ( $1.6 \pm 0.4 \text{ k}\Omega/\square$ ), BM CZTSe ( $5.0 \pm 0.4 \text{ k}\Omega/\square$ ), and BM CZTSSe ( $5.6 \pm 0.2 \text{ k}\Omega/\square$ ). HI CZTS thin film exhibits superior electrical properties by having low sheet resistance and  $p$ -leg resistance

as compared to BM chalcogenides due to its higher density. HI CZTS ink with lower particle size can better maximize the use of space during deposition, resulting in higher density films. A film with higher density will exhibit better electrical properties since the pores in low-density films do not contribute to the material's electrical conductivity<sup>51</sup>. However, possibly due to the surface sensitivity of the 4-point probes method, BM CTS presents the lowest sheet resistance, indicating that the film's surface might be continuous and connected.

For AZO thin film, SEM micrograph collected (Figure 6.S6, Appendix 6.1.11.) showed that the film covers the entirety of the substrate in a continuous and homogenous manner. Some pinholes were observed, possibly due to the presence of contaminants during sputtering. EDXS analysis (Table 6.2) from the same SEM image revealed a high amount of Zn with some traces of Al with 27.6:1 compositional ratio, which is close to the source composition. In addition, a higher atomic fraction of oxygen (O) than what is expected from AZO, along with trace amounts silicon (Si) and calcium (Ca) were also observed, implying the beam was able to penetrate through the deposited AZO layer to the substrate, preventing a precise determination of the sample stoichiometry.

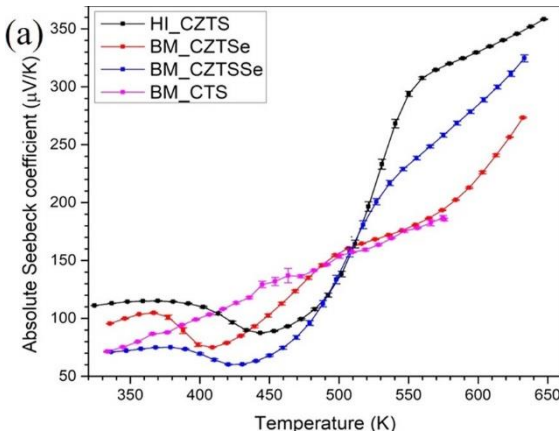
Table 6.2: EDXS atomic percentage for each element in the fabricated AZO thin film.

Element	Atomic Percent (%)
Zn	35.9 ± 1.7
O	54.3 ± 2.7
Al	1.3 ± 1.3
Si	6.7 ± 0.2
Ca	1.8 ± 0.1

The thickness of the AZO film was estimated to be 510±50 nm using a surface profilometer. Besides that, the XRD pattern (Figure 6.S7, Appendix 6.1.11) showed that the fabricated AZO thin film possesses a ZnO-like zincite phase (PDF 00-005-0664). Only sharp Bragg-peaks representing (00l) planes were observed, confirming that the film is made of highly crystalline single-phase material, which has a preferred orientation along the [002] direction, with no observable peaks of spurious phases.

### 6.6.7 TE transport properties

The TE transport properties of the fabricated HI CZTS thin film were performed and reported thoroughly in our previous paper<sup>19</sup>, and briefly discussed in Appendix 6.1.11. Nevertheless, Figure 6.4 shows  $\alpha$ ,  $\rho$ , and power factor ( $PF = \alpha^2/\rho$ ) of other fabricated Cu/Zn/Sn-based chalcogenide thin films, together with HI CZTS. The positive value of  $\alpha$  for all chalcogenides indicates that holes are the major charge carriers, confirming the  $p$ -type conductivities.<sup>42,58</sup> The films generally exhibit low  $\alpha$  and high  $\rho$  values in the low-temperature range, with a further rise in temperature increases  $\alpha$  and decreases  $\rho$ . Besides that,  $\rho$  presented a general decreasing trend, evidencing the non-degenerate semiconducting nature. In addition, quaternary chalcogenides (CZTS, CZTSe, and CZTSSe) display a sharp rise in  $\alpha$  at around 400-500 K, indicating the order-disorder transition from the ordered  $I-4$  to disordered  $I-42m$  tetragonal structure, due to randomization of Cu and Zn atoms among the  $2c$  and  $2d$  sites.<sup>59,179</sup> This phenomenon leads to a dramatic increase in the materials'  $PF$ , as evident in Figure 6.4c.



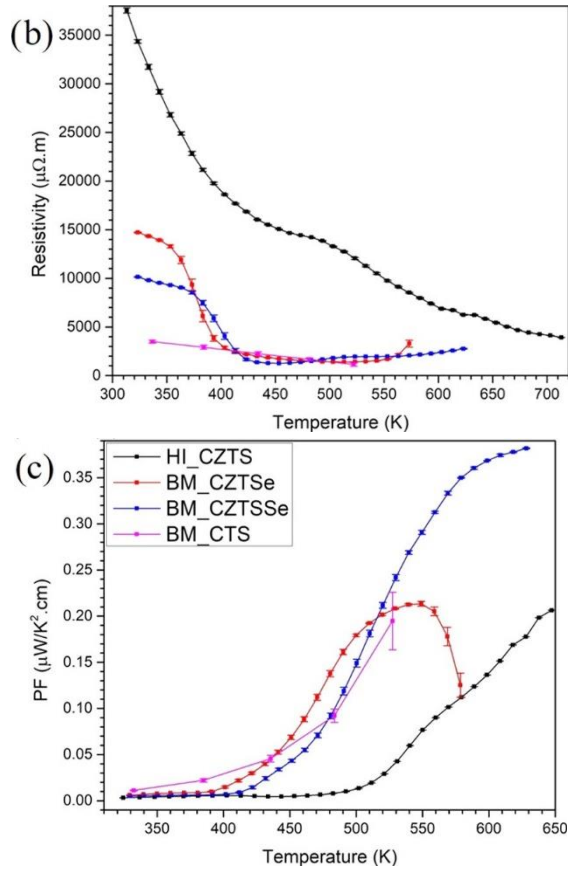
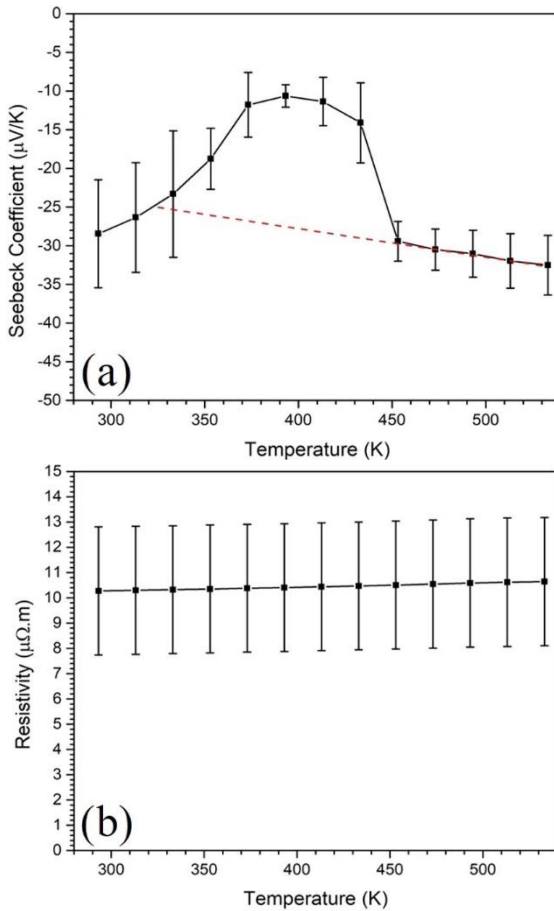


Figure 6.4.(a) Seebeck coefficient ( $\alpha$ ), (b) Electrical resistivity ( $\rho$ ), and (c) calculated power factor ( $PF$ ) of HI CZTS, BM CZTSe, BM CZTSSe, and BM CTS thin films.

On the other hand, TE transport properties of the AZO thin film were measured using Linseis Thin Film Analyser and reported in Figure 6.5 (a).  $\alpha$  showed a negative value, indicating electrons as majority charge carriers.<sup>6</sup> By observing the absolute value,  $\alpha$  decreases with temperature up to  $\sim 393$  K. Further increase in temperature increases  $\alpha$ , leading to a maximum value of  $\sim 33$   $\mu V/K$  at  $\sim 533$  K, in agreement with other reported values.<sup>186</sup> In overall,  $\alpha$  measurement showed a linear trend, but with a slight deviation observed between  $\sim 333$  K and  $\sim 433$  K.<sup>187</sup>

In addition, the electrical resistivity of the AZO thin film (Figure 6.5 (b)) remains around  $\sim 10$   $\mu\Omega\cdot m$  up to  $\sim 533$  K, which is in accordance with other literature results.<sup>186,188</sup> The resistivity of AZO thin films showed a degenerate semiconductor nature, increasing with

temperature, suggesting that AZO possesses a high-carrier concentration. From these two transport properties, the film's  $PF$  (Figure 6.5 (c)) was calculated, which showed a decreasing trend with temperature up to  $\sim 393$  K, followed by an increase up to the maximum measured temperature. The variation of  $PF$  is mainly affected by the variation of  $\alpha$  in temperature, as we observe limited variation in resistivity. The maximum  $PF$  of  $\sim 1.0 \mu\text{W}/\text{K}^2\cdot\text{cm}$  was calculated at  $\sim 293$  K and  $\sim 533$  K.



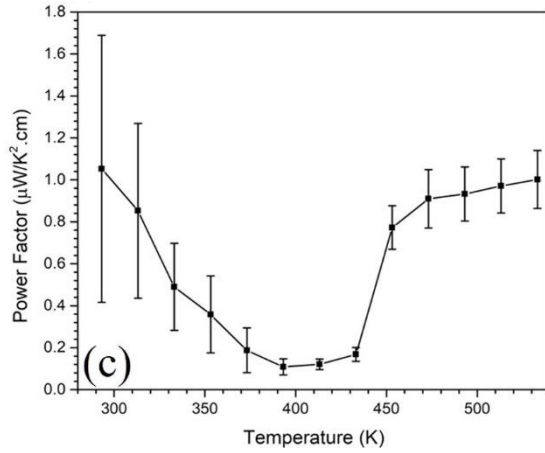
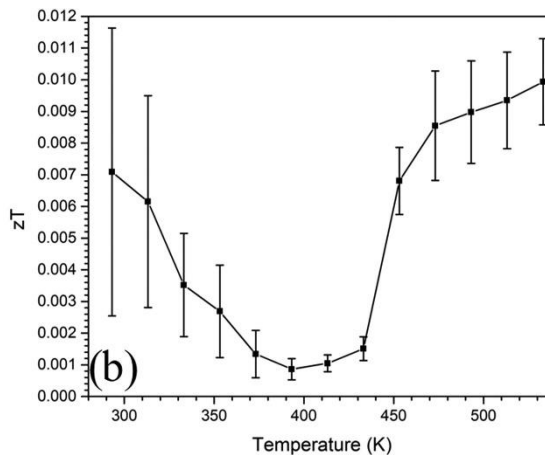


Figure 6.5: a)  $\alpha$ , b)  $\rho$ , and c)  $PF$  of AZO thin film.

Furthermore, in-plane  $\kappa$  measurement (Figure 6.6 (a)) showed the values to be in the range of 4.5-5.5  $\text{W}/\text{m}\cdot\text{K}$  in the  $\sim 293$ -533 K temperature range.<sup>188,187</sup> The TE figure of merit,  $zT$  ( $zT=PF \cdot T/\kappa$ ) is used to assess a material's TE performance, where PF and T are the power factor and the absolute temperature, respectively.  $zT$  was calculated based on the obtained  $PF$  and  $\kappa$  results as illustrated in Figure 6.6 (b). It follows a similar trend to the  $PF$ , reaching a maximum  $zT$  of  $\sim 0.01$  at 533 K.



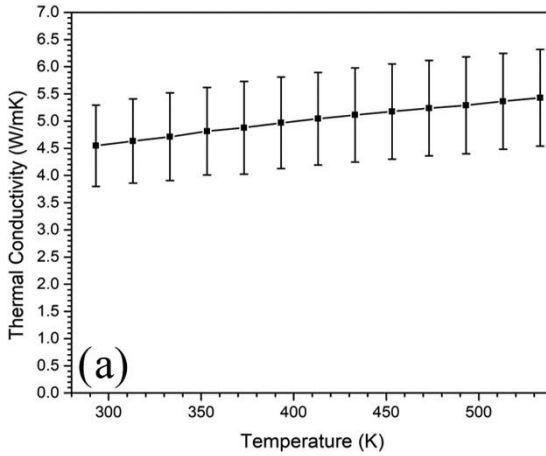


Figure 6.6: a) Thermal conductivity ( $\kappa$ ), and b)  $zT$  of the AZO thin films.

### 6.1.8 Chalcogenides/AZO TEGs performance analysis

$V_{OC}$  vs  $\Delta T$  measurements gives information on the maximum voltage that can be generated by the fabricated chalcogenides/AZO thin films TEGs at specific  $\Delta T$ s. A hotplate was used to control  $T_h$  with a 10 K increment from  $\sim 323$  K up to  $\sim 523$  K, while  $T_c$  was kept at ambient temperature with a metal plate as the heat sink. The measured  $\Delta T$ s did not fully match the set temperature of  $T_h$  and  $T_c$  due to substrate buffer and poor heat sink setup. Substrate buffer may affect the efficiency of the TEG, as some of the temperature gradient will be lost across the substrate.

Figure 6.7 shows the  $V_{OC}$  vs.  $\Delta T$  plot of chalcogenides/AZO thin films TEGs, presenting a linear trend of voltage with  $\Delta T$ . Maximum voltages measured for TEGs with HI CZTS, BM CZTSe, BM CZTSSe, and BM CTS  $p$ -legs at  $\Delta T$  160 K were  $\sim 87$  mV,  $\sim 118$  mV,  $\sim 46$  mV, and  $\sim 98$  mV, respectively. Since AZO is a constant throughout the TEGs, these values are directly related to the  $\alpha$  of the chalcogenides around 480-500 K, as shown in previous Figure 6.4 (a), where BM CZTSe possesses the highest value, followed by CTS, HI CZTS, and BM CZTSSe. The selected temperature range corresponds to the temperature taken by the thermal camera at the TEG's hot side. However, a thorough relation between  $V_{OC}$  and  $\alpha$  has yet to be explored.

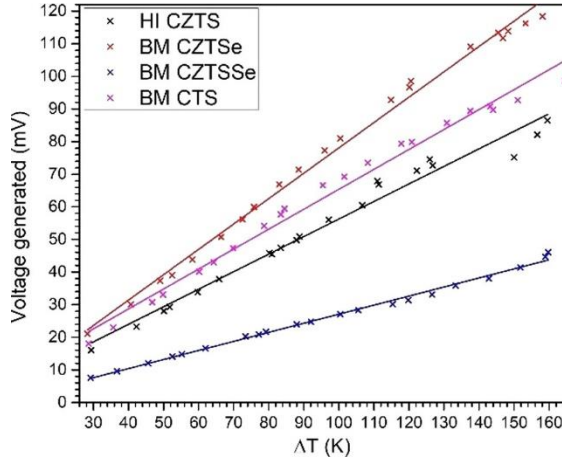


Figure 6.7:  $V_{OC}$  vs  $\Delta T$  measurement of chalcogenides/AZO thin films TEGs.

Figure 6.8 shows the  $I$ - $V$ - $P$  measurements of HI CZTS/AZO thin film TEG at different  $\Delta T$ s. For simplicity, the figures were separated into  $I$ - $V$  (Figure 6.8 (a)) and  $I$ - $P$  (Figure 6.8 (b)) plots. The temperatures indicate the hotplate temperature that was set on the  $T_h$  side of the TEG, since it is the main component in determining  $\Delta T$ , as discussed before. The  $I$ - $V$  plots are linear for all the  $\Delta T$ s, with the slope of the plots indicating the TEG's internal resistance. The values of the slopes reduced from 28.6 k $\Omega$  at 323 K to 14.9 k $\Omega$  at 523 K, which agrees with the reduction of CZTS resistivity at elevated temperature as previously discussed and with the approximately constant trend of resistivity for AZO, neglecting the small resistivity effect of Ag metal contacts.<sup>189</sup> On the other hand, the  $I$ - $P$  curve shows the classical parabolic shape, with maximum power occurring at the point where the load resistance matches the device resistance.<sup>185</sup> Results show that a higher  $\Delta T$  produces a higher power output, that reaches up to ~55 nW at 523 K  $T_h$ .

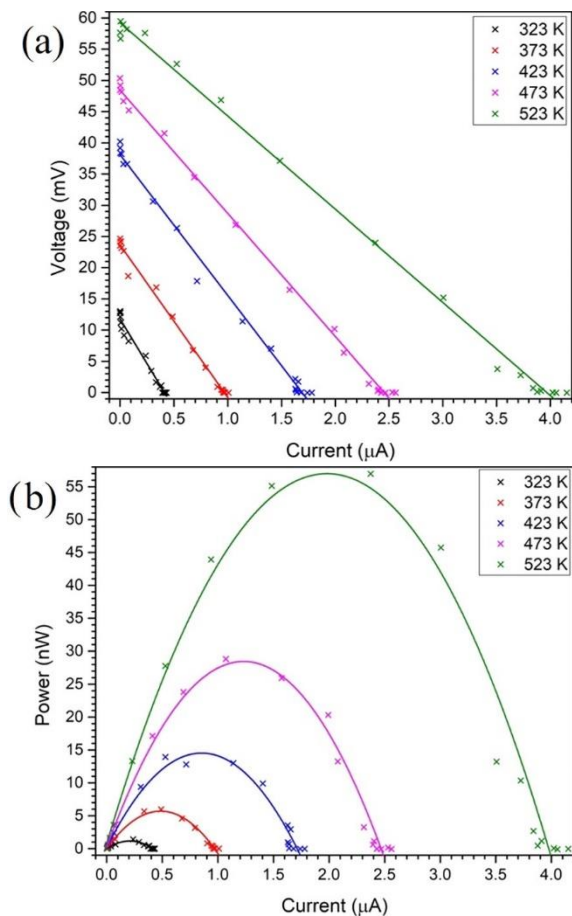


Figure 6.8: (a)  $I$ - $V$  and (b)  $I$ - $P$  plots of thin film HI CZTS/AZO thin film TEG at different  $\Delta T$

In addition to HI CZTS thin film TEG, internal resistances of the other chalcogenide/AZO thin film TEGs were also obtained from the slopes of their respective  $I$ - $V$  plots. At similar  $T_h$  of 523 K and  $\Delta T$  of 160 K, Figure 6.9 (a) shows that the chalcogenide/AZO thin film TEG with BM CZTSe  $p$ -legs possesses the lowest internal resistance (12.2 k $\Omega$ ), followed by HI CZTS (14.9 k $\Omega$ ), BM CZTSSe (17.7 k $\Omega$ ), and BM CTS (27.3 k $\Omega$ ). The internal resistance may be affected by factors including but not limited to the deposited films' thicknesses and materials' resistivities, such as carrier concentrations and carrier mobilities. Besides that, low film density may also result in low carrier mobility. This leads to a smaller effective area of conduction, poorer connectivity

of domains, and carrier scattering (decreasing carrier mean free path), thus providing a major obstacle for electrical conduction.<sup>190</sup>

The  $I$ - $V$  plot in Figure 6.9 (b) reveals that the TEG with BM CZTSe  $p$ -legs performs the best with maximum power output reaching  $\sim 240$  nW, followed by BM CTS ( $\sim 75$  nW), HI CZTS ( $\sim 55$  nW), and BM CZTSSe ( $\sim 30$  nW). From the results obtained, the calculated maximum power output per unit active planar area for each respective TEGs are  $\sim 188$  nW/cm<sup>2</sup>,  $\sim 59$  nW/cm<sup>2</sup>,  $\sim 43$  nW/cm<sup>2</sup>, and  $\sim 23$  nW/cm<sup>2</sup>. The exceptional performance of BM CZTSe is evident from its high  $V_{OC}$  and low internal resistance, compared to the other chalcogenides. From the results obtained, we can deduce that a TEG's performance is significantly affected by two main factors: (1)  $V_{OC}$  which is directly related to  $\alpha$ , and (2) internal resistance which is directly related to the film thickness and density, and  $\rho$ .

Besides that, the fabricated TEGs also showed a significant performance improvement as compared to other thin film TEGs using low-cost and abundant materials such as tin oxide/zinc oxide (SnO<sub>x</sub>/ZnO)<sup>191</sup> and aluminium oxide/zinc oxide (Al<sub>2</sub>O<sub>3</sub>/ZnO)<sup>185</sup>, which only generated maximum power output per unit active planar area of  $\sim 2.8$  nW/cm<sup>2</sup> at  $\Delta T$  160 K and  $\sim 1.6$  nW/cm<sup>2</sup> at  $\Delta T$  80 K, respectively. From this comparison, it can be surmised that this work successfully established a fabrication method of high-performing thin film TEGs using a facile, low-cost, and scalable approach. However, the TEGs performance were still low as compared to TEGs with conventional materials such as bismuth telluride (Bi<sub>2</sub>Te<sub>3</sub>)<sup>192</sup> and antimony telluride (Sb<sub>2</sub>Te<sub>3</sub>)<sup>193</sup> which respectively produced maximum power per unit active planar area of  $\sim 955$  nW/cm<sup>2</sup> at  $\Delta T$  20 K and  $\sim 305$  nW/cm<sup>2</sup> at  $\Delta T$  15 K. Nevertheless, the fabricated  $p$ -type chalcogenides may provide insights for future studies to replace the scarce, expensive, and potentially harmful elements used in the current conventional materials.

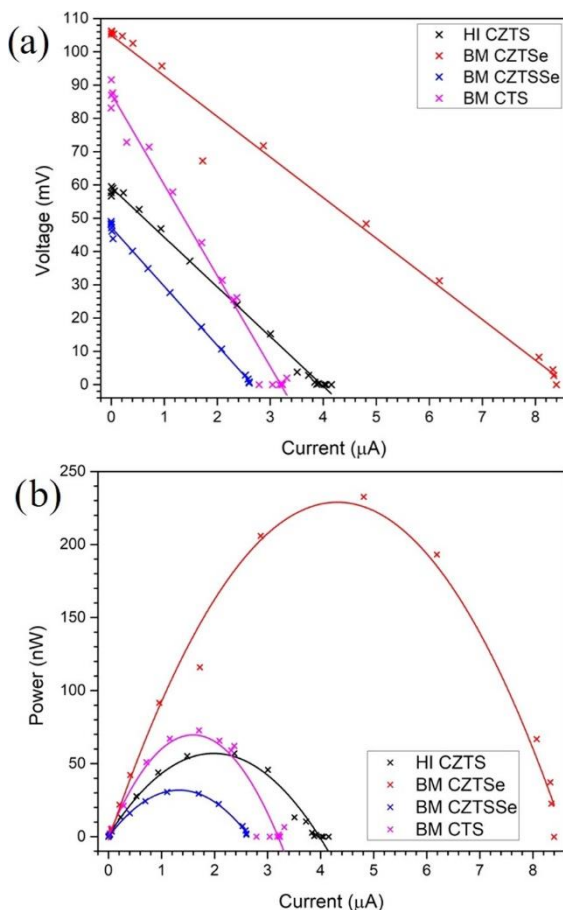


Figure 6.9. (a) I-V and (b) I-P plots of chalcogenides/AZO thin films TEGs.

### 6.1.9 Effect of sulphuration

In a different sample of BM CTS/AZO TEG, the CTS was subjected to a second thermal treatment with the same procedure as the first, but with the addition of an excess amount of S. As shown in Figure 6.10 (a), the TEG with sulphurised CTS performs significantly better compared to non-sulphurised CTS with maximum power output achieved almost  $\sim 230$  nW, which is a staggering 300% increase in performance. This BM CZTSe/AZO TEG provides an alternative for chalcogenides/AZO TEGs with a much safer stoichiometry, which is Se-free.

The main reason for this improvement can be attributed to the suppression of spurious phases, as visible in the XRD patterns of Figure 6.10 (b), including tin (II) oxide (SnO), tin (IV) oxide (SnO<sub>2</sub>), and tin (II) sulphide (SnS), that were formed due to S loss.<sup>194</sup> Even though SnS possesses comparable transport properties to CTS, tin oxides on the other hand have much poorer transport properties (particularly SnO<sub>2</sub>, with *n*-type behaviour)<sup>66</sup> which detrimentally affects the TEG's performance. Besides that, sulphurisation also improves CTS electrical properties by assisting in the formation of void-free CTS films,<sup>195</sup> as can be seen by reduced internal resistance from 27.3 kΩ to 10.8 kΩ from the slope of *I-V* curve, which in turn enhances the TEG's performance.

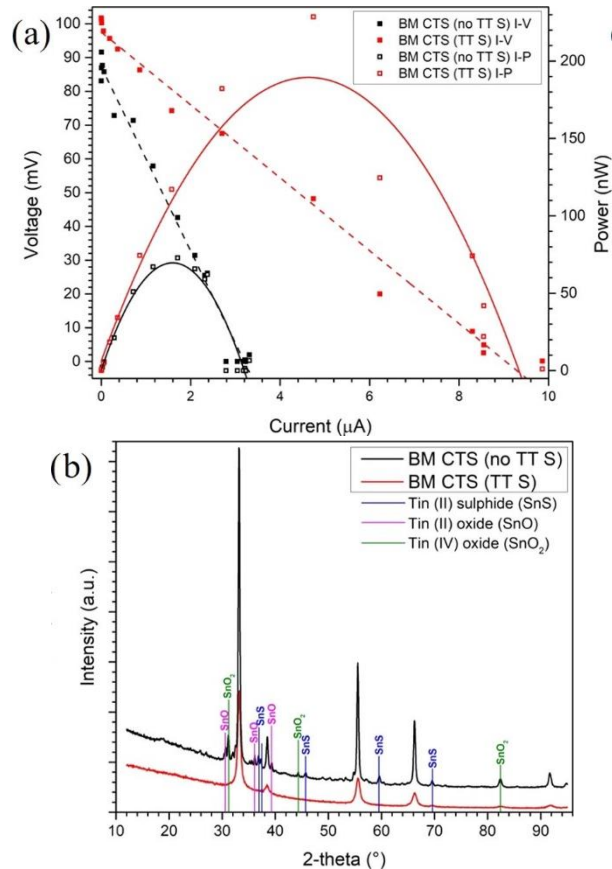


Figure 10. (a) *I-V-P* plots and (b) XRD patterns of sulphurised and non-sulphurised BM CTS/AZO thin film TEG

## 6.1.10 Conclusions

This work presented a complete fabrication method of thin film TEGs using Cu/Zn/Sn-based ternary and quaternary chalcogenide *p*-legs and AZO *n*-legs. Chalcogenide thin films were deposited by spin-coating using chalcogenide inks synthesized either through hot injection or ball-milling, while AZO was deposited by sputtering. Several factors that affect the performance of the fabricated TEGs, including the composition, TEGs' internal resistance,  $V_{OC}$ , and sulphurization, have been thoroughly discussed. The devices are suitable for medium to high-temperature TE applications with the CZTSe/AZO TEG as the champion device, showing the maximum power output of ~240 nW at  $\Delta T$  160 K ( $T_h$  ~483 K,  $T_c$  ~323 K). These fabricated TEGs showed a significant performance improvement for a thin film TEG as compared to other thin film TEGs using abundant, low-cost, and safer materials that only reaches nanowatt<sup>183,196</sup> power output. These chalcogenides/AZO TEGs may provide alternatives or insights in replacing scarce, expensive, and potentially harmful elements used in TE materials such as antimony (Sb),<sup>181</sup> tellurium (Te),<sup>174,192</sup> lead (Pb),<sup>183,197</sup> bismuth (Bi)<sup>8,192</sup> and germanium (Ge)<sup>198</sup>. In conclusion, this work managed to demonstrate the fabrication of a working thin film TEG using abundant and safer materials with facile, low-cost, and scalable approach. Further studies are warranted to better understand and improve the performance of the individual components in the chalcogenides/AZO TEG. Several suggestions from the authors include the studies on film thickness and density improvement, thickness optimization, effects of doping, and device stability. Future work will also involve the investigation of alternative chalcogenide *n*-leg materials in the spirit of fabricating a fully optimized, non-toxic, and low-cost device.

## 6.1.11 Appendix

Synthesis of Cu-Zn-Sn chalcogenides: Synthesis of CZTS nanoparticles ink were followed according to the method from some of authors' previous work.<sup>171</sup> In brief, 0.538 g of Copper (II) chloride dihydrate (CuCl<sub>2</sub>·2H<sub>2</sub>O, >99.0%, Sigma-Aldrich Inc.), 0.414 g of zinc

chloride ( $\text{ZnCl}_2$ , >98.0%, Sigma-Aldrich Inc.), and 0.410 g of tin (II) chloride ( $\text{SnCl}_2$ , 98.0%, Sigma-Aldrich Inc.) were mixed into a three-necked round-bottom flask containing 6.6 ml of oleylamine (OLA, 70%, Sigma-Aldrich Inc.), and the solution was stirred and heated in a silicon (Si) oil bath. The system was connected to a setup with nitrogen ( $\text{N}_2$ ) and vacuum lines as shown in Figure 6.S1. OLA was added to work both as a solvent and as a capping agent for the nanoparticles. The mixture was heated to 130 °C, then degassed and refilled with  $\text{N}_2$  several times before being kept under  $\text{N}_2$  flow. Upon reaching ~260 °C, 10 ml of sulphur (S, Sigma-Aldrich Inc.)/OLA 1 M solution (prepared by dissolving 0.449 g S in 10 ml OLA) was rapidly injected into the solution. The mixture was kept at 260 °C for 30 min after the injection and then cooled naturally to room temperature. The obtained suspension of nanoparticles was washed with a mixture of 5 ml toluene and 25 ml ethanol and centrifuged (MPW-380, MED-Instruments) for 10 min at 12 000 rpm to separate the solvent from the nanoparticles. Finally, the CZTS nanoparticles (~25 nm  $\varnothing$ ) were extracted by removing the supernatant, dispersed in toluene, and sonicated using an ultrasonic bath (Sonorex 35 kHz, Bandelin) to obtain an ink with the concentration of 1 g/ml.

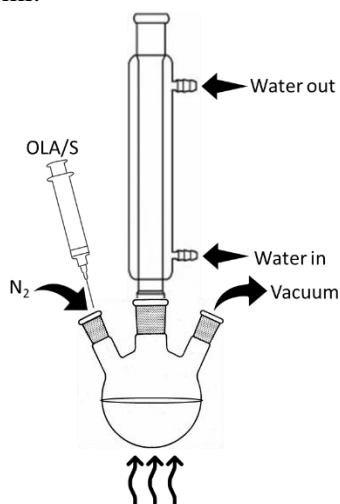


Figure 6.S1: Simplified setup for hot-injection synthesis of CZTS nanoparticles.

Meanwhile, CZTSe and CZTSSe ball-milled powders were synthesized with a similar reactive mechanical alloying procedure<sup>59,92</sup> using selenium powder (Se, 99%, Alfa Aesar) as Se source and 80 ml tungsten carbide (WC) jar with 27 WC balls (12 mm diameter) as milling

medium. The whole procedure of vial filling, milling and powder collection is performed in a glovebox loaded with argon (Ar) atmosphere ( $\text{O}_2$  partial pressure  $<10$  ppm). High energy milling conditions are used, with  $\omega=601.4$  rpm and  $\Omega=310$  rpm, for a fixed ratio  $\omega/\Omega=1.94$ , with a milling time of 120 minutes.

On the other hand, CTS ball-milled powders were synthesised via reactive mechanical alloying of binary sulphides as previously reported in an article from some of our authors.<sup>42</sup> Copper (II) sulphide ( $\text{CuS}$ , 99%, Sigma Aldrich Inc.) and Tin (II) sulphide ( $\text{SnS}$ , 99%, Sigma Aldrich Inc.) were milled in the planetary mill using WC vial and balls with 2:1 stoichiometric ratio, using WC vials and balls with ball-to-powder weight ratio of 100:3. No lubricant was introduced during the milling to avoid any contamination<sup>5</sup>. Main disk and planetary speed were set to 300 rpm and -540 rpm, respectively. Due to its lower formation energy CTS can be produced from either binary sulphides or elemental powders in a relatively short period of milling ( $\sim 0.5 - 1$  h).<sup>71</sup> However, the mill was operated for 3h to get a more homogeneous nanopowder.

The synthesized ball-milled powders were then mixed with excess oleylamine (OLA) and mechanically mixed for 15 minutes in a planetary mill under the same milling conditions used for the synthesis of the nanopowders. This mechanical mixing helped in capping the nanopowders with the ligand OLA. Then, the “capped” nanopowders were washed with a mixture of 5 ml toluene and 25 ml ethanol and centrifuged for 10 min at 12000 rpm to separate the solvent from the nanoparticles, before being dispersed in toluene and sonicated to obtain inks with the concentration of 1 g/ml.

**Dynamic Light Scattering (DLS) analysis:** Dynamic Light Scattering (DLS) measures the intensity of the laser light scattered from suspended particles. The dispersion hydrodynamic diameter is derived from the temporal evolution of the scattered light intensity using the Stokes-Einstein equation. In all the experiments, the nanoparticle dispersions were sonicated for 15 min using an ultrasonic bath prior to the size and zeta potential measurement. All the measurements were carried out at room temperature.

Deposition of thin film chalcogenides: Prior to deposition, the substrates were cleaned with a pH-neutral soap, treated with concentrated potassium hydroxide (KOH) in ethanol, rinsed with distilled water and ethanol, and dried using compressed air. For the deposition, 60-100  $\mu\text{l}$  of the synthesised inks were pipetted onto the substrates and smeared homogeneously using a glass rod prior to spin-coating. Due to varied particle sizes of chalcogenide inks, the substrates were spun between 1000 to 2000 rpm for 30 s during deposition to get a homogeneous layer throughout. Subsequently, thermal treatment of CZTS, CZTSe, and CZTSSe films was performed at 773 K (3 K/min) for 1 h, while CTS thin films were treated at 673 K (3 K/min) for 1 h.

Deposition of AZO *n*-legs and Ag metal contacts in TEG fabrication: Kapton®-tape was used as the deposition mask on the SLG glass substrate during the deposition of *p*-type chalcogenide legs (*p*-legs) via spin-coating. The tape was removed prior to thermal treatment. In the next step, a paper sheet was used as a protective layer on top of the deposited *p*-type legs and the Kapton®-tape mask was reapplied to deposit *n*-type (AZO) legs (*n*-legs) using magnetron sputtering. Finally, silver (Ag) metal contacts were deposited via thermal evaporation. Once the deposition had finished, the deposition mask was removed, and a small dab of silver paint was applied at both terminals of prepared TEGs, to increase the robustness of contacts during measurement.

AZO thin film legs were deposited via radio frequency magnetron sputtering (Leybold-Heraeus LH Z400 MS) equipped with AZO source of 98% zinc oxide (ZnO) and 2% aluminium oxide ( $\text{Al}_2\text{O}_3$ ) in composition (Zn:Al=24.5:1). The sputtering conditions were as follow; 50 W power, 13.56 MHz frequency,  $\sim 5.0 \times 10^{-6}$  mbar minimum working pressure, and 30.8% Argon (Ar) atmosphere, and the sputtering time was fixed to 10 minutes to obtain the desired thickness. After the deposition, the deposition mask was again removed and reapplied with paper sheets on top of the deposited legs.

Ag metal contacts were deposited via thermal evaporation of  $\sim 0.49$  g silver pellets (99.99 % purity, Kurt J. Lesker) using a thermal evaporator (Tecuum AG VCM600 V1). The pellets were put on a tungsten heating boat inside the evaporation chamber. The sample was attached to the substrate holder upside-down with  $\sim 26$  cm of distance

to the boat. The chamber was then vacuumed up to  $\sim 1.5 \times 10^{-5}$  mbar minimum working pressure. The silver was evaporated onto the target via Joule heating using 90 A current. The evaporation stopped once the silver pellets fully evaporated, giving  $\sim 300$  nm thickness. Once the deposition finished, the deposition mask was removed, and a small dab of silver paint was applied at both terminals to increase the robustness of contacts during measurement.

Thin film characterization: The morphology of hot-injection (HI) CZTS thin films was observed via scanning electron microscopy (SEM), using a JEOL JSM-7001F FEG- SEM (JEOL Ltd., Tokyo, Japan) equipped with an Oxford INCA PentaFETx3 energy-dispersive X-ray spectroscopy detector (EDXS, Oxford Instruments Analytical, High Wycombe, UK). Observations were made at 10.0-15.0 keV electron beam energy with a working distance of 5-10 mm. The surface morphology of AZO thin film was observed using a COXEM EM-30AX (COXEM Co. Ltd., Daejeon, Korea), equipped with EDXS detector. The observations were made at 20.0 keV electron beam energy with a working distance of 10.2 mm. Thicknesses of the fabricated thin films were measured using Dektak® 3 Surface Profilometer (Bruker, Karlsruhe, Germany) with 2.5  $\mu\text{m}$  radius diamond-tip stylus, passing 2 mm scan range crossing the film with a perpendicular “trench”.

X-ray diffraction (XRD) patterns of HI CZTS thin films were collected in Bragg-Brentano ( $\theta/2\theta$ ) geometry using a Rigaku PMG D/Max-B diffractometer (Rigaku Corp., Tokyo, Japan), equipped with a graphite bent-crystal monochromator and  $\text{Cu } K_\alpha$  ( $\lambda = 1.5406 \text{ \AA}$ ) source. Rietveld refinement was performed on the obtained XRD patterns using the TOPAS 7 software package, with the aid of Whole Powder Pattern Modelling (WPPM) macros for size analysis.<sup>55-57</sup> Meanwhile, the XRD patterns of other chalcogenides and AZO thin films were collected using Bruker D8 Discover diffractometer (Bruker, Karlsruhe, Germany) equipped with a  $\text{Co-}K_\alpha$  ( $\lambda = 1.7998 \text{ \AA}$ ) radiation source in Bragg-Brentano geometry. Thin films' resistances were measured using a Signatone 4-point resistivity system (Lucas Signatone Corp., California, USA) connected to Keithley 2601A multimeter (Tektronix U.K Ltd., Berkshire, United Kingdom). The probes used had tungsten

carbide (WC) tips with 1.27 mm spacing between tips, 0.127 mm tip radius, and 45 g pressure on the probe tip.

Electrical resistivity and Seebeck coefficient measurements were performed using a Linseis LSR-3 Meter (Linseis Messgeraete GmbH, Selb, Germany) under partial helium pressure (0.1 bar) and a temperature range of 323-673 K. Resistivities were measured in 2-contact configuration with the aid of a thin film adapter for high resistance samples, while the Seebeck coefficient was measured in 4-contact configuration with small Pt foils to improve contacts and a temperature gradient of 10 K. Thermal conductivity ( $\kappa$ ) measurements were performed in-plane using a Linseis Thin Film Analyser (Linseis Messgeraete GmbH, Selb, Germany) on films deposited on a suspended  $\text{Si}_3\text{N}_4$  membrane incorporated on a pre-patterned measurement chip using a quasi-steady-state  $3-\omega$  method, under vacuum and in the dark. The details of this measurement are described elsewhere.<sup>199,200</sup>

Chalcogenides/AZO thin film TEGs performance analysis: Due to the TEG thin film architecture, the heat flow was dominated by the substrate, giving the assumption on  $T_h$  and  $T_c$  more reliable. These assumptions were validated when a TEG coated in graphite gave a homogenous reading throughout  $T_h$  and  $T_c$  regions, as shown in Figure 6.S2 (b).

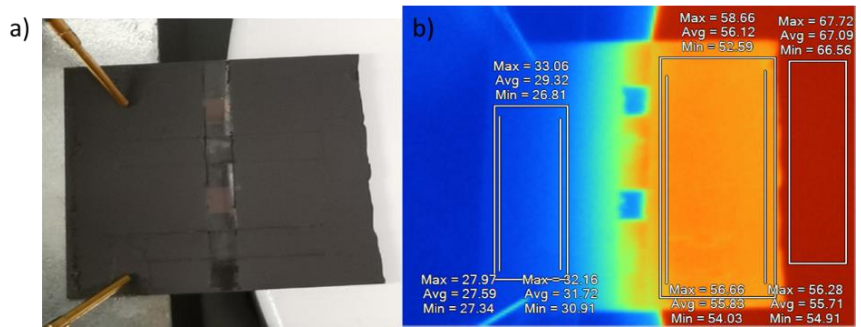


Figure 6.S2.(a, b): $T_h$  and  $T_c$  temperature validation of graphite-coated TEG.

Hot-injection (HI) CZTS thin film preliminary characterization: Preliminary characterization including morphological, compositional, and structural characterization of fabricated HI CZTS thin film was reported in our previous paper.<sup>171</sup> In short, SEM analysis (Figure 6.S3

(a) showed that the fabricated CZTS thin film consists of  $\sim 1.0 \mu\text{m}$  thick uniform layer of CZTS nanoparticles with micrograins ( $>1.0 \mu\text{m}$  in size) scattered on top. Besides that, EDXS analysis as shown in Figure S3 (b) revealed that the fabricated film possesses Cu-poor, Zn-rich composition of an A-type CZTS.<sup>201</sup> In addition, S close to stoichiometry promotes a faster Cu-Zn ordering (or disordering) through a higher density of cation vacancies.<sup>202</sup> However, the micrograins present on the film's surface showed an off-stoichiometry composition, due to S loss and partial segregation of Cu during thermal treatment.<sup>202</sup>

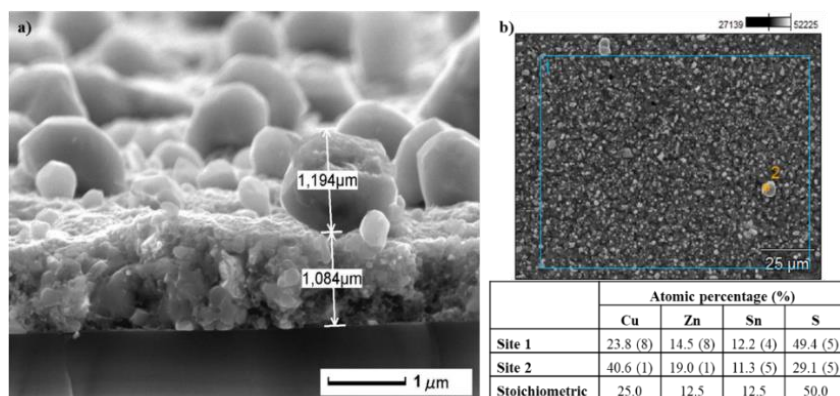


Figure S312: a) Cross-section SEM image, and b) Atomic percentage for each element from EDXS, of fabricated CZTS thin film

Furthermore, XRD structural analysis (Figure S4) showed a good kesterite-CZTS phase purity ( $I-42m$ , S.G.), with a minor fraction of chalcocite  $\text{Cu}_2\text{S}$ , that might be related to the superficial surface micrograins,<sup>202</sup> as discussed in EDXS. The modelling of the kesterite peak profiles requires two CZTS phase fractions with different mean crystal-domain sizes; coarse ( $\sim 0.5 \mu\text{m}$ ) and fine ( $\sim 10.0 \text{ nm}$ ), to account for the large dispersion of crystal-domain dimensions.<sup>59,92</sup> Result revealed that the coarse phase appears to be present in larger fraction (65%) as compared to the fine phase (35%).

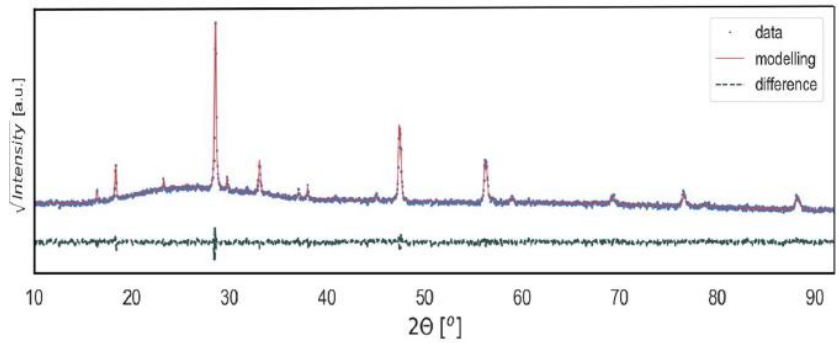


Figure S4: XRD data refinement of the fabricated thin film CZTS.

Cu-Zn-Sn chalcogenides thin films preliminary characterization.

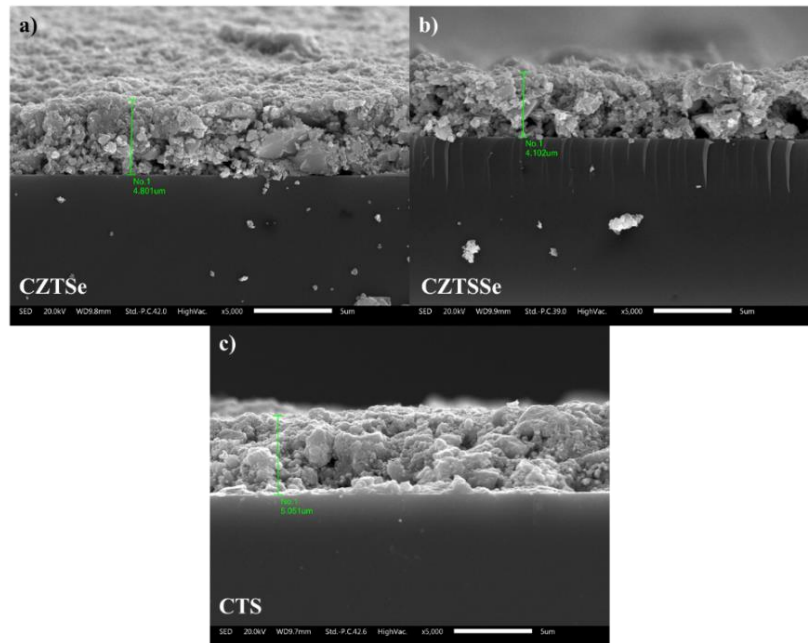


Figure 6.S5: Cross-section SEM image of a) BM CZTSe, b) BM CZTSSe, and c) BM CTS thin films

### AZO thin film characterization



Figure 6.S6: Surface SEM image of an AZO thin film.

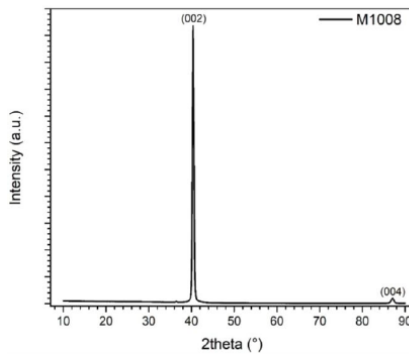


Figure 6.S7: XRD pattern of the fabricated AZO thin film.

TE transport properties of HI CZTS thin film: The TE transport properties of the fabricated HI CZTS thin film were performed and reported thoroughly in our previous paper.<sup>171</sup> In short, the fabricated sample (Figure 6.S8) presented low  $\alpha$  and high values in the low-temperature range. Upon reaching 450-550 K, a sharp rise was observed for the  $\alpha$  value and remained high at high temperature. Meanwhile,  $\rho$  presented a general decreasing trend, evident of a non-degenerate semiconducting nature, with a slight perturbation in the range 450-550 K. The  $\rho$  and  $\alpha$  features around 450-550 K has previously been connected with the Cu-Zn order-disorder transition, from ordered  $I-4$  to disordered  $I-42m$  tetragonal CZTS, which leads to flatter and more converged the electronic bands, strongly affecting the electronic properties.<sup>170</sup> This phenomenon led to a sharp rise in the material's  $PF$ .

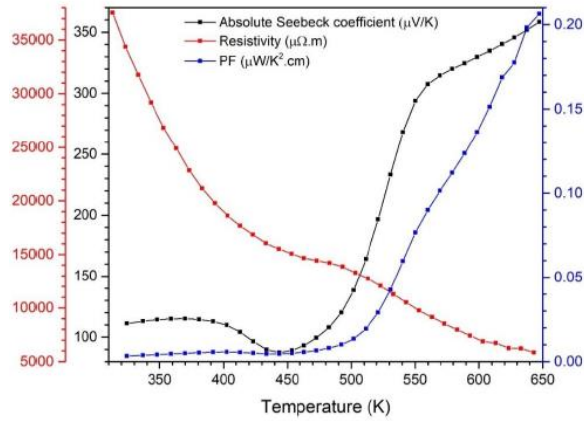


Figure 6.S8: Absolute Seebeck coefficient ( $\alpha$ ), electrical resistivity ( $\rho$ ), and Power Factor ( $PF$ ) of CZTS thin film.

In Figure 6.S9, the calculated  $\kappa$  from the lattice component ( $k_L$ ) of a polycrystalline bulk sample and corrected for the electronic component ( $k_e$ ) of the thin film sample is in the order of  $\sim 0.60$  W/m·K, with an increase upon thermal treatment as high temperature promotes domain growth and improved connection of domains, reducing phonon scattering. From the obtained  $PF$  and calculated  $\kappa$ , an estimate of  $zT$  was estimated, reaching a maximum of 0.023 at  $\sim 650$  K.

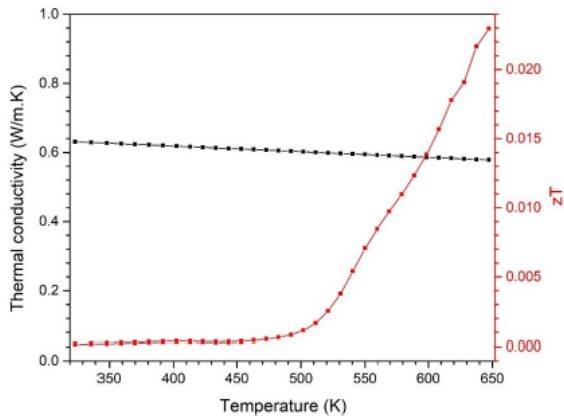


Figure 6.S9: Thermal conductivity ( $\kappa$ ), and  $zT$  of CZTS thin film.

## 7 Conclusions and Outlooks

The present doctoral work investigates thermoelectric materials and devices, based on  $\text{Cu}_2\text{SnS}_3$ , an earth-abundant, non-toxic, and eco-friendly material for medium-temperature thermoelectric applications. The thesis presents a detailed and systematic study on the effects of polymorphism, preparation and sintering techniques, grain size reduction, and Ag-substitution on the thermoelectric properties of CTS. We have also presented a preliminary study on CTS and other chalcogenide-based functioning thermoelectric generators. The individual conclusions of various studies performed during this work are reported with each chapter.

In summary, the literature reports a three-step sample preparation method to synthesize thermoelectric materials. Firstly, the material is prepared from elemental powders using a high-temperature solid-state reaction, and in the next step, the grain size is reduced using ball-milling. Lastly, the ball-milled powder is sintered using hot pressing or spark plasma sintering. This method undergoes two thermal treatments, resulting in highly crystalline and ordered materials with large crystallite sizes, spanning from half to several microns. Literature also shows that external doping in CTS can stabilize disordered polymorphs.

Differently, in this thesis work, CTS samples were prepared via a two-step synthesis method, where high energy ball-milling was combined with various sintering techniques. The as-milled powder showed a sphalerite-like structure identified as disordered cubic CTS polymorph, stable up to 500°C. The disordered CTS polymorph gradually evolved to its ordered or monoclinic phase by increasing the sintering temperature, reaching a complete ordered structure at 650°C.

The novel disordered CTS polymorph presented a lower bandgap and thermal conductivity than its ordered phase. Thus, resulting in many folds higher  $zT$  than its ordered counterpart. However, due to ambient preparation conditions, secondary phase oxides, especially  $\text{SnO}_2$ , were observed, detrimental to the material's thermoelectric properties and stability.

In the subsequent work shown in the thesis, the challenges presented by the evolution of secondary phase oxides were tackled by controlled environment preparation of CTS samples. Moreover, the state-of-art synchrotron and computational method were used to study the origin of the observed ultra-low thermal conductivity.

First principles calculation revealed that structural disorder contributes to the suppression of thermal conductivity. While group velocity of acoustic phonons, as shown both by experiments and by *ab initio* calculations, is similar in the two polymorphs, a strong anharmonicity characterizes the disordered CTS, resulting in the presence of low-lying optical modes acting as traps for heat transmission. DFT/DFPT simulations and nuclear inelastic scattering combined with high-resolution diffraction studies of the lattice parameters showed higher Grüneisen parameters for specific phonon peaks in disordered CTS. The ultralow thermal conductivity in the disordered sample originates from the random arrangement of Sn and Cu atoms and the inhomogeneous nature of Sn-S bonds. However, complete elimination of secondary phase oxides was not possible due to the low partial pressure of the formation. Despite all limitations, the disordered CTS polymorphs prepared in a controlled environment presented a 10-fold increased  $zT$  than ordered.

Overall, this work provides a novel experimental and *ab-initio* perspective to disordered polymorphs of various materials. In a recent report, Zhang et al.<sup>203</sup> showed a similar transition to a cubic phase in  $\text{CuFeS}_2$  chalcopyrite and showed a dramatically reduced lattice thermal conductivity originating from the enlargement of the Grüneisen parameter caused by disordered atom rearrangement and lattice distortion. Moreover, Baláž et al.<sup>158</sup> have explored the two-step method to produce CTS and other Cu-S-based materials on a large scale.

A high-performance thermoelectric material should have high  $zT$ . However, it is not the only important criterion. As thermoelectric materials have to undergo a temperature gradient for a long span of time, thermal and mechanical stability is also vital. Especially, loss of nano and microstructure, the role of secondary phases, and increased density after thermal cycling can alter the thermoelectric properties of materials. Moreover, there is a crucial need to investigate porous

thermoelectric materials, which use a lower quantity of material suitable for cost-effective, portable, and wearable applications.

Therefore, we investigated CTS samples prepared in various synthesis conditions and by different sintering techniques. Six CTS samples were prepared from ball-milled powder followed by traditional sintering (TS) and open die pressing (ODP)<sup>155</sup>, leading to different microstructures and porosities. These sample's phase and chemical composition were investigated via XRD and EDX. Repeated temperature-dependent thermoelectric measurements revealed that the sample prepared in an open environment was not stable, which was confirmed by significant grain growth and segregation of SnS after TE measurements. Although a small fraction of secondary phase oxides were present in all samples, samples prepared in a controlled environment were stable.

The pressure applied during the ODP seems to stabilize the samples better. Overall, this work showed that CTS samples could stabilize with different proportions of porosity successfully. The low density or TS samples showed ~3 times lower thermal conductivity than the high density or ODP sintered samples. However, we did not observe any significant difference in electrical transport properties between the TS and ODP samples. The best performing stable TS sample presented  $zT \sim 0.45$ , whereas the best performing ODP sample showed  $zT$  of  $\sim 0.34$ , around 700 K, a result clearly due to the ultra-low thermal conductivity of the traditionally sintered, porous sample.

The results presented in this work give a general overview of the effects of different experimental conditions and porosity on CTS samples' stability and TE performance. The continuous evolution of secondary phase oxides can be eliminated by using a highly controlled environment, and a small fraction of secondary phase oxides seem to have little effect on the TE properties and stability of the samples. Similar considerations should hold for other Cu-Sn/Fe-S/Se-based systems, chalcogenides, colusites, chalcopyrite, etc., used for various applications, ranging from photovoltaics to thermoelectricity and LED production.

The successful synthesis using the two-step sample preparation method was further investigated by combining ball-milling with spark plasma sintering (SPS). Three dense CTS samples with nanometric grains and an average domain size below 50 nm were synthesized. The experimental results show that the Seebeck coefficient and electrical resistivity decrease with decreasing domain sizes while the thermal conductivity increases. Experimental investigation showed that a smaller domain size correlates with lower resistivity and degenerate semiconductor-like behavior due to higher carrier concentration. Here it is worth mentioning that ODP and, especially, SPS combined with high-energy ball-milling can preserve the nanostructure of the samples while reaching a full density.

A small grain size generally leads to a higher Seebeck coefficient due to the scattering of charge carriers by the grain boundary, otherwise known as energy filtering. This, however, decreases mobility and, in turn, increases the electrical resistivity. The results present in this work are in contrast with the energy filtering mechanism. The samples with smaller domains are more conductive, and we observe a trend of increasing resistivity with an increase in grain size.

First principles density functional theory (DFT) simulations on various CTS crystallite surfaces revealed localized states near the Fermi level and the absence of band gap, indicating the metallic nature of the surfaces. As a result, the sample with the smallest grain size exhibits the highest  $zT$  of  $\sim 0.4$  at 650 K. Moreover, we have also reported the formation energy per unit atom for vacancy and off-stoichiometry in CTS, as obtained from DFT simulations. After the stoichiometric CTS, Cu-vacant, and Cu-rich systems are energetically more viable, whereas Sn-vacant and Sn-rich systems seem less likely to form. Thermodynamically, these conclusions could be generalized to the whole family of Cu–Sn–S systems. Cu-vacant and Cu-rich systems would be more likely to form than Sn-rich and Sn-poor phases in other Cu–Sn–S/Se-based materials.

Moreover, in this family of materials, Cu vacancy, Cu excess, and Sn vacancy would enable *p*-type doping-like effects, whereas Sn excess showed *n*-type behavior. This method also provides an interesting way for many materials to synergize their electrical and thermal properties.

Recent reports by Cherniushok et al.<sup>204</sup> and Sulaiman et al.<sup>205</sup> show similar cases considering some results presented in our work.

To further improve the thermoelectric performance of CTS, the two-step synthesis method (mechanical alloying + SPS) was combined with Ag substitution at the Sn site.  $\text{Cu}_2\text{Ag}_{(x)}\text{Sn}_{(1-x)}\text{S}_3$  ( $0.05 \geq x \leq 0.25$ ) samples were synthesized, and their thermoelectric properties were investigated using experimental and first principles methods. Chemical maps were collected, Cu, Sn, Ag, and S showed a homogeneous chemical distribution for all the samples. However, samples with  $x \geq 0.20$  showed a non-homogeneous chemical distribution of Ag. Rietveld refinement on XRD data showed a systematic reduction of lattice parameters up to  $x=0.20$ , Ag substitution, confirming successful Ag substitution in CTS. Ab-Initio calculations and experimental band gap measurements revealed a band gap reduction with increasing Ag substitution, resulting in a high power factor.

Interestingly, the  $x = 0.15$  sample presented  $\sim 10$  and  $\sim 3$  fold higher power factor than undoped CTS and the sample with the smallest domain size ( $\sim 12$  nm), respectively. Due to the interplay between electrical and thermal conductivity  $x = 0.125$  and  $x = 0.15$ , samples showed a  $zT \sim 0.5$  at 723 K, which is comparable to the results present in the literature for earth-abundant and eco-friendly thermoelectric materials. The high-power factor of Ag substituted CTS makes it suitable for in-plane thermoelectric devices, a possibility that we started testing in the last part of the thesis work.

We present a preliminary study on in-plane thermoelectric generators, where the  $n$ -type leg was fabricated by AZO (aluminium-doped zinc oxide) and various Cu-based chalcogenides were used as  $p$ -type legs. Four different TEGs were fabricated using  $\text{Cu}_2\text{ZnSnS}_4$  (CZTS),  $\text{Cu}_2\text{ZnSnSe}_4$  (CZTSe),  $\text{Cu}_{2.125}\text{Zn}_{0.875}\text{SnS}_3\text{Se}$  (CZTSSe), and  $\text{Cu}_2\text{SnS}_3$  (CTS) chalcogenides. Thermoelectric transport analysis confirmed the respective  $p$ - and  $n$ -type natures of the chalcogenides and AZO, with their Seebeck coefficients compatible to be coupled in a  $p$ - $n$  device. Besides that, a full-device analysis has been carried out, and several factors affecting the performance of TEGs were investigated, including the composition, density, and presence of secondary phases in

chalcogenide thin films. The maximum power obtained for CZTS, CZTSe, CZTSSe, and CTS TEGs at temperature difference ( $\Delta T$ ) 160 K were ~240, ~50, ~25, and ~75 nW, respectively.

Moreover, sulfurization of the *p*-type CTS leg significantly enhanced the device performance, achieving a maximum power output ~230 nW, which is a staggering 300% increase in performance. The per-unit planar area power output results are comparable to some commercially available ( $\text{Al}_2\text{O}_3/\text{ZnO}$  and  $\text{SnO}_x/\text{ZnO}$ ) thermoelectric generators in this temperature range. However, still lower than the state-of-the-art ( $\text{Bi}_2\text{Te}_3$  and  $\text{Sb}_2\text{Te}_3$ ) generators, which, however, involve expensive and/or potentially toxic materials.

Current research efforts are in progress to replace *n*-type AZO-leg with  $\text{CuFeS}_2$  or  $\text{Cu}_4\text{Sn}_7\text{S}_{16}$ . As shown for the bulk material, the high power factor of  $\text{Cu}_2\text{Ag}_{(x)}\text{Sn}_{(1-x)}\text{S}_3$  ( $0.05 \geq x \leq 0.25$ ) systems could be beneficial to improve further the performance of the thermoelectric devices discussed in this work.

Overall, the present thesis work makes a strong case for the use of disordered materials produced from bottom-up techniques for thermoelectric applications. Various procedures to increase the material's thermoelectric performance and stability are studied. The effects of synthesis and sintering conditions are highlighted, vital to synthesizing reliable and high-performing thermoelectric devices based on sustainable materials. The effect of porosity and grain size on the thermoelectric properties are investigated. The study in the thesis is not limited to materials production, as it also makes a case for functioning thermoelectric generators fabricated from low-cost and facile techniques, paving the path to producing high-performing thermoelectric materials and devices.

## Bibliography

- (1) Timperley, J. Why Fossil Fuel Subsidies Are so Hard to Kill. *Nature* **2021**, 598 (7881), 403–405. <https://doi.org/10.1038/d41586-021-02847-2>.
- (2) Forman, C.; Muritala, I. K.; Pardemann, R.; Meyer, B. Estimating the Global Waste Heat Potential. *Renewable and Sustainable Energy Reviews* **2016**, 57, 1568–1579. <https://doi.org/10.1016/j.rser.2015.12.192>.
- (3) Bian, Q. Waste Heat: The Dominating Root Cause of Current Global Warming. *Environmental Systems Research* **2020**, 9 (1), 8. <https://doi.org/10.1186/s40068-020-00169-2>.
- (4) Piccolino, M. Luigi Galvani and Animal Electricity: Two Centuries after the Foundation of Electrophysiology. *Trends in Neurosciences* **1997**, 20 (10), 443–448. [https://doi.org/10.1016/S0166-2236\(97\)01101-6](https://doi.org/10.1016/S0166-2236(97)01101-6).
- (5) Alessandro Volta. New Memoir about the Animal Electricity Split into Three Letters Sent to Abbot Anton Maria Vassalli, Professor of Physics at the Royal University of Turin. *Physico-Medical Journal of Mr. Brugnatelli* **1794**, 2, 248.
- (6) Seebeck, T. J. Ueber Die Magnetische Polarisation Der Metalle Und Erze Durch Temperaturdifferenz [Magnetic Polarization of Metals and Ores by Temperature Differences]. *Abhandlungen der Koniglichen Akademie der Wissenschaften zu Berlin (in German)* **1826**, 82, 265–373.
- (7) Goldsmid, H. J. *Introduction to Thermoelectricity*; Springer Series in Materials Science; Springer Berlin Heidelberg: Berlin, Heidelberg, 2010; Vol. 121. <https://doi.org/10.1007/978-3-642-00716-3>.
- (8) Beretta, D.; Neophytou, N.; Hodges, J. M.; Kanatzidis, M. G.; Narducci, D.; Martin-Gonzalez, M.; Beekman, M.; Balke, B.; Cerretti, G.; Tremel, W.; Zevalkink, A.; Hofmann, A. I.; Müller, C.; Döring, B.; Campoy-Quiles, M.; Caironi, M. Thermoelectrics: From History, a Window to the Future. *Materials Science and Engineering R: Reports* **2018**, 138 (November 2018), 210–255. <https://doi.org/10.1016/j.mser.2018.09.001>.
- (9) Mao, J.; Liu, Z.; Zhou, J.; Zhu, H.; Zhang, Q.; Chen, G.; Ren, Z. Advances in Thermoelectrics. *Advances in Physics* **2018**, 67 (2), 69–147. <https://doi.org/10.1080/00018732.2018.1551715>.
- (10) Snyder, G. J.; Toberer, E. S. Complex Thermoelectric Materials. *Nature Materials* **2008**, 7 (February), 105–114. <https://doi.org/10.1038/nmat2090>.
- (11) Narducci, D.; Selezneva, E.; Cerofolini, G.; Frabboni, S.; Ottaviani, G. Impact of Energy Filtering and Carrier Localization on the Thermoelectric Properties of Granular Semiconductors. *Journal of Solid State Chemistry* **2012**, 193, 19–25. <https://doi.org/10.1016/j.jssc.2012.03.032>.
- (12) Goldsmid, H. Porous Thermoelectric Materials. *Materials* **2009**, 2 (3), 903–910. <https://doi.org/10.3390/ma2030903>.
- (13) Zhao, L.; Chen, C.; Pan, L.; Hu, X.; Lu, C.; Wang, Y. Magnetic Iron Doping in Cu<sub>2</sub>SnS<sub>3</sub> Ceramics for Enhanced Thermoelectric Transport Properties. *Journal of Applied Physics* **2019**, 125 (9), 095107. <https://doi.org/10.1063/1.5065074>.
- (14) Zeier, W. G. New Tricks for Optimizing Thermoelectric Materials. *Current Opinion in Green and Sustainable Chemistry* **2017**, 4, 23–28. <https://doi.org/10.1016/j.cogsc.2017.02.003>.
- (15) Balout, H.; Boulet, P.; Record, M. C. Strain-Induced Electronic Band Convergence: Effect on the Seebeck Coefficient of Mg<sub>2</sub>Si for Thermoelectric Applications. *Journal of Molecular Modeling* **2017**, 23 (4). <https://doi.org/10.1007/s00894-017-3304-1>.
- (16) Zhao, P.; Yu, F.; Wang, B.; Zhao, H.; Chen, C.; Wang, D.; Ying, P.; Wu, Y.;

- Li, P.; Zhang, B.; Liu, B.; Zhao, Z.; Hu, W.; Yu, D.; He, J.; Liu, Z.; Xu, B.; Tian, Y. Porous Bismuth Antimony Telluride Alloys with Excellent Thermoelectric and Mechanical Properties. *Journal of Materials Chemistry A* **2021**, *9* (8), 4990–4999. <https://doi.org/10.1039/D0TA09795K>.
- (17) Hong, M.; Chen, Z. G.; Zou, J. Fundamental and Progress of Bi<sub>2</sub>Te<sub>3</sub>-Based Thermoelectric Materials. *Chinese Physics B* **2018**, *27* (4). <https://doi.org/10.1088/1674-1056/27/4/048403>.
- (18) Lalonde, A. D.; Pei, Y.; Wang, H.; Jeffrey Snyder, G. Lead Telluride Alloy Thermoelectrics. *Materials Today* **2011**, *14* (11), 526–532. [https://doi.org/10.1016/S1369-7021\(11\)70278-4](https://doi.org/10.1016/S1369-7021(11)70278-4).
- (19) Duong, A. T.; Nguyen, V. Q.; Duvjir, G.; Duong, V. T.; Kwon, S.; Song, J. Y.; Lee, J. K.; Lee, J. E.; Park, S.; Min, T.; Lee, J.; Kim, J.; Cho, S. Achieving ZT=2.2 with Bi-Doped n-Type SnSe Single Crystals. *Nature Communications* **2016**, *7*, 1–6. <https://doi.org/10.1038/ncomms13713>.
- (20) Zhou, C.; Lee, Y. K.; Yu, Y.; Byun, S.; Luo, Z. Z.; Lee, H.; Ge, B.; Lee, Y. L.; Chen, X.; Lee, J. Y.; Cojocaru-Mirédin, O.; Chang, H.; Im, J.; Cho, S. P.; Wuttig, M.; Dravid, V. P.; Kanatzidis, M. G.; Chung, I. Polycrystalline SnSe with a Thermoelectric Figure of Merit Greater than the Single Crystal. *Nature Materials* **2021**. <https://doi.org/10.1038/s41563-021-01064-6>.
- (21) Kandemir, A.; Ozden, A.; Cagin, T.; Sevik, C. Thermal Conductivity Engineering of Bulk and One-Dimensional Si-Ge Nanoarchitectures. *Science and Technology of Advanced Materials* **2017**, *18* (1), 187–196. <https://doi.org/10.1080/14686996.2017.1288065>.
- (22) Yin, Y.; Tudu, B.; Tiwari, A. Recent Advances in Oxide Thermoelectric Materials and Modules. *Vacuum* **2017**, *146*, 356–374. <https://doi.org/10.1016/j.vacuum.2017.04.015>.
- (23) Cheikh, D.; Hogan, B. E.; Vo, T.; Von Allmen, P.; Lee, K.; Sniadak, D. M.; Zevalkink, A.; Dunn, B. S.; Fleurial, J. P.; Bux, S. K. Praseodymium Telluride: A High-Temperature, High-ZT Thermoelectric Material. *Joule* **2018**, *2* (4), 698–709. <https://doi.org/10.1016/j.joule.2018.01.013>.
- (24) Han, C.; Sun, Q.; Li, Z.; Dou, S. X. Thermoelectric Enhancement of Different Kinds of Metal Chalcogenides. *Advanced Energy Materials* **2016**, *6* (15). <https://doi.org/10.1002/aenm.201600498>.
- (25) Kovalenker, V. A. Mohite, CU<sub>2</sub>SNS<sub>3</sub>, a New Sulfide of Tin and Copper. *International Geology Review* **1983**, *25* (1), 117–120. <https://doi.org/10.1080/00206818309466683>.
- (26) Lohani, K.; Isotta, E.; Ataollahi, N.; Fanciulli, C.; Chiappini, A.; Scardi, P. Ultra-Low Thermal Conductivity and Improved Thermoelectric Performance in Disordered Nanostructured Copper Tin Sulphide (Cu<sub>2</sub>SnS<sub>3</sub>, CTS). *Journal of Alloys and Compounds* **2020**, *830*. <https://doi.org/10.1016/j.jallcom.2020.154604>.
- (27) Hu, L.; Luo, Y.; Fang, Y. W.; Qin, F.; Cao, X.; Xie, H.; Liu, J.; Dong, J.; Sanson, A.; Giarola, M.; Tan, X.; Zheng, Y.; Suwardi, A.; Huang, Y.; Hippalgaonkar, K.; He, J.; Zhang, W.; Xu, J.; Yan, Q.; Kanatzidis, M. G. High Thermoelectric Performance through Crystal Symmetry Enhancement in Triply Doped Diamondoid Compound Cu<sub>2</sub>SnSe<sub>3</sub>. *Advanced Energy Materials* **2021**, *11* (42). <https://doi.org/10.1002/aenm.202100661>.
- (28) Zhang, D.; Zhang, B.; Zhou, Z.; Peng, K.; Wu, H.; Wang, H.; Wang, G.; Han, G.; Wang, G.; Zhou, X.; Lu, X. Ultralow Lattice Thermal Conductivity of Cubic CuFeS<sub>2</sub> Induced by Atomic Disorder. *Chemistry of Materials* **2021**. <https://doi.org/10.1021/acs.chemmater.1c03785>.
- (29) Zhai, H.; Xiao, Y.; Zhao, L.-D.; Tan, G.; Tang, X. Large Effective Mass and Low Lattice Thermal Conductivity Contributing to High Thermoelectric Performance of Zn-Doped Cu<sub>5</sub>Sn<sub>2</sub>Se<sub>7</sub>. *Journal of Alloys and Compounds*

- 2020, 826, 154154. <https://doi.org/10.1016/j.jallcom.2020.154154>.
- (30) Deng, T.; Qiu, P.; Xing, T.; Zhou, Z.; Wei, T. R.; Ren, D.; Xiao, J.; Shi, X.; Chen, L. A Low-Cost and Eco-Friendly Br-Doped Cu<sub>7</sub>Sn<sub>3</sub>S<sub>10</sub> Thermoelectric Compound With a Round Unity. *Journal of Materials Chemistry A* **2021**, *9* (12), 7946–7954. <https://doi.org/10.1039/d0ta12042a>.
- (31) Nagaoka, A.; Yoshino, K.; Masuda, T.; Sparks, T. D.; Scarpulla, M. A.; Nishioka, K. Environmentally Friendly Thermoelectric Sulphide Cu<sub>2</sub>ZnSnS<sub>4</sub> Single Crystals Achieving a 1.6 Dimensionless Figure of Merit ZT. *Journal of Materials Chemistry A* **2021**. <https://doi.org/10.1039/d1ta02978a>.
- (32) Xu, X.; Zhao, H.; Hu, X.; Pan, L.; Chen, C.; Li, D.; Wang, Y. Synergistic Role of Ni-Doping in Electrical and Phonon Transport Properties of Cu<sub>2</sub>Sn<sub>1-x</sub>Ni<sub>x</sub>S<sub>3</sub>. *Journal of Alloys and Compounds* **2017**, *728*, 701–708. <https://doi.org/10.1016/j.jallcom.2017.08.227>.
- (33) Tan, Q.; Sun, W.; Li, Z.; Li, J. F. Enhanced Thermoelectric Properties of Earth-Abundant Cu<sub>2</sub>SnS<sub>3</sub> via In Doping Effect. *Journal of Alloys and Compounds* **2016**, *672*, 558–563. <https://doi.org/10.1016/j.jallcom.2016.02.185>.
- (34) Shen, Y.; Li, C.; Huang, R.; Tian, R.; Ye, Y.; Pan, L.; Koumoto, K.; Zhang, R.; Wan, C.; Wang, Y. Eco-Friendly p-Type Cu<sub>2</sub>SnS<sub>3</sub> Thermoelectric Material: Crystal Structure and Transport Properties. *Scientific Reports* **2016**, *6* (1), 32501. <https://doi.org/10.1038/srep32501>.
- (35) Zhang, Z.; Zhao, H.; Wang, Y.; Hu, X.; Lyu, Y.; Cheng, C.; Pan, L.; Lu, C. Role of Crystal Transformation on the Enhanced Thermoelectric Performance in Mn-Doped Cu<sub>2</sub>SnS<sub>3</sub>. *Journal of Alloys and Compounds* **2019**, *780*, 618–625. <https://doi.org/10.1016/j.jallcom.2018.11.329>.
- (36) Zhao, H.; Xu, X.; Li, C.; Tian, R.; Zhang, R.; Huang, R.; Lyu, Y.; Li, D.; Hu, X.; Pan, L.; Wang, Y. Cobalt-Doping in Cu<sub>2</sub>SnS<sub>3</sub>: Enhanced Thermoelectric Performance by Synergy of Phase Transition and Band Structure Modification. *Journal of Materials Chemistry A* **2017**, *5* (44), 23267–23275. <https://doi.org/10.1039/c7ta07140j>.
- (37) Deng, T.; Qiu, P.; Song, Q.; Chen, H.; Wei, T.-R.; Xi, L.; Shi, X.; Chen, L. Thermoelectric Properties of Non-Stoichiometric Cu<sub>2+x</sub>Sn<sub>1-x</sub>S<sub>3</sub> Compounds. *Journal of Applied Physics* **2019**, *126* (8), 085111. <https://doi.org/10.1063/1.5115195>.
- (38) Pavan Kumar, V.; Lemoine, P.; Carnevali, V.; Guérou, G.; Lebedev, O. I.; Boullay, P.; Raveau, B.; Al Rahal Al Orabi, R.; Fornari, M.; Prestipino, C.; Menut, D.; Candolfi, C.; Malaman, B.; Juraszek, J.; Guilmeau, E. Ordered Sphalerite Derivative Cu<sub>5</sub>Sn<sub>2</sub>S<sub>7</sub>: A Degenerate Semiconductor with High Carrier Mobility in the Cu–Sn–S Diagram. *Journal of Materials Chemistry A* **2021**, *9* (17), 10812–10826. <https://doi.org/10.1039/D1TA01615F>.
- (39) Baláz, P.; Dutková, E.; Levinský, P.; Daneu, N.; Kubičková, L.; Knížek, K.; Baláz, M.; Navrátil, J.; Kašparová, J.; Ksenofontov, V.; Möller, A.; Hejtmánek, J. Enhanced Thermoelectric Performance of Chalcopyrite Nanocomposite via Co-Milling of Synthetic and Natural Minerals. *Materials Letters* **2020**, *275* (June), 128107. <https://doi.org/10.1016/j.matlet.2020.128107>.
- (40) Deng, T.; Wei, T. R.; Song, Q.; Xu, Q.; Ren, D.; Qiu, P.; Shi, X.; Chen, L. Thermoelectric Properties of N-Type Cu<sub>4</sub>Sn<sub>7</sub>S<sub>16</sub>-Based Compounds. *RSC Advances* **2019**, *9* (14), 7826–7832. <https://doi.org/10.1039/c9ra00077a>.
- (41) Siyar, M.; Cho, J. Y.; Youn, Y.; Han, S.; Kim, M.; Bae, S. H.; Park, C. Effect of Annealing Temperature on the Phase Transition, Band Gap and Thermoelectric Properties of Cu<sub>2</sub>SnSe<sub>3</sub>. *Journal of Materials Chemistry C* **2018**, *6* (7), 1780–1788. <https://doi.org/10.1039/c7tc05180h>.
- (42) Lohani, K.; Isotta, E.; Ataollahi, N.; Fanciulli, C.; Chiappini, A.; Scardi, P. Ultra-Low Thermal Conductivity and Improved Thermoelectric Performance

- in Disordered Nanostructured Copper Tin Sulphide (Cu<sub>2</sub>SnS<sub>3</sub>, CTS). *Journal of Alloys and Compounds* **2020**, 830 (C), 154604. <https://doi.org/10.1016/j.jallcom.2020.154604>.
- (43) K. Rademann, V.S. Raghuvanshi, A. H. Crystallization and Growth Mechanisms of Nanostructures in Silicate Glass. In *Glass Nanocomposites Synthesis, Properties and Applications*; Basudeb Karmakar, K. R. and A. L. S., Ed.; 2016; pp 90–110. <https://doi.org/10.1016/B978-0-323-39309-6.00003-1>.
- (44) Vedernikov, M. V.; Iordanishvili, E. K. A.F. Ioffe and Origin of Modern Semiconductor Thermoelectric Energy Conversion. *17th International Conference on Thermoelectrics* **1998**, No. 1 998, 37–42. <https://doi.org/10.1109/ict.1998.740313>.
- (45) Zhu, H.; Mao, J.; Li, Y.; Sun, J.; Wang, Y.; Zhu, Q.; Li, G.; Song, Q.; Zhou, J.; Fu, Y.; He, R.; Tong, T.; Liu, Z.; Ren, W.; You, L.; Wang, Z.; Luo, J.; Sotnikov, A.; Bao, J.; Nielsch, K.; Chen, G.; Singh, D. J.; Ren, Z. Discovery of TaFeSb-Based Half-Heuslers with High Thermoelectric Performance. *Nature Communications* **2019**, 10 (1), 1–8. <https://doi.org/10.1038/s41467-018-08223-5>.
- (46) Wei, T. R.; Qin, Y.; Deng, T.; Song, Q.; Jiang, B.; Liu, R.; Qiu, P.; Shi, X.; Chen, L. Copper Chalcogenide Thermoelectric Materials. *Science China Materials* **2019**, 62 (1), 8–24. <https://doi.org/10.1007/s40843-018-9314-5>.
- (47) Berg, D. M.; Djemour, R.; Gütay, L.; Siebentritt, S.; Dale, P. J.; Fontane, X.; Izquierdo-Roca, V.; Pérez-Rodríguez, A. Raman Analysis of Monoclinic Cu<sub>2</sub>SnS<sub>3</sub> Thin Films. *Applied Physics Letters* **2012**, 100 (19). <https://doi.org/10.1063/1.4712623>.
- (48) Oliva, F.; Arqués, L.; Acebo, L.; Guc, M.; Sánchez, Y.; Alcobé, X.; Pérez-Rodríguez, A.; Saucedo, E.; Izquierdo-Roca, V. Characterization of Cu<sub>2</sub>SnS<sub>3</sub> Polymorphism and Its Impact on Optoelectronic Properties. *Journal of Materials Chemistry A* **2017**, 5 (45), 23863–23871. <https://doi.org/10.1039/C7TA08705E>.
- (49) Zawadzki, P.; Baranowski, L. L.; Peng, H.; Toberer, E. S.; Ginley, D. S.; Tumas, W.; Zakutayev, A.; Lany, S. Evaluation of Photovoltaic Materials within the Cu-Sn-S Family. *Applied Physics Letters* **2013**, 103 (25), 1–6. <https://doi.org/10.1063/1.4851896>.
- (50) Nguyen, H. T. T.; Zakhvalinskii, V. S.; Pham, T. T.; Dang, N. T.; Vu, T. V.; Pilyuk, E. A.; Rodriguez, G. V. Structural Properties and Variable-Range Hopping Conductivity of Cu<sub>2</sub>SnS<sub>3</sub>. *Materials Research Express* **2019**, 6 (5), 055915. <https://doi.org/10.1088/2053-1591/ab0775>.
- (51) Isotta, E.; Fanciulli, C.; Pugno, N. M.; Scardi, P. Effect of the Order-Disorder Transition on the Seebeck Coefficient of Nanostructured Thermoelectric Cu<sub>2</sub>ZnSnS<sub>4</sub>. *Nanomaterials* **2019**, \ (762), 1–11. <https://doi.org/10.3390/nano9050762>.
- (52) Kapusta, K.; Drygas, M.; Janik, J. F.; Jelen, P.; Bucko, M. M.; Olejniczak, Z. From Magnetic Cubic Pre-Kesterite to Semiconducting Tetragonal Kesterite Cu<sub>2</sub>ZnSnS<sub>4</sub> Nanopowders via the Mechanochemically Assisted Route. *Journal of Alloys and Compounds* **2019**, 770, 981–988. <https://doi.org/10.1016/j.jallcom.2018.08.135>.
- (53) Baranowski, L. Disorder on Carrier Transport in Cu<sub>2</sub>SnS<sub>3</sub>. <https://doi.org/10.1103/PhysRevApplied.4.044017>.
- (54) Rietveld, H. M. Line Profiles of Neutron Powder-Diffraction Peaks for Structure Refinement. *Acta Crystallographica* **1967**, 22 (1), 151–152. <https://doi.org/10.1107/S0365110X67000234>.
- (55) McCusker, L. B.; Von Dreele, R. B.; Cox, D. E.; Louër, D.; Scardi, P. Rietveld Refinement Guidelines. *Journal of Applied Crystallography* **1999**, 32 (1), 36–

50. <https://doi.org/10.1107/S0021889898009856>.
- (56) Scardi, P.; Azanza Ricardo, C. L.; Perez-Demydenko, C.; Coelho, A. A. Whole Powder Pattern Modelling Macros for TOPAS. *Journal of Applied Crystallography* **2018**, *51* (6), 1752–1765. <https://doi.org/10.1107/s160057671801289x>.
- (57) Coelho, A. A. TOPAS and TOPAS-Academic: An Optimization Program Integrating Computer Algebra and Crystallographic Objects Written in C++. *Journal of Applied Crystallography* **2018**, *51* (1), 210–218. <https://doi.org/10.1107/S1600576718000183>.
- (58) Syafiq, U.; Ataollahi, N.; Maggio, R. D.; Scardi, P. Solution-Based Synthesis and Characterization of Cu<sub>2</sub>ZnSnS<sub>4</sub> Nanocrystals. *Molecules* **2019**, *24* (3454). <https://doi.org/10.3390/molecules24193454>.
- (59) Isotta, E.; Pugno, N. M.; Scardi, P. Nanostructured Kesterite (Cu<sub>2</sub>ZnSnS<sub>4</sub>) for Applications in Thermoelectric Devices. *Powder Diffraction* **2019**, *32* (S1), 42–47. <https://doi.org/10.1017/S0885715619000277>.
- (60) Guan, H.; Shen, H.; Gao, C.; He, X. Structural and Optical Properties of Cu<sub>2</sub>SnS<sub>3</sub> and Cu<sub>3</sub>SnS<sub>4</sub> Thin Films by Successive Ionic Layer Adsorption and Reaction. *Journal of Materials Science: Materials in Electronics* **2013**, *24* (5), 1490–1494. <https://doi.org/10.1007/s10854-012-0960-x>.
- (61) Ataollahi, N.; Bazerla, F.; Malerba, C.; Chiappini, A.; Ferrari, M.; Di Maggio, R.; Scardi, P. Synthesis and Post-Annealing of Cu<sub>2</sub>ZnSnS<sub>4</sub> Absorber Layers Based on Oleylamine/1-Dodecanethiol. *Materials* **2019**, *12* (20), 3320. <https://doi.org/10.3390/ma12203320>.
- (62) Lokhande, A. C.; Pawar, S. A.; Jo, E.; He, M.; Shelke, A.; Lokhande, C. D.; Kim, J. H. Amines Free Environmentally Friendly Rapid Synthesis of Cu<sub>2</sub>SnS<sub>3</sub> Nanoparticles. *Optical Materials* **2016**, *58*, 268–278. <https://doi.org/10.1016/j.optmat.2016.03.032>.
- (63) Dong, Y.; He, J.; Li, X.; Zhou, W.; Chen, Y.; Sun, L.; Yang, P.; Chu, J. Synthesis and Optimized Sulfurization Time of Cu<sub>2</sub>SnS<sub>3</sub> Thin Films Obtained from Stacked Metallic Precursors for Solar Cell Application. *Materials Letters* **2015**, *160*, 468–471. <https://doi.org/10.1016/j.matlet.2015.08.028>.
- (64) Wang, W.; Shen, H.; Li, J. Rapid Synthesis of Hollow CTS Nanoparticles Using Microwave Irradiation. *Materials Letters* **2013**, *111*, 5–8. <https://doi.org/10.1016/j.matlet.2013.08.038>.
- (65) Fernandes, P. A.; Salomé, P. M. P.; Da Cunha, A. F. Cu<sub>x</sub>SnS<sub>x+1</sub> (x = 2, 3) Thin Films Grown by Sulfurization of Metallic Precursors Deposited by Dc Magnetron Sputtering. *Physica Status Solidi (C) Current Topics in Solid State Physics* **2010**, *7* (3–4), 901–904. <https://doi.org/10.1002/pssc.200982746>.
- (66) Fernandes, P. A.; Salomé, P. M. P.; Cunha, A. F. D. A Study of Ternary Cu<sub>2</sub>SnS<sub>3</sub> and Cu<sub>3</sub>SnS<sub>4</sub> Thin Films Prepared by Sulfurizing Stacked Metal Precursors. *Journal of Physics D: Applied Physics* **2010**, *43* (21). <https://doi.org/10.1088/0022-3727/43/21/215403>.
- (67) Raadik, T.; Grossberg, M.; Krustok, J.; Kauk-Kuusik, M.; Crovetto, A.; Bolt Ettliger, R.; Hansen, O.; Schou, J. Temperature Dependent Photoreflectance Study of Cu<sub>2</sub>SnS<sub>3</sub> Thin Films Produced by Pulsed Laser Deposition. *Applied Physics Letters* **2017**, *110* (26), 3–7. <https://doi.org/10.1063/1.4990657>.
- (68) Zhai, Y.-T.; Chen, S.; Yang, J.-H.; Xiang, H.-J.; Gong, X.-G.; Walsh, A.; Kang, J.; Wei, S.-H. Structural Diversity and Electronic Properties of Cu<sub>2</sub>SnX<sub>3</sub> (X=S, Se): A First-Principles Investigation. *Physical Review B* **2011**, *84* (7), 075213. <https://doi.org/10.1103/PhysRevB.84.075213>.
- (69) Berg, D. M.; Djemour, R.; Gütay, L.; Zoppi, G.; Siebentritt, S.; Dale, P. J. Thin Film Solar Cells Based on the Ternary Compound Cu<sub>2</sub>SnS<sub>3</sub>. *Thin Solid Films* **2012**, *520* (19), 6291–6294. <https://doi.org/10.1016/j.tsf.2012.05.085>.
- (70) Tan, Q.; Sun, W.; Li, Z.; Li, J.-F. Enhanced Thermoelectric Properties of

- Earth-Abundant Cu<sub>2</sub>SnS<sub>3</sub> via In Doping Effect. *Journal of Alloys and Compounds* **2016**, *672*, 558–563. <https://doi.org/10.1016/j.jallcom.2016.02.185>.
- (71) Lohani, K.; Nautiyal, H.; Ataollahi, N.; Fanciulli, C.; Sergueev, I.; Etter, M.; Scardi, P. Experimental and Ab Initio Study of Cu<sub>2</sub>SnS<sub>3</sub> (CTS) Polymorphs for Thermoelectric Applications. *The Journal of Physical Chemistry C* **2021**, *125* (1), 178–188. <https://doi.org/10.1021/acs.jpcc.0c09139>.
- (72) Sootsman, J. R.; Chung, D. Y.; Kanatzidis, M. G. New and Old Concepts in Thermoelectric Materials. *Angewandte Chemie - International Edition*. 2009, pp 8616–8639. <https://doi.org/10.1002/anie.200900598>.
- (73) Mao, J.; Liu, Z.; Ren, Z. Size Effect in Thermoelectric Materials. *npj Quantum Materials* **2016**, *1* (1), 16028. <https://doi.org/10.1038/npjquantmats.2016.28>.
- (74) Mehta, R. J.; Zhang, Y.; Karthik, C.; Singh, B.; Siegel, R. W.; Borca-Tasciuc, T.; Ramanath, G. A New Class of Doped Nanobulk High-Figure-of-Merit Thermoelectrics by Scalable Bottom-up Assembly. *Nature Materials* **2012**, *11* (3), 233–240. <https://doi.org/10.1038/nmat3213>.
- (75) Ibáñez, M.; Luo, Z.; Genç, A.; Piveteau, L.; Ortega, S.; Cadavid, D.; Dobrozhan, O.; Liu, Y.; Nachtegaal, M.; Zebarjadi, M.; Arbiol, J.; Kovalenko, M. V.; Cabot, A. High-Performance Thermoelectric Nanocomposites from Nanocrystal Building Blocks. *Nature Communications* **2016**, *7* (May 2015), 1–7. <https://doi.org/10.1038/ncomms10766>.
- (76) Fernandes, P. A.; Salomé, P. M. P.; Cunha, A. F. D. A Study of Ternary Cu<sub>2</sub>SnS<sub>3</sub> and Cu<sub>3</sub>SnS<sub>4</sub> Thin Films Prepared by Sulfurizing Stacked Metal Precursors. *Journal of Physics D: Applied Physics* **2010**, *43* (21). <https://doi.org/10.1088/0022-3727/43/21/215403>.
- (77) Pallavolu, M. R.; Minnam Reddy, V. R.; Pejjai, B.; Jeong, D. seob; Park, C. Effect of Sulfurization Temperature on the Phase Purity of Cu<sub>2</sub>SnS<sub>3</sub> Thin Films Deposited via High Vacuum Sulfurization. *Applied Surface Science* **2018**, *462* (August), 641–648. <https://doi.org/10.1016/j.apsusc.2018.08.112>.
- (78) Chen, Q.; Maeda, T.; Wada, T. Optical Properties and Electronic Structures of Cu<sub>2</sub>SnS<sub>3</sub>, Cu<sub>2</sub>GeS<sub>3</sub>, and Their Solid Solution Cu<sub>2</sub>(Ge,Sn)S<sub>3</sub>. In *Japanese Journal of Applied Physics*; Japan Society of Applied Physics, 2018; Vol. 57. <https://doi.org/10.7567/JJAP.57.08RC20>.
- (79) Raadik, T.; Grossberg, M.; Krustok, J.; Kauk-Kuusik, M.; Crovetto, A.; Bolt Etlinger, R.; Hansen, O.; Schou, J. Temperature Dependent Photoreflectance Study of Cu<sub>2</sub>SnS<sub>3</sub> Thin Films Produced by Pulsed Laser Deposition. *Applied Physics Letters* **2017**, *110* (26). <https://doi.org/10.1063/1.4990657>.
- (80) Xi, L.; Zhang, Y. B.; Shi, X. Y.; Yang, J.; Shi, X.; Chen, L. D.; Zhang, W.; Yang, J.; Singh, D. J. Chemical Bonding, Conductive Network, and Thermoelectric Performance of the Ternary Semiconductors Cu<sub>2</sub>SnX<sub>3</sub> (X= Se, S) from First Principles. *Physical Review B - Condensed Matter and Materials Physics* **2012**, *86* (15), 1–14. <https://doi.org/10.1103/PhysRevB.86.155201>.
- (81) Baranowski, L. L.; McLaughlin, K.; Zawadzki, P.; Lany, S.; Norman, A.; Hempel, H.; Eichberger, R.; Unold, T.; Toberer, E. S.; Zakutayev, A. Effects of Disorder on Carrier Transport in Cu<sub>2</sub>SnS<sub>3</sub>. *Physical Review Applied* **2015**, *4* (4), 044017. <https://doi.org/10.1103/PhysRevApplied.4.044017>.
- (82) Zawadzki, P.; Zakutayev, A.; Lany, S. Entropy-Driven Clustering in Tetrahedrally Bonded Multinary Materials. *Physical Review Applied* **2015**, *3* (3), 034007. <https://doi.org/10.1103/PhysRevApplied.3.034007>.
- (83) Crovetto, A.; Chen, R.; Etlinger, R. B.; Cazzaniga, A. C.; Schou, J.; Persson, C.; Hansen, O. Dielectric Function and Double Absorption Onset of Monoclinic Cu<sub>2</sub>SnS<sub>3</sub>: Origin of Experimental Features Explained by First-Principles Calculations. *Solar Energy Materials and Solar Cells* **2016**, *154*,

- 121–129. <https://doi.org/10.1016/j.solmat.2016.04.028>.
- (84) Chen, Q.; Maeda, T.; Wada, T. Optical Properties and Electronic Structures of Cu<sub>2</sub>SnS<sub>3</sub>, Cu<sub>2</sub>GeS<sub>3</sub>, and Their Solid Solution. *Jpn. J. Appl. Phys* **2018**, *57*.  
<https://doi.org/https://iopscience.iop.org/article/10.7567/JJAP.57.08RC20>.
- (85) Kresse, G.; Furthmüller, J. Efficient Iterative Schemes for Ab Initio Total-Energy Calculations Using a Plane-Wave Basis Set. *Physical Review B - Condensed Matter and Materials Physics* **1996**, *54* (16), 11169–11186. <https://doi.org/10.1103/PhysRevB.54.11169>.
- (86) Kresse, G.; Furthmüller, J. Efficiency of Ab-Initio Total Energy Calculations for Metals and Semiconductors Using a Plane-Wave Basis Set. *Computational Materials Science* **1996**, *6* (1), 15–50. [https://doi.org/10.1016/0927-0256\(96\)00008-0](https://doi.org/10.1016/0927-0256(96)00008-0).
- (87) Perdew, J. P.; Burke, K.; Ernzerhof, M. Generalized Gradient Approximation Made Simple. *Physical Review Letters* **1996**, *77* (18), 3865–3868. <https://doi.org/10.1103/PhysRevLett.77.3865>.
- (88) Pack, J. D.; Monkhorst, H. J. “special Points for Brillouin-Zone Integrations”- a Reply. *Physical Review B* **1977**, *16* (4), 1748–1749. <https://doi.org/10.1103/PhysRevB.16.1748>.
- (89) Hinuma, Y.; Pizzi, G.; Kumagai, Y.; Oba, F.; Tanaka, I. Band Structure Diagram Paths Based on Crystallography. *Computational Materials Science* **2017**, *128*, 140–184. <https://doi.org/10.1016/j.commatsci.2016.10.015>.
- (90) Togo, A.; Tanaka, I. First Principles Phonon Calculations in Materials Science. *Scripta Materialia* **2015**, *108*, 1–5. <https://doi.org/10.1016/j.scriptamat.2015.07.021>.
- (91) Perdew, J. P.; Zunger, A. Self-Interaction Correction to Density-Functional Approximations for Many-Electron Systems. *Physical Review B* **1981**, *23* (10), 5048–5079. <https://doi.org/10.1103/PhysRevB.23.5048>.
- (92) Isotta, E.; Mukherjee, B.; Fanciulli, C.; Pugno, N. M.; Scardi, P. Order-Disorder Transition in Kesterite Cu<sub>2</sub>ZnSnS<sub>4</sub>: Thermopower Enhancement via Electronic Band Structure Modification. *Journal of Physical Chemistry C* **2020**, *124* (13), 7091–7096. <https://doi.org/10.1021/acs.jpcc.0c00886>.
- (93) Tiwari, D.; Koehler, T.; Klenk, R.; Fermin, D. J. Solution Processed Single-Phase Cu<sub>2</sub>SnS<sub>3</sub> Films: Structure and Photovoltaic Performance. *Sustainable Energy & Fuels* **2017**, *1* (4), 899–906. <https://doi.org/10.1039/c7se00150a>.
- (94) Shigemi, A.; Maeda, T.; Wada, T. First-Principles Calculation of Cu<sub>2</sub>SnS<sub>3</sub> and Related Compounds. *Physica Status Solidi (B) Basic Research* **2015**, *252* (6), 1230–1234. <https://doi.org/10.1002/pssb.201400346>.
- (95) Gajaria, T. K.; Dabhi, S. D.; Jha, P. K. Ab Initio Energetics and Thermoelectric Profiles of Gallium Pnictide Polytypes. *Scientific Reports* **2019**, *9* (1), 1–20. <https://doi.org/10.1038/s41598-019-41982-9>.
- (96) Lin, S.; Li, W.; Li, S.; Zhang, X.; Chen, Z.; Xu, Y.; Chen, Y.; Pei, Y. High Thermoelectric Performance of Ag<sub>9</sub>GaSe<sub>6</sub> Enabled by Low Cutoff Frequency of Acoustic Phonons. *Joule* **2017**, *1* (4), 816–830. <https://doi.org/10.1016/j.joule.2017.09.006>.
- (97) Zhao, L. D.; Lo, S. H.; Zhang, Y.; Sun, H.; Tan, G.; Uher, C.; Wolverton, C.; Dravid, V. P.; Kanatzidis, M. G. Ultralow Thermal Conductivity and High Thermoelectric Figure of Merit in SnSe Crystals. *Nature* **2014**, *508* (7496), 373–377. <https://doi.org/10.1038/nature13184>.
- (98) Toberer, E. S.; Baranowski, L. L.; Dames, C. Advances in Thermal Conductivity. *Annual Review of Materials Research* **2012**, *42* (1), 179–209. <https://doi.org/10.1146/annurev-matsci-070511-155040>.
- (99) Zhang, S.; Xu, B.; Lin, Y.; Nan, C.; Liu, W. First-Principles Study of the Layered Thermoelectric Material TiNBr. **2018**.

- (100) Zhang, R.; Wen, X.; Xu, F.; Zhang, Q.; Sun, L. A Density Functional Theory Study of the Cu<sub>2</sub>ZnSnS<sub>4</sub> Monolayer as a Photo-Electrointegrated Catalyst for Water Splitting and Hydrogen Evolution. *The Journal of Physical Chemistry C* **2020**, *124* (22), 11922–11929. <https://doi.org/10.1021/acs.jpcc.0c02103>.
- (101) Grin, Y. Inhomogeneity and Anisotropy of Chemical Bonding and Thermoelectric Properties of Materials. *Journal of Solid State Chemistry* **2019**, *274* (November 2018), 329–336. <https://doi.org/10.1016/j.jssc.2018.12.055>.
- (102) Bessas, D.; Sergueev, I.; Wille, H. C.; Peron, J.; Ebling, D.; Hermann, R. P. Lattice Dynamics in Bi<sub>2</sub>Te<sub>3</sub> and Sb<sub>2</sub>Te<sub>3</sub>: Te and Sb Density of Phonon States. *Physical Review B - Condensed Matter and Materials Physics* **2012**, *86* (22), 1–9. <https://doi.org/10.1103/PhysRevB.86.224301>.
- (103) Sergueev, I.; Hermann, R. P.; Bessas, D.; Pelzer, U.; Angst, M.; Schweika, W.; McGuire, M. A.; Sefat, A. S.; Sales, B. C.; Mandrus, D.; Ruffer, R. Effect of Pressure, Temperature, Fluorine Doping, and Rare Earth Elements on the Phonon Density of States of LFeAsO Studied by Nuclear Inelastic Scattering. *Physical Review B - Condensed Matter and Materials Physics* **2013**, *87* (6), 1–9. <https://doi.org/10.1103/PhysRevB.87.064302>.
- (104) Sergueev, I.; Glazyrin, K.; Kantor, I.; McGuire, M. A.; Chumakov, A. I.; Klobes, B.; Sales, B. C.; Hermann, R. P. Quenching Rattling Modes in Skutterudites with Pressure. *Physical Review B - Condensed Matter and Materials Physics* **2015**, *91* (22), 2–8. <https://doi.org/10.1103/PhysRevB.91.224304>.
- (105) Filik, J.; Ashton, A. W.; Chang, P. C. Y.; Chater, P. A.; Day, S. J.; Drakopoulos, M.; Gerring, M. W.; Hart, M. L.; Magdysyuk, O. V.; Michalik, S.; Smith, A.; Tang, C. C.; Terrill, N. J.; Wharmby, M. T.; Wilhelm, H. Processing Two-Dimensional X-Ray Diffraction and Small-Angle Scattering Data in DAWN 2. *Journal of Applied Crystallography* **2017**, *50* (3), 959–966. <https://doi.org/10.1107/S1600576717004708>.
- (106) Lohani, K.; Fanciulli, C.; Scardi, P. Effects of Preparation Procedures and Porosity on Thermoelectric Bulk Samples of Cu<sub>2</sub>SnS<sub>3</sub> (CTS). *Materials* **2022**, *15* (3), 712. <https://doi.org/10.3390/ma15030712>.
- (107) Vining, C. B. An Inconvenient Truth about Thermoelectrics. *Nature Materials* **2009**, *8* (2), 83–85. <https://doi.org/10.1038/nmat2361>.
- (108) He, T.; Lin, N.; Du, Z.; Chao, Y.; Cui, J. The Role of Excess Sn in Cu<sub>4</sub>Sn<sub>7</sub>S<sub>16</sub> for Modification of the Band Structure and a Reduction in Lattice Thermal Conductivity. *Journal of Materials Chemistry C* **2017**, *5* (17), 4206–4213. <https://doi.org/10.1039/C7TC00420F>.
- (109) Lokhande, A. C.; Shelke, A.; Babar, P. T.; Kim, J.; Lee, D. J.; Kim, I. C.; Lokhande, C. D.; Kim, J. H. Novel Antibacterial Application of Photovoltaic Cu<sub>2</sub>SnS<sub>3</sub> (CTS) Nanoparticles. *RSC Advances* **2017**, *7* (54), 33737–33744. <https://doi.org/10.1039/c7ra05194h>.
- (110) Jathar, S. B.; Rondiya, S. R.; Jadhav, Y. A.; Nilegave, D. S.; Cross, R. W.; Barma, S. V.; Nasane, M. P.; Gaware, S. A.; Bade, B. R.; Jadkar, S. R.; Funde, A. M.; Dzade, N. Y. Ternary Cu<sub>2</sub>SnS<sub>3</sub>: Synthesis, Structure, Photoelectrochemical Activity, and Heterojunction Band Offset and Alignment. *Chemistry of Materials* **2021**, *33* (6), 1983–1993. <https://doi.org/10.1021/acs.chemmater.0c03223>.
- (111) Wang, C.; Tian, H.; Jiang, J.; Zhou, T.; Zeng, Q.; He, X.; Huang, P.; Yao, Y. Facile Synthesis of Different Morphologies of Cu<sub>2</sub>SnS<sub>3</sub> for High-Performance Supercapacitors. *ACS Applied Materials and Interfaces* **2017**, *9* (31), 26038–26044. <https://doi.org/10.1021/acsami.7b07190>.
- (112) Wei, Y.; Zhou, Z.; Jiang, P.; Zheng, S.; Xiong, Q.; Zhang, B.; Wang, G.; Lu, X.; Han, G.; Zhou, X. Phase Composition Manipulation and Twin Boundary

- Engineering Lead to Enhanced Thermoelectric Performance of Cu<sub>2</sub>SnS<sub>3</sub>. *ACS Applied Energy Materials* **2021**, acaem.1c01483. <https://doi.org/10.1021/acsaem.1c01483>.
- (113) Li, C.; Song, H.; Cheng, Y.; Qi, R.; Huang, R.; Cui, C.; Wang, Y.; Zhang, Y.; Miao, L. Highly Suppressed Thermal Conductivity in Diamond-like Cu<sub>2</sub>SnS<sub>3</sub> by Dense Dislocation. *ACS Applied Energy Materials* **2021**, 4 (9), 8728–8733. <https://doi.org/10.1021/acsaem.1c01859>.
- (114) Gu, Y.; Ai, W.; Zhao, Y.; Hu, X.; Pan, L.; Zong, P.; Lu, C.; Xu, Z.; Wang, Y. Remarkable Thermoelectric Property Enhancement in Cu<sub>2</sub>SnS<sub>3</sub>-CuCo<sub>2</sub>S<sub>4</sub> Nanocomposites via 3D Modulation Doping. *Journal of Materials Chemistry A* **2021**, No. 207890, 121. <https://doi.org/10.1039/D1TA02812J>.
- (115) Zhao, Y.; Gu, Y.; Zhang, P.; Hu, X.; Wang, Y.; Zong, P.; Pan, L.; Lyu, Y.; Koumoto, K. Enhanced Thermoelectric Performance in Polymorphic Heavily Co-Doped Cu<sub>2</sub>SnS<sub>3</sub> through Carrier Compensation by Sb Substitution. *Science and Technology of Advanced Materials* **2021**, 22 (1), 363–372. <https://doi.org/10.1080/14686996.2021.1920821>.
- (116) Giulia, P. Thermoelectric Materials: The Power of Pores. *Nature Reviews Materials*. Macmillan Publishers Limited February 7, 2017, p 17006. <https://doi.org/10.1038/natrevmats.2017.6>.
- (117) Xu, B.; Feng, T.; Li, Z.; Pantelides, S. T.; Wu, Y. Constructing Highly Porous Thermoelectric Monoliths with High-Performance and Improved Portability from Solution-Synthesized Shape-Controlled Nanocrystals. *Nano Letters* **2018**, 18 (6), 4034–4039. <https://doi.org/10.1021/acs.nanolett.8b01691>.
- (118) Xu, B.; Feng, T.; Agne, M. T.; Zhou, L.; Ruan, X.; Snyder, G. J.; Wu, Y. Highly Porous Thermoelectric Nanocomposites with Low Thermal Conductivity and High Figure of Merit from Large-Scale Solution-Synthesized Bi<sub>2</sub>Te<sub>2.5</sub>Se<sub>0.5</sub> Hollow Nanostructures. *Angewandte Chemie International Edition* **2017**, 56 (13), 3546–3551. <https://doi.org/10.1002/anie.201612041>.
- (119) Hong, M.-H.; Choi, H.; Kim, Y.; Shim, D. Il; Cho, H. H.; Park, H.-H. Thermoelectric Behaviors of ZnO Mesoporous Thin Films Affected by Strain Induced from the Different Dopants Radii (Al, Ga, and In). *Applied Physics Letters* **2021**, 119 (19), 193902. <https://doi.org/10.1063/5.0063497>.
- (120) Tiwari, D.; Chaudhuri, T. K.; Shripathi, T.; Deshpande, U. Synthesis of Earth-Abundant Cu<sub>2</sub>SnS<sub>3</sub> Powder Using Solid State Reaction. *Journal of Physics and Chemistry of Solids* **2014**, 75 (3), 410–415. <https://doi.org/10.1016/j.jpcs.2013.11.012>.
- (121) Aversano, F.; Palumbo, M.; Ferrario, A.; Boldrini, S.; Fanciulli, C.; Baricco, M.; Castellero, A. Intermetallics Role of Secondary Phases and Thermal Cycling on Thermoelectric Properties of TiNiSn Half-Heusler Alloy Prepared by Different Processing Routes. *Intermetallics* **2020**, 127 (October), 106988. <https://doi.org/10.1016/j.intermet.2020.106988>.
- (122) Baranowski, L. L.; Zawadzki, P.; Lany, S.; Toberer, E. S.; Zakutayev, A. A Review of Defects and Disorder in Multinary Tetrahedrally Bonded Semiconductors. *Semiconductor Science and Technology* **2016**, 31 (12). <https://doi.org/10.1088/0268-1242/31/12/123004>.
- (123) Fanciulli, C.; Coduri, M.; Boldrini, S.; Abedi, H.; Tomasi, C.; Famengo, A.; Ferrario, A.; Fabrizio, M.; Passaretti, F. Structural Texture Induced in SnSe Thermoelectric Compound via Open Die Pressing. *Journal of Nanoscience and Nanotechnology* **2017**, 17 (3), 1571–1578. <https://doi.org/10.1166/jnn.2017.13735>.
- (124) Scardi, P.; Leoni, M. Diffraction Line Profiles from Polydisperse Crystalline Systems. *Acta Crystallographica Section A: Foundations of Crystallography* **2001**, 57 (5), 604–613. <https://doi.org/10.1107/S0108767301008881>.

- (125) Lohani, K.; Nautiyal, H.; Ataollahi, N.; Maji, K.; Guilmeau, E.; Scardi, P. Effects of Grain Size on the Thermoelectric Properties of Cu<sub>2</sub>SnS<sub>3</sub>: An Experimental and First-Principles Study. *ACS Applied Energy Materials* **2021**, *4* (11), 12604–12612. <https://doi.org/10.1021/acsaem.1c02377>.
- (126) Ming, H.; Zhu, C.; Qin, X.; Jabar, B.; Chen, T.; Zhang, J.; Xin, H.; Li, D.; Zhang, J. Improving the Thermoelectric Performance of Cu<sub>2</sub>SnSe<sub>3</sub>: Via Regulating Micro-and Electronic Structures. *Nanoscale* **2021**, *13* (7), 4233–4240. <https://doi.org/10.1039/d0nr08045d>.
- (127) Jaldurgam, F. F.; Ahmad, Z.; Touati, F. Low-Toxic, Earth-Abundant Nanostructured Materials for Thermoelectric Applications. *Nanomaterials* **2021**, *11* (4), 895. <https://doi.org/10.3390/nano11040895>.
- (128) Suekuni, K.; Kim, F. S.; Nishiata, H.; Ohta, M.; Tanaka, H. I.; Takabatake, T. High-Performance Thermoelectric Minerals: Colusites Cu<sub>26</sub>V<sub>2</sub>M<sub>6</sub>S<sub>32</sub> (M = Ge, Sn). *Applied Physics Letters* **2014**, *105* (13), 132107. <https://doi.org/10.1063/1.4896998>.
- (129) Guélou, G.; Lemoine, P.; Raveau, B.; Guilmeau, E. Recent Developments in High-Performance Thermoelectric Sulphides: An Overview of the Promising Synthetic Colusites. *Journal of Materials Chemistry C* **2021**, *9* (3), 773–795. <https://doi.org/10.1039/D0TC05086E>.
- (130) Biswas, K.; Zhao, L.-D.; Kanatzidis, M. G. Tellurium-Free Thermoelectric: The Anisotropic n-Type Semiconductor Bi<sub>2</sub>S<sub>3</sub>. *Advanced Energy Materials* **2012**, *2* (6), 634–638. <https://doi.org/10.1002/aenm.201100775>.
- (131) Tan, G.; Hao, S.; Zhao, J.; Wolverton, C.; Kanatzidis, M. G. High Thermoelectric Performance in Electron-Doped AgBi<sub>3</sub>S<sub>5</sub> with Ultralow Thermal Conductivity. *Journal of the American Chemical Society* **2017**, *139* (18), 6467–6473. <https://doi.org/10.1021/jacs.7b02399>.
- (132) Powell, A. V. Recent Developments in Earth-Abundant Copper-Sulfide Thermoelectric Materials. *Journal of Applied Physics* **2019**, *126* (10), 100901. <https://doi.org/10.1063/1.5119345>.
- (133) Baláž, P.; Achimovičová, M.; Baláž, M.; Chen, K.; Dobrozhan, O.; Guilmeau, E.; Hejtmánek, J.; Knížek, K.; Kubičková, L.; Levinský, P.; Puchý, V.; Reece, M. J.; Varga, P.; Zhang, R. Thermoelectric Cu–S-Based Materials Synthesized via a Scalable Mechanochemical Process. *ACS Sustainable Chemistry & Engineering* **2021**, *9* (5), 2003–2016. <https://doi.org/10.1021/acssuschemeng.0c05555>.
- (134) Zhang, X.; Bu, Z.; Shi, X.; Chen, Z.; Lin, S.; Shan, B.; Wood, M.; Snyder, A. H.; Chen, L.; Snyder, G. J.; Pei, Y. Electronic Quality Factor for Thermoelectrics. *Science advances* **2020**, *6* (46), eabc0726. <https://doi.org/10.1126/sciadv.abc0726>.
- (135) Dias, S.; Kumawat, K.; Biswas, S.; Krupanidhi, S. B. Solvothermal Synthesis of Cu<sub>2</sub>SnS<sub>3</sub> Quantum Dots and Their Application in Near-Infrared Photodetectors. *Inorganic Chemistry* **2017**, *56* (4), 2198–2203. <https://doi.org/10.1021/acs.inorgchem.6b02832>.
- (136) Aihara, N.; Matsumoto, Y.; Tanaka, K. Exciton Luminescence from Cu<sub>2</sub>SnS<sub>3</sub> Bulk Crystals. *Applied Physics Letters* **2016**, *108* (9), 092107. <https://doi.org/10.1063/1.4943229>.
- (137) Dahule, R.; Raghav, A.; Hanindriyo, A. T.; Hongo, K.; Maezono, R.; Panda, E. Surface Study of Cu<sub>2</sub>SnS<sub>3</sub> Using First-Principles Density Functional Theory. *Advanced Theory and Simulations* **2021**, *4* (6), 2000315. <https://doi.org/10.1002/adts.202000315>.
- (138) Pavan Kumar, V.; Lemoine, P.; Carnevali, V.; Guélou, G.; Lebedev, O. I.; Boullay, P.; Raveau, B.; Al Rahal Al Orabi, R.; Fornari, M.; Prestipino, C.; Menut, D.; Candolfi, C.; Malaman, B.; Juraszek, J.; Guilmeau, E. Ordered Sphalerite Derivative Cu<sub>5</sub>Sn<sub>2</sub>S<sub>7</sub>: A Degenerate Semiconductor with High

- Carrier Mobility in the Cu–Sn–S Diagram. *Journal of Materials Chemistry A* **2021**, *9* (17), 10812–10826. <https://doi.org/10.1039/D1TA01615F>.
- (139) Black, D. R.; Mendenhall, M. H.; Brown, C. M.; Henins, A.; Filliben, J.; Cline, J. P. Certification of Standard Reference Material 660c for Powder Diffraction. *Powder Diffraction* **2020**, *35* (1), 17–22. <https://doi.org/10.1017/S0885715620000068>.
- (140) Yang, Y.; Ying, P.; Wang, J.; Liu, X.; Du, Z.; Chao, Y.; Cui, J. Enhancing the Thermoelectric Performance of Cu<sub>3</sub>SnS<sub>4</sub>-Based Solid Solutions through Coordination of the Seebeck Coefficient and Carrier Concentration. *Journal of Materials Chemistry A* **2017**, *5* (35), 18808–18815. <https://doi.org/10.1039/c7ta05253g>.
- (141) Kim, H.-S.; Gibbs, Z. M.; Tang, Y.; Wang, H.; Snyder, G. J. Characterization of Lorenz Number with Seebeck Coefficient Measurement. *APL Materials* **2015**, *3* (4), 041506. <https://doi.org/10.1063/1.4908244>.
- (142) Xie, H.; Su, X.; Yan, Y.; Liu, W.; Chen, L.; Fu, J.; Yang, J.; Uher, C.; Tang, X. Thermoelectric Performance of CuFeS<sub>2</sub>+2x Composites Prepared by Rapid Thermal Explosion. *NPG Asia Materials* **2017**, *9* (6), e390–e390. <https://doi.org/10.1038/am.2017.80>.
- (143) Deng, T.; Qiu, P.; Xing, T.; Zhou, Z.; Wei, T.-R.; Ren, D.; Xiao, J.; Shi, X.; Chen, L. A Low-Cost and Eco-Friendly Br-Doped Cu<sub>7</sub>Sn<sub>3</sub>S<sub>10</sub> Thermoelectric Compound with ZT around Unity. *Journal of Materials Chemistry A* **2021**, *9* (12), 7946–7954. <https://doi.org/10.1039/D0TA12042A>.
- (144) Isotta, E.; Mukherjee, B.; Bette, S.; Dinnebier, R.; Scardi, P. Static and Dynamic Components of Debye–Waller Coefficients in the Novel Cubic Polymorph of Low-Temperature Disordered Cu<sub>2</sub>ZnSnS<sub>4</sub>. *IUCrJ* **2022**, *9* (2), 272–285. <https://doi.org/10.1107/S2052252522000239>.
- (145) Zhao, Q.; Qin, B.; Wang, D.; Qiu, Y.; Zhao, L. D. Realizing High Thermoelectric Performance in Polycrystalline SnSe via Silver Doping and Germanium Alloying. *ACS Applied Energy Materials* **2020**, *3* (3), 2049–2054. <https://doi.org/10.1021/acsaem.9b01475>.
- (146) Sharma, S. D.; Khasimsaheb, B.; Chen, Y. Y.; Neeleshwar, S. Enhanced Thermoelectric Performance of Cu<sub>2</sub>ZnSnS<sub>4</sub> (CZTS) by Incorporating Ag Nanoparticles. *Ceramics International* **2019**, *45* (2), 2060–2068. <https://doi.org/10.1016/j.ceramint.2018.10.109>.
- (147) Ballikaya, S.; Chi, H.; Salvador, J. R.; Uher, C. Thermoelectric Properties of Ag-Doped Cu<sub>2</sub>Se and Cu<sub>2</sub>Te. *Journal of Materials Chemistry A* **2013**, *1* (40), 12478–12484. <https://doi.org/10.1039/c3ta12508d>.
- (148) Zhang, L.; Wang, J.; Cheng, Z.; Sun, Q.; Li, Z.; Dou, S. Lead-Free SnTe-Based Thermoelectrics: Enhancement of Thermoelectric Performance by Doping with Gd/Ag. *Journal of Materials Chemistry A* **2016**, *4* (20), 7936–7942. <https://doi.org/10.1039/c6ta01994c>.
- (149) Jin, Z.; Mao, T.; Qiu, P.; Yue, Z.; Wang, L.; Zhao, K.; Ren, D.; Shi, X.; Chen, L. Thermoelectric Properties and Service Stability of Ag-Containing Cu<sub>2</sub>Se. *Materials Today Physics* **2021**, *21*, 100550. <https://doi.org/10.1016/j.mtphys.2021.100550>.
- (150) Cheng, X.; Yang, D.; Su, X.; Xie, H.; Liu, W.; Zheng, Y.; Tang, X. Synergistically Enhanced Thermoelectric Performance of Cu<sub>2</sub>SnSe<sub>3</sub>-Based Composites via Ag Doping Balance. *ACS Applied Materials and Interfaces* **2021**, *13* (46), 55178–55187. <https://doi.org/10.1021/acsaami.1c17460>.
- (151) Mehmood, F.; Wang, H.; Su, W.; Khan, M.; Huo, T.; Chen, T.; Chebanova, G.; Romanenko, A.; Wang, C. Enhanced Power Factor and Figure of Merit of Cu<sub>2</sub>ZnSnSe<sub>4</sub>-Based Thermoelectric Composites by Ag Alloying. *Inorganic Chemistry* **2021**, *963* (February), 0–8. <https://doi.org/10.1021/acs.inorgchem.1c00079>.

- (152) Lohani, K.; Nautiyal, H.; ataollahi, narges; Maji, K.; Guilmeau, E.; Scardi, P. Effects of Grain Size on the Thermoelectric Properties of  $\text{Cu}_2\text{SnS}_3$ : An Experimental and First-Principles Study. *ACS Applied Energy Materials* **4** (11), 12604–12612. <https://doi.org/10.1021/acsaem.1c02377>.
- (153) Scardi, P. Diffraction Line Profiles in the Rietveld Method. *Crystal Growth & Design* **2020**, *20* (10), 6903–6916. <https://doi.org/10.1021/acs.cgd.0c00956>.
- (154) Heyd, J.; Scuseria, G. E. Efficient Hybrid Density Functional Calculations in Solids: Assessment of the Heyd-Scuseria-Ernzerhof Screened Coulomb Hybrid Functional. *Journal of Chemical Physics* **2004**, *121* (3), 1187–1192. <https://doi.org/10.1063/1.1760074>.
- (155) Lohani, K.; Fanciulli, C.; Scardi, P. Effects of Preparation Procedures and Porosity on Thermoelectric Bulk Samples of  $\text{Cu}_2\text{SnS}_3$  (CTS). *Materials* **2022**, *15* (3), 712. <https://doi.org/10.3390/ma15030712>.
- (156) Xie, H.; Su, X.; Hao, S.; Zhang, C.; Zhang, Z.; Liu, W.; Yan, Y.; Wolverton, C.; Tang, X.; Kanatzidis, M. G. Large Thermal Conductivity Drops in the Diamondoid Lattice of  $\text{CuFeS}_2$  by Discordant Atom Doping. *Journal of the American Chemical Society* **2019**, *141* (47), 18900–18909. <https://doi.org/10.1021/jacs.9b10983>.
- (157) Li, Y.; Liu, G.; Cao, T.; Liu, L. M.; Li, J.; Chen, K.; Li, L.; Han, Y.; Zhou, M. Enhanced Thermoelectric Properties of  $\text{Cu}_2\text{SnSe}_3$  by (Ag,In)-Co-Doping. *Advanced Functional Materials* **2016**, *26* (33), 6025–6032. <https://doi.org/10.1002/adfm.201601486>.
- (158) Baláz, P.; Achimovičová, M.; Baláz, M.; Chen, K.; Dobrozhan, O.; Guilmeau, E.; Hejtmánek, J.; Knížek, K.; Kubičková, L.; Levinský, P.; Puchý, V.; Reece, M. J.; Varga, P.; Zhang, R. Thermoelectric Cu–S-Based Materials Synthesized via a Scalable Mechanochemical Process. *ACS Sustainable Chemistry & Engineering* **2021**, *9* (5), 2003–2016. <https://doi.org/10.1021/acssuschemeng.0c05555>.
- (159) Syafiq, U.; Isotta, E.; Ataollahi, N.; Lohani, K.; Luong, S.; Trifiletti, V.; Fenwick, O.; Scardi, P. Facile and Low-Cost Fabrication of Cu/Zn/Sn-Based Ternary and Quaternary Chalcogenides Thermoelectric Generators. *Submitted* **2022**.
- (160) Zeier, W. G.; Zevalkink, A.; Gibbs, Z. M.; Hautier, G.; Kanatzidis, M. G.; Snyder, G. J. Thinking Like a Chemist: Intuition in Thermoelectric Materials. *Angewandte Chemie - International Edition* **2016**, *55* (24), 6826–6841. <https://doi.org/10.1002/anie.201508381>.
- (161) Bell, L. E. Cooling, Heating, Generating Power, and Recovering Waste Heat with Thermoelectric Systems. *Science* **2008**, *321* (5895), 1457–1461. <https://doi.org/10.1126/science.1158899>.
- (162) Hannink, R. H. J.; Hill, A. J. *Nanostructure Control of Materials*; 2006. <https://doi.org/10.1533/9781845691189>.
- (163) Disalvo, F. J. Thermoelectric Cooling and Power Generation. *Science* **1999**, *285* (5428), 703–706. <https://doi.org/10.1126/science.285.5428.703>.
- (164) Fan, P.; Zheng, Z. H.; Li, Y. Z.; Lin, Q. Y.; Luo, J. T.; Liang, G. X.; Cai, X. M.; Zhang, D. P.; Ye, F. Low-Cost Flexible Thin Film Thermoelectric Generator on Zinc Based Thermoelectric Materials. *Applied Physics Letters* **2015**, *106* (7). <https://doi.org/10.1063/1.4909531>.
- (165) Chen, X.; Zhou, Z.; Lin, Y. H.; Nan, C. Thermoelectric Thin Films: Promising Strategies and Related Mechanism on Boosting Energy Conversion Performance. *Journal of Materiomics* **2020**, *6* (3), 494–512. <https://doi.org/10.1016/j.jmat.2020.02.008>.
- (166) Pei, Y. L.; He, J.; Li, J. F.; Fuli, Liu, Q.; Pan, W.; Barreateau, C.; Berardan, D.; Dragoe, N.; Zhao, L. D. High Thermoelectric Performance of Oxyselenides: Intrinsically Low Thermal Conductivity of Ca-Doped  $\text{BiCuSeO}$ . *NPG Asia*

- Materials* **2013**, 5 (5). <https://doi.org/10.1038/am.2013.15>.
- (167) Szczech, J. R.; Higgins, J. M.; Jin, S. Enhancement of the Thermoelectric Properties in Nanoscale and Nanostructured Materials. *Journal of Materials Chemistry* **2011**, 21 (12), 4037–4055. <https://doi.org/10.1039/c0jm02755c>.
- (168) White, M. A.; Medina-Gonzalez, A. M.; Vela, J. Soft Chemistry, Coloring and Polytypism in Filled Tetrahedral Semiconductors: Toward Enhanced Thermoelectric and Battery Materials. *Chemistry - A European Journal* **2018**, 24 (15), 3650–3658. <https://doi.org/10.1002/chem.201704630>.
- (169) Min, G.; Rowe, D. M. Cooling Performance of Integrated Thermoelectric Microcooler. *Solid-State Electronics* **1999**, 43 (5), 923–929. [https://doi.org/10.1016/S0038-1101\(99\)00045-3](https://doi.org/10.1016/S0038-1101(99)00045-3).
- (170) Chen, W. Y.; Shi, X. L.; Zou, J.; Chen, Z. G. Thermoelectric Coolers: Progress, Challenges, and Opportunities. *Small Methods* **2022**, 6 (2), 1–21. <https://doi.org/10.1002/smt.202101235>.
- (171) Isotta, E.; Syafiq, U.; Ataollahi, N.; Chiappini, A.; Malerba, C.; Luong, S.; Trifiletti, V.; Fenwick, O.; Pugno, N. M.; Scardi, P. Thermoelectric Properties of CZTS Thin Films: Effect of Cu-Zn Disorder. *Physical Chemistry Chemical Physics* **2021**, 23 (23), 13148–13158. <https://doi.org/10.1039/d1cp01327k>.
- (172) Shen, Y.; Wang, C.; Yang, X.; Li, J.; Lu, R.; Li, R.; Zhang, L.; Chen, H.; Zheng, X.; Zhang, T. New Progress on Fiber-Based Thermoelectric Materials: Performance, Device Structures and Applications. *Materials*. 2021. <https://doi.org/10.3390/ma14216306>.
- (173) Cao, T.; Shi, X.-L.; Zou, J.; Chen, Z.-G. Advances in Conducting Polymer-Based Thermoelectric Materials and Devices. *Microstructures* **2021**, No. 91223202. <https://doi.org/10.20517/microstructures.2021.06>.
- (174) Bao, D.; Sun, Q.; Huang, L.; Chen, J.; Tang, J.; Zhou, D.; Hong, M.; Yang, L.; Chen, Z. G. Thermoelectric Performance of P-Type (Bi,Sb)<sub>2</sub>Te<sub>3</sub> Incorporating Amorphous Sb<sub>2</sub>S<sub>3</sub> Nanospheres. *Chemical Engineering Journal* **2022**, 430 (P1), 132738. <https://doi.org/10.1016/j.cej.2021.132738>.
- (175) Isotta, E.; Mukherjee, B.; Fanciulli, C.; Ataollahi, N.; Sergueev, I.; Stankov, S.; Edla, R.; Pugno, N. M.; Scardi, P. Origin of a Simultaneous Suppression of Thermal Conductivity and Increase of Electrical Conductivity and Seebeck Coefficient in Disordered Cubic Cu<sub>2</sub>ZnSnS<sub>4</sub>. *Physical Review Applied* **2020**, 14 (6), 064073. <https://doi.org/10.1103/PhysRevApplied.14.064073>.
- (176) Kush, P.; Deka, S. Multifunctional Copper-Based Quaternary Chalcogenide Semiconductors Toward State-of-the-Art Energy Applications. *ChemNanoMat* **2019**, 5 (4), 373–402. <https://doi.org/10.1002/cnma.201800321>.
- (177) Jo, E.; Gang, M. G.; Shim, H.; Suryawanshi, M. P.; Ghorpade, U. V.; Kim, J. H. 8% Efficiency Cu<sub>2</sub>ZnSn(S,Se)<sub>4</sub> (CZTSSe) Thin Film Solar Cells on Flexible and Lightweight Molybdenum Foil Substrates. *ACS Applied Materials and Interfaces* **2019**, 11 (26), 23118–23124. <https://doi.org/10.1021/acsami.9b03195>.
- (178) Gunavathy, K. V.; Tamilarasan, K.; Rangasami, C.; Arulanantham, A. M. S. Solution Processed Copper Zinc Tin Sulfide Thin Films for Thermoelectric Device Applications. *Ceramics International* **2020**, 46 (18), 28342–28354. <https://doi.org/10.1016/j.ceramint.2020.07.338>.
- (179) Jiang, Q.; Yan, H.; Lin, Y.; Shen, Y.; Yang, J.; Reece, M. J. Colossal Thermoelectric Enhancement in Cu<sub>2+x</sub>Zn<sub>1-x</sub>SnS<sub>4</sub> solid Solution by Local Disorder of Crystal Lattice and Multi-Scale Defect Engineering. *Journal of Materials Chemistry A* **2020**, 8 (21), 10909–10916. <https://doi.org/10.1039/d0ta01595d>.
- (180) Guo, H.; Wang, S.; Wang, L.; Jin, K. J.; Chen, S.; Fu, G.; Ge, C.; Lu, H.; Wang, C.; He, M.; Yang, G. Electrical Properties of Thermoelectric Cobalt

- Ca<sub>3</sub>Co 4O<sub>9</sub> Epitaxial Heterostructures. *Journal of Applied Physics* **2013**, *113* (11). <https://doi.org/10.1063/1.4795767>.
- (181) Takayama, K.; Takashiri, M. Multi-Layered-Stack Thermoelectric Generators Using p-Type Sb<sub>2</sub>Te<sub>3</sub> and n-Type Bi<sub>2</sub>Te<sub>3</sub> Thin Films by Radio-Frequency Magnetron Sputtering. *Vacuum* **2017**, *144*, 164–171. <https://doi.org/10.1016/j.vacuum.2017.07.030>.
- (182) Lu, Z.; Layani, M.; Zhao, X.; Tan, L. P.; Sun, T.; Fan, S.; Yan, Q.; Magdassi, S.; Hng, H. H. Fabrication of Flexible Thermoelectric Thin Film Devices by Inkjet Printing. *Small* **2014**, *10* (17), 3551–3554. <https://doi.org/10.1002/sml.201303126>.
- (183) Harman, T. C.; Taylor, P. J.; Walsh, M. P.; LaForge, B. E. Quantum Dot Superlattice Thermoelectric Materials and Devices. *Science* **2002**, *297* (5590), 2229–2232. <https://doi.org/10.1126/science.1072886>.
- (184) Venkatasubramanian, R.; Siivola, E.; Colpitts, T.; The, K.; Kanatzidis, G.; Zt, T.; Vining, B. Thin-Film Thermoelectric Devices with High Room-Temperature Figures of Merit. *October* **2001**, 597–602.
- (185) Park, N. W.; Ahn, J. Y.; Park, T. H.; Lee, J. H.; Lee, W. Y.; Cho, K.; Yoon, Y. G.; Choi, C. J.; Park, J. S.; Lee, S. K. Control of Phonon Transport by the Formation of the Al<sub>2</sub>O<sub>3</sub> Interlayer in Al<sub>2</sub>O<sub>3</sub>-ZnO Superlattice Thin Films and Their in-Plane Thermoelectric Energy Generator Performance. *Nanoscale* **2017**, *9* (21), 7027–7036. <https://doi.org/10.1039/c7nr00690j>.
- (186) Abutaha, A. I.; Sarath Kumar, S. R.; Alshareef, H. N. Crystal Orientation Dependent Thermoelectric Properties of Highly Oriented Aluminum-Doped Zinc Oxide Thin Films. *Applied Physics Letters* **2013**, *102* (5). <https://doi.org/10.1063/1.4790644>.
- (187) Jantrasee, S.; Moontragoon, P.; Pinitsoontorn, S. Thermoelectric Properties of Al-Doped ZnO: Experiment and Simulation. *Journal of Semiconductors* **2016**, *37* (9). <https://doi.org/10.1088/1674-4926/37/9/092002>.
- (188) Jood, P.; Mehta, R. J.; Zhang, Y.; Peleckis, G.; Wang, X.; Siegel, R. W.; Borca-Tasciuc, T.; Dou, S. X.; Ramanath, G. Al-Doped Zinc Oxide Nanocomposites with Enhanced Thermoelectric Properties. *Nano Letters* **2011**, *11* (10), 4337–4342. <https://doi.org/10.1021/nl202439h>.
- (189) De Vries, J. W. C. Temperature and Thickness Dependence of the Resistivity of Thin Polycrystalline Aluminium, Cobalt, Nickel, Palladium, Silver and Gold Films. *Thin Solid Films* **1988**, *167* (1–2), 25–32. [https://doi.org/10.1016/0040-6090\(88\)90478-6](https://doi.org/10.1016/0040-6090(88)90478-6).
- (190) Choi, S. K.; Lee, J. I. Effect of Film Density on Electrical Properties of Indium Tin Oxide Films Deposited by Dc Magnetron Reactive Sputtering. *Journal of Vacuum Science & Technology A: Vacuum, Surfaces, and Films* **2001**, *19* (5), 2043–2047. <https://doi.org/10.1116/1.1371326>.
- (191) Vieira, E. M. F.; Silva, J. P. B.; Veltruská, K.; Istrate, C. M.; Lenzi, V.; Trifiletti, V.; Lorenzi, B.; Matolín, V.; Ghica, C.; Marques, L.; Fenwick, O.; Goncalves, L. M. All-Oxide p-n Junction Thermoelectric Generator Based on SnO<sub>x</sub> and ZnO Thin Films. *ACS Applied Materials and Interfaces* **2021**, *13* (29), 35187–35196. <https://doi.org/10.1021/acsami.1c09748>.
- (192) Ding, D.; Sun, F.; Xia, F.; Tang, Z. A High-Performance and Flexible Thermoelectric Generator Based on the Solution-Processed Composites of Reduced Graphene Oxide Nanosheets and Bismuth Telluride Nanoplates. *Nanoscale Advances* **2020**, *2* (8), 3244–3251. <https://doi.org/10.1039/d0na00118j>.
- (193) Yamamuro, H.; Takashiri, M. Power Generation in Slope-Type Thin-Film Thermoelectric Generators by the Simple Contact of a Heat Source. *Coatings* **2019**, *9* (2). <https://doi.org/10.3390/coatings9020063>.
- (194) Ashfaq, A.; Jacob, J.; Mahmood, K.; Mehboob, K.; Ikram, S.; Ali, A.; Amin,

- N.; Hussain, S.; Rehman, U. Effect of Sulfur Amount during Post-Growth Sulfurization Process on the Structural, Morphological and Thermoelectric Properties of Sol-Gel Grown Quaternary Chalcogenide Cu<sub>2</sub>ZnSnS<sub>4</sub> Thin Films. *Physica B: Condensed Matter* **2020**, *602*, 412497. <https://doi.org/10.1016/j.physb.2020.412497>.
- (195) Zhao, Y.; Han, X.; Xu, B.; Dong, C.; Li, J.; Yan, X. Effect of Sulfurization Process on the Properties of Solution-Processed Cu<sub>2</sub>SnS<sub>3</sub> Thin Film Solar Cells. *Journal of Materials Science: Materials in Electronics* **2019**, *30* (19), 17947–17955. <https://doi.org/10.1007/s10854-019-02148-5>.
- (196) Burton, M. R.; Liu, T.; McGettrick, J.; Mehraban, S.; Baker, J.; Pockett, A.; Watson, T.; Fenwick, O.; Carnie, M. J. Thin Film Tin Selenide (SnSe) Thermoelectric Generators Exhibiting Ultralow Thermal Conductivity. *Advanced Materials* **2018**, *30* (31). <https://doi.org/10.1002/adma.201801357>.
- (197) Biswas, K.; He, J.; Blum, I. D.; Wu, C. I.; Hogan, T. P.; Seidman, D. N.; Dravid, V. P.; Kanatzidis, M. G. High-Performance Bulk Thermoelectrics with All-Scale Hierarchical Architectures. *Nature* **2012**, *489* (7416), 414–418. <https://doi.org/10.1038/nature11439>.
- (198) Li, Y.; Wang, G.; Akbari-Saatlu, M.; Procek, M.; Radamson, H. H. Si and SiGe Nanowire for Micro-Thermoelectric Generator: A Review of the Current State of the Art. *Frontiers in Materials* **2021**, *8* (March), 1–24. <https://doi.org/10.3389/fmats.2021.611078>.
- (199) Linseis, V.; Völklein, F.; Reith, H.; Nielsch, K.; Woias, P. Advanced Platform for the In-Plane ZT Measurement of Thin Films. *Review of Scientific Instruments* **2018**, *89* (1). <https://doi.org/10.1063/1.5005807>.
- (200) Liu, T.; Zhao, X.; Li, J.; Liu, Z.; Liscio, F.; Milita, S.; Schroeder, B. C.; Fenwick, O. Enhanced Control of Self-Doping in Halide Perovskites for Improved Thermoelectric Performance. *Nature Communications* **2019**, *10* (1), 1–9. <https://doi.org/10.1038/s41467-019-13773-3>.
- (201) Lafond, A.; Choubac, L.; Guillot-Deudon, C.; Deniard, P.; Jobic, S. Crystal Structures of Photovoltaic Chalcogenides, an Intricate Puzzle to Solve: The Cases of CIGSe and CZTS Materials. *Zeitschrift für Anorganische und Allgemeine Chemie* **2012**, *638* (15), 2571–2577. <https://doi.org/10.1002/zaac.201200279>.
- (202) Chen, L.; Park, C. Effects of Annealing Temperature on Cu<sub>2</sub>ZnSnS<sub>4</sub> (CZTS) Films Formed by Electrospray Technique. *Korean Journal of Chemical Engineering* **2017**, *34* (4), 1187–1191. <https://doi.org/10.1007/s11814-017-0011-7>.
- (203) Zhang, D.; Zhang, B.; Zhou, Z.; Peng, K.; Wu, H.; Wang, H.; Wang, G.; Han, G.; Wang, G.; Zhou, X.; Lu, X. Ultralow Lattice Thermal Conductivity of Cubic CuFeS<sub>2</sub> Induced by Atomic Disorder. *Chemistry of Materials* **2021**. <https://doi.org/10.1021/acs.chemmater.1c03785>.
- (204) Cherniushok, O.; Smitiukh, O. V.; Tobola, J.; Knura, R.; Marchuk, O. V.; Parashchuk, T.; Wojciechowski, K. T. Crystal Structure and Thermoelectric Properties of Novel Quaternary Cu<sub>2</sub>MHf<sub>3</sub>S<sub>8</sub> (M—Mn, Fe, Co, and Ni) Thiospinels with Low Thermal Conductivity. *Chemistry of Materials* **2022**, *8*. <https://doi.org/10.1021/acs.chemmater.1c03593>.
- (205) Sulaiman, S.; Izman, S.; Uday, M. B.; Omar, M. F. Review on Grain Size Effects on Thermal Conductivity in ZnO Thermoelectric Materials. *RSC Advances* **2022**, *12* (9), 5428–5438. <https://doi.org/10.1039/d1ra06133j>.

Taking advantage of the fact that disordered materials present better thermoelectric performance due to their suppressed thermal conductivity. Novel disordered CTS polymorph was produced and stabilized via bottom-up high-energy reactive ball-milling without any chemical alteration. The effects of various synthesis and sintering techniques (traditional, ODP, and SPS) were investigated. Moreover, the impact of grain size and porosity on thermoelectric properties was studied. Ag-doping was used to enhance the thermoelectric properties of CTS. Finally, functioning CTS thin film (synthesized using spin-coating and sputtering) thermoelectric generators were fabricated and optimized. The experimental work was followed by state-of-the-art synchrotron source measurements and computational techniques.

**Ketan Lohani** was born on 9 December 1996 in Almora, India. He obtained B.Sc. (Hons.) Physics in 2016 from the University of Delhi and M.Sc. Physics in 2018 from the Central University of Haryana, India. In his master's thesis work, he studied nickel-ferrite nanoparticles using various beamlines of Indus-II synchrotron source at Raja Ramanna Centre of Advanced Technology, India. Ketan, started his Ph.D. Project in Advanced Energy Materials in November 2018 at Department of Civil, Environmental and Mechanical Engineering, University of Trento, Italy. During this, he investigated Cu-Sn-S-based thermoelectric materials and devices.